Computer-Aided Model Development, Process Design and Operating Strategies for Transient Liquid Multiphase Systems

Dissertation
zur Erlangung des akademischen Grades

Doktoringenieur

(Dr.-Ing.)

von M.Sc. Karsten Hans Georg Rätze
geb. am: 02. Februar 1992 in Helmstedt

genehmigt durch die Fakultät für Verfahrens- und Systemtechnik
der Otto-von-Guericke-Universität Magdeburg

Promotionskommission:	Professor Dr.-Ing. habil. Christof Hamel (Vorsitz)
	Professor Dr.-Ing. habil. Kai Sundmacher (Gutachter)
	Professor Dr.-Ing. Sebastian Engell (Gutachter)
	Professor Michael Doherty, Ph.D. (Gutachter)

eingereicht am:	25. Oktober 2022
Promotionskolloquium am:	8. September 2023

My favorite things in life don't cost any money. It's really clear that the most precious resource we all have is time.

— **Steve Jobs**

Abstract

Presented with the challenges of digitalization and the transformation toward a sustainable and biomass-based chemicals production, the chemical industry faces the necessity for a rapid design of new processes to meet recent governmental, supply chain-related and technical requirements. Due to the short time horizon of this transformation, systematic and model-based design approaches are necessary to allocate time and money only to the most promising process candidates. As model-based process design starts with the identification of a suitable reaction kinetic model and continuous with the conceptual design, process construction, and operation, this work encompasses all major steps of the design process and provides new methodological approaches and investigations for the design of liquid multiphase systems.

Liquid multiphase systems appear in many homogeneously catalyzed, industrially relevant processes so that the development of model-based tools for the design of innovative and sustainable processes became the major goal of the trans-regional collaborative research center on *Integrated Chemical Processes in Liquid Multiphase Systems (InPROMPT)*. Exemplified on the homogeneously rhodium-catalyzed hydroformylation and hydroaminomethylation of long-chain olefins, approaches for the process development, ranging from the identification of an unknown reaction kinetic network over the selection of suitable solvent systems to the operation and control under miniplant-scale conditions, were developed. The presented work reflects a subset of these developments and aims at the extension of existing and the creation of new methodologies for the model-based process design.

A suitable reaction kinetic model represents the foundation for all subsequent steps in a quantitative model-based process design. By utilizing an initial reaction kinetic model, model-based optimal experimental design (mbOED) can be applied to identify experiments with high information content and, thus, reduce experimental time and cost. Additionally, mbOED enables the incorporation of non-linear system constraints which is essential for the prevention of phase separation and mass transfer limitations in the design of kinetic experiments for the homogeneously, rhodium-catalyzed hydroaminomethylation in a thermomorphic multiphase system. After training an artificial neural network for the prediction of activity coefficients using the PC-SAFT equation of state, rigorous phase equilibrium calculations are incorporated

in the simultaneous design of five experiments to prevent the occurrence of multiple phases. With the reaction kinetic experimental data from these experiments, an initial candidate for the hydroaminomethylation kinetics is structurally refined and calibrated to achieve high quality predictions under various operating conditions.

For the next step in process design, the kinetic model of the hydroaminomethylation is used in the conceptual design of reactor-network candidates using the elementary process functions (EPF) methodology. Due to catalyst leaching to an aqueous phase in a potentially optimal reactor-network candidate with multiple phases, the EPF methodology is extended toward the rigorous consideration of multiphase systems under transient conditions. This multiphase elementary process functions (mpEPF) formulation incorporates phase equilibrium calculations in the EPF methodology to gain and act on information regarding the composition and number of system phases. In addition to the identification of optimal control profiles under multiple operating scenarios with a product selectivity of over 98 % under full conversion, the mpEPF is applied to a generic example reaction to demonstrate its capability to actively use multiple phases for the design of a reactor-separator sequence.

In the last process design step, the translation of an optimal reactor-network candidate into a miniplant-scale process with an innovative reactor unit is exemplified for the hydroformylation sub-reaction network of the hydroaminomethylation. At its core, a repeatedly operated semibatch reactor is interfaced to the continuously operated rest of the process for the application of the optimal control profiles from the EPF calculations. As accurate estimates on the volume flows between different process units and the time required to achieve the cyclic steady-state are valuable information for the process operation, a rigorous, dynamic process model is formulated and used for the preparation of experimental miniplant campaigns. Different operating conditions with an increasing number of degrees of freedom are simulated, optimized, and compared to experimental results to achieve model validation and the demonstration of an experimentally verified increase of conversion and yield over the reference process by 15 and 17 percentage points, respectively.

This work presents methodological extensions to (i) the optimal design of reaction kinetic experiments, (ii) the optimal design of reactor-separator sequences, and (iii) the optimal operation of chemical processes in the context of liquid multiphase systems and demonstrates their value by experimental validation. Because of the promising results achieved in this work, many more ideas for refinement and improvement arise. These ideas are summarized and discussed to provide motivation for future research.

Zusammenfassung

Neben neuen gesetzlichen Regelungen, lieferkettenbedingten Anpassungen und veränderten technischen Voraussetzungen sind die Digitalisierung und die vermehrte Nutzung nachhaltiger, Biomasse-basierter Rohstoffe Hauptgründe für die Notwendigkeit einer schnellen Entwicklung neuer Herstellungsprozesse in der chemischen Industrie. Durch den kurzen Zeitraum, der für die Umsetzung der Umstrukturierung zur Verfügung steht, ist ein systematisches und modellgestütztes Vorgehen bei der Auslegung unabdingbar, um wertvolle Zeit und Geld ausschließlich in die vielversprechendsten Prozesskandidaten zu investieren. Aufgrund des mehrstufigen Auslegungs- und Entwicklungsprozesses, welcher die Identifizierung geeigneter reaktionskinetischer Modelle, den konzeptionellen Prozessentwurf, die Konstruktion sowie den Prozessbetrieb beinhaltet, ist das Ziel der vorliegenden Arbeit neue Methodiken und Analysen zu den wichtigsten Schritten im Prozessentwurf von flüssigen Mehrphasensystemen vorzuschlagen und zu untersuchen.

Flüssige Mehrphasensysteme sind häufig in homogenkatalysierten, industriell relevanten Prozessen anzutreffen, sodass sich der trans-regionale Sonderforschungsbereich *Integrierte Chemische Prozesse in flüssigen Mehrphasensystemen (InPROMPT)* die Entwicklung von modellgestützten Werkzeugen zum Entwurf innovativer und nachhaltiger chemischer Produktionsprozesse zum Ziel erklärt hat. Alle Schritte des Prozessentwurfs werden am Beispiel von homogenkatalysierten Hydroformylierungs- und Hydroaminomethylierungsreaktionen langkettiger Olefine mit Rhodiumkatalysatoren demonstriert. Dies beinhaltet neben der Identifikation von unbekannten reaktionskinetischen Netzwerken und der Auswahl geeigneter Lösungsmittelsysteme den Betrieb, die Steuerung und Reglung von Anlagen im Miniplant Maßstab. In dieser Arbeit wird eine Teilmenge dieser Entwicklungen mit dem Fokus auf der Erweiterung bestehender und dem Entwurf neuer Methodiken zum modellgestützten Prozessentwurf präsentiert.

Das Fundament eines jeden modellgestützten Prozessentwurfs bildet die Formulierung geeigneter reaktionskinetischer Modelle. Falls bereits ein vorläufiges kinetisches Modell existiert, bietet sich die Nutzung von modellgestütztem experimentellen Design (mbOED) an, welches in der Lage ist hochinformative Experimente zu identifizieren, um so Zeit und Kosten bei der experimentellen Untersuchung zu reduzieren. Weiterhin ist es durch den Einsatz von mbOED möglich, experimentelle Designs

mit Zwangsbedingungen zu belegen, welche insbesondere im Fall von nichtlinearen Systemen beispielhaft dafür eingesetzt werden können, um einen Phasenzerfall und daraus resultierende Stoffübertragungswiderstände während des Experiments zu verhindern. Gerade diese Eigenschaft ist für das experimentelle Design der homogenkatalysierten Hydroaminomethylierung in einem thermomorphen Mehrphasensystem unabdingbar, da hier die Gefahr eines Phasenzerfalls besteht. Um diese Art der Zwangsbedingungen zu berücksichtigen, wurde zunächst ein künstliches neuronales Netzwerk auf Basis von Daten der PC-SAFT Zustandsgleichung trainiert, mit dessen Hilfe Aktivitätskoeffizienten vorhergesagt werden können. Dies wird für die Einbettung von Phasengleichgewichtsberechnungen in das mbOED von fünf simultanen Experimenten benötigt, um die Entstehung mehrerer Phasen effektiv zu verhindern. Auf Basis der sich daraus ergebenden, reaktionskinetischen Experimentaldaten wird eine vorläufige Hydroaminomethylierungskinetik strukturell verbessert und kalibriert, sodass akkurate Vorhersagen des Reaktionsgeschehens unter verschiedenen Betriebsbedingungen möglich sind.

Im nächsten Schritt des Prozessentwurfs wird die Hydroaminomethylierungskinetik verwendet, um mithilfe der Methode der elementaren Prozessfunktionen (EPF) optimale Reaktor-Netzwerk Kandidaten zu identifizieren. Aufgrund von Katalysatorverlust im Falle einer potentiellen Mehrphasigkeit während des Betriebs eines der Reaktor-Netzwerk Kandidaten wird die EPF Methode um die Berücksichtigung transienter Mehrphasensysteme erweitert. Diese Formulierung der elementaren Prozessfunktionen für Mehrphasensysteme (mpEPF) erlaubt die Kombination von Phasengleichgewichtsberechnungen mit der EPF Methode, um so Informationen zu der Komposition und der Anzahl mehrerer Phasen im System nutzen zu können. Angewendet auf die Hydroaminomethylierung können so optimale Steuerprofile für verschiedene Betriebsszenarien identifiziert werden, welche durchweg eine Produktselektivität von 98 % bei Vollumsatz ermöglichen. Weiterhin wird die mpEPF Formulierung auf ein generisches Beispiel angewendet, um ihr Potential durch die aktive Nutzung mehrerer Phasen zum Entwurf einer Reaktor-Separator Sequenz zu demonstrieren.

Im letzten Schritt des Prozessentwurfs erfolgt die Überführung der optimalen Reaktor-Netzwerk Kandidaten in reale Prozesse im Miniplant Maßstab. Dieser Schritt wird am Beispiel der Hydroformylierung demonstriert, welches ein Subnetzwerk der Hydroaminomethylierung darstellt. Zur Umsetzung der optimalen Steuerprofile aus den EPF Berechnungen wird ein innovativer, periodisch betriebener Semibatch Reaktor verwendet, welcher über Puffertanks mit dem kontinuierlich betriebenen Rest des Prozesses verbunden ist. Als Vorbereitung des experimentellen Betriebs der Miniplant Anlage erfolgt die Entwicklung eines rigorosen, dynamischen Pro-

zessmodells, welches verwendet wird, um die Flüsse zwischen den Prozesseinheiten und die notwendige Zeit bis zur Erreichung eines zyklisch stationären Zustands vorherzusagen. Unter der Nutzung verschiedener Betriebsbedingungen und einer stetig steigenden Anzahl an Freiheitsgraden, erfolgt die Validierung des dynamischen Modells und die experimentell demonstrierte Verbesserung von Umsatz und Ausbeute gegenüber einem Referenzprozess um jeweils 15 und 17 Prozentpunkte auf Basis einer modellgestützten Identifizierung optimaler Prozessbedingungen.

Zusammenfassend werden in dieser Arbeit methodische Weiterentwicklungen (i) zum optimalen Design reaktionskinetischer Experimente, (ii) zur optimalen Auslegung von Reaktor-Separator Sequenzen und (iii) zum optimalen Betrieb chemischer Prozesse im Kontext der flüssigen Mehrphasensysteme präsentiert und anhand von experimentellen Daten validiert. Durch die vielversprechenden Ergebnisse gibt es viele weitere Ideen und Verbesserungsvorschläge, welche zusammengefasst und diskutiert werden, um zukünftige Forschung anzustoßen und zu motivieren.

Preface

During the time of writing this dissertation, many scientific results and outcomes were presented and published in various journal articles and book chapters. The following list assigns these publications to the different chapters in this work.

- The introduction of the elementary process functions (EPF) methodology in Section 2.3.3 and all its derivatives is partially taken from Rätze et al. [RJS22].

- Chapter 3 on the model-based identification of the kinetic reaction network of the hydroaminomethylation of 1-decene is based on the journal article by Rätze et al. [Rät+23].

- Chapter 5 on the cyclic operation of a semibatch reactor in a continuous overall process is based on the publications by Jokiel et al. [Jok+19] and Rätze et al. [Rät+19]. While the mathematical and algorithmic formulations as well as the model validation (sections 5.2, 5.3 and 5.4.1) are partially taken from [Rät+19], the residence time assignment, simulation and experimental results from section 5.4.2 are based on the work by Jokiel et al. [Jok+19]. Due to the collaborative work together with Michael Jokiel, section 5.4.3 utilizes experimental results from Jokiel [Jok20] and combines them with original simulations from this dissertation. The control profiles in fig. 5.6, which lie the foundation of the presented experimental results from Jokiel [Jok20], are also an outcome of this dissertation.

- In the outlook in section 6.2, the paragraph on the computer-aided phase system selection and process design is inspired by Rätze et al. [Rät+22].

Journal articles used for this dissertation:

[Rät+19] K. H. G. Rätze, M. Jokiel, N. M. Kaiser, and K. Sundmacher. "Cyclic Operation of a Semi-Batch Reactor for the Hydroformylation of Long-Chain Olefins and Integration in a Continuous Production Process". In: *Chemical Engineering Journal 377* (2019), p. 120453.

[Jok+19] M. Jokiel, K. H. G. Rätze, N. M. Kaiser, et al. "Miniplant-Scale Evaluation of a Semibatch-Continuous Tandem Reactor System for the Hydroformylation of Long-Chain Olefins". In: *Industrial & Engineering Chemistry Research 58.7* (2019), pp. 2471–2480.

[Rät+23] K. H. Rätze, W. Kortuz, S. Kirschtowski, et al. "Optimal Experimental Design for the Identification of a Reaction Kinetic Model for the Hydroaminomethylation of 1-Decene in a Thermomorphic Multiphase System". In: *Chemical Engineering Journal 469* (2023), p. 143713.

Book chapters used for this dissertation:

[Rät+22] K. H. G. Rätze, S. Linke, A. Weber, et al. "Selection Criteria for Liquid Multi- phase Systems". In: *Integrated Chemical Processes in Liquid Multiphase Systems - From Chemical Reaction to Process Design*. Ed. by M. Kraume, S. Enders, A. Drews, et al. 1st ed. De Gruyter, 2022.

[RJS22] K. H. G. Rätze, M. Jokiel, and K. Sundmacher. "Optimal Design of Reactors for Complex Reaction Systems". In: *Integrated Chemical Processes in Liquid Multiphase Systems - From Chemical Reaction to Process Design*. Ed. by M. Kraume, S. Enders, A. Drews, et al. 1st ed. De Gruyter, 2022.

Contents

1 Introduction

Research Vision

The Role of the Chemical Industry. In the first half of the 21st century, digitalization and the renunciation of a fossil-based society are two ambitions of developed and developing countries across the world with strong implications for the (sustainable) evolution of all industries [Uni15a; Tas20; Uni15b]. While this industrial twin transition is challenging in itself, the chemical industry, which serves as a "backbone to many end-market industries" [vThi+16], faces two additional challenges—the transition toward a circular economy while simultaneously adhering to the Registration, Evaluation, Authorisation and Restriction of Chemicals (REACH) legislative of the European Union [Mat21; Eur06].

Example Case: Germany. The most suitable, efficient, and, most importantly, effective steps to achieve a completely sustainable and CO_2-neutral chemicals production are still subject to discussions. Nonetheless, the progressing consequences of the climate change force the regulatory bodies of major economically relevant countries to enforce the fast adaptation and implementation of climate protection regulations with significant consequences due to the dependency on fossil feedstocks and the energy intensive nature of the chemical industry. With a total production and export revenue of chemical and pharmaceutical products in 2020 of 225.9 and 192.1 billion Euro [Ver21], respectively, Germany is among the top three of chemical producing countries and represents the most important exporter for such goods. Therefore, it serves as a good example for the efforts required to achieve a sustainable chemical industry.

The Time Horizon. In 2021, the European Climate Law [Eur21] was ratified in which the European Union commits to the goal of net-carbon-neutrality until 2050. In Germany, the goal of greenhouse gas neutrality was scheduled until 2045 [Bun19] (changed by [Bun21]), leaving 23 years in which major parts of the chemical production processes and supply chains need to be redesigned. If an average time to commercialization from the project initiation until achieving a positive return

of up to 19 years [MMO13] is assumed, the transformation of the entire chemical industry is a challenging task. Besides simplified and shorter planning and approval procedures, speeding up the development of new production processes is required in which digitalization may take a decisive role. New methodologies are required which combine established process design principles with state-of-the-art, digital technologies to achieve the rapid development of new, innovative, and sustainable processes.

InPROMPT. With the intend to contribute to the transformation of the chemical industry, the collaborative research center/transregio 63 *Integrated Chemical Processes in Liquid Multiphase Systems (InPROMPT)* was formed between 2010 and 2022. In a combined effort between major German universities and research facilities, the research center aimed at the development of new methodological approaches and tools for the design of efficient chemical production processes [InP21] which adhere to the principles of Green Chemistry [AW00]. With special emphasis on homogeneously catalyzed, liquid multiphase processes which utilize renewable substrates, strategies for the environmentally friendly, energy, and resource efficient production of chemicals were investigated [InP21].

The Role of PSE. Achieving all of these goals requires the collaboration of different disciplines with expertise in the fields of natural science, engineering, information technology, as well as, the integration of knowledge across multiple process scales. Structuring all of these sources of knowledge, so that they complement each other and aid in the fulfillment of the intended task, requires a holistic view on the process and awareness of its sub-components and their respective links with each other. Process sytems engineering (PSE) acknowledges and approaches the complexity created by these interactions by "systems thinking" or the consideration of systems as a whole [Hab+19]. One important tool for this complex task is the abstraction and simplification of real world phenomena using model formulations. As systems become more complex either by design, due to additional and new constraints or by extension of the system boundaries (broadening of the scope), the importance of incorporating model-based approaches in the decision making process grows significantly. Consequently and in line with the trends of digitalization and Industry 4.0, extending and improving existing or developing new model-based methodologies in terms of accuracy, performance, and applicability, while simultaneously striving for greater accessibility and adoption of these tools, will have a major effect on how current and future challenges can and will be approached and solved.

Research Goals and Motivation

Research Goal. The goal of this work is the extension of the toolbox of model-based methods for a faster and more accurate chemical process development. With the rapid transition toward a sustainable chemical industry, efficient approaches are required in each step of the process design process to drive innovation and confront challenges following the substitution of fossil- with biomass-based raw materials.

Work Context. Accounting for the vast scope of this task, two subprojects in the InPROMPT research center build the foundation on which this work arose. While the first subproject focused on the methodological advancement of model-based approaches for the design of reactor- and reactor-separator-networks, the second subproject was dedicated to their application and experimental validation on selected homogeneously noble-metal catalyzed reactions in liquid multiphase systems.

Primary Methodology. The methodology of elementary process functions (EPF) from Freund and Sundmacher [FS08] is particularly suited to serves as a basis onto which frameworks for the process design and extensions with respect to (w.r.t.) accuracy and prediction reliability can be build. This is due to its unique abstraction of the unit operations in a chemical process as continuously applied functional modules which progress and alter the state of a Lagrangian fluid element in state space over time.

Scope. In this thesis, the core idea of the EPF methodology is borrowed to formulate a multi-step framework in which all major requirements for the successful design of an efficient and performant chemicals production process for liquid multiphase systems (under transient conditions) are met. These major steps comprise the systematic model-based identification of suitable reaction kinetic models, the model-based reactor-separator sequence design, and the translation of process candidates into high performance unit operations alongside their operation. In addition to the theoretical introduction of each step, the steps are applied to industrially relevant processes such as the rhodium-catalyzed hydroaminomethylation and hydroformylation of long-chain olefins for exemplification.

Step 1: Model Identification. The first step deals with the identification of suitable reaction kinetic information in liquid multiphase systems which lies the foundation for the application of all subsequent model-based approaches. Depending on the

design of the reaction system and the type of reaction, the appearance of liquid phases in the process operating window is possible. These multiple phases introduce mass transfer limitations at the interface boundaries which presents a challenge to kinetic measurements of the reaction system if no accurate information about the mass transfer kinetics are available and if these mass transfers are not accounted for in the reaction model. Therefore, it is usually favorable to operate the system under monophasic conditions for reaction kinetic measurements. For these kinds of reaction systems, box constraints may not be sufficient to ensure one liquid phase due to strong non-linear behaviors. As a consequence, model-based optimal experimental design (mbOED) techniques are required which have to be extended by reliable phase equilibrium calculations to maximize the information content of each experiment and the valid operating window under monophasic conditions.

Step 2: Process Design. In the second step, the EPF methodology is extended toward the consideration of multiple transient liquid phases in the form of the multiphase elementary process functions (mpEPF) methodology. The appearance and disappearance of multiple liquid phases due to miscibility gaps between two and more liquid species is not considered in any prior extension but rises in significance in the face of increasing biomass-based feedstock and its direct application as raw material for chemicals production. While the consideration of phase equilibria can be used to prevent the appearance of multiple liquid phases during the reaction to restrict mass transfer limitations in homogeneously catalyzed reactions, it also introduces additional degrees of freedom for the process design which may lead to increased process performance by opening new process routes in state space. These process routes can then be exploited in the design of reactor-separator networks and integrated reactor-separator systems (e.g., reactive distillation).

Step 3: Process Operation. In the third step, alternatives for the realization of sophisticated reactor control trajectories are discussed which may arise from calculations using the EPF methodology. As the realization of complex controls for, e.g., temperature, pressure or the dosing of reactants normally requires significant constructional efforts and approximations, the underlying model-based predictions need to be reliable and accurate to ensure a profitable investment. However, in the early stages of designing a new process, accurate and reliable information on the reaction kinetics are scarce, leading to delays in the process design and prolonged planning phases. Direct realization of the control trajectories in time using a semibatch reactor (SBR) minimizes the constructional effort, simplifies the selection of a suitable reactor unit

and enables the flexible adaptation of the reaction conditions under changing conditions or as an answer to new and updated information. By combining these strengths of a discontinuously operated SBR with a continuously operated downstream process in the form of a repeatedly operated semibatch reactor (RSBR), optimal process performance is achieved and combined with increased operating flexibility as well as additional optimization potential via improved reaction kinetic models, more accurate parameter estimates or relaxed constraints due to new peripheral equipment as "software updates".

Structure of this Work

In chapter 2, the groundwork for this thesis is established by discussing the requirements and possible models for the calculation of phase equilibria in section 2.1. As the reaction kinetic model represents a key asset for the model-based process design, different approaches on the design of kinetic experiments are presented in section 2.2 with special focus on model-based optimal experimental design (mbOED). The subsequent step of process synthesis and conceptual design with all its sub-areas and classifications is introduced concisely in section 2.3 alongside a thorough overview over the EPF methodology and its extension. Finally, the chapter concludes with general information on the production of amines and a detailed look on the hydroaminomethylation reaction with its sub-reaction networks in section 2.4. This lies the foundation for the industrially relevant example process of this work.

Chapter 3 is dedicated to the identification of a reaction kinetic model for the hydroaminomethylation of 1-decene. After a brief motivation on the benefits of mbOED and its relevance for the successful identification of a reaction kinetic model for the example process in section 3.1, a reaction kinetics candidate alongside a suitable reactor vessel model is proposed in section 3.2. In addition to the systematic consideration of the influence of different parameters and expressions on the kinetic model, the intended operating window is presented and a formulation for the model-based design of multiple experiments with simultaneous prevention of multiphasic system behavior is provided. After a short introduction of the initialization algorithm necessary to prevent local optima in section 3.4, the optimal experimental designs are analyzed and discussed. By using experimental data which was generated based on the experimental designs, a detailed reactor vessel model is formulated in section 3.5 with which the structural extension of the reaction kinetics and the subsequent model calibration is performed. Finally, the results are discussed in section 3.6 and a concluding summary and outlook is provided in section 3.7.

With a suitable reaction kinetic model identified, the next step in process design is presented in chapter 4 with the extension of the EPF methodology toward the consideration of multiphase reaction systems under transient conditions. The chapter begins by motivating the need for the rigorous consideration of multiphasic processes in section 4.1. Afterward, the methodological contribution of this work is stated in section 4.2. Subsequent to the theoretical foundation of the multiphase elementary process functions (mpEPF) concept, the formulation is applied to the previously identified hydroaminomethylation reaction kinetics in section 4.3. Multiple scenarios are analyzed and an optimal reactor sequence is proposed before advancing in section 4.4 toward the first hypothetical example case where the mpEPF formulation is successfully used for the design of a reactor-separator sequence. After this demonstration of the capabilities of the mpEPF formulation and a brief chapter summary in section 4.5, an extended discussion on the directions for future research and possible pitfalls in the application of the multiphasic formulation is outlined in section 4.6.

Chapter 5 builds on top of the previous chapter as optimal reactor network candidates, designed based on the EPF methodology, are translated into real-world processes. In section 5.1, the necessity for a closer look at the translation of reactor candidates into process setups and innovative reactor concepts is motivated. Based on the hydroformylation, a sub-reaction network of the hydroaminomethylation, the reasoning behind and the design of a production process using a repeatedly operated semibatch reactor (RSBR) is summarized in section 5.2. Due to the benefits of the cyclic operation, a methodological approach for the formulation of a rigorous, dynamic simulation and optimization model for a RSBR-based hydroformylation process is presented in section 5.3. After a first verification of the results integrity in section 5.4, the dynamic RSBR process model is employed to design experimental investigations on miniplant scale. By increasing the degree of freedoms (DoFs) for each experiment, the potential of the RSBR process is investigated while simultaneously verifying the predicting capabilities of the model. The chapter finishes in section 5.5 with a visual overview over all simulated and experimentally investigated operating points and provides an outlook for possible future investigations.

In the last chapter of this thesis, the work is concluded by summarizing the key results of each chapter followed by an assessment of the insights in a broader context and recommendations for future work.

For the interested reader, background information, implementational details, and additional resources are curated in appendices A to H.

2 Background

Due to the vast scope of this work in which phase equilibrium calculations are combined with mbOED and process design techniques, this background chapter is only able to provide a brief introduction to each of these research fields. As a consequence, no exhaustive discussion of the state of the art is intended but rather a general overview and placement of this work in the literature.

Chapter Overview. In the first section, the thermodynamic and mathematical foundation for the calculation of phase equilibria using different mathematical formulations is provided to describe liquid multiphase systems with coexisting liquid and gaseous phases. Since kinetic models of reaction networks are required for all subsequent model-based applications, the next section discusses the evolution of systematic experimental design and introduces the core concepts and selected extensions of model-based optimal experimental design for reaction kinetic network identification. The next step in process design represents the conceptual process design and process synthesis. Therefore, the third section introduces these two terms and concepts with special focus on the model-based design of reactor and reactor-separator networks. In particular, this includes the elementary process functions methodology as it represents the approach which is extended by phase equilibrium formulations to form the multiphase elementary process functions formulation. In the last section, the hydroaminomethylation and its sub-reactions, the hydroformylation and the reductive amination, are introduced as industrially relevant example processes onto which the methodologies of this work are applied. In addition to general information over the economic relevancy of the amine production and the discussion of different production processes, this section provides reaction kinetic information for the example processes which are used throughout the remainder of this work.

2.1 Phase Equilibria

The calculation of phase equilibria is a necessary part for rigorous modeling of liquid multiphase processes. Independent of the kind of coexisting phases (solid, gaseous,

liquid), the equilibrium for n phases is defined as the simultaneous fulfillment of the thermal

$$T^{(I)} = T^{(II)} = \cdots = T^{(\pi)} = \cdots = T^{(n)}, \tag{2.1a}$$

mechanical

$$p^{(I)} = p^{(II)} = \cdots = p^{(\pi)} = \cdots = p^{(n)}, \tag{2.1b}$$

and chemical

$$\mu_i^{(I)} = \mu_i^{(II)} = \cdots = \mu_i^{(\pi)} = \cdots = \mu_i^{(n)}, \tag{2.1c}$$

equilibrium conditions with $\mu_i^{(\pi)}$ denoting the chemical potential of species $i \in \mathcal{SPC}$ in phase $\pi \in \Pi$. The chemical potential can be derived from the fundamental equations of thermodynamics which is illustrated in appendix A. For the calculation of liquid-liquid equilibriums (LLEs), the formulation via the activity a and activity coefficients γ is the most useful because of a beneficial reference state. With eq. (A.10) from appendix A, eq. (2.1c) simplifies for two arbitrary phases $\pi_1, \pi_2 \in \Pi$ to

$$a_i^{(\pi_1)} = \gamma_i^{(\pi_1)} x_i^{(\pi_1)} = \gamma_i^{(\pi_2)} x_i^{(\pi_2)} = a_i^{(\pi_2)}, \tag{2.2}$$

with the distribution coefficient

$$K_i^{(\pi_1,\pi_2)} := \frac{x_i^{(\pi_1)}}{x_i^{(\pi_2)}} = \frac{\gamma_i^{(\pi_2)}}{\gamma_i^{(\pi_1)}}. \tag{2.3}$$

The activity coefficients for each species i can be taken from measurement data or results from calculations using equations of state (EoS) like Peng-Robinson [PR76], Soave-Redlich-Kwong [Soa72], perturbed-chain statistical associating fluid theory (PC-SAFT) [GS01; GS02] or the group contribution (GC) equivalent GC-PC-SAFT [Tih+08] and quantum-chemical approximations with COSMO and COSMO-RS [Kla11]. In addition, G^{E} models like the Porter [Por20] and Redlich-Kister [RK48] approach, the Wilson equation [Wil64], the non-random two liquid (NRTL) model [RP68], the universal quasi-chemical (UNIQUAC) [AP75; MP78], universal functional activity coefficient (UNIFAC) [FGR77] and modUNIFAC(Dortmund) [WG87; GLS93; Gme+98] models, and volume-translated Peng-Robinson (VTRP) [SG10; SG11; SG16] are possible sources for simulated activity coefficient data.

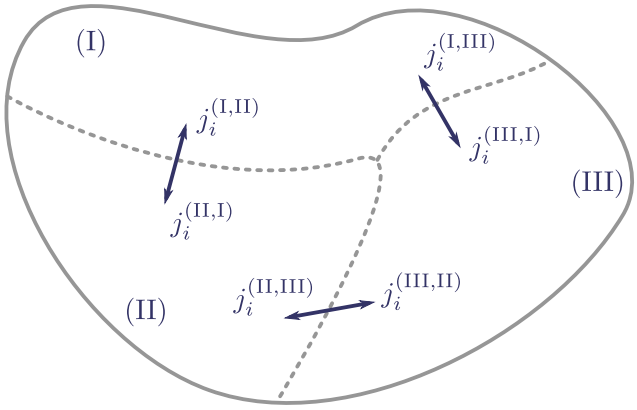

Fig. 2.1.: Phase equilibrium calculation reformulated using mass balances between phases (I) – (III) (adopted from [ZRS16]). The diffusion flows for each species $i \in \mathcal{SPC}$ between two arbitrary phases $\pi_1, \alpha \in \Pi$ are equivalent, so that $j_i^{(\pi_1,\alpha)} = -j_i^{(\alpha,\pi_1)}$.

Phase Equilibrium Calculation

Most phase equilibrium calculations are performed using either the K-value (Rachford-Rice) method [LN95] or the Gibbs enthalpy minimization (GEM) of G^{M} (see eq. (A.11)) [Was+96; MRO17]. While the first method is popular for LLE calculations and performs accurately also for poor initial guesses, the GEM is more reliable for systems with a higher number of species [MRO17]. Despite the availability of efficient algorithms for the GEM [MF97], identification of the global minimum of G^{M} is required which is computationally expensive and challenging to solve.

An alternative method for the solution of not only phase equilibria but also of a combination of phase and chemical equilibria was proposed by Zinser et al. [ZRS16]. In contrast to the direct minimization of the Gibbs enthalpy, the optimization problem is formulated as a mass transfer problem via an ordinary differential equation (ODE) system and solved until the steady-state is reached. An illustration of the method is shown in fig. 2.1. One possible formulation of the ODE system for the calculation of a LLE can be summarized for an exemplary phase $\pi \in \Pi$ and species $i \in \mathcal{SPC}$ as

$$\frac{\mathrm{d}n_i^{(\pi)}}{\mathrm{d}t} = \sum_{\alpha \in \Pi} j_i^{(\pi,\alpha)}, \quad n_i^{(\pi)}(t=0) = n_i^{(\pi),0}, \tag{2.4a}$$

with the species diffusion flow

$$j_i^{(\pi,\alpha)} = -k_{\mathrm{eff},i}^{(\pi,\alpha)} \mathcal{A}^{(\pi,\alpha)} \phi \left(a_i^{(\pi)} - a_i^{(\alpha)} \right), \tag{2.4b}$$

consisting of the activity difference as driving force, the surface area $\mathcal{A}^{(\pi,\alpha)} = \mathcal{A}^{(\alpha,\pi)}$ at which the mass transfer occurs and the overall mass transfer coefficient $k_{\text{eff},i}^{(\pi,\alpha)} = k_{\text{eff},i}^{(\alpha,\pi)}$. With regard to the two-film theory [Cus09], the effective mass transfer coefficient can be expressed as

$$k_{\text{eff},i}^{(\pi,\alpha)} = \frac{1}{{\beta_i^{(\pi)}}^{-1} + K_{\text{N},i}^{(\pi,\alpha)} {\beta_i^{(\alpha)}}^{-1}}, \tag{2.5}$$

with $\beta_i^{(\pi)}, \beta_i^{(\alpha)}$ denoting the mass transfer coefficient of species $i \in \mathcal{SPC}$ in phase $\pi, \alpha \in \Pi$ and $K_{\text{N},i}^{(\pi,\alpha)}$ representing the distribution or Nernst coefficient of the respective species between both phases. Since no accurate values for any of these distribution and mass transfer parameter are required due to their role as tuning parameters to reach steady-state, a symmetric profile $\beta = \beta_i^{(\pi)} = \beta_i^{(\alpha)}\, \forall \pi, \alpha \in \Pi$ may be assumed alongside $K_{\text{N},i}^{(\pi,\alpha)} = 1$. With β as kinetic tuning parameter, eq. (2.5) can be simplified by setting $\mathcal{A}^{(\pi,\alpha)} = 1$ and limiting the integration interval to $t \in [0, 1]$. Alternatively, $\mathcal{A}^{(\pi,\alpha)}$ is used as a tuning parameter so that $k_{\text{eff},i}^{(\pi,\alpha)} = 1$ may be used.

Special care is necessary when selecting $n_i^{(\pi),0}$ for each phase since identical molar fractions, e.g., $x_i^{(\pi),0} = x_i^{(\alpha),0}$ for arbitrary phases $\pi, \alpha \in \Pi$ result in $j_i^{(\pi,\alpha)} = 0$. Consequently, each phase needs to be initialized with different molar fractions. Assuming an initial, monophasic molar amount vector n_i with $i \in \mathcal{SPC}$, an heuristically chosen maximum number of phases $n_{\text{phase,max}}^0 \in \mathbb{N}_+$ and an initial estimate on the primary association of a species to a specific phase $g : \mathcal{SPC} \to \Pi$ with $\Pi = \left\{1, 2, \ldots, n_{\text{phase,max}}\right\}$, the initial molar amount of species $i \in \mathcal{SPC}$ in phase $\pi \in \Pi$ may be calculated according to

$$n_i^{(\pi),0} = \begin{cases} (1-\kappa)\, n_i^0 & \text{if } g(i) = \pi, \\ \kappa \left(n_{\text{phase,max}} - 1\right)^{-1} n_i^0 & \text{else.} \end{cases} \tag{2.6}$$

Here, κ is referred to as *bleed* and represents the percentage of species i which is distributed between all phases except for the species' primary phase.

To improve the numerical stability of solving eq. (2.4), an activation function ϕ can be applied to limit the driving force which results in smoother concentration profiles. A good candidate for the activation function is the hyperbolic tangent

$\tanh : \mathbb{R} \to [-1,\, 1]$ with $\tanh(0) = 0$. Additionally, the convergence of this approach may be improved by substituting $n_i^{(\pi)}$ by the total molar fractions

$$x_{\mathrm{t},i}^{(\pi)} = \frac{n_i^{(\pi)}}{\sum_{\alpha\in\Pi}\sum_{i\in\mathcal{SPC}} n_i^{(\alpha)}}. \tag{2.7}$$

Convergence Validation

Convergence of the integration to the steady-state is easily verifiable by evaluating the right hand side (RHS) of eq. (2.4a) for each phase concentration candidate $x^{(\pi)}$, $\pi \in \Pi$ and ensuring that

$$\sum_{\alpha\in\Pi}\left(j_i^{(\pi,\alpha)}\right)^2 < \varepsilon, \tag{2.8}$$

with an appropriately small value ε, e.g, $\varepsilon = 10^{-3}$. Additionally, it needs to be checked if the solution of eq. (2.4a) also represents a solution to the GEM problem. One way to achieve this is the calculation of the tangent plane distance (TPD)

$$d_{\mathrm{TPD}}\left(x^{(\pi_1)},\, x^{(\pi_2)}\right) = \frac{G^{\mathrm{M}}}{RT}\left(x^{(\pi_1)}\right) - \mathrm{Tp}\left(x^{(\pi_1)},\, x^{(\pi_2)}\right) \tag{2.9}$$

with the tanget line

$$\mathrm{Tp}\left(x^{(\pi_1)},\, x^{(\pi_2)}\right) = \frac{G^{\mathrm{M}}}{RT}\left(x^{(\pi_2)}\right) + \left.\frac{\partial\left(\frac{G^{\mathrm{M}}}{RT}\right)}{\partial x}\right|_{x^{(\pi_2)}}\left(x^{(\pi_1)} - x^{(\pi_2)}\right), \tag{2.10}$$

and ensuring $d_{\mathrm{TPD}}\left(x^{(\pi_1)},\, x^{(\pi_2)}\right) \geq 0$ for each phase composition candidate $\pi_1,\, \pi_2 \in \Pi$ and $x^{(\pi_1)},\, x^{(\pi_2)} \in [0,1]^{|\mathcal{SPC}|}$. Please note that the operator Tp denotes the first order Taylor polynomial. A visualization of the criterion is depicted in fig. 2.2 for a simplified system of two species and two phases. Despite being a more computationally expensive convergence check, the TPD criterion can also be extended to check for the global optimality of the solution. By formulating the criterion as

$$d_{\mathrm{TPD}}\left(x,\, x^{(\pi)}\right) \geq 0, \quad \forall x \in [0,1]^{|\mathcal{SPC}|}, \tag{2.11}$$

the tangent line at each phase candidate $\pi \in \Pi$ needs to lie below the $G^{\mathrm{M}}(RT)^{-1}$ curve to ensure global optimality.

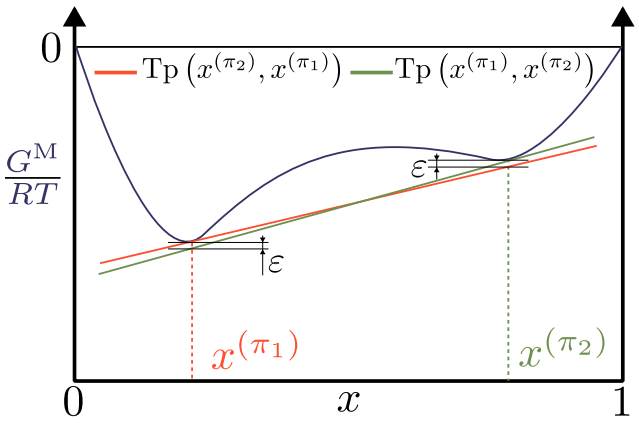

Fig. 2.2.: Dimensionless Gibbs enthalpy of mixing of a binary system. The overlapping tangents at $x^{(\pi_1)}$ and $x^{(\pi_2)}$ indicate two stable phases (adopted from [MRO17]). Please note that ε denotes a small value and is not necessarily identical to the one in eq. (2.8).

2.2 Design of Kinetic Experiments

In the beginning of each model-based design of chemical processes, an accurate model of the chemical reaction kinetics is required which enables predictions of the reaction performance under consideration of a constrained (reaction-)time. Even though data-driven models become more popular in these days in contrast to classical mechanistic kinetic models, the lack of physical insight and the dependency on significant amounts of data impedes the application in early stages of the process development in which data is scarce and expensive to generate. As a consequence, the formulation and application of mechanistic kinetic models, especially for catalyzed reactions, are integral parts in chemical engineering.

Model Generation Procedure. After one or potentially multiple catalytic cycles are identified, simplifications are applied to reduce the complexity of the set of reaction rate equations and to limit the number of parameters for lumped reaction rate equations. Now, experimental data is required to differentiate between multiple possible kinetic models and for the determination of suitable values for the model parameters. Due to limited personnel and financial resources as well as other restrictions such as safety measures, the efficient and systematic generation of the necessary data is a requirement which drives the fields of design of experiments (DoE) and, in recent time, model-based optimal experimental design.

Section Overview. In the following sub-sections, the field of experimental design is briefly outlined and major advances in model-based optimal experimental design are summarized. Before going into detail on the formulation of mbOED problems, a general mathematical model formulation is provided to simplify all subsequent discussions. After introducing the Fisher information matrix (FIM) as one of the central concepts in mbOED, different procedures for designing multiple experiments are discussed and summarized in the form of dynamic optimization programs (DOPs) for the model-based design of experiments for model calibration. Finally, the generalized least-squares (LSQ) problem for parameter estimation is stated.

Design Strategies and State of the Art

The field of experimental design can be subdivided into three categories, (i) designs based on heuristics such as the "one factor at a time (OFAT)" strategy, (ii) statistical or black-box designs like the factorial design (FD), latin-hypercube and Box-Behnken designs and (iii) model-based optimal experimental design using linear and non-linear process models [FM08]. For over 40 years, mbOED is in the focus of academic research and received numerous improvements and extensions w.r.t. the formulation and solution of the underlying optimization problem [LBS92; Kör+99; Bau+00; Lei+03; HSB11; Hoa+13; Tel+13], global [BVV02; BAB08; BB10] and multi-objective optimization [Log+11; Tel+12; Bou+15; MSG17], the consideration of robustness aspects [AM02; Kör+04], Bayesian approaches [Mos+12; WR19] as well as the utilization of the exact confidence region [GP17; MP19].

General Model Formulation

All process models considered for mbOED in this work may be summarized as differential algebraic equation (DAE) systems

$$\frac{\mathrm{d}\chi}{\mathrm{d}t} = f\left(\chi(t), u(t), p, \theta, c\right), \qquad \chi\left(t^0\right) = \chi^0, \tag{2.12a}$$

$$0 = g\left(\chi(t), y(t), u(t), p, c\right), \tag{2.12b}$$

with the time-dependent state vector $\chi(t) \in \mathbb{R}^{n_\chi}$ governed by the ODE RHS f, time dependent and independent controls $u(t) \in \mathbb{R}^{n_u}$ and $p \in \mathbb{R}^{n_p}$, respectively, uncertain parameters $\theta \in \mathbb{R}^{n_\theta}$, constant parameters $c \in \mathbb{R}^{n_c}$ and initial states $\chi^0 \in \mathbb{R}^{n_\chi}$. In many applications, the states χ are not directly measurable. As a consequence, the implicit algebraic equation (AE) g maps the states χ to the measurable variables $y \in \mathbb{R}^{n_y}$.

Fisher Information Matrix

The mbOED for model calibration aims at determining favorable experimental conditions to achieve a minimal parameter estimate uncertainty Σ_θ after the evaluation of all available experiment data. While Σ_θ is equal to the FIM inverse for linear models, mbOED often relies on the local, linear approximation of the parameter uncertainty in the form of the FIM inverse $C = F^{-1} \approx \Sigma_\theta$ which serves as a lower bound to the true uncertainty region according to the Cramér-Rao lower bound (CRLB) [Lju99]. The local FIM provides the information content of one measurement, whereas the integral FIM expresses the parameter uncertainty considering all available experimental data [Sag13]. In the remainder of this work, FIM is used as a synonym for the integral FIM

$$F = F_{\text{prior}} + \sum_{i=1}^{n_{\text{exp}}} \int_{t_i^0}^{t_i^{\text{f}}} \omega_i(t) \left(\left. \frac{\mathrm{d}y_i}{\mathrm{d}\theta} \right|_{\hat{\theta}_i} (t) \right)^\top \Sigma_{y,i}^{-1} \left(\left. \frac{\mathrm{d}y_i}{\mathrm{d}\theta} \right|_{\hat{\theta}_i} (t) \right) \mathrm{d}t, \tag{2.13}$$

in continuous form. Please note that the sensitivities $\left. \frac{\mathrm{d}y_i}{\mathrm{d}\theta} \right|_{\hat{\theta}_i} (t)$ of the measurement variables y depend on θ in the case of non-linear system behavior and need to be evaluated at the parameter estimate of the respective experiment $\hat{\theta}_i$. Prior information on the measured system is incorporated in F via the prior FIM F_{prior} and the measurement covariance matrix $\Sigma_{y,i}$ which scales y according to the measurement uncertainty. By introducing the scalar parameters $\omega_i(t) \in \{0, 1\}$ which serve as decision variables, the available information content can be limited to n_{sp} measurement times via

$$\int_{t_i^0}^{t_i^{\text{f}}} \omega_i(t) \, \mathrm{d}t = n_{\text{sp},i}. \tag{2.14}$$

The sensitivities in eq. (2.13) are calculated by extending eq. (2.12) by the variational equations

$$\frac{\mathrm{d}}{\mathrm{d}t} \left(\frac{\mathrm{d}\chi}{\mathrm{d}\theta} \right) = \frac{\partial f}{\partial \chi} \frac{\mathrm{d}\chi}{\mathrm{d}\theta} + \frac{\partial f}{\partial \theta}, \qquad \frac{\mathrm{d}\chi}{\mathrm{d}\theta} \left(t^0 \right) = 0, \tag{2.15a}$$

$$0 = \frac{\mathrm{d}g}{\mathrm{d}\theta} = \frac{\partial g}{\partial \chi} \frac{\mathrm{d}\chi}{\mathrm{d}\theta} + \frac{\partial g}{\partial y} \frac{\mathrm{d}y}{\mathrm{d}\theta} + \frac{\partial g}{\partial \theta}, \tag{2.15b}$$

with $\frac{\mathrm{d}y}{\mathrm{d}\theta} \in \mathbb{R}^{n_y \times n_\theta}$ being the solution to (2.15b). For the sake of brevity, the function inputs and dependencies are omitted.

Even though mbOED can be used for model discrimination and model calibration [FM08], the focus of this work lies on the non-linear mbOED of multiple experiments for model calibration. In the literature, mainly two approaches, the sequential design (SQ) and simultaneous design (SM) (also known as parallel design), are frequently used [GMB07]. The SM represents a general formulation of the design problem since multiple experiments are designed simultaneously with the solution of one, highly non-linear optimization problem. A schematic representation of this approach is visualized in fig. 2.3. Due to the simultaneous consideration of

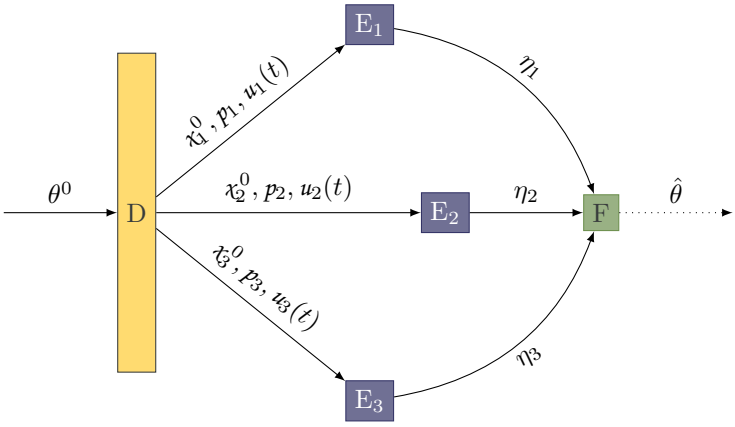

Fig. 2.3.: Schematic representation of the simultaneous design strategy in mbOED for three experiments. The initial parameter guess θ^0 is used for the design of $n_{\text{exp}} = 3$ experiments, resulting in the optimized initial states x_k^0 and controls p_k, $u_k(t)$ with $k \in \{1, 2, 3\}$. After executing each experiment $\text{E}_{(\text{i})}$ with the respective optimized controls, the measurement data η_k is used in the parameter estimation F, leading to the parameter estimates $\hat{\theta}$.

all decision variables, the optimizer is able to design experiments which optimally complement each other. At the same time, this approach suffers from a great number of local optima and a significant increase in computational demand for solving n_{exp} instances of the same non-linear model in a large-scale optimization problem.

The SQ strategy takes a different approach as it focuses on the alternating design and execution of experiments to remedy the problem of computational load while simultaneously incorporation the latest information in the next experimental design. A visual representation of this strategy can be found in fig. 2.4. While this approach cannot leverage the benefits of simultaneously designing all experiments simultaneously, the decreased number of local optima and the incorporation of the newest data make this approach the most popular in literature [PLM90; PLM91].

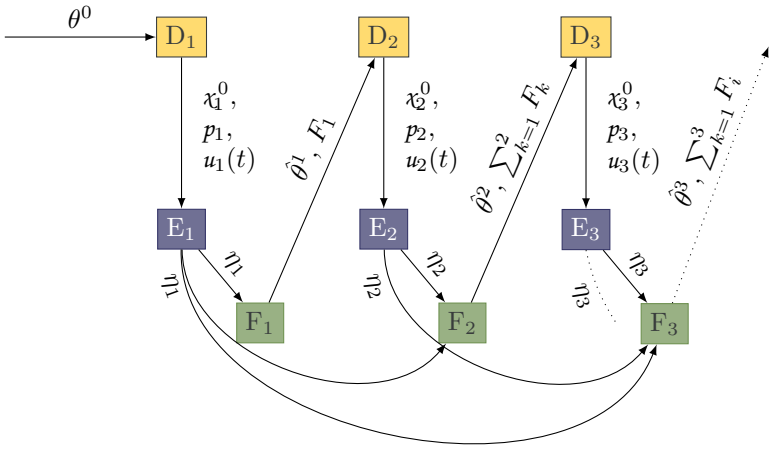

Fig. 2.4.: Schematic representation of the sequential design strategy in mbOED for three experiments. The initial parameter guess θ^0 is used for the design of $n_{\text{exp}} = 1$ experiment, resulting in the optimized initial states x_1^0 and controls $p_1, u_1(t)$. The optimized parameters are applied in the first experiment from which the measured data η_1 is used in the parameter estimation F_1. The estimated parameter values $\hat{\theta}^1$ and the FIM F_1 are used for designing the next experiment in D_2. This sequence is executed for all subsequent experimental designs. In all parameter estimation F_k and experiment design E_k steps with $k \in \{2, 3, \ldots, n_{\text{exp}}\}$, all previous experimental data η_j and FIMs F_j with $j \in \{1, 2, \ldots, n_{\text{exp}} - 1\}$ are used, respectively.

In addition to these two strategies, hybrid approaches are also possible with first applications shown by Barz et al. [BAW10].

Model-Based Optimal Experimental Design Formulation

A general mbOED problem for the design of multiple experiments may take the form of an optimal control problem (OCP)

$$\min_{\substack{u_1(t),\, u_2(t),\, \ldots,\, u_{n_{\mathrm{exp}}}(t),\\ p_1,\, p_2,\, \ldots,\, p_{n_{\mathrm{exp}}},\\ \chi_1^0,\, \chi_2^0,\, \ldots,\, \chi_{n_{\mathrm{exp}}}^0}} \quad \phi^{\Sigma_\theta}(F) \tag{2.16}$$

s. t.

$$\left.\begin{aligned}
\text{Process Model: (2.12)},\\
\text{FIM Definition: (2.13)},\\
\text{Variational Equations: (2.15)},\\
\text{Path Equality Constraints: } h_i,\\
\text{Path Inequality Constraints: } g_i,\\
\text{Terminal Equality Constraints: } {h^{\mathrm{f}}}_i,\\
\text{Terminal Inequality Constraints: } {g^{\mathrm{f}}}_i,\\
u_i(t) \in \mathcal{U}_i,\\
p_i \in \mathcal{P}_i,\\
\chi_i^0 \in \mathcal{X}_i^0,\\
t_i \in \mathcal{T}_i.
\end{aligned}\right\} i \in \{1, 2, \ldots, n_{\mathrm{exp}}\}$$

or mixed-integer OCP when optimal measurement times are considered as well. In addition to the problem specific path and terminal equality and inequality constraints, the equality path constraint eq. (2.14) is appended to restrict the number of measurements in each experiment. The objective function $\phi^{\Sigma_\theta}(F)$ consists of the Fisher information matrix F which is reduced to a scalar value using the general function $\phi^{\Sigma_\theta} : \mathbb{R}^{n_\theta \times n_\theta} \to \mathbb{R}$. Table 2.1 provides a brief overview over the most frequently used optimality criteria in mbOED for parameter estimation. Whether the optimality criterion is applied to the FIM or its inverse, the parameter confidence matrix C, is denoted using the superscript $\square^F$ or $\square^{\Sigma_\theta}$, respectively. Besides these criteria, the interested reader is referred to the literature for additional criteria which range from combinations of the common criteria [VCV98; Tel+12; MSG17] over modified criteria [PLM90; PLM91; LBS92; VV98; GMB07; FM08] to completely new approaches [AM02; BAM05; BM06; Log+11; Hou+15; Bou+15].

Because of the complexity of the optimization problem, eq. (2.16) needs to be reformulated to be solvable with standard solvers like the interior point optimizer

Tab. 2.1.: Selection of frequently used optimality criteria operating on the Fisher information matrix F (maximization) or the parameter covariance matrix C (minimization). n_θ denotes the number of uncertain parameters and eig represents the eigenvalue operator. An overview over different optimality criteria is provided in [FM08].

Criterion	Definition	Description
A	$\phi_A^F(F) \coloneqq \frac{1}{n_\theta} \operatorname{trace}(F)$ $\phi_A^{\Sigma_\theta}(F) \coloneqq \frac{1}{n_\theta} \operatorname{trace}(C)$	Optimization of the main diagonal elements neglecting the covariance.
D	$\phi_D^F(F) \coloneqq \det(F)^{1/n_\theta}$ $\phi_D^{\Sigma_\theta}(F) \coloneqq \det(C)^{1/n_\theta}$	Optimization of the volume and, therefore, taking into account the covariance.
E	$\phi_E^F(F) \coloneqq \max(\operatorname{eig}(F))$ $\phi_E^{\Sigma_\theta}(F) \coloneqq \max(\operatorname{eig}(C))$	Optimization of the principle component with the highest impact.

(IPOPT) [WB06]. The infinite dimensional problem is reduced to finite dimensions using time discretization techniques such as single-, multiple shooting [Bau+00] or orthogonal collocation on finite elements [Hoa+13], leading to the class of mixed-integer non-linear optimization programs (MINLPs). In a second step, the integer decisions $\omega_i(t)$ are either relaxed to the interval [0, 1] [Sag13] or fixed in each finite time element $i \in \{1, 2, \ldots, n_{\mathrm{FE}}\}$ with the finite element width $h_{\mathrm{FE},i}$ being subject to optimization. These reformulations transform the (mixed-integer) OCP into a non-linear optimization program (NLP). While the former strategy is regularly applied in the literature and converges to the integer solution if a suitable time grid is chosen [Sag13], rounding strategies need to be applied if an adequate grid cannot be found [Bau+00; Jos+16]. The latter strategy does not suffer from these numeric issues and enables the introduction of a minimum time span between two consecutive measurements. However, it ties the number of finite elements to the number of measurement points which might pose a challenge for models with steep gradients and a limited number of measurement points.

Generalized Least-Squares Problem

In the case of available experimental data comprising n_{exp} datasets with n_{sp} samples each, the parameter estimate $\hat{\theta}$ can be determined by solving the generalized LSQ problem

$$\begin{aligned} \min_{\theta} \quad & \phi = \frac{1}{2} \sum_{i=1}^{n_{\text{exp}}} \sum_{j=1}^{n_{\text{sp},i}} \epsilon_{i,j}^{\top} \Sigma_{y,j} \epsilon_{i,j} \\ \text{s.t.} \quad & \text{Process Model (k) according to eq. (2.12)}, \\ & k \in \{1, 2, \ldots, n_{\text{exp}}\}, \\ & \theta \in \Theta, \end{aligned} \tag{2.17}$$

with $\epsilon_{i,j} = \eta_{i,j} - y_{i,j}$ representing the deviation of the measurement data $\eta_{i,j} \in \mathbb{R}^{n_y}$ from the model responses $y_{i,j} \in \mathbb{R}^{n_y}$. The feasible set of parameter values θ is bounded by $\Theta \subset \mathbb{R}^{n_\theta}$ in which the true parameter values θ^* are assumed. Both eqs. (2.13) and (2.17) assume no correlation of the measurements across time and neglect multi-sampling at specific time points as it is assumed in the remainder of this work. A relaxation of this assumption is discussed in the literature (see e.g., [Hoa+13]).

2.3 Process Synthesis and Conceptual Design

This section commences with a general and concise overview of the area of process synthesis and conceptual design due to the vast scope and numerous sub-areas in this research field. In this overview, a definition of process synthesis is provided, the main sub-areas are summarized and a brief introduction to the two general approaches for process synthesis is given. With one of the foci of this work lying on the consideration of multiple phases in the design of reactor and reactor-separator networks, the state-of-the-art approaches in this sub-area are categorized and discussed. Finally, the EPF methodology is introduced in detail to lie the foundation for the introduction of its multiphase equivalent in chapter 4.

2.3.1 Overview

Definition. In the literature, the terms “Process Synthesis” [BS04], “Conceptual (Process) Design” [CG17; Mit+18] and combinations such as “Conceptual Process Synthesis” [LK04] are frequently used interchangeably to refer to the act of creating

a new or altering an existing (retrofit design) flowsheet for a (chemical) process to achieve a predefined objective. Due to the rich history of this research area and the formal definition of the term "synthesis" [Wes04] dating back to the beginning of the last century [LK04], multiple review articles [Wes04; LK04; Cre15; CG17] can be found with slightly different definitions of these terms. By combining the definitions from Chen and Grossmann [CG17] and Cremaschi [Cre15], process synthesis and conceptual design describe the process of creating process flowsheets or selected sub-structures therein comprising (inter-)connected process units which optimally transform a given set of raw materials using optional auxiliary substances and/or energy into a desired set of products via physical and chemical phenomena. In this context, the measure of optimality needs to be defined a priori and may be subject to economic, environmental, and/or social objectives.

Sub-Areas of Process Synthesis. When utilizing this definition, process synthesis encompasses multiple sub-areas with different foci. By considering the scope of the design task, (i) general process flowsheet design in which the entire process flowsheet is optimized and (ii) the design of flowsheet parts, such as the reaction and separation section, can be differentiated. Depending on which part of the flowsheet is considered, major areas in process synthesis comprise (ii.a) the reactor and reactor-separator-network design and the design of auxiliary systems such as (ii.b) heat exchanger networks, (ii.c) separation trains (e.g., distillation sequences), (ii.d) steam and power supplies, (ii.e) water networks and (ii.f) mass exchanger networks [LK04; Wes04; CG17]. In addition to this strict division based on scope, process intensification (PI) represents a hybrid which opts for the simultaneous consideration and integration of multiple process parts. Likewise, retrofit design is not necessarily limited to one specific process part but can be associated with process synthesis [Wes04] as it aims at improving the performance of an existing process by designing new or altering existing parts of a process.

Methodological Approaches

Independent of the sub-area in process synthesis, modern approaches and methods for handling the design task(s) can be generally classified into two categories: decomposition- or knowledge-based and optimization-based methods [LK04; CG17].

Decomposition-Based. Decomposition-based approaches try to compartmentalize the design problem into separate sub-tasks which are solved sequentially. This limits the

interactions between sub-tasks, resulting in simpler problems with reduced problem sizes. While this approach makes the design of complex processes feasible in the face of limited resources, it may prohibit the identification of the optimal solution due to a limited design space and the negligence of complex interactions between multiple sub-tasks. Two examples for the category of decomposition approaches represent the hierarchical heuristic procedure [Dou85] and the more recent phenomena-based process synthesis and intensification methodology [Lut+13].

Optimization-Based. Optimization-based approaches strongly increased in popularity with the advances in computing power and numerical solvers due to the formulation of the process synthesis task as a mathematical optimization problem [Wes04]. Enabled by the simultaneous consideration of the complete design problem, the full design space is available to identify the optimal process configuration. However, this assumes that (i) the design space encompasses the optimal solution and (ii) the optimization problem can be solved using existing optimization algorithms. Existing methods for the definition of the design space frequently rely on the formulation of a superstructure comprising sets of unit operations for each task in the process from which the optimizer identifies the optimal process configuration [CG17]. Alternative approaches try to remedy the restriction on predefined process units by using generic process units, phenomena-based descriptions of process units or other process abstractions which are suitable to maximize the design space while simultaneously enabling the identification of innovative and integrated process units.

In the following sub-section, both process synthesis concepts are discussed further on the basis of state-of-the-art approaches to the sub-area of reactor- and reactor-separator-network design.

2.3.2 State-of-the-Art Reactor-Separator-Network Design

In the literature, many excellent reviews on the history and current status of reactor-separator- but most importantly reactor-network design are available (e.g., [CG17; Kai19; XF18a]). Seeking a comprehensive overview of the current status, the frequently used differentiation into heuristics-based, attainable region (AR) and optimization-based approaches is extended by additional categories w.r.t. the formulation of the synthesis problem and the utilized abstraction. While the aforementioned literature mainly focuses on the reactor-network design, this section aims to provide an overview over process synthesis approaches which combine the design of reactors and separators, including advances in the design of integrated

reactor-separator units from the field of PI. For linguistic simplicity, the terms "reactor-network design" and "reactor-separator-network design" will also include the design of reactor-recycle and (integrated) reactor-separator-recycle networks, respectively. Since limited literature can be found on alternative methodologies to superstructure-based reactor-separator-network design methodologies in the category of optimization-based approaches, these alternative methodologies will be discussed alongside the introduction of the EPF methodology in section 2.3.3. Approaches which are able to handle multiple phases in the reaction section are highlighted in a dedicated paragraph as they represent alternative ways in handling multiple phases in the reactor- and reactor-separator-network design to the multiphase extension of the EPF methodology proposed in this work.

Heuristics

Due to the nature of heuristics and decomposition-based synthesis approaches, frameworks for the design of reactor networks can be extended toward the inclusion of separation units and, thus, reactor-separator-network synthesis. While simple in application and reliably yielding feasible process variants, heuristic approaches cannot consider the complete design space of the synthesis task and, therefore, result in sub-optimal solutions. Nevertheless, industrial practice still relies on these approaches so that the formulation of advanced heuristics is subject to ongoing research. Examples for advanced heuristics include the consideration of multiple recycles [Luy11] and specialized heuristics for designing processes for the production of biofuel additives [UQH11].

Attainable Region

AR approaches were originally designed for the synthesis of reactor networks without the need for a predefined set of existing unit operations [Hor64; GCH87; FH97]. Besides multiple extensions addressing limitations w.r.t. high problem dimensionality [Roo+00; BWM02; Kau+02; AF04; ZM08], consideration of multiple feeds [PM08] and the application to alternative reactor concepts [DM08; MGH13; AHG14], the introduction of separation enabled the application of AR approaches for reactor-separator-network synthesis [FE01; Fei02], the design of integrated reactor-separator units [ATM08; Aga+08] and the identification of optimal heat exchanger networks [Yue20].

Superstructure

Superstructure-based reactor- and reactor-separator-network synthesis uses mathematical optimization approaches to identify the optimal process configuration using predefined sets of process units. These process units are interconnected either manually or via algorithmic support [Nez+18; GGB21], leading to complex, large-scale optimization problems of the MINLP type. This problem category is the result of the simultaneous consideration of non-linear models for, e.g., the reaction kinetics, heat and mass transfer, and the introduction of integer variables to switch selected process units on or off. Solving these types of problems is challenging and requires specialized, deterministic (global) solvers [FAC89; AAF00; EF02], stochastic approaches [Cor+97; MK99; MLK01; LK03b; Váz+13], genetic algorithms [GR98; SS15], hybrid heuristic/optimization-based strategies [Exl+08] or more recent machine learning techniques [GGB21]. While superstructure optimization is only able to identify an optimal configuration which can be constructed from the predefined set, introduction of new process units or additional constraints is straightforward. Due to this flexibility, superstructure optimization is used in many different methodological approaches. Examples for these methodologies are provided in the following paragraphs.

Classical Approach. The classical approach to superstructure optimization refers to the utilization of predefined process units in the superstructure generation. In the early work of Kokossis and Floudas [KF91], isothermal reactor-separator-recycle systems were synthesized by decomposing the flowsheet into a reactor and a separator network. Different configurations for each network as well as their interconnection were defined and optimized using a MINLP formulation. Seeking for a more efficient and accurate solution of the superstructure optimization, Dowling and Biegler [DB15] proposed an equation-oriented framework using automatic differentiation including thermodynamic models for the calculation of phase equilibria and distillation column models with different degrees of complexity. Alternative formulations using generalized disjunctive programming and convex-hull approximations to reduce the problem complexity [Ma+19] and the addition of sidestream column models to the separation units set [Ye+21] represent two examples of recent research directions.

Generic Process Units. In contrast to the utilization of a set of predefined process units, generic process units can be formulated which fulfill different tasks depending on the requirements in the flowsheet. Stein et al. [Ste+99] formulated a two-phase reactor-condenser model which enables the superstructure optimization using NLP

approaches and exemplified their framework using a reactive distillation column. Later, Linke and Kokossis [LK03a] extended the approach using a combination of reactor and mass exchanger unit in a MINLP superstructure optimization to include discrete decisions without being limited to vapor-liquid (V/L) separation phenomena. In a different approach by Demirel et al. [DLH17; DLH19], a grid of generalized unit blocks is generated and used in a MINLP superstructure optimization. Based on the fluxes between block units, the process structure and flowsheet can be identified. In a recent study, this block-based approach was extended toward membrane-assisted reactive separation units [Mon+21].

Phenomena-Based. Instead of using a bottom-up approach as in the superstructure optimization with generic process units, phenomena-based reactor-separator design utilizes known physical and chemical phenomena to build optimal process flowsheets. Lutze et al. [Lut+13] proposed a decomposition-based approach in which the initial search space is successively constrained on a structural, phenomenal, and operational level so that the framework can lead to intensified configurations. Subsequent studies extend this framework by systematic consideration of membrane-supported operations [Bab+14], the inclusion of live cycle assessment (LCA) factors in addition to economic criteria [Bab+14; Bab+15], and additional phase combinations including solid-liquid (S/L) and liquid-liquid (L/L) systems [Gar+19]. An optimization-based approach using superstructure optimization on phenomenological modules in a three-stage process is introduced by ŽivkoviL and NikaLeviL [ŽN16]. Based on the initial reaction screening, relevant phenomena blocks are selected and interconnected in a superstructure before optimization using dynamic, mixed-integer and stochastic optimization approaches commences. Similar to the sequential optimization procedure in [Rec+14], Kuhlmann et al. [Kuh+18] utilizes phenomenological building blocks for the identification of flowsheet candidates including reactor networks, V/L and L/L separation as well as reactive separation before performing a detailed simulation and optimization using regular process equipment.

Shortcut Models. Even though shortcut models are used extensively in reactor-separator synthesis to reduce model complexity, two distinct approaches are worth highlighting. Recker et al. [Rec+14; Rec+15] formulate a three-step procedure in which systematic and rapid screening of possible flowsheet variants using shortcut models is included prior to the rigorous modeling and optimization of a reduced set of process variants. For a multiphase system with a complex reaction network, McBride et al. [MKS17] used Kriging surrogate modeling to approximate the L/L phase equilibrium in the decanter and Fenske-Underwood-Gilliland correlations for

the distillation columns to create a decanter cascade for efficient catalyst recovery in the homogeneously catalyzed hydroformylation reaction.

Multiphase Reactors

In addition to reactor-separator-network design, many authors, especially in the area of PI, considered and extended their process synthesis approaches to integrated reactor-separator units by simultaneously considering coexisting phases in the process unit. Early frameworks which incorporate these considerations stem from Krishna and Sie [KS94] and Schembecker et al. [Sch+95] which are primarily based on systematic procedures and heuristics. Optimization-based approaches were first shown by Mehta and Kokossis [MK97] and Mehta and Kokossis [MK00] in the form of stochastic optimization of a process superstructure for isothermal and non-isothermal cases. In addition to AR-based considerations of multiphase reactors [ATM08; Aga+08], the previously mentioned categories of generic-unit-based [KN00; DLH17; DLH19; Mon+21], shortcut-model-based [Rec+15], and phenomena-based [Lut+13; ŽN16; Kuh+18; Gar+19] approaches also contain examples in which multiphase and intensified reactor units are systematically incorporated.

2.3.3 Elementary Process Functions (EPF) Methodology

In addition to heuristic-, AR-, and superstructure-optimization-based approaches, dynamic optimization was identified early as a promising alternative for optimally controlling batch and continuous reactors [Ari60]. Consequently, it also qualifies for the identification of optimal reactor designs. Many authors introduced frameworks for the design of optimal plug flow reactors considering minimum entropy production [JK04], optimal temperature [NK71] as well as temperature and flux profiles [Roj+93; Roj+96]; the design of reactors with different dispersion properties [PH70; Log+09] and in- and outlet configurations [BB92]; and the design of reactor networks comprising ideal reactor types [Hil04; Hil05]. However, except for the extension of the targeting strategy by Balakrishna and Biegler [BB93] w.r.t. a species-dependent distribution function allowing for the consideration of separation in a cross flow reactor model, few proposed methodologies have the ability to systematically consider more complex phenomena and technical realizations such as the design of (integrated) reactor-separator networks. Aiming to provide a methodological foundation which is able to encompass and combine various physico-chemical phenomena to identify process designs with innovative and integrated process units, the elementary process functions (EPF) methodology was introduced conceptually

and mathematically by Freund and Sundmacher [FS08] as well as Sundmacher and Freund [SF10], respectively.

Categorization. In terms of the process synthesis categories, the EPF methodology can be generally associated to the category of reactor and reactor-separator-network design approaches even though extensions are available [Lie+18; LSS19] which also allow for the design of separators as well as entire process flowsheets. This optimization-based approach does not rely on predefined process units and is similar to AR-based approaches (a comparison can be found in [Kai19]) as it aims at identifying the maximum process potential before introducing approximations and restrictions to approach feasible process flowsheets. At its core, the EPF methodology decomposes process units into individual phenomena, operations, tasks or *functional modules* such as *reacting*, *heating* and *separating* which can be freely combined to design innovative and integrated process units in addition to already existing apparatuses. A schematic representation of the methodological shift in process synthesis from unit operations to functional modules is depicted in fig. 2.5.

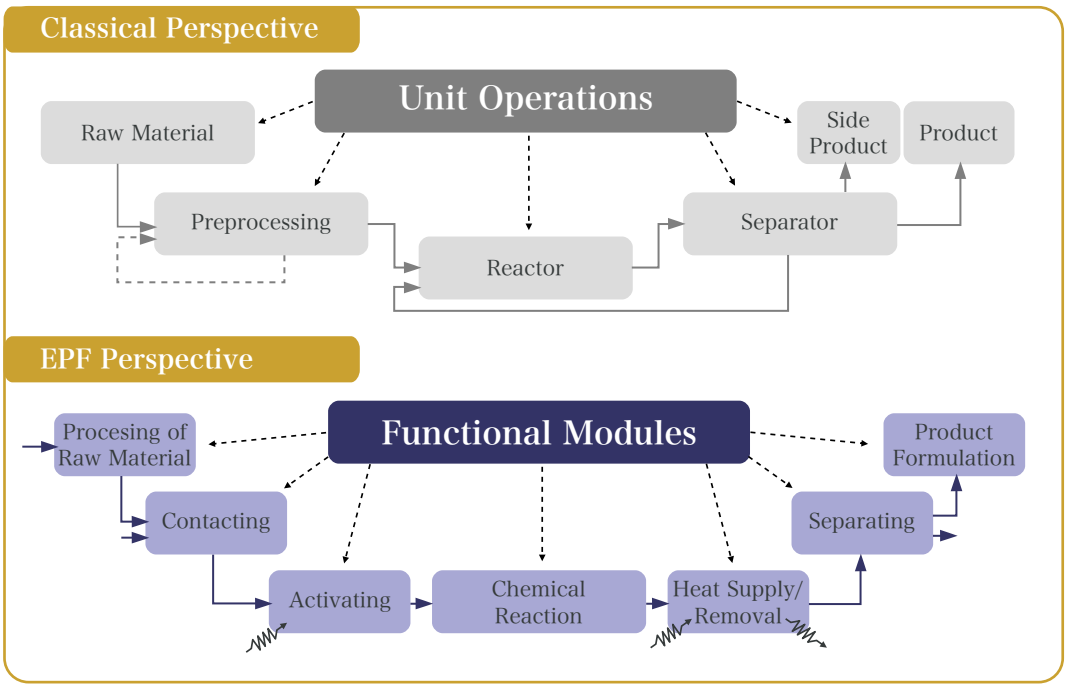

Fig. 2.5.: Process unit versus functional-modules-based process design (adapted from [FS08]).

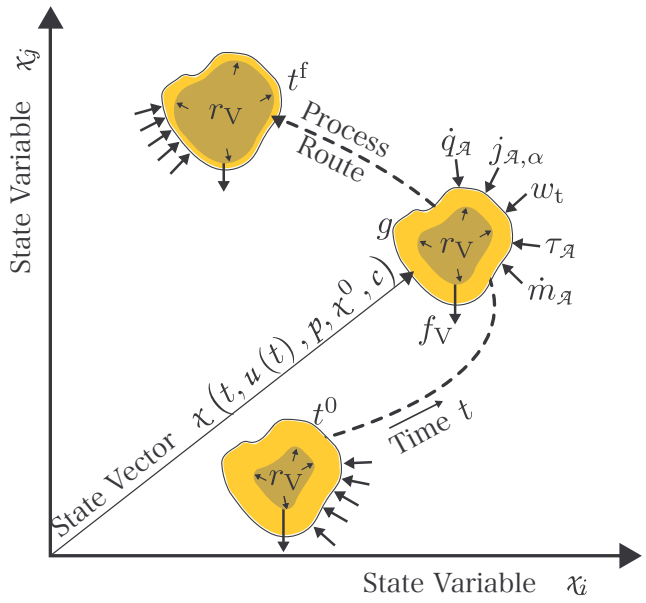

Fig. 2.6.: Schematic representation of a fluid element traversing the n-dimensional thermodynamic state space from $\chi\left(t^0\right)$ to $\chi\left(t^{\mathrm{f}}\right)$. The path of the fluid element can be influenced via internal fluxes like the volumetric reaction flux r_{V}, external fluxes like heat fluxes $\dot{q}_{\mathcal{A}}$, diffusion fluxes $j_{\mathcal{A},\alpha}$ of various species $\alpha \in \mathcal{SPC}$ and the total mass flux $\dot{m}_{\mathcal{A}}$, volume forces f_{V}, technical work w_{t}, stress τ_{A} as well as the rate of change of the fluid element's geometrical shape g. All indices $\square_{\mathrm{V}}$ indicate volume-based variables whereas $\square_{\mathcal{A}}$ denote surface-related fluxes (adapted from [FS08; SF10]).

Mathematical Representation

For a more intuitive representation, the concept of combining multiple functional modules into process units and process flowsheets can be abstracted as the manipulation of the trajectory of a Lagrangian fluid element in state space, see fig. 2.6. In analogy to the in- and outlet of a process (unit), the initial state $\chi(t = t^0) = \chi^0$ and the final state $\chi(t = t^{\mathrm{f}})$ of the fluid element determine the starting- and endpoint of the process with $\chi\left(t\right) \in \mathcal{X} \subset \mathbb{R}^{n_\chi} = \left(T(t), p(t), w^\top(t), v(t), G(t)\right)$ denoting the state vector comprising the time-dependent temperature $T\left(t\right)$, pressure $p\left(t\right)$, concentration measures like mass fractions $w_\alpha\left(t\right)$ of each chemical species $\alpha \in \mathcal{SPC}$, the fluid element velocity $v\left(t\right)$ and geometrical state $G\left(t\right)$ [SF10]. These points can be fixed a priori or may be determined by the optimizer in accordance with one or multiple objective functions and constraints. The time $t \in \left[t^0, t^{\mathrm{f}}\right]$ acts as the independent coordinate indicating the progress inside of the process and, therefore, across all sequentially connected process units. Between t^0 and t^{f}, the path of the fluid element is constrained with thermodynamic and process specific requirements in the form of equality $h\left(\chi(t), u(t), p, c\right) = 0$ and inequality $g\left(\chi(t), u(t), p, c\right) \leq 0$ constraints and

can be influenced, following the predefined objective function(s), via various kinds of controls in the form of fluxes $u(t) \in \mathcal{U}$, time-independent controls $p \in \mathcal{P}$ and the initial state vector $\chi^0 \in \mathcal{X}^0$. Additional constants c are included for completeness. As shown in fig. 2.6, the flux vector $u(t) \in \mathcal{U} \subset \mathbb{R}^{n_u}$ contains internal reaction fluxes $r_\mathrm{V}(t)$, total mass $\dot{m}_\mathcal{A}(t)$ and diffusion fluxes $j_\mathcal{A}(t)$, heat fluxes $\dot{q}_\mathcal{A}(t)$, volume forces $f_\mathrm{V}(t)$, technical work $w_\mathrm{t}(t)$, stress $\tau_\mathrm{A}(t)$ as well as the rate of change of the fluid element's state $g(t)$ [SF10]. Thus, the design task can be compactly formulated as a DOP following

$$\min_{u(t),p,\chi^0} \quad \phi\left(\chi(t), u(t), p, \chi^0, c\right) \tag{2.18a}$$

s. t.

$$C\left(\chi(t), p, c\right) \frac{\mathrm{d}\chi}{\mathrm{d}t} = W\left(\chi(t), p, c\right) u(t), \quad \chi(t^0) = \chi^0, \tag{2.18b}$$

$$h\left(\chi(t), u(t), p, c\right) = 0, \tag{2.18c}$$

$$g\left(\chi(t), u(t), p, c\right) \leq 0, \tag{2.18d}$$

$$\chi(t) \in \mathcal{X}, \quad \chi^0 \in \mathcal{X}^0, \quad u(t) \in \mathcal{U}, \quad p \in \mathcal{P}, \tag{2.18e}$$

with the Bolza type objective function $\phi(\cdot)$, the state-dependent capacity and weight factor matrices C and W, respectively, and additional restrictions on the spaces of $\chi(t)$, χ^0, $u(t)$ and p. Please note that these restrictions of the available spaces may also include limitations due to thermodynamic or chemical equilibria. If the capacity matrix is invertible, the linearly independent elementary vectors span the column space of $E = C^{-1}W$, further restricting the attainable subspace $\mathcal{X}$ [RJS22].

Design Approaches based on the EPF Methodology

Based on the conceptual and mathematical concept of the EPF methodology, many process design frameworks, methodological extensions and applications to concrete design tasks can be found in the literature. Before focusing on methodological extensions w.r.t. the reactor- and reactor-separator-network design, fig. 2.7 provides an overview over a selected number of EPF applications. The categories are selected in terms of methodological contributions, e.g., reactor-separator-network design and back-mixing, as well as applications and scale, e.g., processes and multiple phases, so that repetitions of literature elements may occur.

In terms of reactor- and reactor-separator-network design approaches, mainly three procedures can be found in the literature which focus on the systematic translation of the results from eq. (2.18) into process units and process flowsheets:

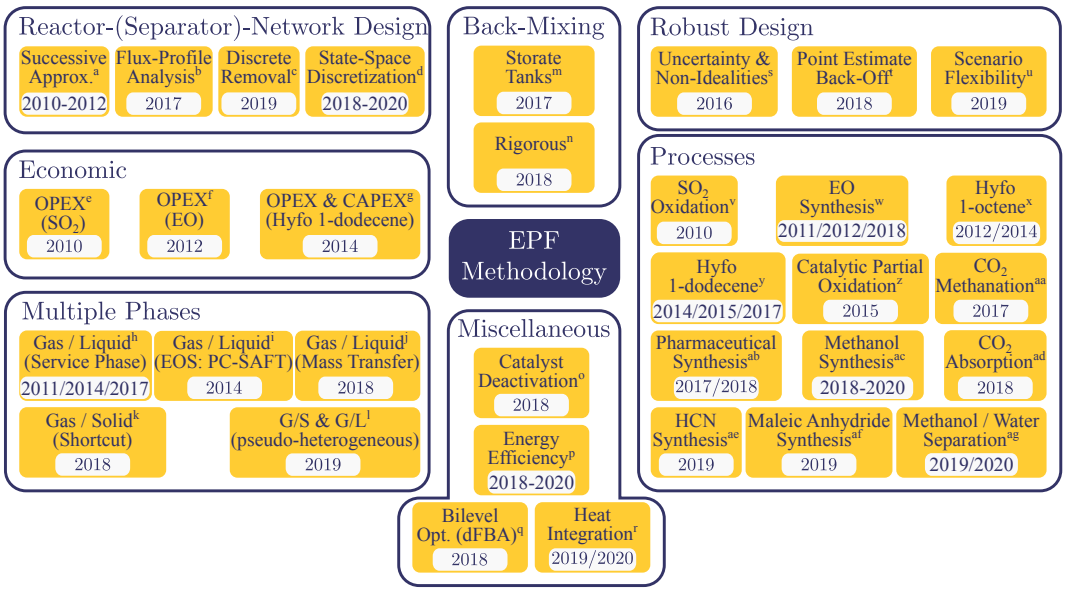

Fig. 2.7.: Selected and categorized approaches, extensions, and applications of the EPF methodology since its introduction in 2008. [a][PFS10; Pes+11b; Pes+12a; Pes+12b]; [b][Kai+17; KFS17]; [c][Kai19]; [d][Lie+18; LSS19; SLS19; SLS20; Sch+20]; [e][PFS10]; [f][Pes+12b]; [g][Hen+14a]; [h][Pes+11a; Hen+14a; Kai+17]; [i][Hen+14b]; [j][XF18c]; [k][PKF18]; [l][KF19]; [m][Kai+17; KFS17]; [n][XF18a]; [o][XF18b]; [p][PF18; LSS19; Sch+20; SLS20]; [q][ESK18]; [r][LSS19; SLS19; Sch+20; SLS20]; [s][KFS16]; [t][Eme+18]; [u][Mau+19]; [v][Pes+11b]; [w][Pes+11b; Pes+12b; XF18b]; [x][Pes+12a; Hen+14b]; [y][Hen+14a; Hen+15; Kai+17]; [z][Kar+15]; [aa][ERS17]; [ab][ESK17; ESK18; Eme+18]; [ac][Lie+18; KF19; SLS20]; [ad][XF18c]; [ae][LSS19]; [af][Mau+19]; [ag][SLS19; SLS20; Sch+20] (adapted and extended from [RJS22]). A similar overview with different categories can be found in [Fre+19].

1. **Multi-level reactor design (MLRD)**
   The solution of the EPF-based DOP yields unlimited optimal control trajectories $u^*(t)$ which might not be feasible in real life due to limitations of the external fluxes as their respective driving force is regularly dependent on the distance between the current state and its equilibrium $x(t) - x^{eq}(t)$. As a consequence, the MLRD approach successively refines eq. (2.18) by increasing the degree of detail of the flux formulation, i.e., by introducing transport kinetics which limit the previously unlimited fluxes $u(t)$. In the final step, the optimal control profiles are approximated using process units, leading to the generation of technically feasible reactor networks. All three steps of the design procedure are summarized in table 2.2. Over time, this approach has seen many extensions including the consideration and optimization of the catalyst particle bed [PKF18] and catalyst degradation [XF18b], the inclusion of axial dispersion and process-wide recycle streams [XF18a], the simultaneous consideration of multiple, permanently available phases [Pes+12a; Hen+14a;

Tab. 2.2.: Three-level multi-level reactor design (MLRD) approach for the successive approximation and translation of the optimal EPF controls p^* and control trajectories $u^*(t)$ into technical reactor networks (adopted from [PFS10; Fre+19; RJS22]).

	Description	Characteristics
Level 1	Identification of the optimal route in state space	• Unlimited external fluxes • Identification of the maximum potential of the reaction system (optimal route in state space)
Level 2	Identification of an ideal reactor concept	• Limited external fluxes via transport kinetics • Selection of a suitable subset of $u(t)$ and p
Level 3	Identification of an optimal technical reactor (network)	• Approximation of the controls using detailed reactor models • Consideration of non-idealities

XF18c] and introduction of various kinds of uncertainty and operating scenarios leading to robust design [KFS16; Mau+19].

2. **Flux Profile Analysis (FPA)**
   Identical in the first level to the MLRD approach, the flux profile analysis (FPA) introduced by Kaiser et al. [KFS17] takes a slightly different route in approximating the optimal control trajectories. Instead of introducing limitations to the external fluxes successively, the control trajectories are subdivided into characteristic sections which can be approximated using ideal reactor types, such as continuously stirred tank reactors (CSTRs), plug-flow reactors (PFRs) or differential side-stream reactors (DSRs). Naturally, the subdivision of the control profiles is subjective as the practitioner identifies, combines, and interprets branching points according to systematic but not automated procedures. This leads to multiple reactor network candidates which need to be evaluated in the last step with regard to economic and performance criteria. An overview over the framework steps can be found in table 2.3. In contrast to the MLRD framework, the FPA also relies on the interpretation of derived fluxes like the differential reaction flux

$$\varphi(t) = \frac{\text{moles of desired product formed}}{\text{moles of main reactant consumed}} = \frac{\frac{\mathrm{d}n_{\mathrm{prod}}}{\mathrm{d}t}}{\frac{\mathrm{d}n_{\mathrm{sub}}}{\mathrm{d}t}}, \tag{2.19}$$

Tab. 2.3.: Four-step FPA-based reactor-network design procedure based on the EPF methodology (adopted from [KFS17; Kai19; RJS22] and extended).

	Description	Characteristics
Step 1	Identification of the optimal route in state space	• Unlimited outer fluxes • Identification of the maximum potential of the reaction system (optimal route in state space)
Step 2	Subdivision of the time horizon into characteristic sections & reduction of controls	• The control profiles $u(t)$ are subdivided based on distinct profile changes • Sections with a minor impact on the objective function can be neglected or combined with others
Step 3	Association with ideal reactor types	• Each remaining flux-profile section is associated with one ideal reactor type based on specific characteristics (elaborated in [Kai19]) of ideal reactor units
Step 4	Evaluation of reactor network candidates	• The idealized reactor networks from Step 3 are modeled rigorously • The reactor network candidates are evaluated and compared in terms of performance and economic feasibility

in addition to internal and external fluxes. Without rigorously incorporating computationally expensive formulations of axial dispersion in eq. (2.18), the sign of $\varphi(t)$ hints at the advantage (positive sign) or disadvantage (negative sign) of axial dispersion in control trajectory sections under the prerequisite of absent dosing fluxes. In addition, the concept of storage tanks holding a specified amount of each species in the reaction network at t^0 is introduced which allows for the approximation of process-wide recycles in the design framework. Using these storage tanks, the optimizer is able to freely dose not only substrate(s) but also (by)products which may be used to increase selectivity and hint at beneficial product recycling as well as axial dispersion, especially in complex reaction networks [Kai+17]. In order to ensure feasibility of this approach, additional constraints are introduced which ensure the dosing of all substrate and prevent excess dosing of products which cannot be sustainably produced in the process. Additionally, this design framework was extended toward the design of reactor-separator networks by introducing a predefined number of ideal separators in the EPF calculation to assess the upper most potential of a given reaction network [Kai19].

3. **FluxMax**

   The most recent process design framework based on the EPF methodology was introduced and exemplified first by Liesche et al. [Lie+18; LSS19] and takes a different route than the MLRD and FPA approaches as no DOP is solved. Instead, the thermodynamic state space is first analyzed and then discretized based on computations of various shortcut and rigorous process unit models. This prior computation of the process unit models and the discretized layout of the state space lead to a linear optimization problem with an underlying graph representation which can be solved to guaranteed global optimality as the sources of non-linearities reside in the process unit models. For a concise overview of the FluxMax framework, table 2.4 provides an outline of the three major steps. Since arbitrary process unit models as well as phenomena

Tab. 2.4.: Three-step procedure of the FluxMax representation applied to the EPF methodology (adopted from [Lie+18; LSS19]).

	Description	Characteristics
Step 1	Discretization of thermodynamic state space	• Identification of the feasible region in state space • Creation of a grid of thermodynamic state-nodes via evaluation of shortcut or rigorous process models
Step 2	Modeling of elementary processes between state space nodes	• Identification of feasible paths between state space nodes • Assignment of cost contributions to each elementary process edge
Step 3	Network heat and mass flow optimization	• Introduction of equality and inequality constraints for heat integration • Solution of the linear superstructure optimization problem in graph representation

models can be evaluated to form the discretized state space, the framework is not limited to the synthesis of reactor networks but can be used for any process including compressor cascades [Lie+18], distillation columns [SLS19; Sch+20] or entire flowsheets [LSS19; SLS20]. In addition, the systematic inclusion of heat integration in the design framework is possible [SLS20; Sch+20].

2.4 Example Processes: Hydroaminomethylation

The model-based optimal experimental design and process synthesis methodologies for liquid multiphase processes are applied to the autotandem hydroaminomethylation (HAM) reaction of long-chain olefins in a thermomorphic multiphase system (TMS) as an example process. The next few paragraphs motivate this promising but challenging reaction by briefly talking about the significance of the reaction's intermediate and final products in the chemical industry. Alternative production processes are introduced and compared to the HAM with regard to substrate utilization, operating conditions, process limitations and process efficiency. Furthermore, the application and benefits of TMS in homogeneous catalysis are discussed before the previous work on the reaction kinetics of the two reactions composing the HAM, the homogeneously rhodium-catalyzed hydroformylation (Hyfo) of 1-decene (nC10en) and the reductive amination (RA) of 1-undecanal (nC11al), is revisited to provide the foundation for the formulation of a HAM reaction kinetic model.

2.4.1 Amine Production

Economic Significance. With a total production capacity of $1.9 \times 10^6\,\mathrm{t\,a^{-1}}$ in 2013 [Roo+15], aliphatic amines are indispensable for the production of herbicides, plastics, pharmaceuticals, surfactants, and agrochemicals [Roo+15; FSV18]. While branched amines, where the NH_2-group is located on secondary or higher carbon atoms, are mainly important in the fine-chemical industry as intermediates for organic and natural-product synthesis, production volumes of linear amines significantly exceed branched amine volumes because of their utilization as bulk-chemical intermediates [Bel+04].

Product Categories. When limiting the discussion to the class of aliphatic amines, lower and higher alkylamines (fatty amines) with C_2–C_5 [Hay01] and C_8–C_{24} [Roo+15] carbon atoms, respectively, are generally differentiated. Due to the short length of the alkyl chain and a relatively low vapor pressure, lower alkylamines can be produced in either gas or liquid phase processes with alcohols, ethers, and water as possible solvents [Roo+15]. Higher alkylamines, on the other hand, normally require liquid phase processes in which, depending on the alkyl chain length, polar or non-polar organic solvents are used. Additional categories comprising cycloamines, diamines, polyamines, and aromatic amines are also of industrial interest but will not be discussed in this work.

Process Routes. A variety of processes using different substrates, such as alcohols, carbonyl compounds (aldehydes/ketones), alkyl halides, nitro compounds, nitriles, and olefines are known and commercially applied. Figure 2.8 provides an overview over the most important industrial routes and necessary base chemicals and reagents.

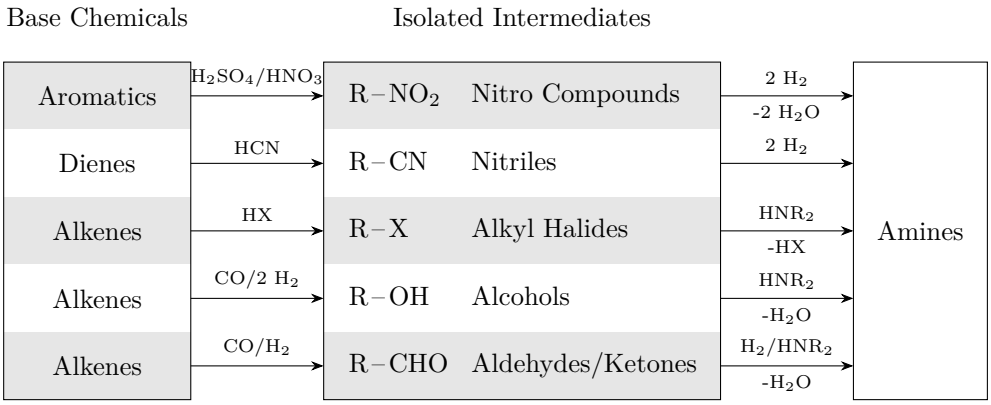

Fig. 2.8.: Industrial process routes for the production of amines (adopted from [Bia+20b] with data from [Hay01; Roo+15]).

In the following, the alcohol and carbonyl route will be presented in more detail owing to its importance for the production of lower and higher alkylamines [Hay01; Roo+15]. Additionally, direct utilization of olefines for the amine production is introduced which forms the basis for the one-pot autotandem HAM. For a concise overview over alternative production processes and processes for the production of amines from the other categories, the interested reader is referred to [Hay01; Roo+15; VG00].

Production from Alcohols and Carbonyl Compounds

Alcohols and carbonyl compounds are both converted to amines using the catalytic reductive amination (compare fig. 2.8). Therefore, major decision factors for this process route comprise the availability and prices of the substrates, hydrogen, the availability of equipment, and political considerations [Roo+15].

Reaction Conditions. Both, gas and liquid phase reductive amination processes are performed using heterogeneous catalysis with silica or alumina supported nickel, cobalt [GC81; MF82], or bimetallic [Rei+96; Ved+99] catalysts. The latter catalyst type is often preferred because of an extended period of catalyst activity while

simultaneously exhibiting reduced byproduct formation [Hay01]. Fixed-bed vapor-phase reactors or liquid-phase tickle bed and stirred tank reactors are generally used with reaction temperatures at around 150 °C to 210 °C. For the carbonyl route, stronger exothermic behavior leads to higher cooling duties but improved selectivities if appropriate solutions for the heat removal, such as high recycle rates and multitubular reactors, are employed [Roo+15]. In terms of pressure, gas phase reactors are operated at relatively mild 1 bar to 30 bar while liquid phase reactors require 50 bar to 300 bar.

Downstream Process. The removal of the co-product water with an amine/water separator is followed by multiple distillation columns for the separation and recycling of unused substrates as well as unwanted mono-, di- or triamines which form an equilibrium [Hay01; Roo+15].

Production from Olefins

Direct Synthesis. Direct synthesis of alkylamines from olefins can be achieved over different reaction routes. The Ritter reaction in which hydrogen cyanide is attached to the olefin in concentrated sulfuric acid at 30 °C to 60 °C is applicable to form lower and higher alkylamines. While this reaction has multiple drawbacks such as (i) the production of positional isomers for higher α-olefins [MDM68], (ii) corrosion issues caused by the hydrocyanic acid, (iii) the necessity for large quantities of salt and (iv) poor atom efficiency, it is often used for the production of (lower) amines with tertiary alkyl groups next to the nitrogen atom. This includes *tert*-butylamine which are difficult to produce with other processes [Roo+15].

Anti-Markovnikov Route. By using hydrogen bromide, long-chain α-olefins are first converted to the anti-Markovnikov [Bel+04] product 1-bromoalkanes before forming linear and branched primary or tertiary alkylamines with ammonia and secondary amines [Roo+15].

Zeolite Application. Without the formation of intermediates, ammonia and other amines react directly with short-chain olefins only in special cases with activated amines, activated carbon double bounds or under elevated temperatures around 250 °C to 300 °C and high pressure at 300 bar using acidic zeolites. Especially the catalytic reaction with zeolites, which allows the synthesis of *tert*-butylamine [Tag+85],

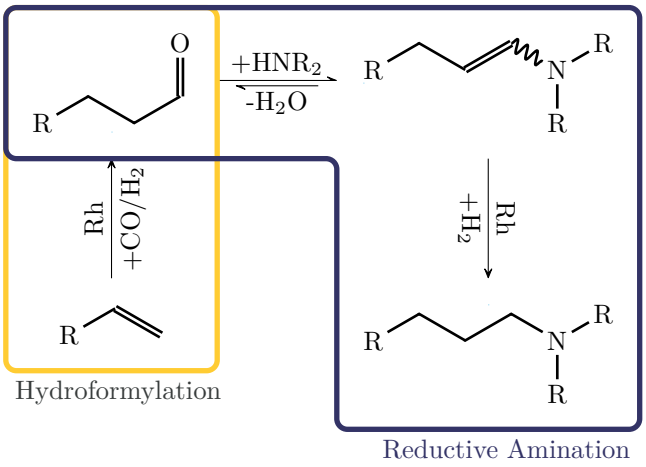

Fig. 2.9.: General hydroaminomethylation reaction sequence for a linear olefin [Faß+17].

represents a promising approach if the zeolite stability can be ensured with selectivities over 95 % at 10 % to 15 % conversion [Roo+15].

Homogeneous Catalysis. While all of the previously mentioned reactions are performed using heterogeneous conditions, direct conversion of olefins to amines using homogeneous catalysis in a one-pot hydroaminomethylation (HAM) represents an atom efficient route to amines with only water as a co-product and without the need for intermediate purification [Bia+20b]. By combining the reductive amination (RA) from the carbonyl and alcohol route (see fig. 2.9) with the hydroformylation (Hyfo) in the presence of noble metal catalysts (e.g., rhodium), long- and short-chain olefins form a mixture of Markovnikov and anti-Markovnikov products [Bel+04] with significant amounts of alcohols if no catalyst ligands or custom substrate feeding strategies are used [Kni+93; RE99]. Application of suitable catalyst ligands leads to anti-Markovnikov/Markovnikov or linear/branched ratios of up to 99 % at comparatively mild 80 °C to 135 °C and 8 bar to 120 bar [RE97; RE99; Bel+04].

These mild operating conditions and promising selectivities make the HAM to a reaction of significant academic and industrial interest. After initial proof-of-concept processes which were operated discontinuously [Eil+99], development of a continuously operated HAM for industrial applications is actively pursued.

Catalyst Recycling – Short Alkyl Chain. One important aspect for the HAM is the immobilization or recycling of the active catalyst and the selection of suitable solvents. For water-soluble amines, generally with short alkyl chain lengths, utilization of water as a solvent is a compelling option with regard to the goals of Green

Chemistry [AW00] and the European REACH initiative [Eur06]. For these systems, first processes using supported ionic liquid phase catalysts (SILPs) [Sch+13] as well as aqueous separation strategies with biphasic solvent systems to enable the synthesis of water-soluble amines from hydrophobic olefins were presented [FSV18; Jag+18]. However, despite high yields [FSV18], stable conversions over 90 % and a successful recycling of the active catalyst [Jag+18], the continuation of the research activities is required because of high rhodium leaching [FSV18] or phase-transfer limitations [Jag+18; Bia+20b].

Catalyst Recycling – Long Alkyl Chain. One way to accomplish the hydroaminomethylation of long-chain, hydrophobic olefins involves the utilization of polar solvents [KU18] or biphasic (reactive) ionic liquids (ILs). Especially the latter approach already shows a promising behavior in terms of conversion, selectivity, catalyst leaching and recycling of the active catalyst, leading to an average amine yield of 32 % [Ham+08; Faß+17; Bia+20b]. In addition to these solvent systems, utilization of thermomorphic multiphase systems [Bia+19] for catalyst recycling represents a compelling alternative to the previously mentioned solvent systems because of excellent results for the HAM's first reaction mechanism, the hydroformylation, on production scale [MKS17]. With the initial proof-of-concept [BV14], investigations regarding catalyst leaching [Vor+17] as well as separation of the co-product water [Sch+21] and the design of a first miniplant-scale process [Bia+20b], it is time for the application of process systems engineering methods for the conceptual process design to enable optimal process operation for the commercial application.

2.4.2 Thermomorphic Multiphase Systems

Concept. Thermomorphic multiphase systems can be applied in homogeneous catalysis for the simplified recovery of the, mostly noble metal, catalysts and ligands [Bia+19]. They are members of the class of switchable solvent systems which combine the absence of phase-transfer limitations due to phase boundaries during the reaction with the immobilization of the catalyst in a separate phase in the downstream process. This hybrid behavior is achieved by combining at least two solvents, one polar and one non-polar, which exhibit a strongly temperature-dependent miscibility gap [BLO98]. In applications where liquid extraction could alternatively be used to recover the catalyst with a, generally, polar or non-polar extracting agent, TMSs achieve the same result with reduced process complexity [Bia+19]. The fundamental principle of a TMS is illustrated in fig. 2.10. While the operating point of the reaction unit(s) lies outside of the miscibility gap in the homogeneous region, cooling

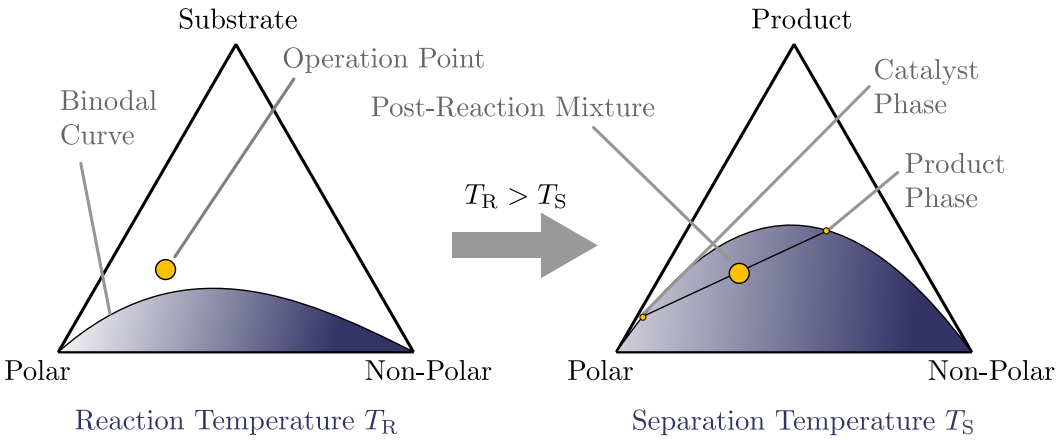

Fig. 2.10.: Temperature-dependent switchable solvent system exemplified for a type I TMS (adapted from [Beh08; McB17; Kai19]).

of the reaction mixture initiates the phase separation into a polar and non-polar phase because of an expanding miscibility gap.

TMS Types. As only a limited amount of selected solvent pairs form a TMS with the substrates and products of a reaction, additional, semi-polar solvents may be introduced to facilitate the switching behavior. Therefore, TMSs are categorized as type I and II for systems comprising three solvents and as type III if the reactants serve as semi-polar solvent [Beh08]. The difference between type I and type II TMSs lies in the shape of the miscibility gap. Closed miscibility gaps, as shown by type I TMSs, lead to an incomplete immobilization of the catalyst as traces are available in both phases. In contrast, type II systems provide excellent catalyst separation because of an open miscibility gap at separation conditions [Beh08].

Solvent Selection. Next to general requirements for solvents in industrial applications such as chemical stability, low toxicity, inert behavior, and low price, detailed information on the polarity of TMS components and their interaction with the species inherent to the reaction system are necessary [Beh08]. It needs to be ensured that the switching behavior of the solvent system is maintained at reaction and separation conditions despite the presence of substrates, products, co-products, undesired byproducts and impurities. Additionally, the polar and non-polar phases need to provide the necessary solution behavior for the catalyst in one and the products and unconverted substrates in the other phase [Kai19].

With the first TMSs being composed based on known thermomorphic behavior of solvent pairs [BLO98] and liquid phase separation behavior of solvent mixtures, later

works by Behr et al. employ Hansen solubility parameters [Han07; BR05; Beh+05; Beh08] and upper critical solution temperatures (UCSTs) of the combined reaction and phase system [BW11]. In addition to physico-chemical properties and experimental data, the selection of TMS components was extended by quantum chemical calculations using COSMO-RS [McB+16] which not only provides a systematic framework for the selection based on the catalyst, substrate, and product solubilities but also w.r.t. environmental, toxicological, and safety criteria [McB+18; Keß+19; LMS20].

2.4.3 Hydroaminomethylation of 1-Decene

While section 2.4.1 briefly introduced the hydroaminomethylation as a promising, homogeneously catalyzed production route for a variety of alkylamines under mild conditions and provided some insight together with section 2.4.2 in possible immobilization techniques for the valuable noble metal catalyst, this section focuses on the rhodium-catalyzed HAM of nC10en in a type III TMS of methanol (MeOH) as a polar and n-dodecane (nC12an) as a non-polar solvent. With the goal of formulating a reaction network model for the mbOED and its utilization in the conceptual design of a HAM process for long-chain olefins, a HAM reaction network candidate is introduced before discussing previous works on the sub-reactions comprising the hydroformylation of 1-decene and the reductive amination of 1-undecanal.

Reaction Network. A (lumped) reaction network candidate for the HAM of nC10en was proposed by Bianga et al. [Bia+20b] and is depicted in fig. 2.11 with the main and possible side reactions. In the main reaction, the α-olefin nC10en is converted in the hydroformylation with syngas (CO/H_2) to the linear aldehyde 1-undecanal. In the subsequent reductive amination, diethylamine (DEA) or another suitable amine reacts with the aldehyde to form the enamine n,n-diethylundecylamine and its corresponding imine which is hydrogenated to the amine n,n-diethylundecylamine (hydrogenated). While the hydroformylation and hydrogenation are irreversible, the condensation represents an equilibrium reaction [Kir+20a].

Catalyst Ligands. Even though rhodium is introduced to the reaction system to facilitate the hydroformylation reaction and the hydrogenation of the enamine to the amine, it also enables the direct hydrogenation of the olefin to an alkane and the aldehyde to an alcohol. To suppress these predominant reactions, phosphine ligands like tributylphosphine (PBu3) [RE99], Xantphos [Kir+20b; Kir+20a], the

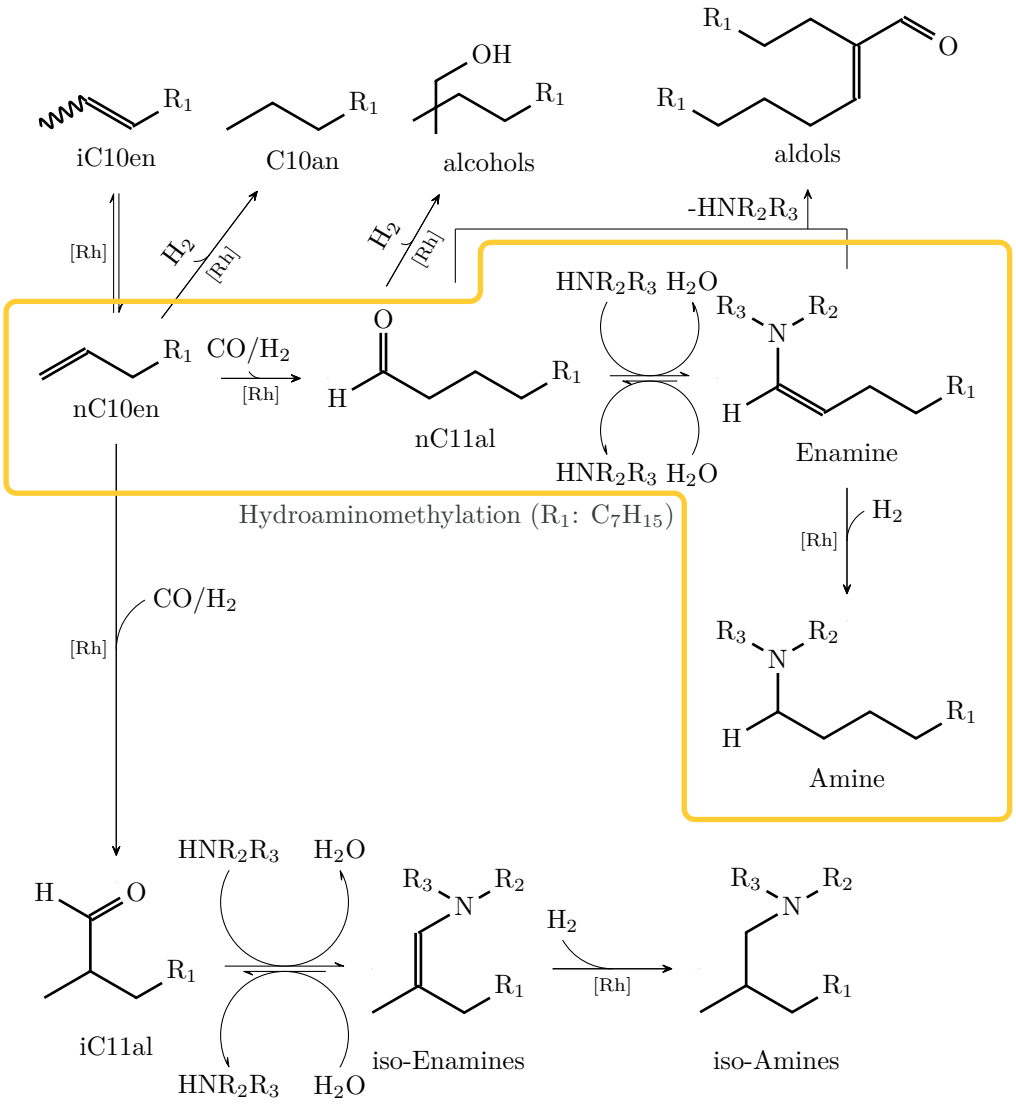

Fig. 2.11.: Detailed reaction network of the rhodium-catalyzed HAM with side reactions (adopted from [Bia+20b]).

water-soluble TPPTS [BKB13] and SulfoXantphos [Bia+20b] represent additives alongside the catalyst precursor Rh(acac)(COD) or Rh(acac)$(CO)_2$. In addition to the hydrogenation, isomerization of the α-olefin leads to separate HAM branches and the synthesis of aldehyde isomers as well as iso-amines. However, these side reactions can be reduced successfully by regioselective catalyst ligands [MBS10] in combination with suitable operating conditions [KFS17].

Aldol Condensation. Another side reaction, which occurs especially at high aldeyhde concentrations, is the organocatalyzed aldol formation from two aldehydes or aldehydes and enamines [Bia+20a]. Even though the literature is not clear about whether the aldol addition [Kir+20b; Kir+20a; Bia+20b] or the aldol condensation [Bia+20a; Bia+20b] represents the predominant reaction route, consideration of this byproduct is necessary in cases of elevated aldehyde concentrations over a prolonged period of time.

Hydroformylation of 1-Decene

The hydroformylation reaction or oxo-synthesis represents the first step in the autotandem HAM. Due to the importance of long-chain olefins as intermediates for the production of alcohols, amines, and perfumes [Koh+13], many studies on the applicability of TMSs for the efficient recovery and recycling of the rhodium catalyst and its ligands can be found [Bia+19]. Of particular interest for the derivation of a reaction network model for the HAM are the works by Markert et al. [Mar+13], Kiedorf et al. [Kie+14], Jörke et al. [Jör+17], and Hentschel et al. [Hen+15].

C12 Kinetics. For the derivation of a suitable (lumped) reaction network, the authors focused on the description of the catalytic cycle of the rhodium catalyst with BiPhePhos ligands in a TMS of n,n-dimethylformamide (DMF) and n-decane (C10an). The first candidate for a Hyfo model with 1-dodecene (nC12en) is provided from Markert et al. [Mar+13] and Kiedorf et al. [Kie+14] who formulated a reduced reaction network in which all dodecene isomers (iC12en) and branched aldehydes (iC13al) are lumped together as pseudo-species. Therefore, the model considers five species including the α-olefin, the linear aldehyde and the hydrogenation product nC12an. Because of inaccurate predictions of semibatch and perturbed-batch experiments, this reaction network was extended and reparameterized by Hentschel et al. [Hen+15].

C10 Kinetics. Based on these results, Jörke et al. [Jör+15; JSH15] investigated the olefin isomerization in more detail for the equivalent 1-decene with nC12an as the non-polar solvent. In addition to an improved catalytic cycle of the isomerization reaction, a rigorous formulation of the gas phase composition dependency of the catalyst pre-equilibrium with rhodium-BiPhePhos is provided. With these insights and detailed experimental investigations to determine all relevant active catalytic species [JSH17], Jörke et al. [Jör+17] extended the catalytic cycle toward the Hyfo of nC10en. It was found that the catalyst pre-equilibrium, which was already investigated in prior studies [Kie+14; Jör+15; JSH15], can be safely approximated with the inhibition constant $K_{\mathrm{cat,CO}}$ under hydroformylation conditions by

$$c_{\mathrm{cat}} = \frac{c_{\Sigma\mathrm{cat}}}{1 + K_{\mathrm{cat,CO}} c_{\mathrm{CO}}}, \tag{2.20}$$

with the molar concentrations of the active catalyst species c_{cat}, the provided catalyst precursor $c_{\Sigma\mathrm{cat}}$, and the dissolved CO, c_{CO}.

Kinetic Model. The reaction network which comprises (i) the Hyfo of nC10en to the linear (r_{Hyfon}) nC11al and branched (r_{Hyfoni}) undecanal isomers (iC11al), (ii) the hydrogenation of nC10en to C10an (r_{HydDec}), (iii) the successive isomerization of nC10en to 5-decene ($r_{\mathrm{Iso},i}$, $i = \{1, 2, \ldots, 4\}$) and (iv) the hydroformylation of a lumped decene isomer species to the branched aldehyde iC11al is depicted in fig. 2.12 and summarized with the reaction rate equations

$$r_{\mathrm{Iso},i} = k_{\mathrm{Iso},i} \left(c_{i-\mathrm{decene}} - \frac{c_{(i+1)-\mathrm{decene}}}{K^{\mathrm{eq}}_{\mathrm{Iso},i}(T)} \right) c_{\mathrm{cat}}, \tag{2.21a}$$

$$r_{\mathrm{Hyfon}} = \frac{k_{\mathrm{Hyfon}} c_{1-\mathrm{decene}} c_{\mathrm{CO}} c_{\mathrm{H_2}} c_{\mathrm{cat}}}{1 + K_{\mathrm{Hyfo,I}} c_{\mathrm{H_2}} + K_{\mathrm{Hyfo,II}} c_{\mathrm{CO}} c_{\mathrm{H_2}}}, \tag{2.21b}$$

$$r_{\mathrm{Hyfoni}} = \frac{k_{\mathrm{Hyfoni}} c_{1-\mathrm{decene}} c_{\mathrm{CO}} c_{\mathrm{H_2}} c_{\mathrm{cat}}}{1 + K_{\mathrm{Hyfo,III}} c_{\mathrm{H_2}} + K_{\mathrm{Hyfo,IV}} c_{\mathrm{CO}} c_{\mathrm{H_2}}}, \tag{2.21c}$$

$$r_{\mathrm{Hyfoi}} = \frac{k_{\mathrm{Hyfoi}} \sum_{i=2}^{5} c_{i-\mathrm{decene}} c_{\mathrm{CO}} c_{\mathrm{H_2}} c_{\mathrm{cat}}}{1 + K_{\mathrm{Hyfo,III}} c_{\mathrm{H_2}} + K_{\mathrm{Hyfo,IV}} c_{\mathrm{CO}} c_{\mathrm{H_2}}}, \tag{2.21d}$$

$$r_{\mathrm{HydDec}} = \frac{k_{\mathrm{HydDec}} c_{1-\mathrm{decene}} c_{\mathrm{H_2}} c_{\mathrm{cat}}}{1 + K_{\mathrm{HydDec}} c_{\mathrm{H_2}}}. \tag{2.21e}$$

For each reaction $j \in \mathcal{RCT}^{\mathrm{Hyfo}} = \{\mathrm{Iso}_i, \mathrm{Hyfon}, \mathrm{Hyfoni}, \mathrm{Hyfoi}, \mathrm{HydDec}\}$ with $i \in \{1, 2, 3, 4\}$, the temperature-dependent reaction rate coefficient $k_j(T)$ is expressed using the temperature-centered Arrhenius approach

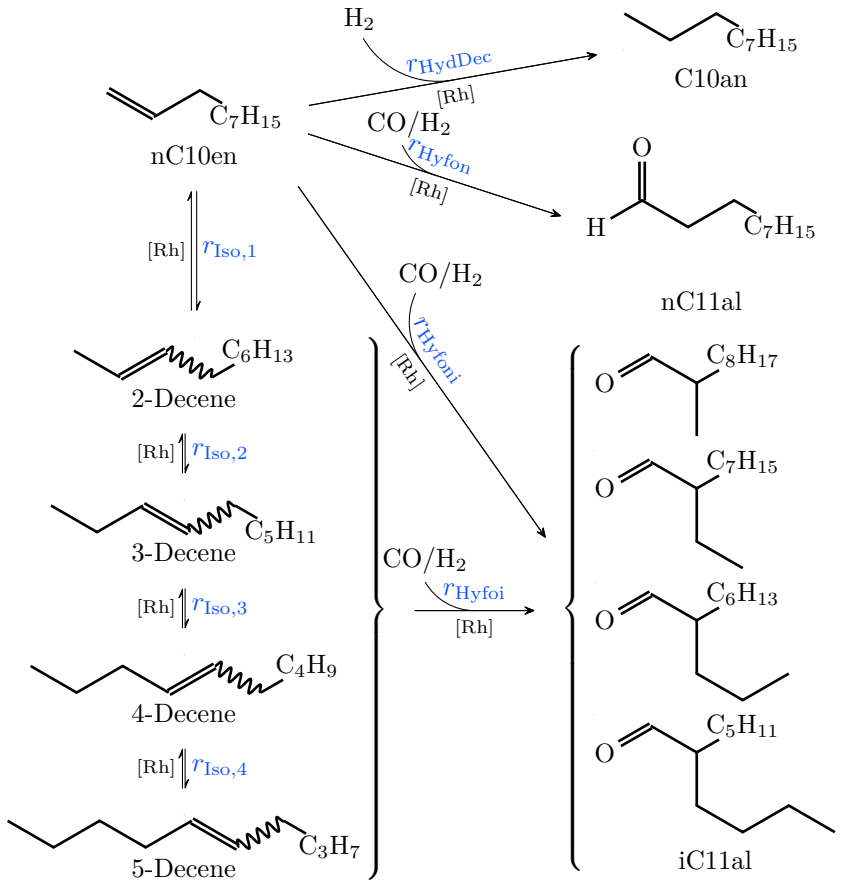

Fig. 2.12.: Reaction network of the Hyfo of 1-decene in a DMF/C10an TMS (adopted from [Jör+17]).

$$k_j(T) = \exp\left(A_j + B_j \frac{T - T_{\text{ref}}}{T}\right), \tag{2.22}$$

with the dimensionless parameters A_j and B_j and the reference temperature $T_{\text{ref}} = 378\,\text{K}$. The collision factor k_0 and the activation energy E_A of the standard Arrhenius approach can be derived from the dimensionless parameters and the universal gas constant $R = 8.314\,\text{J}\,\text{mol}^{-1}\,\text{K}^{-1}$ with

$$k_{0,j} = \exp\left(A_j + B_j\right), \tag{2.23a}$$

$$E_{\text{A},j} = B_j R T_{\text{ref}}. \tag{2.23b}$$

All kinetic parameters, equilibrium, and inhibition constants are summarized in appendix B.1 in table B.1 and table B.2, respectively.

Gas Phase Model. For the concentration of all gaseous species $i \in \mathcal{SPC}^{\mathrm{Gas}} = \{H_2, CO\}$ in the liquid phase, mass balances were used with the difference between the saturate and liquid phase concentration $\left(c_i^{\mathrm{sat}} - c_i\right)$ as driving force and scaled by the apparatus specific effective mass transfer coefficient β_{eff}. The saturate concentrations were calculated using Henry coefficients H_i according to

$$c_i^{\mathrm{sat}}(T) = p y_i H_i(T)^{-1}, \tag{2.24}$$

with the temperature-centered formulation eq. (B.1) for $H_i(T)$ and all gas-liquid phase transfer parameters summarized in appendix B.1 in table B.3 [Jör+15].

Operating Window. Since the reaction rate equations approximate complex chemical interactions, reliable model predictions can only be expected in the experimentally validated operating window summarized in table 2.5 with the molar ratios

$$\phi^{\mathrm{n},0}_{\mathrm{sub,iC10en}} = c^0_{\mathrm{sub}}\left(c^0_{\mathrm{sub}} + c^0_{\mathrm{iC10en}}\right)^{-1}, \tag{2.25a}$$

$$\phi^{\mathrm{n},0}_{\mathrm{cat,sub}} = c^0_{\Sigma\mathrm{cat}}\left(c^0_{\mathrm{sub}} + c^0_{\mathrm{iC10en}}\right)^{-1}, \tag{2.25b}$$

$$\phi^{\mathrm{n}}_{\mathrm{Lig,cat}} = c_{\mathrm{Lig}} c^{-1}_{\Sigma\mathrm{cat}}, \tag{2.25c}$$

$$\phi^{\mathrm{n},0}_{\mathrm{sub,DMF}} = c^0_{\mathrm{sub}} {c^0_{\mathrm{DMF}}}^{-1}, \tag{2.25d}$$

$$\phi^{\mathrm{n}}_{\mathrm{nC12an,DMF}} = c_{\mathrm{nC12an}} c^{-1}_{\mathrm{DMF}}. \tag{2.25e}$$

In this context, the subscript $\square_{\mathrm{sub}}$ represents nC10en. Please note that all molar, mass, and volumetric ratios are denoted as ϕ^{n}, ϕ^{m} and ϕ^{V}, respectively. If a condition is only valid at the start of the reaction, the superscript $\square^0$ is used.

Tab. 2.5.: Investigated operating window for the Hyfo of 1-decene [Jör+17]. The subscript $\square_{\mathrm{sub}}$ represents nC10en.

ϑ / °C	[95, 135]
$p_{\mathrm{CO,H_2}}$ / bar	[0, 22]
$\phi^{\mathrm{n},0}_{\mathrm{sub,iC10en}}$ / mol mol^{-1}	[0, 1]
$\phi^{\mathrm{n},0}_{\mathrm{cat,nC10en}}$ / mol mol^{-1}	$\left[1 \times 10^{-5}, 2 \times 10^{-3}\right]$
$\phi^{\mathrm{n}}_{\mathrm{Lig,cat}}$ / mol mol^{-1}	[3, 5]
$\phi^{\mathrm{n},0}_{\mathrm{sub,DMF}}$ / mol mol^{-1}	1 / 4
$\phi^{\mathrm{n}}_{\mathrm{nC12an,DMF}}$ / mol mol^{-1}	3 / 4
ligands	BiPhePhos
operation mode	{batch, semibatch}

Reductive Amination of 1-Undecanal

Kinetic Model. The second step of the HAM is the reductive amination of 1-undecanal. Only recently, investigations on the kinetics of the homogeneously catalyzed reductive amination of long-chain aldehydes commenced due to the rising interest in the homogeneously catalyzed HAM. Kirschtowski et al. [Kir+20b] were the first to propose a kinetic model for the homogeneously rhodium-catalyzed RA in a TMS with MeOH/nC12an and Xantphos/SulfoXantphos as catalyst ligands. Besides the condensation of the substrate to the intermediate n,n-diethylundecylamine (enamine) and subsequent hydrogenation toward n,n-diethylundecylamine (hydrogenated) (amine), major side reactions such as the formation of alcohols and aldols (see fig. 2.11) are considered. In addition to experimental batch and semibatch investigations, quantum chemical calculations w.r.t. the equilibrium-controlled condensation of the enamine were performed [Kir+20a], leading to the reaction rate equations

$$r_{\mathrm{Cond}} = k_{\mathrm{Cond}} \left(c_{\mathrm{nC11al}}\, c_{\mathrm{DEA}} - \frac{c_{\mathrm{En}}\, c_{\mathrm{H_2O}}}{K^{\mathrm{eq}}_{\mathrm{Cond}}} \right), \tag{2.26a}$$

$$r_{\mathrm{HydEn}} = k_{\mathrm{HydEn}}\, c_{\Sigma\mathrm{cat}}\, c_{\mathrm{En}}\, c_{\mathrm{H_2}}, \tag{2.26b}$$

$$r_{\mathrm{HydUndec}} = k_{\mathrm{HydUndec}}\, c_{\Sigma\mathrm{cat}}\, c_{\mathrm{nC11al}}\, c_{\mathrm{H_2}}, \tag{2.26c}$$

$$r_{\mathrm{Add}} = k_{\mathrm{Add}}\, c_{\mathrm{nC11al}}\, c_{\mathrm{En}}, \tag{2.26d}$$

with the reaction rate coefficients k_j for all reaction rate expressions $j \in \mathcal{RCT}^{\mathrm{RA}} = \{\mathrm{Cond}, \mathrm{HydEn}, \mathrm{HydUndec}, \mathrm{Add}\}$ as a function of the temperature according to the standard Arrhenius approach

$$k_j(T) = k_{0,j} \exp\left(\frac{-E_{\mathrm{A},j}}{RT} \right). \tag{2.27}$$

Please note that no catalyst pre-equilibrium is assumed so that the total amount of catalyst is considered as an active species. To improve the accuracy of the model, the equilibrium constant $K^{\mathrm{eq}}_{\mathrm{Cond}}$ of the condensation equilibrium is modeled as a function of the temperature and the Gibbs free enthalpy using

$$K^{\mathrm{eq}}_{\mathrm{Cond}}(T) = \exp\left(\frac{-\Delta G_{\mathrm{r,Cond}}}{RT} \right). \tag{2.28}$$

The corresponding reaction network is visualized in fig. 2.13 and all thermodynamic and kinetic parameters are presented in table B.5 and table B.6 of appendix B.2. The

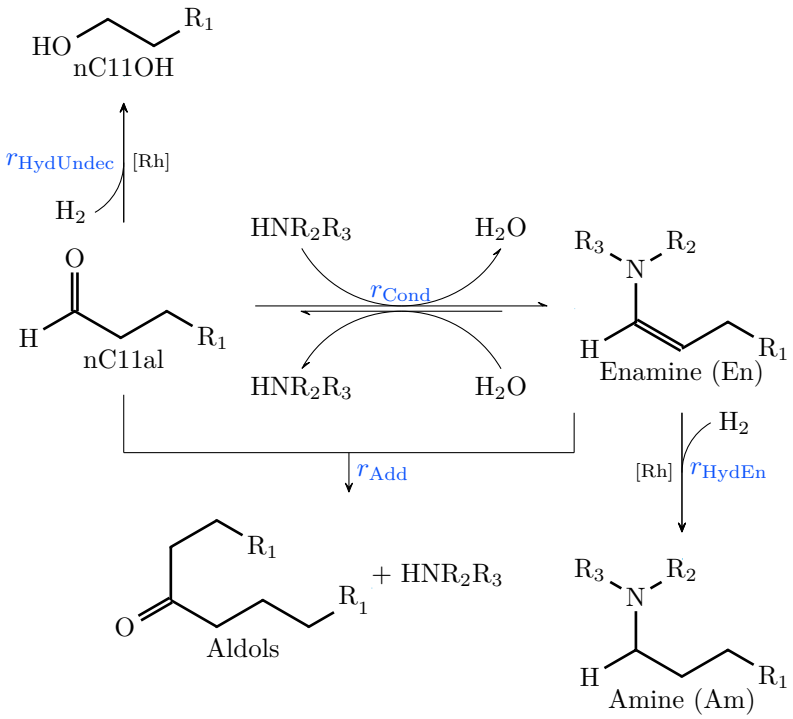

Fig. 2.13.: Reaction network of the RA of 1-undecanal in a MeOH/nC12an TMS (adopted from [Kir+20a]). R_1: C_8H_{17}.

liquid phase concentrations are calculated using mass balances and Henry coefficients for the saturate gas concentrations according to eq. (2.24). The corresponding parameters can be found in table B.7.

Operating Window. Similar to the hydroformylation, reliable predictions using the RA kinetics are limited to the experimentally investigated operating window. In addition to the temperature and hydrogen pressure window in table 2.6, the catalyst ligand to precursor ratio from eq. (2.25c), the molar and mass ratios

$$\phi^{\mathrm{n},0}_{\mathrm{cat,sub}} = c^0_{\Sigma\mathrm{cat}} {c^0_{\mathrm{sub}}}^{-1}, \tag{2.29a}$$

$$\phi^{\mathrm{n},0}_{\mathrm{DEA,sub}} = c^0_{\mathrm{DEA}} {c^0_{\mathrm{sub}}}^{-1}, \tag{2.29b}$$

$$\phi^{\mathrm{m}}_{\mathrm{MeOH,nC12an}} = m_{\mathrm{MeOH}} m^{-1}_{\mathrm{nC12an}}, \tag{2.29c}$$

the inital volumetric water fraction

$$\phi^{\mathrm{V},0}_{\mathrm{H_2O}} = V^0_{\mathrm{Liq,H_2O}} \left(\sum_{i \in \mathcal{SPC}} V^0_{\mathrm{Liq},i} \right)^{-1}, \tag{2.29d}$$

and the initial mass fraction of the substrate,

$$w_{\mathrm{sub}}^{0} = m_{\mathrm{sub}}^{0} \left(\sum_{i \in \mathcal{SPC}} m_{i}^{0} \right)^{-1}, \tag{2.29e}$$

where $\mathcal{SPC}$ covers all species in the liquid phase, need to be considered. In the context of the RA, the subscript $\square_{\mathrm{sub}}$ refers to nC11al.

Tab. 2.6.: Investigated operating window for the RA of 1-undecanal [Kir+20a]. The subscript $\square_{\mathrm{sub}}$ represents nC11al.

ϑ / °C	[85, 115]
$p_{\mathrm{H_2}}$ / bar	[10, 30]
$\phi^{\mathrm{n}}_{\mathrm{Lig,cat}}$ / mol mol^{-1}	1
$\phi^{\mathrm{n,0}}_{\mathrm{cat,sub}}$ / mol mol^{-1}	$\left[2.5 \times 10^{-4}, 1 \times 10^{-3}\right]$
$\phi^{\mathrm{n,0}}_{\mathrm{DEA,sub}}$ / mol mol^{-1}	[1, 4]
$\phi^{\mathrm{m}}_{\mathrm{MeOH,nC12an}}$ / g g^{-1}	[1, 99]
$\phi^{\mathrm{V,0}}_{\mathrm{H_2O}}$ / L L^{-1}	[0, 0.1]
w^{0}_{sub} / g g^{-1}	[0.02, 0.04]
operation mode	{batch, semibatch}
ligands	{Xantphos, SulfoXantphos}

3 Model-Based Identification of Kinetic Reaction Networks in Complex Multiphase Systems

3.1 Motivation

For all subsequent model-based investigations of the homogeneously rhodium-catalyzed autotandem hydroaminomethylation (HAM), the formulation and parameterization of a suitable reaction kinetic model is a prerequisite. Even though kinetic models for the sub-networks comprising the hydroformylation of 1-decene and the reductive amination of 1-undecanal are available (see section 2.4.3), non-overlapping operating windows, the utilization of different catalyst ligands and solvent systems complicate direct combination of both models. Consequently, additional experiments and a critical evaluation of all reaction pathways in the detailed reaction network (see fig. 2.11) are necessary to formulate a suitable and manageable set of reaction kinetics for the HAM.

Experimental Design Approaches. In contrast to heuristic experimental design approaches which struggle to identify complex, non-linear system behavior, systematic approaches like factorial design plans are preferable as they are designed to account for it. These plans are able to effectively sample the design space and capture interactions of design variables for the parameterization of response surfaces. While the application of these techniques is well suited in cases where a general idea about the process behavior is required without any prior assumptions on a suitable process model, parameterization of an available process model is more efficient using model-based optimal experimental design (mbOED) techniques. This is especially the case for high dimensional design spaces since mbOED is able to exploit the process model structure. Besides the efficiency aspect, optimization-based mbOED enables the consideration of additional, non-linear constraints which may be necessary to ensure experimental feasibility by limiting the design space and/or the execution in a chemically and physically reasonable operating window.

Benefits of Model-Based Optimal Experimental Design. In the case of the HAM, a suitable model structure is already available in addition to good initial parameter guesses which makes mbOED a particularly appealing approach to design a minimal number of highly informative experiments. Additional arguments for the application of mbOED comprise the incorporation of (i) device restrictions which limit the speed of temperature and pressure changes in the reactor vessel, (ii) bounds on the maximum number of and minimum time interval between sample points due to a limited liquid hold-up and maximum possible workload for the experimenter and (iii) measures against the formation of multiple liquid phases. Especially the latter point is crucial since multiple liquid phases introduce mass transfer limitations which can confound the resulting parameter estimates. In the case of the HAM, two liquid phases are possible because of the formation of water as a couple product during the enamine condensation (see fig. 2.11) in combination with the limited water tolerance of the methanol (MeOH)/n-dodecane (nC12an) TMS. Preventing this phase separation during the experiments is essential as it not only introduces mass transfer limitations between both phases but may also lead to catalyst and co-substrate leaking to the aqueous phase. Therefore, the formulation of a mbOED problem needs to be extended by phase equilibrium calculations to ensure monophasic conditions throughout the experiments.

Chapter Overview. In this chapter which is based on the published work by Rätze et al. [Rät+23], a reduced reaction network with suitable kinetic equations is proposed to accurately capture the essential behavior of the HAM for a broad range of operating conditions. For the identification of this kinetic model, a reactor vessel model is formulated in section 3.2 based on literature information and preliminary experiments. This reactor vessel model is embedded in a mbOED problem in section 3.3 for the simultaneous design of multiple experiments. To ensure monophasic conditions during all experiments, the mbOED problem is expanded by a phase equilibrium formulation with a PC-SAFT-based activity coefficient surrogate model. In the next step after the experimental application of the computed designs, the measured concentration profiles are used to improve the reactor vessel model and the kinetic model for the parameter identification in section 3.5. After a discussion of the results in section 3.6, the chapter terminates with a brief summary and an outlook in section 3.7.

3.2 Reactor Vessel Model

The hydroaminomethylation of 1-decene (nC10en) represents the combination of the hydroformylation (Hyfo) of 1-decene and the reductive amination (RA) of 1-undecanal. Therefore, the connection of the reaction mechanisms from section 2.4.3 including the model structure and the parameter estimates represent a suitable initial guess for the HAM reaction since the solvent system and the catalyst ligand were already used in the RA. However, because of the complexity of the Hyfo and RA networks, a reduced mechanistic model with a limited number of identifiable parameters is required for the application in mbOED and the subsequent parameter estimation. In a preliminary, unpublished work by Kortuz [Kor20], a reaction network candidate for the HAM is proposed which simplifies the network structure by (i) lumping all decene isomers into a pseudo-species iC10en (similar to the work from Hentschel et al. [Hen+15]) and (ii) neglecting all secondary and intermediate products, such as alcohols, aldols, branched aldehydes, branched enamines and branched amines, due to negligible yields of under 5 % of the total product yield in the final reaction mixture. Consequently, the remaining set of reaction rate equations is reduced to $\mathcal{RCT}^{\mathrm{HAM}} = \{\mathrm{Hyfo}, \mathrm{Iso}, \mathrm{HydDec}, \mathrm{Cond}, \mathrm{HydEn}\}$. A schematic representation of this network can be found in fig. 3.1.

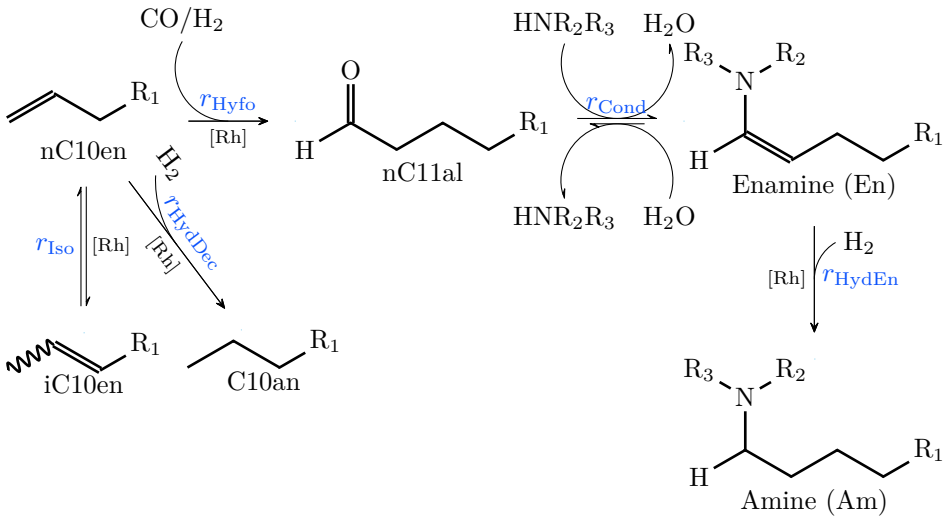

Fig. 3.1.: Reduced reaction network of the HAM of 1-decene in a MeOH/nC12an TMS (adopted from [Kor20; Kor+22]).

Structurally, the reaction rate equations for the isomerization, hydroformylation and hydrogenation of 1-decene are adopted from Jörke et al. [Jör+17] while the enamine condensation and enamine hydrogenation are taken from Kirschtowski et al. [Kir+20a] and Kortuz [Kor20], respectively. Due to the reduced kinetic model, only the first isomerization expression in eq. (2.21a) is used to describe the reaction rate and chemical equilibrium between 1-decene and the lumped decene isomers. Additionally, branched aldehydes are neglected because of the selectivity increasing effect of the catalyst ligand so that the expression in eq. (2.21b) suffices to describe the hydroformylation toward the intermediate product 1-undecanal. The reduced reaction kinetic model can be summarized as

$$r_{\mathrm{Iso}} = k_{\mathrm{Iso}} c_{\mathrm{cat}} \left(c_{\mathrm{nC10en}} - \frac{c_{\mathrm{iC10en}}}{K_{\mathrm{Iso}}^{\mathrm{eq}}} \right), \tag{3.1a}$$

$$r_{\mathrm{Hyfo}} = \frac{k_{\mathrm{Hyfo}} c_{\mathrm{cat}} c_{\mathrm{nC10en}} c_{\mathrm{H_2}} c_{\mathrm{CO}}}{1 + K_{\mathrm{Hyfo,I}} c_{\mathrm{H_2}} + K_{\mathrm{Hyfo,II}} c_{\mathrm{H_2}} c_{\mathrm{CO}}}, \tag{3.1b}$$

$$r_{\mathrm{HydDec}} = \frac{k_{\mathrm{HydDec}} c_{\mathrm{cat}} c_{\mathrm{nC10en}} c_{\mathrm{H_2}}}{1 + K_{\mathrm{HydDec}} c_{\mathrm{H_2}}}, \tag{3.1c}$$

$$r_{\mathrm{Cond}} = k_{\mathrm{Cond}} \left(c_{\mathrm{nC11al}} c_{\mathrm{DEA}} - \frac{c_{\mathrm{En}} c_{\mathrm{H_2O}}}{K_{\mathrm{Cond}}^{\mathrm{eq}}(T)} \right), \tag{3.1d}$$

$$r_{\mathrm{HydEn}} = \frac{k_{\mathrm{HydEn}} c_{\mathrm{cat}} c_{\mathrm{En}} c_{\mathrm{H_2}}}{1 + K_{\mathrm{HydEn}} c_{\mathrm{H_2}}}. \tag{3.1e}$$

To unify the mathematical description of the temperature-dependent kinetic factors $k_j(T)$ with $j \in \mathcal{RCT}^{\mathrm{HAM}}$, the dimensionless formulation of the temperature-centered Arrhenius approach from eq. (2.22) is used with $T_{\mathrm{ref}} = 373.15\,\mathrm{K}$. In the next paragraphs, the decisions on different aspects of the kinetic model structure are discussed.

Reaction Equilibria. Figure 3.1 contains two reversible reactions – the isomerization of 1-decene and the condensation of 1-undecanal toward the enamine. While the calculation of the equilibrium constant for the condensation reaction $K_{\mathrm{Cond}}^{\mathrm{eq}}(T)$ can directly be used from eq. (2.28) because of the utilization and identification of the Gibbs free reaction enthalpy $\Delta G_{\mathrm{r,Cond}}$ in the MeOH/nC12an TMS [Kir+20a], the equilibrium constant of the isomerization reaction $K_{\mathrm{Iso}}^{\mathrm{eq}}$ needs to be investigated in more detail.

Jörke et al. [JSH15] performed thermodynamic calculations and measurements to identify the equilibrium constants of the isomerization reactions for the first five decene isomers. Additionally, an equilibrium constant was proposed for a lumped decene isomer species in a DMF/nC12an TMS which follows the polynomial

$$K_{\mathrm{Iso}}^{\mathrm{eq}}(\vartheta) = a\vartheta^4 + b\vartheta^3 + c\vartheta^2 + d\vartheta + e, \tag{3.2}$$

where ϑ denotes the Celsius-scale temperature. The parameters for the lumped isomerization reaction can be found in table B.4. Unfortunately, direct utilization of this model without prior validation in the MeOH/nC12an solvent system is not recommended because of possible solvent effects. Therefore, the isomerization equilibrium constant is measured experimentally at selected temperatures of the targeted operating window in preliminary experiments. The experimental setup and results can be found in table B.8 with a visual comparison to the lumped isomerization constant from Jörke et al. [JSH15] in fig. 3.2.

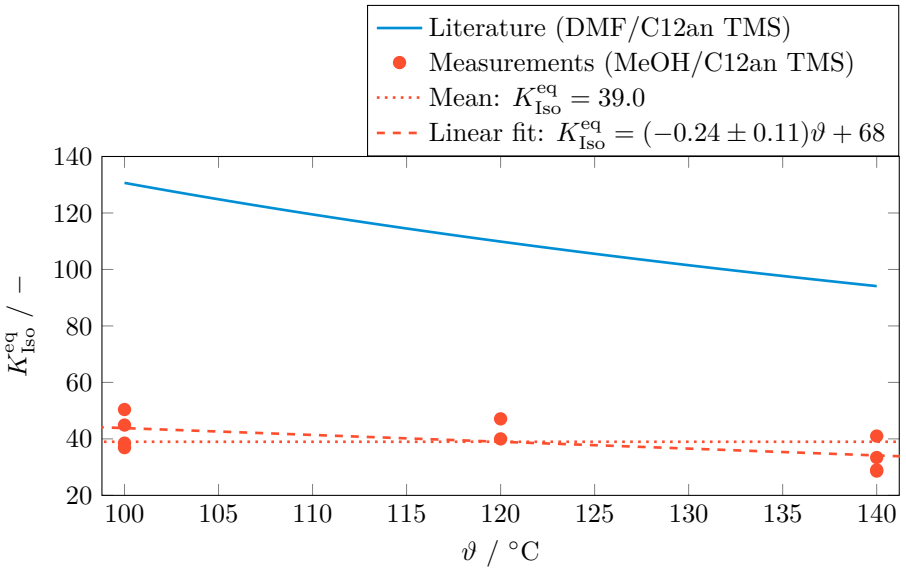

Fig. 3.2.: Comparison of the lumped isomerization equilibrium constant $K_{\mathrm{Iso}}^{\mathrm{eq}}(\vartheta)$ for the DMF/nC12an [JSH15] and MeOH/nC12an TMS. The parameter values for eq. (3.2) and the measurements under HAM conditions can be found in table B.4 and table B.8, respectively. Linear approximation of the measurement data results in a $R^2 = 0.39$. One standard deviation is assumed for the slope of the linear fit.

The measurements under HAM conditions deviate strongly from the literature data so that the measurement data is approximated over its mean value of 39.0 mol mol^{-1}. Even though the lack of fit test with a p-value of 0.09 indicates additional information about the temperature dependency of the equilibrium constant, the simplified description over the data mean is chosen due to the minor temperature effect, a significant standard deviation above 45 % over the nominal slope, a low R^2-value, and

the negligible influence of $K_{\text{Iso}}^{\text{eq}}$ in the parameter sensitivity study in appendix E.1 (see fig. E.1).

Catalyst Pre-Equilibrium. Owing to the corrosive nature of DEA, the application of Fourier transform infrared spectroscopy (FTIR) measurements for the identification of the catalyst cycles and possible catalyst inhibitions is not possible in the available experimental setup. Therefore, the concentration of the active catalyst species c_{cat} is calculated according to eq. (2.20) with the catalyst inhibition constant $K_{\text{cat,CO}} = 5496.70\,\text{L}\,\text{mol}^{-1}$ [Jör+17]. Even though $K_{\text{cat,CO}}$ is considered constant during the mbOED, the catalyst pre-equilibrium has a significant impact on nearly all reactions in the reduced HAM network. Thus, special attention needs to be paid to the catalyst pre-equilibrium during the parameter identification.

Gas-Liquid Mass Transfer. Analogous to the Hyfo and RA reaction kinetics, the mass transfer of the gaseous species $i \in \{\text{H}_2, \text{CO}\} = \mathcal{SPC}^{\text{Gas}}$ to the liquid phase is modeled using the concentration differences $\left(c_i^{\text{sat}} - c_i\right)$ together with Henry coefficients for the saturate gas concentration according to eq. (2.24). The constant Henry coefficients H_i and effective mass transport coefficients $\beta_{\text{eff},i}$ identified in preliminary experiments for the experimental setup can be found in appendix B.3 in table B.10.

Inhibition Constants. Inhibition constants in eqs. (3.1b), (3.1c) and (3.1e) are the result of complex reaction networks and kinetic formulations, compressed to a reduced formulation according to the rate determining step. While the formulations for the hydroformylation and the hydrogenation of 1-decene are directly taken from eqs. (2.21b) and (2.21e), a hydrogen inhibition is added for the enamine hydrogenation in eq. (3.1e) by Kortuz [Kor20] who identified the inhibition constant based on multiple experiments with varying gas compositions, pressures, and operating modes. Even prior to the sensitivity analysis which can be found in appendix E, these parameters can be expected to have a minor effect on the reaction kinetics under nominal conditions where sufficient hydrogen concentrations in the liquid phase are present. In the absence of hydrogen and/or carbon monoxide (CO), detailed investigations specific to the respective reaction are necessary. However, as this work focuses on an update of the available initial parameter guesses using a limited number of optimally designed experiments, these inhibition parameters are kept constant during the mbOED and parameter identification. The parameter values for the inhibition constants are summarized in table B.9 of appendix B.3

Liquid Phase Mass Balances. Finally, the dynamic behavior of the species molar amount $i \in \{\text{nC10en, iC10en, nC11al, DEA, En, Am, C10an, } H_2O\text{, CO, } H_2\text{, nC12an, MeOH}\} = \mathcal{SPC}$ in the liquid phase can be formulated as

$$\frac{\mathrm{d}n_i}{\mathrm{d}t} = \begin{cases} V_{\text{Liq}}\beta_{\text{eff},i}\left(c_i^{\text{sat}} - c_i\right) + V_{\text{Liq}}\sum_{j\in\mathcal{RCT}^{\text{HAM}}}\nu_{i,j}r_j & \text{if } i \in \mathcal{SPC}^{\text{Gas}}, \\ V_{\text{Liq}}\sum_{j\in\mathcal{RCT}^{\text{HAM}}}\nu_{i,j}r_j & \text{else,} \end{cases} \tag{3.3a}$$

$$n_i\left(t^0\right) = n_i^0, \tag{3.3b}$$

with the stoichiometric matrix $\nu_{i,j}$ and $j \in \mathcal{RCT}^{\mathcal{RCT}^{\text{HAM}}}$. All parameter values including initial guesses for the kinetic parameters A_j and B_j are summarized in tables B.9 to B.12.

Operating Window

Similar to the Hyfo and RA, process constraints need to be introduced to ensure the feasibility of the reaction with regard to economical and monophasic operation as well as the separation of the TMS components in the subsequent downstream process. These constraints encompass the ratio of the polar to non-polar TMS components eq. (2.29c), the substrate to co-substrate ratio eq. (2.29b), the catalyst precursor to substrate ratio eq. (2.29a) and the initial volumetric water fraction eq. (2.29d). Please note that in contrast to the RA, the substrate for the HAM is 1-decene. While $\phi^{\text{m}}_{\text{nC12an,MeOH}}$ and $\phi^{\text{n,0}}_{\text{cat,sub}}$ will be fixed for the mbOED calculations according to table 3.1, $\phi^{\text{n,0}}_{\text{DEA,sub}}$ and $\phi^{\text{V,0}}_{\text{H}_2\text{O}}$ are considered as control variables. However, especially the feasible region of the latter variable will be restricted further besides the range provided in table 3.1 to ensure monophasic behavior according to the phase equilibrium model and constraint in eq. (3.6). For the same reason, a lower temperature bound of 105 °C in the operating window is selected at which monophasic behavior using regular operating conditions can be ensured. In addition to the previous ratios, the catalyst metal to ligand ratio only needs to be specified in an experimental environment since no ligand concentrations or any other constraint are considered in eq. (3.1). The volume fraction introduced in eq. (2.29d) requires density correlations for all species $i \in \mathcal{SPC} \setminus \mathcal{SPC}^{\text{Gas}}$ following

$$\rho_i = \begin{cases} a_i b_i^{-\left(1-T/d_i\right)^{c_i}} & \text{if } i \notin \{\text{En, Am}\}, \quad (3.4a) \\ \tilde{M}_i a_i b_i^{-1-\left(1-T/c_i\right)^{d_i}} & \text{else,} \quad (3.4b) \end{cases}$$

Tab. 3.1.: Investigated operating window for the HAM of 1-decene. The subscript $\square_{\text{sub}}$ represents 1-decene. Initial amounts of decene isomers (iC10en) and n-decane (C10an) stem from substrate impurities. Initial gas concentrations in the liquid phase are remnants from the catalyst preforming. Measurement uncertainties Σ_y are determined based on gas chromatography sensitivity and data. For the definition and mathematical consideration of the slopes s in the HAM model, please refer to eq. (3.5). $\mathcal{SPC}^{\text{prod}}$ = {iC11al, En, Am}, $\mathcal{SPC}^{\text{rest}}$ = {DEA, H_2O, MeOH, nC12an}.

t^{f} / min	[50, 180]
ϑ, ϑ^0 / °C	[105, 140]
p, p^0 / bar	[30, 50]
y_{H_2}, $y^0_{H_2}$ / −	[0, 1]
y_{CO}, y^0_{CO} / −	[0, 1]
$\phi^{\text{m}}_{\text{MeOH,nC12an}}$ / g g^{-1}	1
$\phi^{\text{n}}_{\text{Lig,}\Sigma\text{cat}}$ / mol mol^{-1}	3.5
$\phi^{\text{n,0}}_{\text{cat,sub}}$ / mol mol^{-1}	0.08×10^{-2}
$\phi^{\text{n,0}}_{\text{DEA,sub}}$ / mol mol^{-1}	[0, 2]
$\phi^{\text{V,0}}_{\text{H}_2\text{O}}$ / L L^{-1}	[0, 0.02]
V^0_{Liq} / mL	50
operation mode	semibatch
ligands	SulfoXantphos
Σ_y / mol L^{-1}	diag(4×10^{-4})

n^0_{sub} / mmol	27.20
n^0_{iC10en} / mmol	0.82
n^0_{C10an} / mmol	0.07
$n^0_{H_2}$ / mmol	1.1
n^0_{CO} / mmol	1.6
n^0_i, $i \in \mathcal{SPC}^{\text{prod}}$ / mmol	0
n^0_i, $i \in \mathcal{SPC}^{\text{rest}}$ / mmol	[0, ∞]
s_T / K min^{-1}	[0, 2.5]
s_p / bar min^{-1}	[0, 20]
$s_{y_{H_2}}$ / min^{-1}	0
$s_{y_{CO}}$ / min^{-1}	0

with the species molar mass $\tilde{M}_i$ and all density parameters for eqs. (3.4a) and (3.4b) summarized in tables B.13 to B.15, respectively.

Model Summary

For simplified reference, the HAM process model can be formulated as a DAE system comprising the following sets of equations and data

$$\text{Mass balance: Equation (3.3), table B.12,} \tag{3.5a}$$

$$\text{Reaction kinetics: Equation (3.1), tables B.8 and B.9,} \tag{3.5b}$$

$$\text{Saturate gas concentration: Equation (2.24), table B.10,} \tag{3.5c}$$

$$\text{Arrhenius equation: Equation (2.22), table B.11,} \tag{3.5d}$$

$$\text{Catalyst pre-equilibrium: Equation (2.20),}$$

$$\text{Enamination equilibrium: Equation (2.28),}$$

$$\text{Control States: } \begin{cases} \frac{\mathrm{d}T}{\mathrm{d}t} = s_T(t),\ T(t_0) = T^0, \\ \frac{\mathrm{d}y_i}{\mathrm{d}t} = s_{y_i}(t),\ y_i(t_0) = y_i^0,\ i \in \{H_2, CO\}, \\ \frac{\mathrm{d}p}{\mathrm{d}t} = s_p(t),\ p(t_0) = p^0, \end{cases} \tag{3.5e}$$

$$\text{Composition ratios: Equations (2.29a) to (2.29d),} \tag{3.5f}$$

$$\text{Gas fraction } N_2\text{: } y_{N_2}(t) = 1 - \sum_{i \in \mathcal{SPC}^{\text{Gas}}} y_i(t), \tag{3.5g}$$

$$\text{Concentration: } c_i(t) = n_i(t) V_{\text{Liq}}(t)^{-1}, \quad i \in \mathcal{SPC}, \tag{3.5h}$$

$$\text{Liquid Volume: } \begin{cases} V_{\text{Liq}}(t) = \sum_{i \in \mathcal{SPC}} V_{\text{Liq},i}(t), \\ V_{\text{Liq},i}(t) = m_i(t) \rho_i(T)^{-1}, \quad i \in \mathcal{SPC}, \\ m_i(t) = \tilde{M}_i n_i(t), \quad i \in \mathcal{SPC}, \\ \text{Equation (3.4)}, \\ \text{Tables B.13 to B.15}, \end{cases} \tag{3.5i}$$

$$\text{Reference Temperature: } T_{\text{ref}} = 373.15\,\text{K}, \tag{3.5j}$$

$$\text{Outputs: } y_i = c_i, \quad i \in \mathcal{SPC}^y, \tag{3.5k}$$

$$\text{Sets: } \begin{cases} \mathcal{SPC} = \{\text{nC10en, iC10en, C10an, DEA, nC11al,} \\ \qquad \text{En, Am, } H_2O\text{, MeOH, nC12an, } H_2\text{, CO}\}, \\ \mathcal{SPC}^y = \{\text{nC10en, iC10en, C10an, DEA,} \\ \qquad \text{nC11al, En, Am, } H_2O\}, \\ \mathcal{SPC}^{\text{Gas}} = \{H_2, \text{CO}\}, \\ \mathcal{RCT}^{\text{HAM}} = \{\text{Iso, Hyfo, HydDec, Cond, HydEn}\}. \end{cases}$$

Besides the mass balances, reaction kinetics, mass transfer correlations and various constitutive equations for the calculation of the concentrations and liquid volume, an additional set of ODEs is introduced for the dynamically controllable temperature, pressure, and gas phase compositions. This allows for the consideration of experimental restrictions w.r.t. the rate of change of the respective control parameter. Consequently, these rate variables represent the new set of adjustable controls. In summary, the process model contains the differential states $\chi(t) = \left(n^\top(t), T(t), p(t), y_{H_2}(t), y_{\text{CO}}(t)\right)^\top$, control trajectories $u(t) = \left(s_T(t), s_p(t), s_{y_{H_2}}(t), s_{y_{\text{CO}}}(t)\right)^\top$ and control parameters $p = \left(t^{\text{f}}, \phi^{\text{n,0}}_{\text{DEA,sub}}, \phi^{\text{V,0}}_{H_2O}\right)^\top$. Bounds on these controls are summarized in table 3.1. Moreover, the process model is extended by the molar concentrations c_i with $i \in \mathcal{SPC}^y \subset \mathcal{SPC}$ as experimentally measurable model outputs y_i.

3.3 Formulation of the mbOED Problem

With the reactor vessel model from the previous section, a suitable formulation of the mbOED optimization problem can be summarized as

$$\min_{\substack{u_1(t),\,u_2(t),\,\ldots,\,u_{n_{\mathrm{exp}}}(t),\\ p_1,\,p_2,\,\ldots,\,p_{n_{\mathrm{exp}}},\\ x_1^0,\,x_2^0,\,\ldots,\,x_{n_{\mathrm{exp}}}^0}} \quad \phi^{\Sigma_\theta}\left(F\right) \tag{3.6a}$$

s. t.

Process Model k: Equation (3.5),

FIM Definition k: Equation (2.13),

Variational Equations k: Equation (2.15),

Experimental Restrictions k:

$$\left\{ t_{\mathrm{sp},j} - t_{\mathrm{sp},j-1} \geq 5\,\mathrm{min}, \quad \forall j \in \left\{2, 3, \ldots, n_{\mathrm{sp}}\right\}, \right. \tag{3.6b}$$

Monophase Condition k:

$$\begin{cases} \Delta x_i^{(\pi,\alpha)} = \left(x_i^{(\pi)} - x_i^{(\alpha)} \right) (t = t^{\mathrm{f}}, t_{\mathrm{PhaseEq}} = 1), \\ |\Delta x_i^{(\pi,\alpha)}| = 0, \quad \forall i \in \mathcal{SPC},\, \pi, \alpha \in \Pi, \end{cases} \tag{3.6c}$$

Phase Equilibrium k:

$$\begin{cases} \text{ODE System: Equation (2.4) substituting } t \text{ with } t_{\mathrm{PhaseEq}}, \\ \text{Phase Split: Equation (2.6) applied to } n_i(t = t^{\mathrm{f}}) \text{ from eq. (3.5)}, \\ \qquad T^{(\pi)}(t_{\mathrm{PhaseEq}}) = T(t = t^{\mathrm{f}}), \\ \qquad \forall i \in \mathcal{SPC}, \pi \in \Pi, \end{cases} \tag{3.6d}$$

Thermodynamic Activities k:

$$\begin{cases} \text{Input Scaling: Equation (C.1) applied to each } u^{(\pi)}(t_{\mathrm{PhaseEq}}), \\ \text{ANN: Equation (C.2)}, \\ \qquad \ln \gamma_{\mathrm{nC10en}}^{(\pi)} = \ln \gamma_{\mathrm{iC10en}}^{(\pi)} = \ln \gamma_{\mathrm{C10an}}^{(\pi)}, \\ \qquad \ln \gamma_{\mathrm{Am}}^{(\pi)} = \ln \gamma_{\mathrm{En}}^{(\pi)}, \\ \qquad a_i^{(\pi)} = \gamma_i^{(\pi)} x_i^{(\pi)}, \\ \qquad x_i^{(\pi)} = n_i^{(\pi)} \sum_{j \in \mathcal{SPC}} {n_j^{(\pi)}}^{-1}, \\ \qquad \forall i \in \mathcal{SPC}, \pi \in \Pi, \end{cases} \tag{3.6e}$$

$$
\underbrace{\text{Variables, Controls, Bounds } k\text{:}\begin{cases}
\chi(t) = \{n_i(t) \mid i \in \mathcal{SPC}\} \cup \{T(t), p(t), y_{\mathrm{H_2}}(t), y_{\mathrm{CO}}(t)\}\,, \\
y(t) = \{c_i(t) \mid i \in \mathcal{SPC}^y\}, \\
u(t) = \left\{s_T(t), s_p(t), s_{y_{\mathrm{H_2}}}(t), s_{y_{\mathrm{CO}}}(t)\right\}, \\
p = \left\{t^{\mathrm{f}}, \phi^{\mathrm{n,0}}_{\mathrm{DEA,sub}}, \phi^{\mathrm{V,0}}_{\mathrm{H_2O}}\right\}, \\
\chi^0 = \{n_i^0 \mid i \in \mathcal{SPC}\} \cup \left\{T^0, p^0, y^0_{\mathrm{H_2}}, y^0_{\mathrm{CO}}\right\}, \\
t \in \left[0, t^{\mathrm{f}}\right], \\
t_{\mathrm{PhaseEq}} \in [0,1]\,, \\
\text{Operating Window: Table 3.1,} \\
\text{Discretization Parameters and Constants: Table B.16,}
\end{cases}}_{\forall k \in \mathcal{EXP}}
$$

$$
\text{Sets:}\begin{cases}
\mathcal{SPC}^{\mathrm{ANN}} = \{\text{nC10en, DEA, nC11al, Am, } \mathrm{H_2O}\text{, MeOH, nC12an}\}, \\
\Pi = \left\{1, 2, \ldots, n_{\mathrm{phases,max}}\right\}, \\
\mathcal{EXP} = \{1, 2, \ldots, n_{\mathrm{exp}}\}\,.
\end{cases}
$$

Please note that a simultaneous design strategy is chosen similar to eq. (2.16) because of good initial guesses in the form of thoroughly investigated reaction network structures, kinetic expressions and model parameters. The index k which identifies the experiment number is omitted in the variables and constraints of eq. (3.6) for improved readability. Specific aspects of the mbOED problem including the prediction of the phase equilibrium, the calculation of the necessary activity coefficients and the incorporation of experimental restrictions are discussed in the following paragraphs.

Phase Equilibrium Calculation. The formation of water in the HAM can lead to multiple liquid phases during experiments and process operation (see [Sch+21]) owing to the limited water uptake capacity of the methanol/n-dodecane TMS. Therefore, measures are required to prevent phase separation in the experimental designs as phase boundaries introduce transport resistances which complicate the identification of reaction kinetic parameters. Because of complex, non-linear dependencies of the phase equilibrium on the adjustable control parameters which describe the operating window, rigorous consideration of monophasic constraints like eq. (3.6c) based on phase equilibrium calculations in the mbOED are required in contrast to simple box constraints. To reduce this additional computational load, the monophase constraint is only enforced at the final time of each experiment t_k^{f} with $k \in \mathcal{EXP}$. Even though this simplification appears as an assumption since multiple phases may appear and

disappear over the entire time horizon of the reaction, the experimental conditions prevent the disappearance of a second, liquid phase due to the absence of cooling while water is formed and accumulated continuously (see table 3.1).

The prediction of the phase equilibrium requires two modeling decisions—the description of the activities/fugacities or activity/fugacity coefficients and a formulation which is able to identify the chemical equilibrium from eq. (2.1c). For the identification of the chemical equilibrium of all species and phases, the mass transfer problem formulation in eq. (3.6d) from section 2.1 is selected because of its beneficial convergence properties and the absence of an underlying optimization problem. By distributing each species of the initial molar amount vector into its own separate phase with eq. (2.6), the trivial solution of equal molar fractions in each phase due to the chosen boundary condition is prevented. Additionally, the monophase constraint in eq. (3.6c) ensures the convergence to a solution with one liquid phase so that explicitly checking for eq. (3.6d) to reach a steady-state according to eq. (2.8) is not necessary. All parameters for the phase equilibrium calculation are summarized in table B.16 in appendix B.3.

Activity Coefficient Model. The complex reaction mixture of the HAM with the large number of chemical species excludes most of the widely applied activity coefficient models as they require a great number of measurements for model parameterization. Due to its group-contribution structure, modified UNIFAC(Dortmund) (modUNIFAC) [GLS93] represents a promising model choice. However, it is not suited to describe the liquid phase activity coefficients since, contrary to experimental investigations, multiple liquid phases are predicted in the operating temperature window despite the absence of water (see fig. C.2) [Bia+20b]. Therefore, sophisticated, parsimonious, and experimentally validated activity coefficient models like PC-SAFT [GS01] are necessary to reliably predict the LLE.

Huxoll et al. [Hux+21] investigated the LLEs of the HAM reaction mixture and parameterized the pure-component and binary interaction parameters for all species based on data from multiple binary subsystems. Unfortunately, direct utilization of the PC-SAFT model in the optimization is challenging because of its iterative nature. Therefore, a surrogate model for the prediction of activity coefficients in the form of an artificial neural network (ANN) is designed for the application in eq. (3.6e). Detailed information on the surrogate model design, parameterization, validation and a discussion on alternative model formulations can be found in appendix C.

Experimental Restrictions. In addition to the phase equilibrium calculation, eq. (3.6) contains constraints which ensure the practicability of the experimental designs. One example represents the introduction of a minimum time interval between two measurement times $t_{\mathrm{sp},j-1}$ and $t_{\mathrm{sp},j}$ with $j \in \{2,3,\ldots,n_{\mathrm{sp}}\}$ to account for the minimum time required for drawing samples from the reaction mixture manually. To circumvent integer decisions w.r.t. the measurement times, the DOP in eq. (3.6) is discretized in time into finite elements of length $h_{\mathrm{FE},j}$ with $j \in \{1,2,\ldots,n_{\mathrm{FE}}\}$. At the end of each finite element, a measurement is performed which structurally interconnects the number of measurements and the number of finite elements $n_{\mathrm{sp}} = n_{\mathrm{FE}}$. Even though this design decision may lead to inaccuracies or convergence issues of the solver depending on the stiffness of the DAE system, the concentration profiles of the HAM are sufficiently smooth. Consequently, this restriction is favorable in comparison to the introduction of integer variables, leading to a MINLP in discretized form, or the incorporation of a complex multilayer grid structure given the complexity of the process model and mbOED problem. By introducing the finite element widths as additional controls, the equality constraints

$$0 = \sum_{j=1}^{n_{\mathrm{FE}}} h_{\mathrm{FE},j} - 1, \tag{3.7}$$

$$0 = t_{\mathrm{sp},i} - t^{\mathrm{f}} \sum_{j=1}^{i} h_{\mathrm{FE},j}, \quad \forall i \in \{1,2,\ldots,n_{\mathrm{FE}}\}, \tag{3.8}$$

need to be appended to eq. (3.6) in discretized form.

Discretization and Computation. After discretization of the time into finite elements, the solution of the ODE systems eq. (2.4) and eq. (3.5) on these time intervals requires the application of techniques like single shooting, multiple shooting or further discretization of each finite element using orthogonal collocation. For eq. (3.6), the latter approach is selected with $n_{\mathrm{FE}} = 10$ (compare (cf.) table B.16) and three collocation points per finite element using the Radau scheme. The resulting NLP is solved using IPOPT [WB06] in the algorithmic differentiation and non-linear optimization software CasADi [And+19].

3.4 Design of Experiments for the Hydroaminomethylation of 1-Decene

The HAM process model is based on previous investigations of the underlying hydroformylation and reductive amination reactions. Thus, good initial parameter guesses can be assumed which allows for the SM scheme (see section 2.2) to benefit from the simultaneous consideration of all DoF by the optimizer. This helps to prevent trivial solutions in which all experiments are designed identically [GMB07]. The simultaneous design strategy also enables the extension toward a sequential/simultaneous design hybrid for increased robustness of the designs if necessary [Bar+13]. Due to computational and experimental limitations, a maximum of $n_{\text{exp}} = 5$ simultaneously designed experiments is selected together with the D-optimal design applied to the FIM inverse. In this example process, the D-optimal design provides a suitable compromise between the information content, i.e., the consideration of parameter correlation, and computational complexity which significantly increases for eigenvalue- or singular value-based criteria (see [GMB07]). The vector containing the uncertain parameters $\theta = \left[B_{\text{Iso}}, B_{\text{Hyfo}}, B_{\text{Cond}}, B_{\text{HydEn}}\right]$ is selected based on a sensitivity study, mathematical, and physical considerations and can be found in appendix E.

3.4.1 Initialization

With the increase in decision variables for the simultaneous design of multiple experiments, the number of local optima grows significantly so that initialization strategies for the mbOED problem are necessary even for comparatively simple process models [BAW10]. Therefore, a multi-step initialization procedure is drafted which takes the phase equilibrium calculation into account and ensures monophasic initialization data for eq. (3.6).

Control Parameter Selection. Inspection of the reaction network in fig. 3.1 leads to a small subset of decision variables which significantly influence the reaction pathway. A preliminary investigation of possible experimental designs w.r.t. these variables thus enables the identification of promising designs. These promising parameters include the gas phase compositions $y_i(t)$ with $i \in \{\text{H}_2, \text{CO}\}$ as they control the hydrogenation and hydroformylation activity. For example, by reducing the synthesis gas content (or the pressure) in the gas phase in a suitable experimental setup, it is possible to isolate the isomerization reaction. Additionally, the substrate

ratio $\phi^{\mathrm{n,0}}_{\mathrm{DEA,sub}}$ and the initial water content $\phi^{\mathrm{V,0}}_{\mathrm{H_2O}}$ enable the manipulation of the condensation reaction and may be used to control the amount of intermediates. Lastly, the temperature $T(t)$ represents an interesting control parameter since it does not only influence the relative significance of each reaction depending on the activation energy but it can also be used to control the activity of the entire reaction system. While this limited set of decision variables may be used to perform an initial grid search, the infinite dimensional nature of $T(t)$, $y_{\mathrm{H_2}}(t)$ and $y_{\mathrm{CO}}(t)$ prevent a manageable grid size. Consequently, these controls need to be restricted to a small set of controls, e.g., via discretization in time or by focusing on their respective initial values and setting $s_T(t) = s_{y_{\mathrm{H_2}}}(t) = s_{y_{\mathrm{CO}}}(t) = 0$. The bounds and number of grid points of each of these decision variables can be found in table 3.2. Please

Tab. 3.2.: Bounds and number of grid points (n_{sp}) for each decision variable in the mbOED initialization grid search.

	Lower Bound	Upper Bound	n_{sp}
ϑ^0 / °C	105	140	3
p^0 / bar	50	50	1
$y^0_{\mathrm{H_2}}$ / mol mol^{-1}	0.05	0.95	3
y^0_{CO} / mol mol^{-1}	0.05	0.95	3
$\phi^{n,0}_{\mathrm{DEA,sub}}$ / mol mol^{-1}	0	2	3
$\phi^{\mathrm{V,0}}_{\mathrm{H_2O}}$ / L L^{-1}	0.00	0.02	2

note that the lower and upper bounds of the gas phase compositions deviate from the ones found in table 3.1 since both gases are required for the catalyst activation. Additionally, the closing condition $y^0_{\mathrm{H_2}} + y^0_{\mathrm{CO}} + y^0_{\mathrm{N_2}} = 1$ is enforced during the grid generation and equal molar compositions of the synthesis gas are replaced by $y^0_{\mathrm{H_2}} \left(y^0_{\mathrm{CO}}\right)^{-1} = 2$. In the case of multiphasic behavior under the specified operating conditions, the initial water amount is reduced until only one liquid phase is achieved.

Initialization Strategy. After simulating the process model for all operating conditions in the grid search and determining the FIM per design, all possible experiment combinations for the required total number of experiments are evaluated and the best combination w.r.t. the chosen optimality criterion is selected. Subsequent to the grid search which results in a candidate set of experimental designs, eq. (3.6) is solved with $n_{\mathrm{exp}} = 1$ for each experimental candidate to be design while considering the influence of all other, fixed designs via the FIM prior. The detailed initialization algorithm can be found in algorithm 1 in appendix D.

3.4.2 Results

Solving eq. (3.6) for $n_{\text{exp}} = 5$ results in a set of distinct concentration and control profiles which are depicted in fig. 3.3 with the corresponding optimal control parameters summarized in table 3.3.

Tab. 3.3.: Optimal control parameters for the D-optimal SM-mbOED solution of eq. (3.6) with $n_{\text{exp}} = 5$.

Design	1	2	3	4	5
t^{f} / min	54	50	144	55	146
$\phi^{\text{n,0}}_{\text{DEA,sub}}$ / mol mol^{-1}	0.48	0.71	2.00	2.00	2.00
$\phi^{\text{V,0}}_{\text{H}_2\text{O}}$ / L L^{-1}	0.00	0.00	0.00	0.014	0.0134
y_{H_2} / mol mol^{-1}	0.92	0.90	0.05	0.35	0.11
y_{CO} / mol mol^{-1}	0.07	0.10	0.14	0.64	0.88

Control Profile Analysis. The inspection of the control profiles clearly shows the experimental and monophasic restrictions which are considered in the process model in eq. (3.5). These restriction of the control trajectory gradients generally lead to minimal dynamic changes in the pressure and the resulting partial pressures in addition to negligible temperature changes throughout each experimental design. The only exceptions to these observations can be found in design 1 and 3. Whereas the first design contains a characteristic increase of the hydrogen partial pressure in the first minutes to boost the hydrogenation and isomerization activity, the latter design is unique in its linear pressure increase over the first 100 min by predominantly elevating the nitrogen content in the gas phase. As nitrogen only serves as an inert gas in the process model, reducing the partial pressures of CO and H_2 by lowering the total pressure in eq. (3.5) would have the same effect on the reaction kinetics. However, the solver does not choose this approach due to the lower limit of the total pressure at 30 bar (see table 3.1). With these minor effects of the dynamic control trajectories on the reaction kinetics, the selection of the optimal control parameters and initial conditions are primarily responsible for the differences in the concentration profiles and lead to experimental conditions in which specific reaction pathways are favored.

While the temperature has a minor impact on the concentration trajectories in contrast to the gas phase composition, the absence of distinct temperature profiles or variations in the initial temperature is surprising since temperature variations are normally used for the identification of the (dimensionless) activation energy. Because of the initial water content in designs 4 and 5, maximum temperatures are necessary

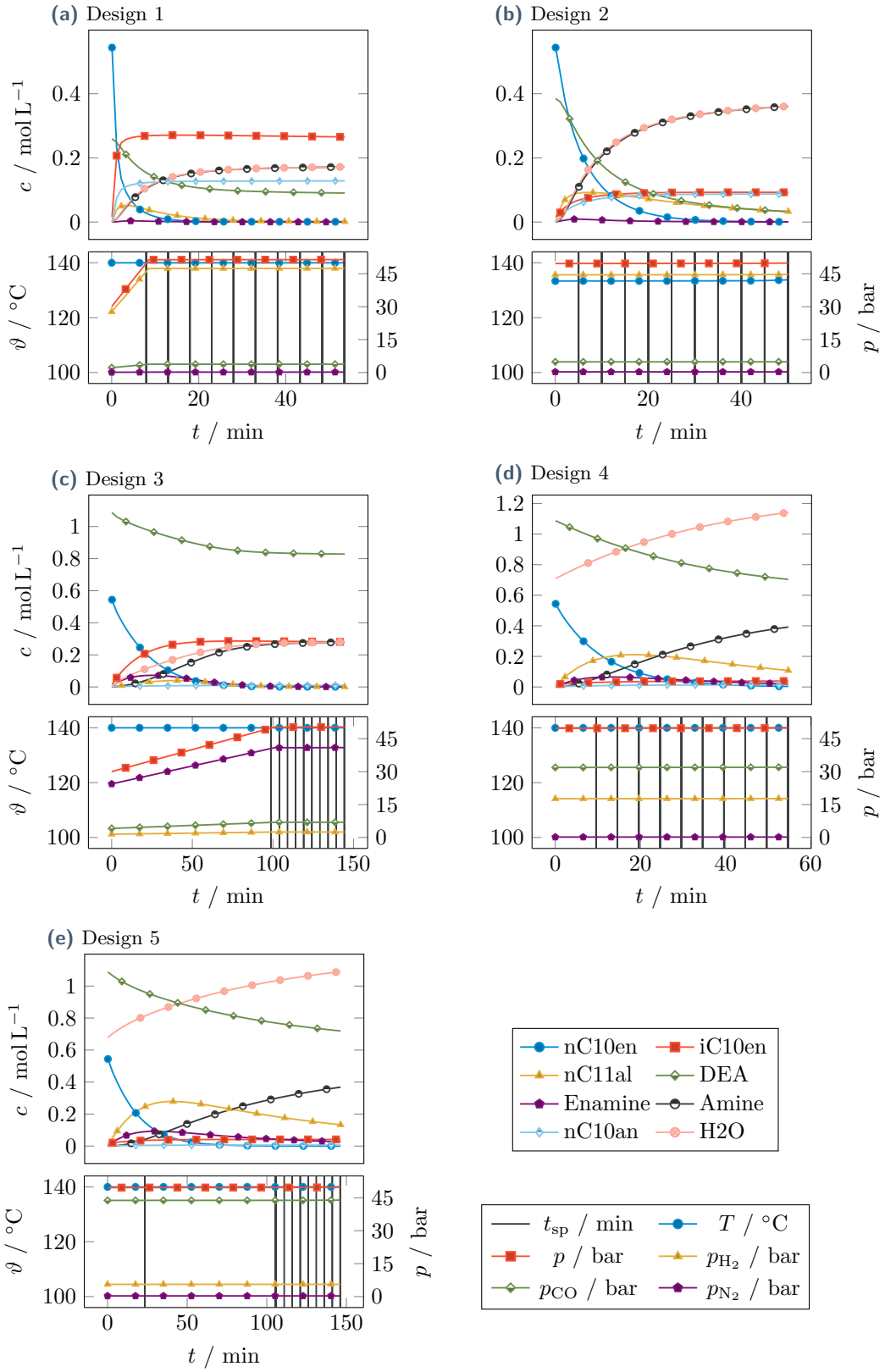

Fig. 3.3.: D-optimal concentration and control trajectories resulting from the SM-mbOED solution of eq. (3.6) with $n_{\text{exp}} = 5$. The vertical lines in the control profile plots represent the optimal measurement points. The corresponding optimal control parameter p^* can be found in table 3.3.

to prevent phase separation. However, designs 1 to 3 could, theoretically, contain a temperature ramp for additional information over the model system. Possible reasons for their absence include (i) the reduced DEA content in designs 1 and 2 which elevates the amount of non-polar species in the reaction mixture and may cause phase separation at lower temperatures, (ii) the desired sharp increase in the decene isomer content in design 1 which requires a fast isomerization, (iii) the low reaction rates in design 3 which are not able to reach the desired steady-state in the case of reduced temperatures, and (iv) the identification of a local optimum despite or even due to the initialization strategy from algorithm 1.

Measurement Time Discussion. Besides the control parameters and control profiles, eq. (3.6) also describes the identification of optimal measurement times. On a time horizon of 180 min, 10 measurement points are distributed with a minimum interval of 5 min between measurements. By treating t^{f} as a control parameter, the experimental designs exhibit a variation of the reaction time from 50 min, which represents the constrained lower limit, to 146 min. While decreasing the time horizon enables the optimizer to improve the sampling rate in areas with high reaction rates and strong reaction activity (see figs. 3.3a, 3.3b and 3.3d), long time horizons are coupled with control parameters which decrease the reactivity of the system to gather steady-state information (see fig. 3.3c) or complement another design which cannot be continued because of phase splitting (compare figs. 3.3d and 3.3e).

3.4.3 Design Discussion

The impact of a selected experimental design on the identification of a particular parameter subset can be identified using a similar approach as in the calculation of the total order Sobol indices (see appendix E). First, simple performance measures such as the uncertainty ellipsoid volume, parameter standard deviation and correlation are computed for the nominal case where the set of all experimental designs $\mathcal{EXP}$ is considered. Next, the same calculation is performed but with the set $\mathcal{EXP} \setminus \{k\}$ where k represents the experimental design which is analyzed. Naturally, removing one experiment from the calculation of the FIM has a decremental effect on the overall, absolute information content. However, the relative impact of each design on the information gain per uncertain parameter may be used to associate the relevancy of an experiment design to a specific reaction. An overview of these performance measure differences can be found in table 3.4.

Tab. 3.4.: Uncertainty ellipsoid volume $\det F^{-1}$, standard deviation σ and correlation matrix ρ based on the experimental designs from fig. 3.3 and table 3.3. The relative impact of each experimental design on these performance measures is identified by removing the contribution of design k from the FIM. The relative performance measures follow $\Delta \det F^{-1} = \det F \left(\det F_{\neg i}^{-1} - \det F^{-1} \right)^{-1}$, $\Delta\sigma_i = \left(\sigma_{i,\neg k} - \sigma_i\right) \sigma_i^{-1}$ and $\Delta|\rho_{i,j}| = |\rho_{i,j,\neg k}| - |\rho_{i,j}|$ with $i, j \in \{\text{Iso}, \text{Hyfo}, \text{Cond}, \text{HydEn}\}$ where the index $\square_{\neg k}$ denotes the removal of design k. Positive values negatively impact the respective performance measure. All results are based on the initial parameter guesses θ^0. The standard deviations and correlation coefficient matrix relate to the dimensionless activation energy B.

	$\det F^{-1}$ / 10^{-15}	σ / 10^{-2}		Correlation Matrix ρ			
				Iso	Hyfo	Cond	HydEn
	3.31	Iso	0.56	Iso	-	0.02	0.08	−0.01
		Hyfo	0.68	Hyfo	-	-	0.00	−0.29
		Cond	4.53	Cond	-	-	-	−0.14
		HydEn	3.58	HydEn	-	-	-	-
	$\Delta \det F^{-1}$ / %	$\Delta\sigma_i$ / %		Absolute Correlation Difference $\Delta\|\rho_{i,j}\|$			
Design 1	364.77	Iso	26.45	Iso	-	0.43	0.00	0.17
		Hyfo	59.08	Hyfo	-	-	0.26	0.12
		Cond	24.23	Cond	-	-	-	−0.11
		HydEn	4.88	HydEn	-	-	-	-
Design 2	321.33	Iso	2.35	Iso	-	0.02	0.02	0.01
		Hyfo	11.89	Hyfo	-	-	0.28	0.06
		Cond	87.09	Cond	-	-	-	0.11
		HydEn	2.62	HydEn	-	-	-	-
Design 3	433.03	Iso	119.34	Iso	-	0.46	0.09	0.23
		Hyfo	19.96	Hyfo	-	-	0.08	0.09
		Cond	1.18	Cond	-	-	-	−0.05
		HydEn	3.83	HydEn	-	-	-	-
Design 4	169.87	Iso	0.63	Iso	-	0.00	0.01	0.04
		Hyfo	3.58	Hyfo	-	-	0.02	0.00
		Cond	0.95	Cond	-	-	-	0.05
		HydEn	57.69	HydEn	-	-	-	-
Design 5	126.66	Iso	0.32	Iso	-	−0.01	0.01	0.01
		Hyfo	16.06	Hyfo	-	-	0.02	−0.12
		Cond	0.06	Cond	-	-	-	−0.03
		HydEn	25.00	HydEn	-	-	-	-

For example, designs 1 to 3 have a strong influence on the volume of the uncertainty ellipsoid for two reasons. First, all three designs strongly impact the standard deviations with their main focus on the isomerization, hydroformylation, and condensation reaction. Second, in addition to the beneficial effect on the standard deviations, all of these designs significantly reduce parameter correlations. Designs 1 and 3 majorly contribute to the reduction of the correlation between the hydroformylation and isomerization as well as the isomerization and enamine hydrogenation. In contrast, design 2 heavily influences the parameter correlation between the hydroformylation and the condensation reaction. Interestingly, removing experimental designs from the calculation of the correlation matrix does not only have negative consequences. For example, designs 1 and 3 negatively influence the parameter correlation between the condensation and enamine hydrogenation reaction.

The other two designs, designs 4 and 5, do not have a strong impact on the parameter correlations but majorly improve the standard deviation of the enamine hydrogenation which is neglected in all previous designs. Intriguingly, this elevated information content for the enamine hydrogenation is achieved by increasing the CO/H_2 ratio to 1.8 and 8 , respectively, which effectively limits not only the enamine hydrogenation but all reaction rates except for the condensation caused by the inhibiting effect of CO on the catalyst activity (see eq. (2.20)). With this minor impact of designs 4 and 5 on the objective function, the question rises if the initial feeding of water is a numeric artifact or if the additional experimental effort and the risk of phase separation during the experiment are justified. The answer to this question can be found in appendix E.3.

3.4.4 Summary of Results

The mbOED problem from eq. (3.6) is initialized for the hydroaminomethylation of 1-decene using a multi-step procedure to prevent local optima of the complex DOP. The calculation of five experimental designs yields distinct concentration profiles for all designs. These concentration profiles are achieved by dynamic pressure increases, non-stoichiometric gas phase compositions and DEA to substrate ratios, dosing of nitrogen as an inert component, the initial feed of water and the variation of the reaction time. The investigation of the impact of each design on the expected parameter uncertainty and parameter correlations hints at a significant importance of designs 1 to 3 with designs 4 and 5 exhibiting a minor reduction of the parameter uncertainty.

3.5 Model Identification

The experimental designs for the hydroaminomethylation of 1-decene from section 3.4 were applied in experiments performed by Wieland Kortuz from the Otto von Guericke University. In the following subsections, the insight based on these experiments is summarized concisely. Starting with the extension of the reactor vessel model by a rigorous gas phase model, the structural modification of the catalyst equilibrium's inhibition constants is motivated and the final parameter estimates alongside a selection of characteristic concentration profiles are presented. An overview over all experiments can be found in table F.1 with additional information regarding the experimental setup (see fig. F.1), procedure and experiment choices in appendix F.1.

3.5.1 Rigorous Gas Phase Model

In the first step, the predictions from eq. (3.5) using the nominal parameters from tables B.9 and B.11 are compared to the experimental results to assess the prediction accuracy without any structural or parametric adjustments of the reaction kinetics. These comparisons lead to the discovery that a rigorous gas phase model is required for the accurate replication of the experimental setup. By assuming ideal gas behavior, the molar amount of each species $i \in \mathcal{SPC}^{\mathrm{Gas}}$ in the gas phase can be described via

$$\frac{\mathrm{d}n_i^{\mathrm{Gas}}}{\mathrm{d}t} = \frac{1}{R}\frac{\mathrm{d}}{\mathrm{d}t}\left(\frac{p_i V^{\mathrm{Gas}}}{T}\right) = \frac{1}{R}\left(\frac{V^{\mathrm{Gas}}}{T}\frac{\mathrm{d}p_i}{\mathrm{d}t} + \frac{p_i}{T}\frac{\mathrm{d}V^{\mathrm{Gas}}}{\mathrm{d}t} - \frac{p_i V^{\mathrm{Gas}}}{T^2}\frac{\mathrm{d}T}{\mathrm{d}t}\right). \tag{3.9}$$

Reordering of the terms and the addition of expressions for dosing and releasing gas from the reactor vessel leads to

$$\frac{\mathrm{d}p_i}{\mathrm{d}t} = \Delta\dot{p}_i^{+} + \Delta\dot{p}_i^{-} + \frac{T}{V^{\mathrm{Gas}}}\left(R\frac{\mathrm{d}n_i^{\mathrm{Gas}}}{\mathrm{d}t} - \frac{p_i}{T}\frac{\mathrm{d}V^{\mathrm{Gas}}}{\mathrm{d}t} + \frac{p_i V^{\mathrm{Gas}}}{T^2}\frac{\mathrm{d}T}{\mathrm{d}t}\right), \tag{3.10a}$$

$$p_i\left(t^0\right) = p^0 y_i^0, \tag{3.10b}$$

with the definitions

$$\frac{\mathrm{d}V_{\mathrm{Gas}}}{\mathrm{d}t} = -\frac{\mathrm{d}V_{\mathrm{Liq}}}{\mathrm{d}t} = -\sum_{k\in\mathcal{SPC}}\left(\frac{\tilde{M}_k}{\rho_k}\frac{\mathrm{d}n_k}{\mathrm{d}t} - \frac{n_k\tilde{M}_k}{\rho_k^2}\frac{\mathrm{d}\rho_k}{\mathrm{d}t}\right), \tag{3.10c}$$

$$\frac{\mathrm{d}\rho_k}{\mathrm{d}t} = g\left(\frac{\mathrm{d}T}{\mathrm{d}t}\right), \tag{3.10d}$$

$$\frac{\mathrm{d}T}{\mathrm{d}t} = s_T, \tag{3.10e}$$

$$\frac{\mathrm{d}n_i^{\mathrm{Gas}}}{\mathrm{d}t} = -V_{\mathrm{Liq}}\beta_{\mathrm{eff},i}\left(c_i^{\mathrm{sat}} - c_i\right). \tag{3.10f}$$

Please note that all time dependencies of p_i, V_{Gas}, V_{Liq}, T, ρ_k, n_k, n_i^{Gas}, c_i^{sat} and c_i are neglected for improved readability and $g(\frac{\mathrm{d}T}{\mathrm{d}t})$ in eq. (3.10d) is calculated based on eq. (3.4). The controls for dosing $\Delta\dot{p}_i^+(t)$ and releasing $\Delta\dot{p}_i^-(t)$ gas into and from the reactor vessel are defined according to

$$\Delta\dot{p}_i^+(t) = \frac{\max(p_{\mathrm{set}}(t) - p(t), 0)y_{i,\mathrm{set}}}{\Delta t_{\mathrm{set}}}, \tag{3.11a}$$

$$\Delta\dot{p}_i^-(t) = \frac{\min(p_{\mathrm{set}}(t) - p(t), 0)y_i(t)}{\Delta t_{\mathrm{set}}}, \tag{3.11b}$$

with $p_{\mathrm{set}}(t)$ and $y_{i,\mathrm{set}}$ denoting the pressure in the reactor vessel and gas phase composition in the gas burette, respectively. While the pressure is taken from the data of the process control system, the gas phase composition is equivalent to the initial filling ratio of the burette. The time difference Δt_{set} is used as a control parameter to define the speed at which the controller adjusts the reactor pressure. Owing to the absence of manufacturer information and the adjustment speed used in table 3.1, $\Delta t_{\mathrm{set}} = 1\,\mathrm{min}$ is set heuristically. In addition to the gas dosing by the controller, the gas release is also modeled via $\Delta\dot{p}_i^-(t)$ to describe the manual, periodic release of gas from the vessel. This periodic release was used in some experiments (compare table F.1 for *Mod. Setup*) to increase gas mixing and to recalibrate the gas phase in the reactor. An improved mixing of the gas phase is motivated by the assumption of gas layers forming with elevated concentrations of specific gases. Besides the gas mixing, the recalibration of the gas phase is necessary due to the accumulation of species in the gas phase caused by an imbalance of the dosed and consumed gas composition ratio. The unavailability of information regarding the actual gas composition requires the utilization of the predicted composition $y_i(t)$ in eq. (3.11b). A similar set point tracking approach is used to accurately describe the temperature fluctuations in the experiments.

Concentration Profile Comparison. The major impact of rigorously modeling the reactor vessel gas phase can be seen in fig. 3.4 where the middle and left column contain the concentration profiles with and without a rigorous gas phase model,

respectively, for a selected number of experiments. The right column contains the control profiles from the process control system. While the differences for designs 2 and 4 are negligible due to either minor changes of the gas phase ratio (design 2) or despite a significant accumulation of CO (design 4), design 3 shows a completely different behavior based on the exhaustion of hydrogen (H_2) in the gas phase after 20 min. This exhaustion is favored by the low initial partial pressure of hydrogen and cannot be reverted by the periodic release and replenishment of the gas phase (see the pressure control in experiment 53c_D3 in fig. 3.4). The reason for this is a limitation on the gas release because of the low vapor pressure of DEA in the mixture.

Gas Phase Model Limitations. Even though the concentration profiles of design 3 can be accurately predicted with the rigorous gas phase model, the influence of this model adjustment on design 1 is minor so that the characteristic isomerization activity cannot be fully explained yet. This is surprising because the mbOED result for design 1 (see fig. 3.3a) predicts this isomerization activity. Despite the experimental limitation of fixing the hydrogen content in the burette at 80 % instead of the designed 92 % (see table 3.3), the accumulation of hydrogen is not able to describe the experimental results. There are two possible explanations for this behavior. First, the accumulation of hydrogen in the gas phase is occurring significantly faster in comparison to the model predictions. However, the validity of this hypothesis is unlikely because of the accurate description the rigorous gas model provides for all other designs. Second, this design shows an increased sensitivity toward the CO inhibition in the catalyst equilibrium due to the low initial partial pressure (see the pressure ramp of experiment 49a_D1 in fig. 3.4) of CO. A parametric adjustment and the inclusion of an exponent for the CO concentration as an additional degree of freedom similar to the rigorous description from Jörke et al. [Jör+15] may present a remedy.

3.5.2 Modified Catalyst Pre-Equilibrium

Besides the consideration of an exponent for the CO concentration in the inhibition term of the catalyst pre-equilibrium in eq. (2.20), a second inhibition term describing the effect of low hydrogen concentrations in the liquid phase is required. Evidence for this addition can be found in experiment 53c_D3 in fig. 3.4 and 53b_D3 (see fig. F.2 in appendix F.1) where elevated isomerization activity is predicted contrasting the experimental results in the absence of hydrogen. While it is possible to introduce an inhibition constant to the isomerization reaction in eq. (3.1a), the negative influence

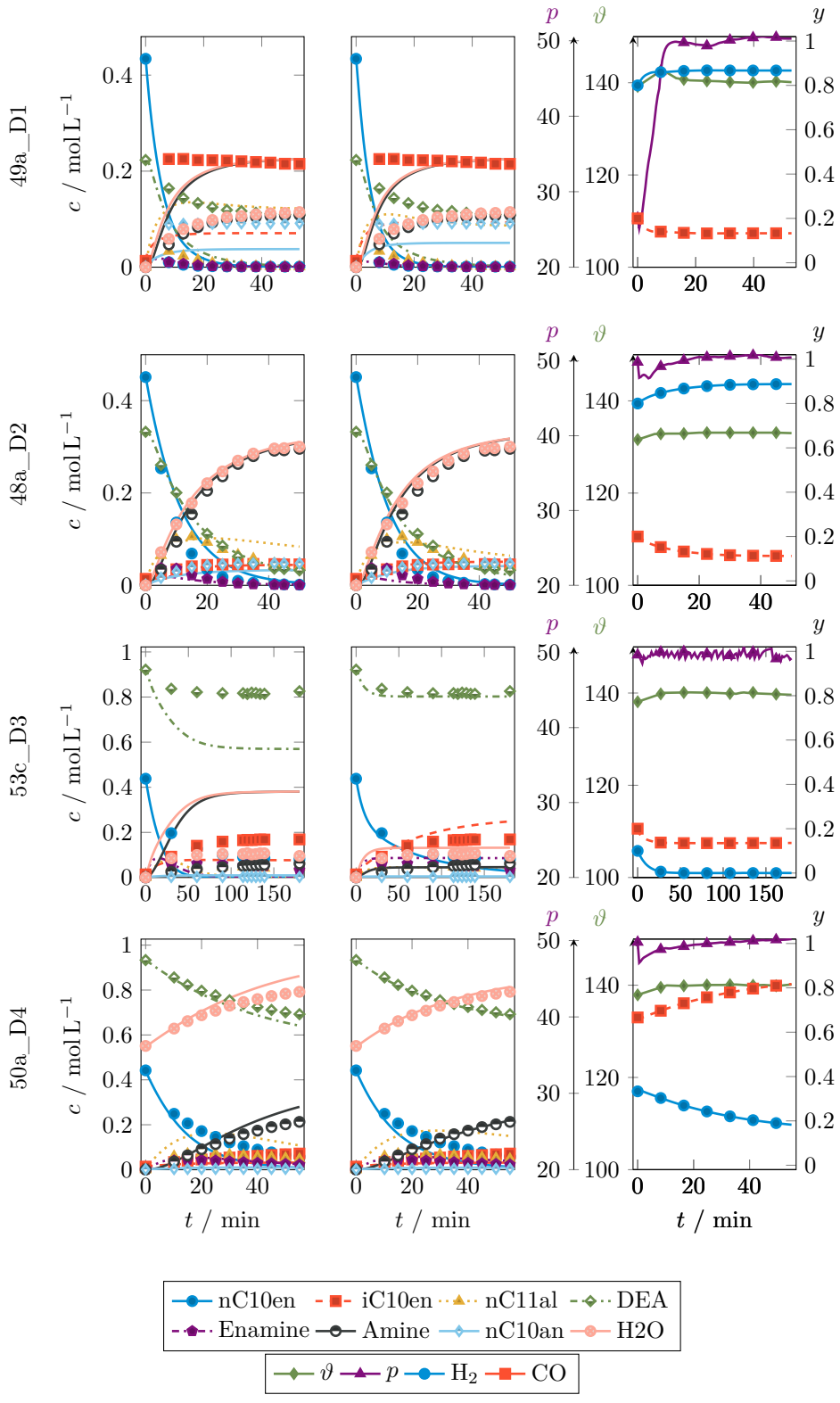

Fig. 3.4.: Comparison of predicted concentration profiles of selected experiments using the parameters from tables B.9 and B.11. Concentration profiles visualized via continuous lines represent the simulation results while marks are used for the experimental data. Left: Ideal control of the gas phase composition. Middle: Rigorous gas phase model from eq. (3.10). Right: Experimental control profiles and predicted gas phase composition using the rigorous gas phase model.

of low hydrogen concentrations on the catalyst has already been identified by Kiedorf et al. [Kie+14]. The absence of hydrogen leads to an increased formation of an inactive dimer catalyst species. Other hydroformylation reaction kinetics such as the 1-dodecene kinetics from Kiedorf et al. [Kie+14] and Hentschel et al. [Hen+15] contain this inhibition term (see eq. (B.10)) so that the catalyst pre-equilibrium is adjusted according to

$$c_{\mathrm{cat}} = \frac{c_{\Sigma\mathrm{cat}}}{1 + K_{\mathrm{cat,CO}} c_{\mathrm{CO}}^{a_{\mathrm{cat,CO}}} + K_{\mathrm{cat,H_2}} c_{\mathrm{H_2}}^{a_{\mathrm{cat,H_2}}}}. \tag{3.12}$$

In contrast to the mechanistic formulation from Kiedorf et al. where the CO-to-hydrogen concentration ratio is used in the inhibition term, a heuristic but similar formulation is employed with the direct application of the absolute hydrogen concentration to prevent numeric issues in edge cases. Please note that $a_{\mathrm{cat,H_2}}$ is expected to be negative under these conditions. Unfortunately, it is not possible to investigate the occurrence of different catalyst species experimentally using operando FTIR under hydroaminomethylation conditions due to the corrosive effect of DEA on the measurement equipment. Therefore, identification of the inhibition constants and the exponents for the concentrations of CO and hydrogen in eq. (3.12) needs to be performed based on the data from the kinetic experiments.

3.5.3 Parameter Identification

With the structural modifications of the reactor vessel model and the catalyst pre-equilibrium in sections 3.5.1 and 3.5.2, parameter identification is possible.

Parameter Selection. In contrast to the parameter restrictions during mbOED (see section 3.4 and appendix E.1), the number of parameters during parameter identification can be increased. In addition to all dimensionless activation energies B_j with $j \in \mathcal{RCT}^{\mathrm{HAM}}$, the dimensionless parameters A_j and the inhibition constants $K_{\mathrm{cat},i}$ and exponents $a_{\mathrm{cat},i}$ with $i \in \mathcal{SPC}^{\mathrm{Gas}}$ for the catalyst pre-equilibrium are estimated. Besides the isomerization equilibrium constant which was identified in preliminary experiments (see section 3.2), the remaining inhibition constants for the hydroformylation, enamine condensation and 1-decene hydrogenation are fixed to improve the FIM condition number and ensure the identifiability of the other parameters.

Estimation Results. Parameter identification is performed by solving the generalized LSQ problem from eq. (2.17) using a multi-start heuristic. Additionally, parameter scaling and local parameter subset selection [Bar+13] is employed to ensure parameter identifiability. An overview over the experiment data used for the parameter identification is summarized in table F.1. The interested reader may find a detailed description of the parameter identification algorithm in algorithm 2 in appendix F.2. The parameter estimates are displayed in table 3.5.

Tab. 3.5.: Kinetic parameter estimates for the HAM of 1-decene. All parameters are identifiable according to the local parameter subset selection approach from Barz et al. [Bar+13] with the numerical threshold from Jörke et al. [Jör+17]. The presented uncertainties represent one standard deviation.

i	A_i / −	B_i / −
Iso	4.9207± 0.0005	51.0316± 0.0053
Hyfo	17.5367± 0.0012	26.0423± 0.0019
Cond	−1.5277± 0.0005	12.6183± 0.0035
HydEn	15.3488± 0.2172	26.1398± 2.3242
HydDec	9.8808± 0.0007	33.1396± 0.0019

$K_{\mathrm{cat,CO}}$ / −	82 305.0902 ± 2.3631
$a_{\mathrm{cat,CO}}$ / −	1.6017 ± 0.0002
$K_{\mathrm{cat,H_2}}$ / −	0.035 00± 0.000 01
$a_{\mathrm{cat,H_2}}$ / −	−1.2669 ± 0.0002
$^{*}K_{\mathrm{Hyfo,I}}$ / L mol^{-1}	92.1
$^{*}K_{\mathrm{Hyfo,II}}$ / L^2 mol^{-2}	1063.6
$^{+}K_{\mathrm{Iso}}^{\mathrm{eq}}$ / −	39.0
$^{*}\Delta G_{\mathrm{r,Cond}}$ / J mol^{-1}	4000
$^{*}K_{\mathrm{HydEn}}$ / L mol^{-1}	6.49
$^{*}K_{\mathrm{HydDec}}$ / L mol^{-1}	10.2

*Fixed at initial guess.
+Estimated from preliminary experiments.

According to the subset selection, all parameters are identifiable with only minor parameter uncertainties. If compared to the initial guesses for A_j with $j \in \mathcal{RCT}^{\mathrm{HAM}}$ (see table B.11), only minor adjustments occur which supports the prior assumption of good parameter guesses. In terms of the activation energies, the parameter variations are more distinct. While the activation energy for the 1-decene hydrogenation is practically unchanged, greater differences appear for the activation energies of the hydroformylation and, especially, for the isomerization reaction. In non-dimensionless form, the hydroformylation activation energy rises by approximately 13 kJ mol^{-1} while the isomerization requires additional 35 kJ mol^{-1}. Despite this strong increase, the isomerization activation energy lies with 158 kJ mol^{-1} in

the same order of magnitude as the initial guess. In contrast to the activation energies, the CO inhibition constant in the catalyst pre-equilibrium grows by one order of magnitude. The exponent for the CO concentration matches this increase and reaches a similar value as the one identified by Jörke et al. [Jör+15] (1.6017 instead of 1.7406). For the hydrogen influence, a negative exponent is achieved as expected by the inhibiting effect on the active catalyst species concentration in the case of hydrogen absence in the liquid phase.

Prediction Quality. With the parameter estimates from table 3.5, the quality of the predicted concentration profiles increases dramatically. Figure 3.5 contains a selected subset of the experiments in which the benefits of the adjusted formulation of the catalyst pre-equilibrium and the parameter identification are visible. For a better impression on the prediction capabilities of the improved HAM kinetics, the interested reader is referred to fig. F.4 in appendix F.2 which contains the experimental and predicted concentration profiles for all experiments from table F.1.

The adjusted CO inhibition and isomerization activation energy enables the reproduction of the sharp increase in the experimental isomer concentration in experiment 49a_D1. Despite the improvements in the hydroformylation and enamine condensation activity, the aldehyde, amine, and water concentrations are still overestimated. Even though the initial parameter guesses are able to accurately predict all major species concentrations in experiment 48a_D2, the improved model is now able to match the aldehyde concentration profile at the expense of slightly overestimating the 1-decene hydrogenation and underestimating the enamine concentration. This trade-off in the enamine prediction, which is caused by the elevated activation energy, directly translates to an improvement in experiment 54a_D3 since the enamine condensation is the only reaction in the reaction network which is not catalyzed (see eq. (3.1d)). Simultaneously, this experiment prediction benefits from the newly added inhibition term for hydrogen absence in the form of limited isomerization activity under hydrogen depletion. Similarly, experiment 53a_D3 takes advantage of the additional inhibition term in the catalyst pre-equilibrium which effectively reduces the predicted isomer concentration.

3.5.4 Summary of Results

Prior to the parameter identification using a multi-start heuristic with local parameter subset selection, the reactor vessel model is extended via a rigorous gas phase model to improve the description of the experimental setup. Additionally, the structure

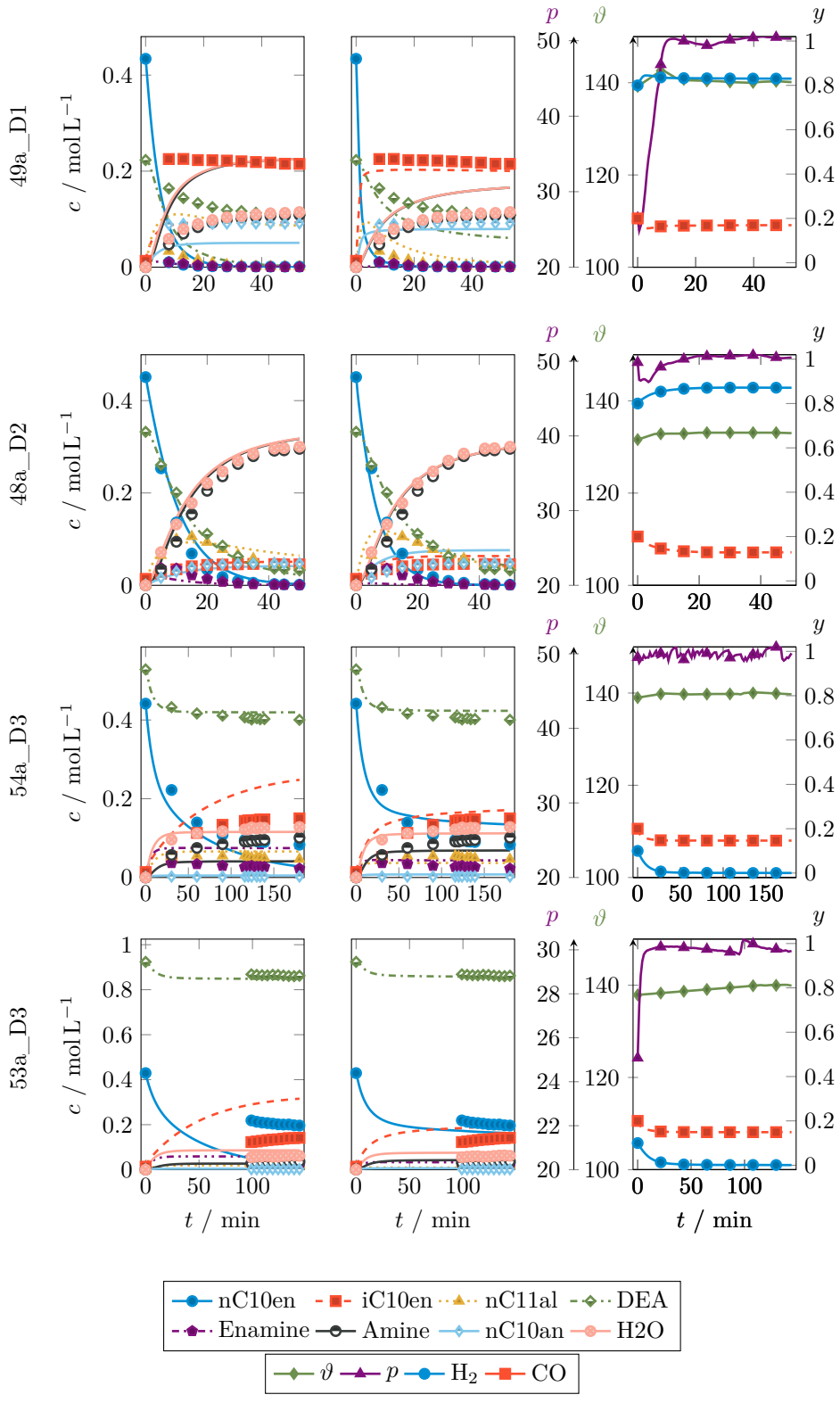

Fig. 3.5.: Comparison of predicted (lines) and experimental concentration profiles (marks) of selected experiments. Left: Reactor vessel model from eq. (3.5) with rigorous gas phase description from eq. (3.10) and initial parameter guesses from table B.11. Middle: Reactor vessel model form eq. (3.5) with rigorous gas phase description from eq. (3.10) and estimated parameter values from table 3.5. Right: Experimental control profiles and predicted gas phase composition using the rigorous gas phase model with the estimated parameter values from table 3.5. A comparison between all predicted and experimental results using the parameters from table 3.5 and the rigorous gas model can be found in fig. F.4 in appendix F.

of the catalyst pre-equilibrium is extended by a hydrogen-related inhibition term to predict the reduced isomerization activity in the absence of hydrogen in the gas phase. All kinetic parameters A_j and B_j with $j \in \mathcal{RCT}^{\mathrm{HAM}}$ next to the inhibition constants and the exponential factor for the concentration of CO and hydrogen in the catalyst pre-equilibrium are considered during parameter estimation and can be identified with small standard deviations. These modifications and improved parameter estimates enable the accurate prediction of not only nominal operating conditions with a sufficient gas supply to drive the hydroformylation and reductive amination but also the prediction of edge cases with CO or hydrogen limitation.

3.6 Discussion

Heuristic and Model-Based Experimental Design. In contrast to prior belief in the mbOED, the experimental setup has a significant influence on the gas phase composition which majorly impacts the hydroaminomethylation. While the experimental designs using the simplified gas phase model led to the discovery of the hydrogen exhaustion of the gas phase and the limiting effect of a reduced hydrogen pressure on the concentration of the active catalyst species, direct consideration of the rigorous gas phase model would result in better experimental designs. Following the idea of a sequential/simultaneous hybrid strategy for mbOED, performing a follow-up experimental design with the new information is possible and advisable even though it is not pursued in this work due to a limited experimental contingent and a satisfactory approximation of the experimental trajectories. Nevertheless, this result is achieved by not only relying on the designed experiments but also on experiments which result from the exploration of different hypotheses on the positive or negative influence of the experimental setup or chemical species. These exploratory experiments fall into the category of OFAT strategies for experimental design which are not considered economical and informative. However, in the investigation of the HAM, experiments following this strategy provided a valuable contribution to the mbOED results. Examples for this conclusion include (i) the prevention of local optima during the parameter estimation by considering experiments which explore different operating conditions and (ii) the identification of structural deficits in the reaction kinetic and the reactor vessel model. Despite the availability of suitable model-based counterparts of the heuristic exploration [BM09], application of these algorithms may lead to additional computational load which either cannot be handled or increases the time for the experimental design to an unmanageable degree for complex models. Therefore, a combination of both, model-based and heuristic, experimental design strategies can be advisable.

Experimental Restrictions. During the application of the experimental designs, trade-offs were made w.r.t. the accurate adjustment of the gas phase composition. While major experimental limitations such as the heating and cooling as well as the pressure control rate, a minimum time interval between subsequent measurements and the total number of measurements are considered in the mbOED, control trajectories of minor importance and discrete values for the gas composition in the burette were approximated after the computation of the designs. Especially the inclusion of integer decisions, for instance in the form of relaxed continuous formulations to preserve the complexity class of the optimization problem, poses an experimentally necessary but computationally demanding challenge. Therefore, additional research is required to formulate models for mbOED which take into account all experimental restrictions to systematically and reliably identify experiments with the maximum information content.

Model Limitations. With respect to the parameter identification and the prediction quality of the HAM model, it is apparent from the experiments in fig. 3.5 that the kinetic model only represents an approximation of the true reaction kinetics. In spite of significant improvements in the edge cases alongside an accurate description of the nominal, production relevant operating conditions, the approximative character of the model can be seen in fig. 3.6 which depicts two repetitions of an adjusted experiment based on design 3. Caused by a reduced total pressure of 30 bar, the rigorous gas phase model predicts an elongated depletion of the hydrogen content in the gas phase over the reaction time. This transition region cannot be described by the HAM model as the amine and water concentrations are significantly overestimated. The experimental results display a decrease in the reactivity of the overall system at around 20 min where approximately 6 bar hydrogen is remaining in the gas phase. This hints at a threshold concentration at which increased catalyst dimer formation commences. For an accurate description of this transition region, a more detailed model for the catalyst pre-equilibrium and additional experiments are advisable. Due to the infeasibility of FTIR measurements if DEA is present in the reaction system, either alternative measurement strategies need to be explored to validate the catalytic cycle of the catalyst or more exploratory data is required to deduce the catalyst pre-equilibrium model from the concentration profiles of the other species. At the same time, accurate measurements of the true gas phase composition and a careful verification of the gas-liquid mass transfer rates and Henry coefficients of all gaseous species are necessary to support the experiment evaluation.

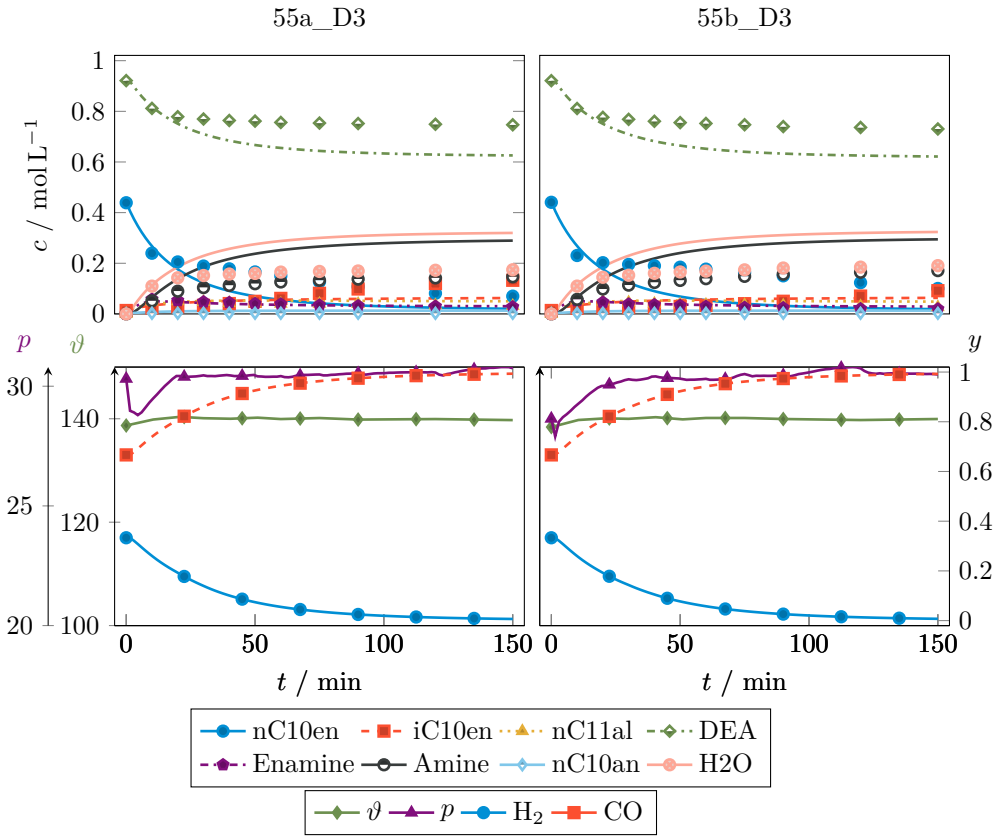

Fig. 3.6.: Comparison of the predicted and experimental concentration profiles of experiment 55a_D3 and 55b_D3 (see table F.1). The predicted concentration profiles are calculated using the estimated parameter values from table 3.5. Concentration profiles visualized via continuous lines represent the simulation results while marks are used for the experimental data.

Besides the structural limitation of the HAM kinetic model, the complexity of the reaction network presents additional challenges during parameter identification. Despite the effort taken to prevent local optima using the multi-start procedure from algorithm 2, it cannot be guaranteed that the global parameter optimum is found. One of the reasons for the complexity of this parameter identification problem is the sequential combination of the hydroformylation and reductive amination. Multiple intermediates are formed during the HAM so that the same concentration profiles of the products are achievable via adjustments of any of the reaction rates along the main branch of the reaction network. Therefore, good initial parameter guesses alongside sophisticated globalization strategies are mandatory but not sufficient to achieve reasonable parameter estimates. If applicable for this complex reaction network in terms of computational load, utilization of global optimization strategies would pose a great addition to the parameter identification task as they would either aid in finding good initial guesses for local, gradient-based algorithms (e.g., in the case of heuristic approaches such as evolutionary algorithms) or wrap the local optimization algorithms to systematically identify global parameter estimates (e.g., using a branch and bound scheme or successive approximation).

3.7 Chapter Summary and Outlook

Summary. In this chapter, the application of modern, model-based optimal experimental design (mbOED) strategies is exemplified for the identification of the complex, rhodium-catalyzed hydroaminomethylation of 1-decene reaction network under consideration of multiple phases. Besides the phase separation of the methanol/dodecane TMS below the reaction temperature, phase separation can also occur at elevated temperatures during the reaction as water is formed as a co-product in the enamine condensation step. This phase separation introduces additional mass transfer limitations to the reaction system and complicates the identification of an accurate reaction kinetic model. Therefore, mbOED is used together with phase equilibrium calculations to prevent conditions at which phase separation occurs while simultaneously designing five experiments for optimal identification of the kinetic parameters.

By incorporating experimental restrictions in the reactor vessel model, the experimental designs can be applied directly with only minimal approximations and adjustments. Analysis of the experimental concentration profiles enables the structural modification of the reactor vessel model and the reaction kinetics to accurately describe changes in the gas phase composition in the reactor and edge cases such as

the behavior at CO and hydrogen depletion. All kinetic parameters and inhibition constants in the catalyst equilibrium are identified and enable a good agreement of experimental results and predictions under all operating conditions.

Outlook. Even though the improved kinetic model for the hydroaminomethylation of 1-decene is able to accurately predict the experimental results, multiple improvements of the kinetic model as well as the mbOED design procedure are possible. While practical and directly realizable suggestions for the improvement of the hydroaminomethylation model are already presented in the discussion in section 3.6, the following two ideas present possible routes for reaction network agnostic future research in the area of kinetic model and parameter identification for liquid multiphase systems.

- **Model-Based Model Structure and Parameter Identification.** The experimental results have shown that the initial reactor vessel model and catalyst pre-equilibrium are insufficient in describing the HAM at the boundaries of the operating window. Even though heuristically designed additional experiments are able to narrow down possible explanations for the observed behavior, systematic, model-based approaches should be preferred to reduce the number of experiments and, therefore, save time and minimize cost. By incorporating the model structure in an outer optimization problem around the mbOED for parameter identification, experiments are designed which aid in the systematic identification of a suitable model structure. While numerous publications can be found on the topic of model discrimination and T-optimal design (see [FM08] for a review), two or more kinetic models are frequently discriminated. However, the investigation of the hydroaminomethylation reaction indicates that also the entire model of the experimental setup is highly relevant and should be incorporated in the discrimination as well. This is necessary since reducing the complexity of the experimental setup model to a sufficient degree directly translates into reduced computational loads which can be used to (i) raise the number of simultaneously designed experiments, (ii) increase the number of parameters considered during mbOED for parameter identification and (iii) perform multiple phase equilibrium calculations along the reaction coordinate in cases where a second liquid phase may not only appear but can also vanish due to temperature variations.

- **Automation.** The formulation of a mbOED problem with phase equilibrium calculations requires significant preparations in terms of finding a suitable model for the calculation of the activity and fugacity coefficients. Therefore,

automatized techniques are essential in reducing the identification effort of these secondary models to allow for a generalized application of mbOED for complex liquid multiphase systems. Even though the mass transfer formulation for the phase equilibrium calculation used in this work can be directly applied to arbitrary reaction systems, the process of identifying suitable activity or fugacity coefficient models is currently still a manual and time intensive process. Because of the challenging description of LLEs and the laborious generation of measurement data, standardized procedures should be formulated which simplify the selection of accurate yet parametically parsimonious activity and fugacity models. Frequently, these types of models are challenging in their direct application in gradient-based optimization algorithms so that the selection and validation of performant and task specific surrogate models should be included in the automatized procedure. Efforts in this direction would greatly simplify the inclusion of phase equilibrium calculations in different applications, even outside of mbOED, improve the model prediction accuracies and, simultaneously, raise additional optimization potential.

4 Multiphase Elementary Process Functions Methodology

4.1 Motivation

After the successful identification of a suitable reaction kinetic model, the prerequisite for the application of model-based reactor design approaches is fulfilled. In contrast to heuristics- or decomposition-based methods, these design approaches are able to identify non-intuitive solutions due to a rigorous consideration of the, usually non-linear and constrained, design space (see section 2.3 for an extended discussion on different process design approaches). One of the model-based process design methodologies is based on elementary process functions (EPF) and uses dynamic optimization to compute the optimal path of a fluid element in state space. The desired final state is described via an objective function which regularly uses performance measures such as conversion, yield, selectivity or cost/profit. For the identification of the optimal path, the algorithm utilizes different DoFs depending on the reaction system and technical restrictions. Frequently used DoF are the temperature, pressure, and the dosing of species native to the reaction system. However, by limiting oneself to reaction kinetic information, the EPF methodology can only identify optimal reactor(-networks) which are encompassed by the feasible region of the underlying model. Thus, the design of more complex process configurations including reactor-separator networks is currently only feasible by introducing either simplifications or assumptions w.r.t. the simultaneous consideration of multiple phases (see fig. 2.7 for a overview over multiple phases in the EPF methodology). While the a priori definition of the existence or absence of multiple phases is a prerequisite in previous extensions of the EPF methodology, the appearance and disappearance of phases during process operation has not yet been discussed.

Methodological Idea. In this chapter, reaction kinetic models are combined with thermodynamic information on the non-ideality of the reaction mixture to form the multiphase elementary process functions (mpEPF) formulation. This extension to the EPF methodology enables the description and exploitation of the appearance and disappearance of multiple phases in the reaction system. Instead of assuming a fixed

number of phases prior to the EPF calculation, mpEPF incorporate phase equilibrium calculations to capture the, possibly transient, mono- and multiphasic system behavior over the reaction time. This rigorous consideration of the reaction mixture's thermodynamics represents an addition to the EPF idea which is independent of any prior extension, such as the incorporation of axial dispersion or parameter uncertainties (see section 2.3.3). Therefore, it is suited for any reaction system where additional DoF are either beneficial and positively impact the objective function or necessary to ensure the fulfillment of system and process constraints.

Phase System Subset. Even though a rigorous consideration of non-ideal reaction system behavior enables the description of arbitrary phase equilibria such as L/L, V/L, S/L, this chapter focuses on reaction systems which allow for L/L separation. By only considering this subset of phase equilibria, separation processes primarily represented by extraction can be described. Additionally, phase separations due to temperature variations (TMS) or because of the accumulation/consumption of chemical species during the reaction are encompassed. Ultimately, this combination of reaction kinetics and thermodynamic information in the EPF methodology enables the calculation of integrated processes like reactive extractions which will be discussed in the outlook.

Chapter Overview. After briefly introducing the methodological idea behind the mpEPF formulation in section 4.2, it is applied to the HAM reaction kinetics from chapter 3 for the identification of optimal reactor networks in section 4.3. In the next step, the potential of the mpEPF formulation is presented in section 4.4 where the calculation of a reactor-separator sequence is performed using a generic example reaction. Finally, the results are summarized in section 4.5 and an outlook is provided to motivate further research and to discuss potential pitfalls when applying the mpEPF formulation in practice.

4.2 Methodological Contribution

In the EPF methodology, the trajectory of a fluid element through state space is altered in accordance with an objective function using predefined DoF represented by mass, heat, and energy fluxes. In a recent extension of the methodology, multiple fluid elements are considered with each of the fluid elements representing a separate phase [XF18c]. The trajectories of these fluid elements in state space are tracked simultaneously while they are able to interact with each other using internal, in

contrast to the externally supplied, fluxes. Even though Xie and Freund [XF18c] only show the application of this idea using a biphasic system comprising a liquid and gaseous phase with a permanent gas, the concept generalizes as it enables the introduction of additional DoF to describe and exploit more complex system behaviors.

Capabilities and Classification of the mpEPF Formulation. In this contribution, the interaction between and the control of multiple fluid elements in state space is extended toward dynamic non-equilibrium systems, i.e., systems that evolve over time such that multiple phases may appear or disappear over the considered time horizon. While the case of vanishing phases is less relevant for practical applications, the appearance of additional phases represents the core concept of a variety of downstream process operations such as crystallization, distillation, and extraction. Therefore, adding the capability to rigorously describe the thermodynamic state of the reaction system w.r.t. the number and composition of phases, the EPF methodology becomes a tool to synthesis (integrated) reactor-separator networks. While previous extensions already introduced the concept of ideal separators in the EPF methodology [Kai19], rigorously calculating the phase equilibria significantly improves upon the feasibility of the reactor-separator design. For instance, mpEPF does not require the a priori definition of a fixed number of separators or the assumption of a feasible separation. However, despite this edge in technical realizability, the mpEPF formulation is not supposed to replace but complement previous EPF extensions as it operates on level 2 rather than level 1 of the three-level MLRD approach (see table 2.2).

mpEPF Idea and Assumptions. In an ideal case, both, phase equilibrium kinetics and (thermodynamically consistent) reaction kinetics, are available to accurately predict the formation of the phase equilibrium during the reaction progress. When combined in a multiphase-aware EPF formulation, the resulting state and optimal control profiles would not only reflect but also exploit the effects of mutually affecting reaction and mass transfer kinetics. Unfortunately, kinetic information on the phase equilibrium formation are rarely available in practice. Therefore, assumptions for the phase equilibrium formation speed relative to the reaction kinetics are necessary. In regular EPF calculations, the implicit assumption of one reactive phase with an infinitely slow formation of the phase equilibrium is employed by not considering the non-ideality of the reaction mixture. In contrast, the mpEPF formulation uses the inverse assumption of an infinitely fast phase equilibrium formation due to the lack of accurate kinetic information. While the assumption on the phase equilibrium

formation speed (fast mass transfer kinetics in combination with comparatively slow reaction kinetics) requires validation for each system where mpEPF are applied, regular EPF in conjunction with mpEPF are able to provide estimates on both extrema. Thus, both concepts effectively provide lower and upper bounds on the expected process performance w.r.t. the phase system behavior.

Even though the knowledge about the phase equilibrium at each point in time is desirable during the reaction progress, an excessive amount of phase equilibrium calculations is impossible from a computational perspective. Therefore, a discretization of the time horizon in finite elements is recommendable. Instead of directly connecting neighboring finite elements, a phase equilibrium calculation can be performed using the preceding finite element's state information as input. The equilibrium states are then used as inputs in the subsequent finite element, thus effectively connecting both finite elements (FEs). A visualization of this approach can be found in fig. 4.1. In this visualization, the phase equilibrium calculation is

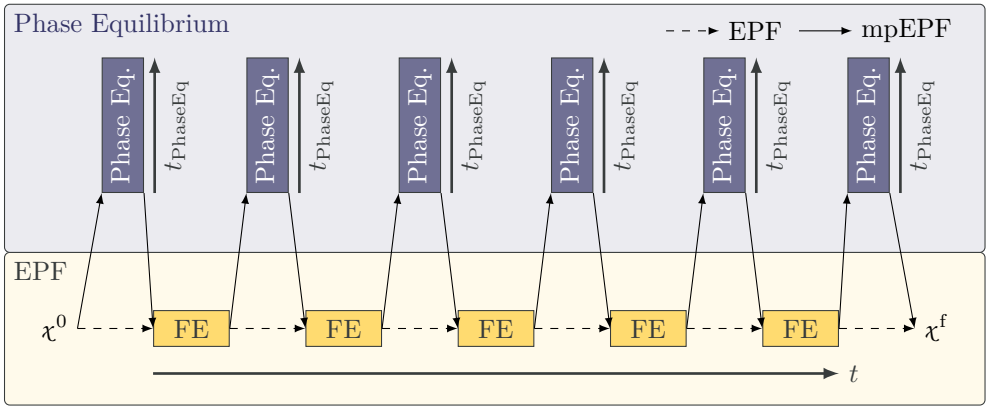

Fig. 4.1.: Methodological idea behind mpEPF. The time axis is discretized in finite elements at which the control variables $u(t_{\mathrm{FE}})$ are parameterized. Instead of interconnecting the finite elements sequentially as performed in the EPF methodology, mpEPF introduces phase equilibrium calculations between two neighboring finite elements. The equilibrium states are used in the subsequent finite element as inputs. This formulation represents an approximation of the simultaneous consideration of reaction and phase equilibrium kinetics by orthogonally decoupling both phenomena. A separate time t_{PhaseEq} is introduced for each phase equilibrium calculation so that the formation of the phase equilibrium is assumed instantaneous.

performed using the mass-transfer formulation from section 2.1, so that a fictive time t_{PhaseEq} is introduced for each phase equilibrium calculation which is orthogonal to the real time coordinate t. Naturally, it is also possible to select only the FEs between which a phase equilibrium calculation is beneficial to save computational time. The other FEs are then interconnected using the approach of the regular EPF methodology.

Implementation of Multiple Phases. With the phase equilibrium calculation providing information on the amount of species $i \in \mathcal{SPC}$ in phase $\pi \in \Pi$, mpEPF need to incorporate these information by tracking the molar amounts $n_i^{(\pi)}(t)$ as states throughout the computation. Starting with an equal distribution between all phases $\pi, \alpha \in \Pi$ with $n_i^{(\pi)}(t=0) = n_i^{(\alpha)}(t=0)$, the molar fractions $x_i^{(\pi)}(t)$ or rather their difference between phases $\Delta x_i^{(\pi,\alpha)}$ serves as an indicator for the appearance and disappearance of phases. External fluxes from the storage tanks (please refer to Kaiser et al. [KFS17] for a detailed discussion on the incorporation of axial dispersion in the EPF methodology) are adapted to the multiphasic formulation by enforcing an equal dosing into both phases with $j_i^{(\pi)}(t) = j_i^{(\alpha)}(t)$. Even though this restriction reduces the DoFs and, thus, limits the maximum achievable performance, this assumption is recommendable if a specific system does not provide the capability of accurate, phase-selective species dosing from a technological perspective. Finally, mpEPF-specific formulations of constraints or objective functions become possible in which the indicative nature of the molar fraction differences $\Delta x_i^{(\pi,\alpha)}(t)$ w.r.t. the number of phases is used to enforce a desired system state at a specific point in time. Exemplarily, this can be used to ensure a multiphasic state at the final time without the need for integer decisions. This constraint and the corresponding controls can then be associated with actions necessary to achieve product purification in a downstream process.

In the following two sections, the mpEPF formulation is applied to the hydroaminomethylation kinetics from chapter 3 and generic example kinetics to exemplify two strengths of the simultaneous consideration of phase equilibria in the EPF methodology — the ability to detect and prevent phase separation and the potential to exploit a multiphasic state of the reaction system to achieve a predefined goal.

4.3 Application to the Hydroaminomethylation

With the rhodium-catalyzed hydroaminomethylation kinetics for 1-decene identified in section 3.5, the application of model-based process synthesis approaches, such as EPF or mpEPF, becomes possible. While the model formulation and the implementation of the mpEPF DOP are summarized in appendix G.1, this section focuses on the presentation of the results.

Scenario Definition. The combination of reaction kinetic and thermodynamic information in the mpEPF formulation leads to the special case that the consideration

of theoretically inert species may have a significant influence on the reaction performance. This is the case if these species have the potential to cause phase separation in the reaction system which, in turn, causes concentration gradients in the overall system. However, if no phase separation occurs, the maximum potential of the reaction system cannot be identified due to the dilution with an inert species which is contrary to the EPF methodology idea. The hydroaminomethylation is such a system so that multiple scenarios are analyzed to identify the impact of solvents and the availability of species dosing on the system performance. While the former analysis provides valuable information on the risk of phase separation in the absence and presence of solvents, the latter case is able to deliver insight in the benefits and disadvantages of a one-pot synthesis (all reaction-critical species are provided when the reaction is started) versus a two-pot synthesis with dedicated reaction sections for the hydroformylation and reductive amination. The overall residence time for the reaction is set to 180 min which aligns with previous investigations of the reaction kinetics in chapter 3. Please note that in all subsequent scenarios, the phase equilibria are calculated after the optimization using the regular EPF methodology. This is possible since monophasic conditions are achieved for each scenario without penalization of multiple phases as the optimal process performance coincides with monophasic operation.

4.3.1 One-Pot Synthesis

In the absence of substrate and product dosing with $j_i^{(\pi)}(t) = 0$ for all species $i \in \mathcal{SPC}$ and phases $\pi \in \Pi$, the influence of the solvent system on the reaction performance is analyzed. As the addition of solvents requires enforcing constraints in cases where solvents do not have a positive impact on the reaction performance, the solvent ratio and the total amount relative to the substrate amount need to be provided.

Scenario 1: w/o Dosing & w/ Solvent. In the first scenario, solvent is added with a solvent ratio identical to the one in chapter 3 with $\phi^{\mathrm{m}}_{\mathrm{MeOH,nC12an}} = 1$. In addition, the maximal summed amount of each solvent $i \in \{\mathrm{MeOH}, \mathrm{nC12an}\}$ in all phases is constrained by $\sum_{\pi\in\Pi} n_i^{(\pi)}(t) < 1$ with the condition of one species i being fully added to the fluid elements. This effectively leads to methanol being present in the reactor with $\sum_{\pi\in\Pi} n_{\mathrm{MeOH}}^{(\pi)}(t) = 1$ due to its lower molar mass. The results of this scenario case can be found in fig. 4.2.

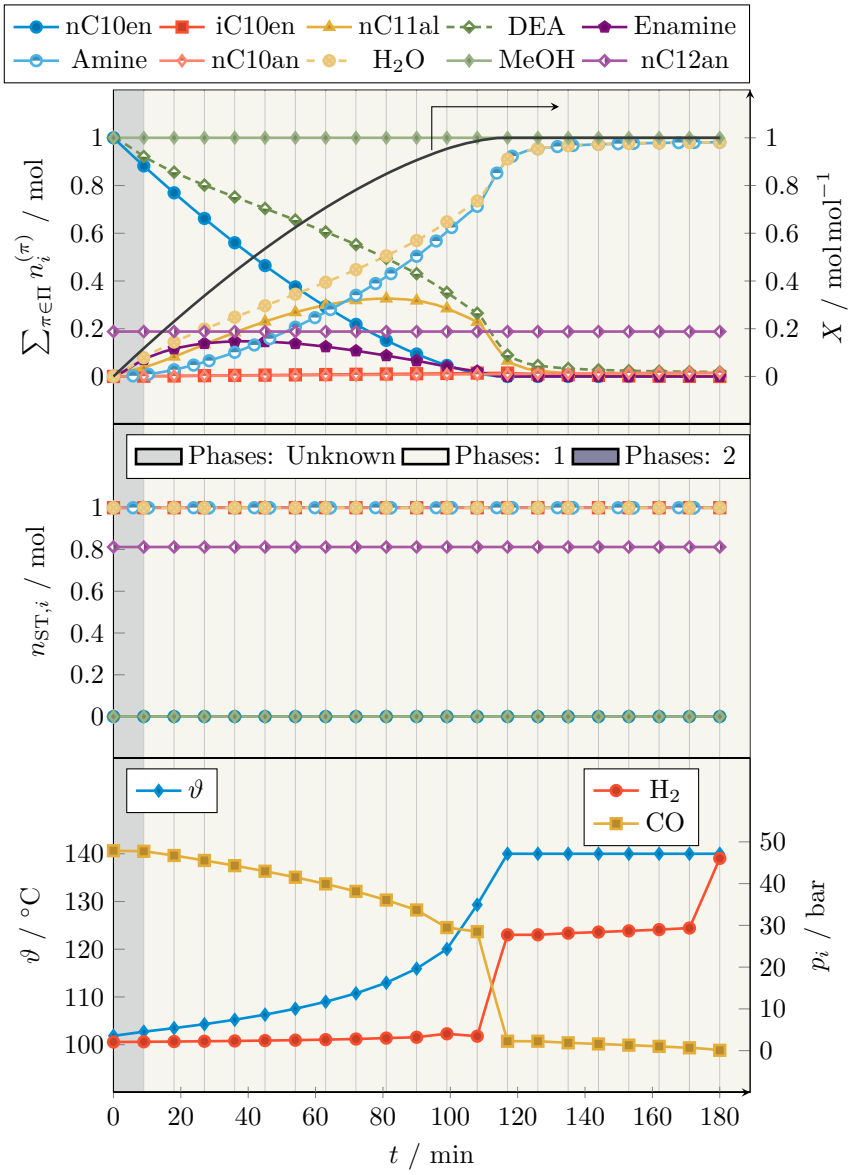

Fig. 4.2.: Molar trajectories and control profiles of the mpEPF formulation for the HAM. The case study neglects dosing of species over t and requires the addition of necessary substances at $t = 0$. Additionally, the presence of both solvents, methanol and dodecane, is enforced according to $\phi^{\mathrm{m}}_{\mathrm{MeOH,nC12an}} = 1$. Top: Summed molar trajectories of species i for all phases $\pi \in \Pi = \{\pi_1, \pi_2\}$ and overall conversion X. Middle: Storage tank hold-up of species i. Bottom: Temperature $\vartheta(t)$ and partial pressure $p_i(t)$ control trajectories with $i \in \{\mathrm{H_2}, \mathrm{CO}\}$. The figure background contains information on the number of phases in each finite element. An unknown number of phases is caused by the absence of phase equilibrium calculations.

1-Decene and DEA enter the reaction system at $t = 0$ so that a one-pot hydroaminomethylation reaction is occurring. Without any addition of intermediate and final products, minimal axial dispersion seems beneficial for the reaction system for which two distinct reaction zones can be identified. The first reaction zone is characterized by a significant but gradually decreasing CO excess in addition to a dynamic yet steadily increasing temperature profile from lower to upper bound in the first 120 min. In the second reaction zone, a constant temperature at the upper bound in addition to a distinct and constant hydrogen excess are identifiable. This leads to the conclusion that a decoupling of the hydroaminomethylation into its component reactions, the hydroformylation and reductive amination, is preferred. While the control profiles of the first reaction zone suggest a reactor unit with minimal axial dispersion, constant gas dosing and separately controllable temperature zones, the second reaction zone can be approximated via either a plug flow reactor or CSTR. For a more accurate identification of the optimal reactor for the second reaction zone, the derivative of the differential reaction flux needs to be calculated (see [KFS17]). However, due to the different focus of this work, this analysis remains for a future work. Interestingly, without further identification of the optimally suited reactor units, the optimal control profiles for the hydroaminomethylation are very similar to the ones for the hydroformylation. This suggests that reactor networks similar to the ones suggested by Kaiser et al. [Kai+17] should be able to provide a near optimal process performance with a maximum theoretical selectivity achieved in this scenario of 98.1 % at full conversion.

Scenario 2: w/o Dosing & w/o Solvent. In the second scenario, no solvent is added to prevent the dilution of the reaction system. The corresponding results can be found in fig. 4.3.

As expected, the control profiles are nearly identical to the ones from scenario 1. The only difference can be found in the transition region between reaction zone one and two where a temporal jump in the CO content of the gas phase occurs. This numerical artifact is the result of loosely bounded control state gradients (see table G.1) in combination with the high sensitivity of the reaction model in the transition region. Since monophasic operation is ensured in both scenarios due to the intermediate polarity of the product amine and its favorable water solubility, the absence of solvents with their diluting effect on the reaction system leads to a slightly higher selectivity of 98.4 % at full conversion.

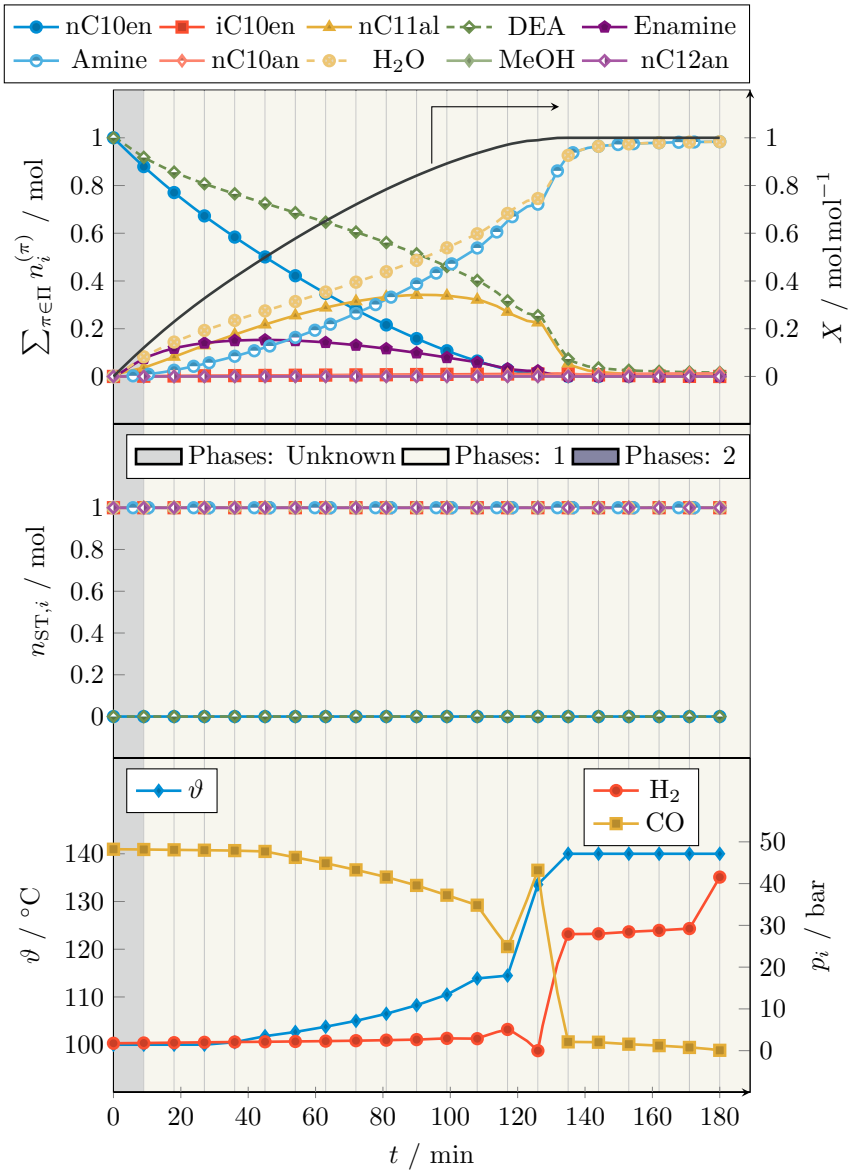

Fig. 4.3.: Molar trajectories and control profiles of the mpEPF formulation for the HAM. The case study neglects dosing of species over t and requires the addition of necessary substances at $t = 0$. The addition of solvents is not enforced. Top: Summed molar trajectories of species i for all phases $\pi \in \Pi = \{\pi_1, \pi_2\}$ and overall conversion X. Middle: Storage tank hold-up of species i. Bottom: Temperature $\vartheta(t)$ and partial pressure $p_i(t)$ control trajectories with $i \in \{\mathrm{H_2}, \mathrm{CO}\}$. The figure background contains information on the number of phases in each finite element. An unknown number of phases is caused by the absence of phase equilibrium calculations.

4.3.2 Two-Pot Synthesis

In the following two scenarios, the dosing of species is allowed to identify the maximum potential of the reaction system.

Scenario 3: w/ Dosing & w/ Solvent. If the addition of solvents at $t = 0$ is enforced similar to scenario 1, the permission of species dosing leads to a clear separation of the hydroformylation and reductive amination in two reaction zones as shown in fig. 4.4. Without any notable changes in the temperature and gas phase composition profiles for both reaction zones over scenario 1, the entire DEA amount is dosed after 100 min in a 10 min interval to initiate the reductive amination. This leads to a minor increase of the selectivity over scenario 1 to 98.3 % at full conversion.

Scenario 4: w/ Dosing & w/o Solvent. The maximum performance of an optimal hydroaminomethylation reactor network can be identified in the absence of solvents in conjunction with species dosing. The results of this scenario are visualized in fig. 4.5. In comparison to scenario 3, the temperature and gas phase composition profiles remain identical so that the selectivity improvement toward 98.7 % at full conversion can be attributed to the absence of reaction system dilution.

4.3.3 Conclusion

The comparison of all four scenarios reveals that the consideration of solvents leads to a minor decrease in process selectivity due to their diluting effect and the absence of phase separation under optimal conditions. By incorporating additional DoF in the form of species dosing to the EPF calculation, the optimizer identifies an optimal reactor network in which the hydroformylation is separated from the reductive amination via two distinct reaction zones. Hence, a two-pot synthesis or a process setup which allows for the distributed dosing of DEA (see chapter 5 for an alternative and suitable, dynamically operated reactor setup) should be favored over the one-pot approach in which all substrates enter the reaction system simultaneously. Nevertheless, due to the minor increase in selectivity achieved by the distributed DEA dosing, a simplified reactor setup using the one-pot strategy is also viable in the case of limitations on the technical equipment, process operation or cost.

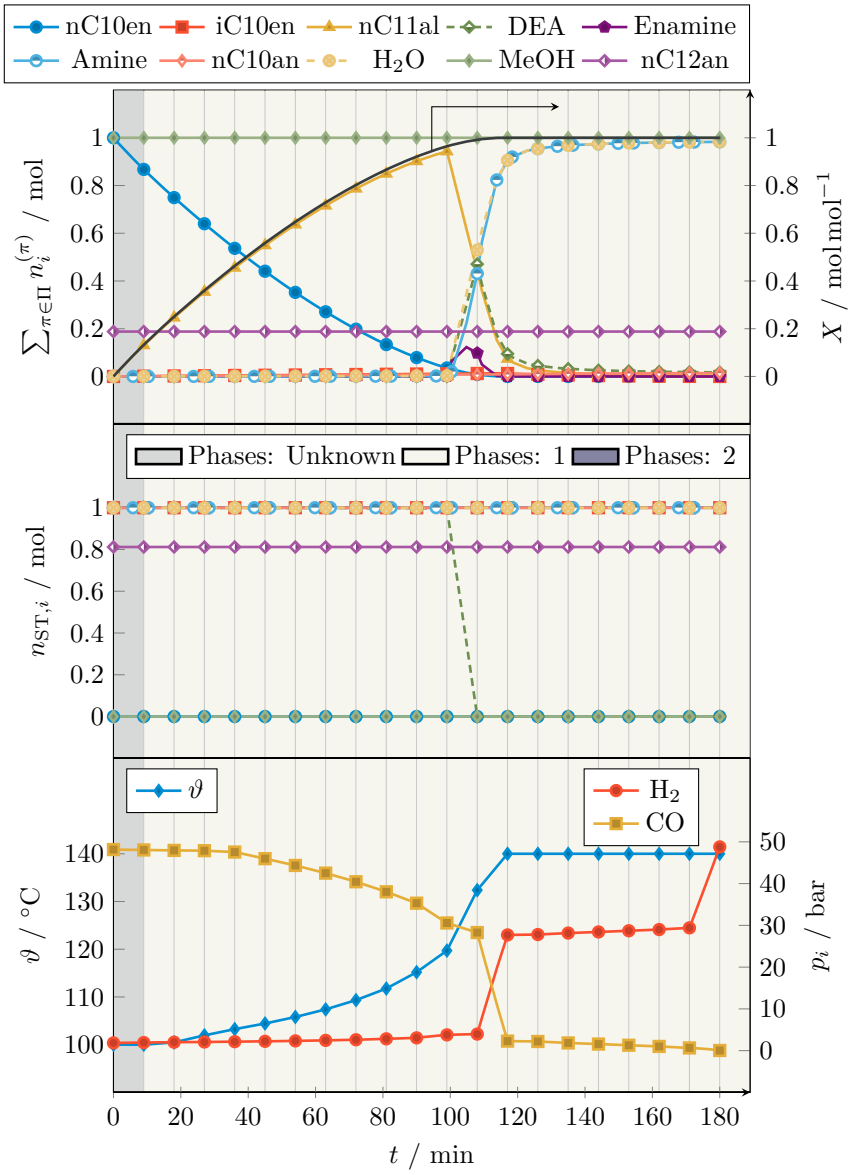

Fig. 4.4.: Molar trajectories and control profiles of the mpEPF formulation for the HAM. The case study allows dosing of all species $i \in \mathcal{SPC}^{\mathrm{HAM}}$ and enforces the addition of both solvents, methanol and dodecane, according to $\phi^{\mathrm{in}}_{\mathrm{MeOH,nC12an}} = 1$ at $t = 0$. Top: Summed molar trajectories of species i for all phases $\pi \in \Pi = \{\pi_1, \pi_2\}$ and overall conversion X. Middle: Storage tank hold-up of species i. Bottom: Temperature $\vartheta(t)$ and partial pressure $p_i(t)$ control trajectories with $i \in \{\mathrm{H_2}, \mathrm{CO}\}$. The figure background contains information on the number of phases in each finite element. An unknown number of phases is caused by the absence of phase equilibrium calculations.

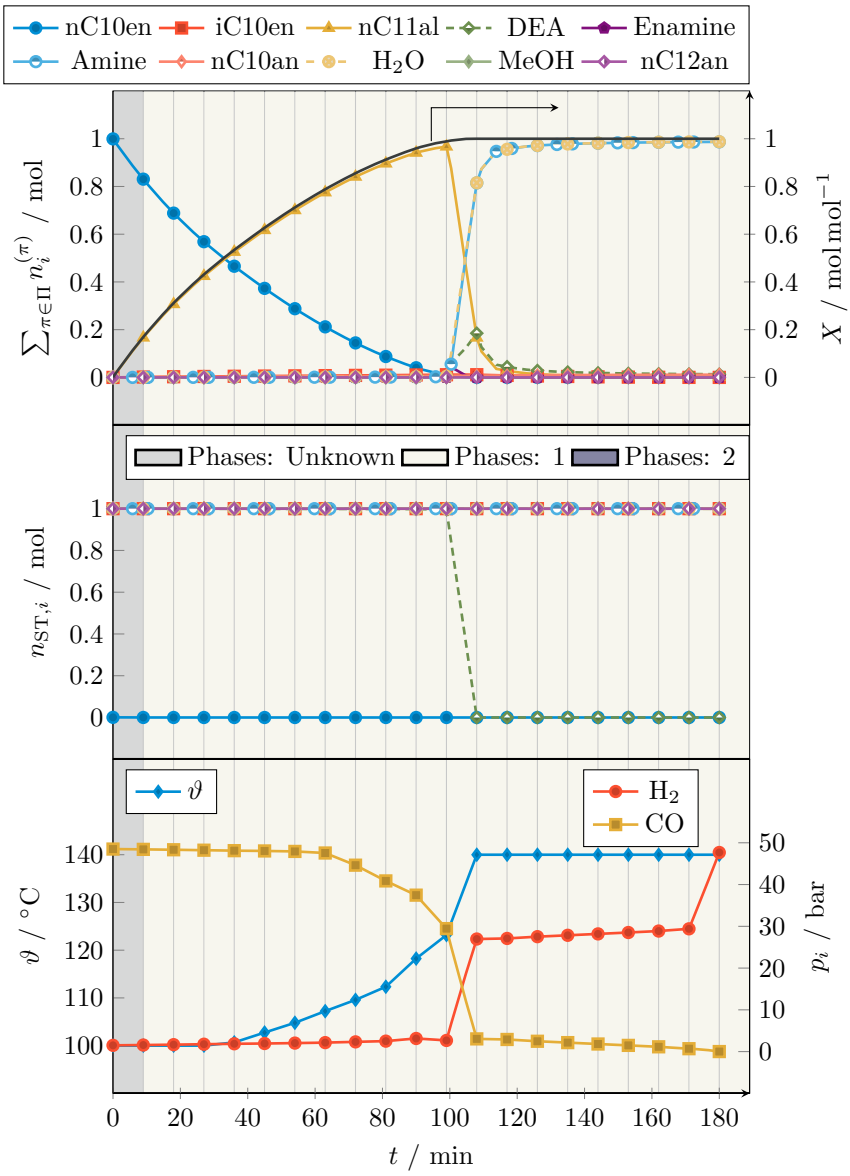

Fig. 4.5.: Molar trajectories and control profiles of the mpEPF formulation for the HAM. The case study allows dosing of all species $i \in \mathcal{SPC}^{\mathrm{HAM}}$. The addition of solvents is not enforced. Top: Summed molar trajectories of species i for all phases $\pi \in \Pi = \{\pi_1, \pi_2\}$ and overall conversion X. Middle: Storage tank hold-up of species i. Bottom: Temperature $\vartheta(t)$ and partial pressure $p_i(t)$ control trajectories with $i \in \{\mathrm{H_2}, \mathrm{CO}\}$. The figure background contains information on the number of phases in each finite element. An unknown number of phases is caused by the absence of phase equilibrium calculations.

Model Inadequacies. Even though both, one- and two-pot synthesis, appear comparatively matched for the hydroaminomethylation, the influence of side reactions at elevated intermediate product concentrations needs to be investigated in more detail. While high aldehyde concentrations in scenario 3 and 4 are only critical w.r.t. aldol condensation at elevated temperatures over a prolonged residence time (see the discussion on the distillation column by Dreimann et al. [Dre+16b]), high enamine concentrations in scenario 1 and 2 may lead to non-negligible aldol formation in the reaction system. In the kinetic model for the hydroaminomethylation from chapter 3, this side reaction is not considered. Consequently, careful consideration of a potential model extension in future research is necessary if the one-pot synthesis strategy is pursued further.

4.4 Hypothetical Example Sequential Reaction & Extraction

While the application of the mpEPF formulation on the hydroaminomethylation reaction is not able to adequately demonstrate its capabilities and future directions for development, the generic reaction model with the reaction equilibrium

$$2\mathrm{A} \rightleftharpoons \mathrm{C}$$

is employed. The goal of this hypothetical example is the calculation of control trajectories which can be interpreted using the FPA into a reactor-separator sequence. In particular, the separation shall be performed using a L/L extraction via the extracting agent E.

Model Design. To leverage the features of the mpEPF formulation, thermodynamic information in the form of activity coefficients need to be specified for all species. Due to the generic nature of the example, activity coefficients of real substances are attached to the hypothetical molecules using modUNIFAC. The real substances are selected carefully in order to show the desired behavior, i.e., complete miscibility of molecule A and C with the formation of a temperature-dependent miscibility gap in the presence of molecule E. One selection which is particularly suited for illustrative purposes associates the polarities of molecule A, C, and E with the polarities of 1-decene (nC10en), 1-butanol and DMF, respectively. Naturally, this system does not conform to a real-world process use case. However, by selecting any system with a substrate and product of slightly different polarity, L/L extraction can be performed when using a third species which enables phase separation with a preferential accumulation of either the substrate or the product in one phase.

In addition to the selection of an equilibrium reaction, the generic reaction model also contains an inhibition term w.r.t. the extracting agent E. Therefore, the reaction rate equation for phase $\pi \in \Pi$ can be written as

$$r^{(\pi)} = k(T) \frac{c_{\mathrm{A}}^2 - \frac{c_{\mathrm{C}}}{K^{\mathrm{eq}}}}{1 + K_{\mathrm{E}} c_{\mathrm{E}},} \tag{4.1}$$

with the Arrhenius equation

$$k(T) = k_0 \exp\left(\frac{-E_{\mathrm{A}}}{RT}\right), \tag{4.2}$$

and the necessary kinetic, equilibrium, and auxiliary parameters summarized in appendix G.2 in table G.2. Even though the incorporation of a reaction equilibrium and an inhibition term is not strictly required to demonstrate the control profiles of the desired reactor-separator sequence, it makes the generic model applicable for the demonstration of alternative reactor-separator sequences and integrated unit operations such as reactive extractions. More information on this scenario are provided in the outlook. Similar to the hydroaminomethylation, the following paragraphs focus on the discussion of additional modeling restrictions and the presentation of the results while implementational aspects are summarized in appendix G.2.

Operating Constraints and Objective. Despite the general assumption in the EPF methodology of unlimited fluxes on level 1 of the MLRD approach (see table 2.2), dosing fluxes and especially the rate of change of the temperature are constrained in this hypothetical example (see table G.3 in appendix G.2). While the maximum dosing fluxes are only bounded to improve numerical stability, the temperature rate of changed is intentionally limited to improve the interpretability of the resulting control profiles. In contrast to the hydroaminomethylation case in which the product yield is used as the objective function in addition to a penalization of multiphasic behavior, a maximum isolation of product C in one phase at the final time t^{f} is promoted (see eq. (G.6) in appendix G.2).

4.4.1 Results

The results of the mpEPF calculation are presented in fig. 4.6.

Control Profile Discussion. In this figure the molar amount of each species $i \in \mathcal{SPC} = \{\mathrm{A}, \mathrm{C}, \mathrm{E}\}$ in all fluid elements as well as in the buffer tanks are shown in addition

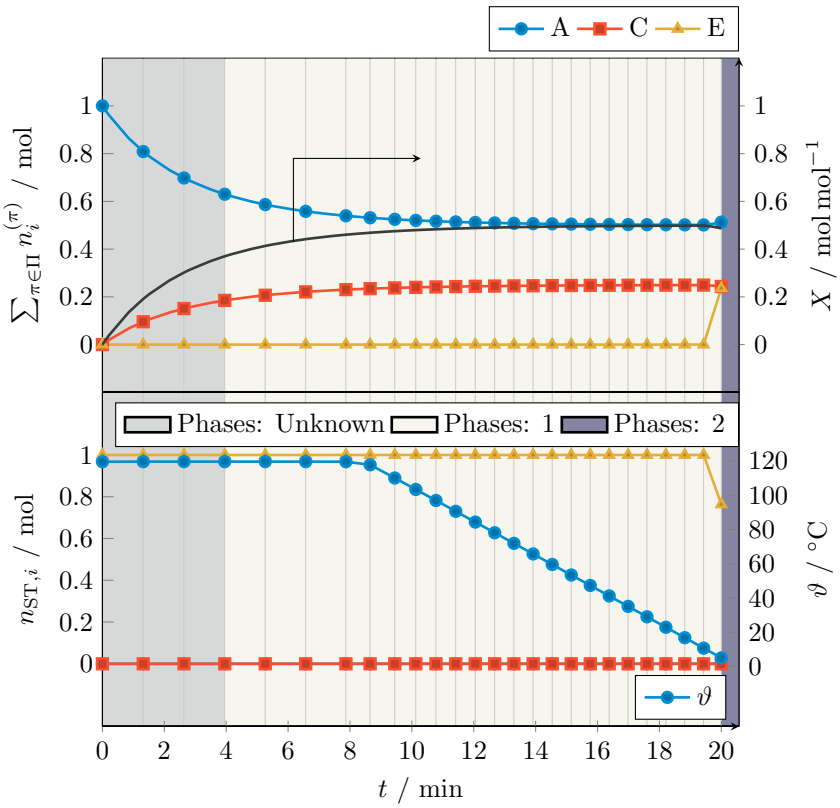

Fig. 4.6.: Molar trajectories and control profiles of the mpEPF formulation for the generic example model. Top: Summed molar trajectories of species $i \in \{\mathrm{A,B,C}\}$ for all phases $\pi \in \Pi = \{\pi_1, \pi_2\}$ and overall conversion X. Bottom: Storage tank hold-up of species i and temperature control trajectory $\vartheta(t)$. The figure background contains information on the number of phases in each finite element. An unknown number of phases is caused by the absence of phase equilibrium calculations.

to the conversion and temperature profile. In the background of each plot, the finite elements are depicted with the information on the number of phases visualized via different colors. Here, gray is used to symbolize the absence of phase equilibrium calculations to save computational resources while beige and blue indicate the presence of one and two liquid phases, respectively.

The formation of the reaction equilibrium is achieved in the first 20 min where the substrate A is converted according to the stoichiometry to the desired product C with a conversion of 50 %. While substrate A is entirely present in the fluid element at $t = 0$, the hypothetical example is designed so that no product C is available in the storage tank for simplicity. Over the reaction time, the extracting agent E is kept in the storage tank until a small amount is dosed into the fluid elements in the last FE to initiate phase separation. Only a fraction of the available extracting agent is necessary to induce this phase separation because of the prior decrease in

temperature from its upper to its lower bound after minute 8 onward. Theoretically, this early decrease in temperature has a negative effect on the reaction speed and has the potential to decrease the product yield. However, the available reaction time is sufficient for the formation of the reaction equilibrium so that the presented control profiles represent a feasible option out of the set of equivalently valid alternatives.

Ternary Diagram Discussion. An alternative view on the reaction progress can be achieved by studying the ternary diagram of substrate A, product C and extracting agent E in fig. 4.7. In this figure, the phase and reaction equilibria are depicted

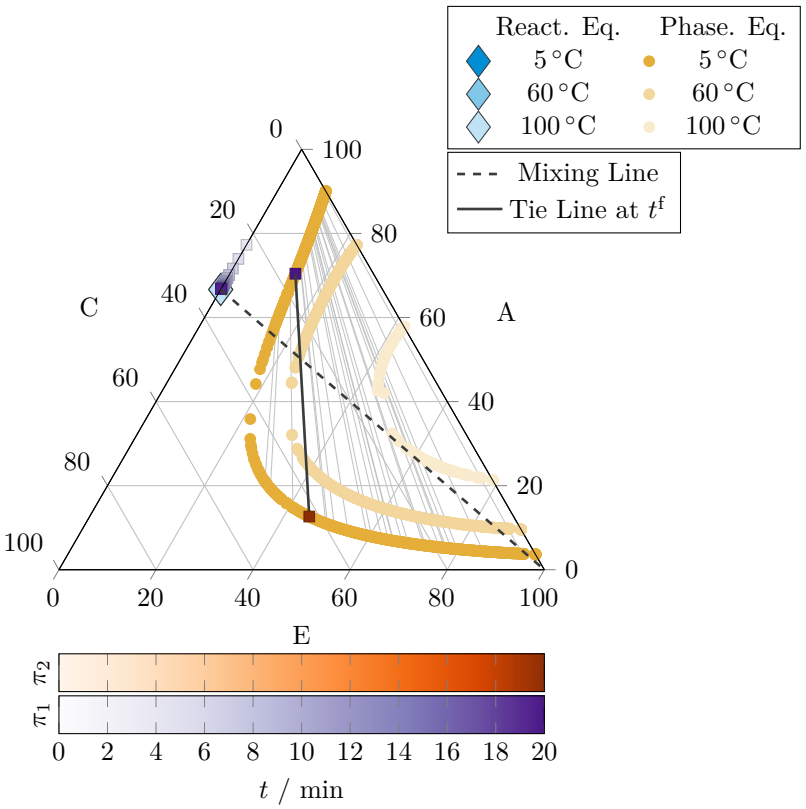

Fig. 4.7.: Ternary diagram containing the substrate A, product C and extracting agent E of the generic example model. The binodal curves for 5 °C, 60 °C and 100 °C are available with tie lines at selected compositions for 5 °C. Additionally, the reaction equilibrium for $x_E = 0$ is visualized for the same temperatures. The tie line between both phases of the final reaction mixture at t^f is highlighted. The intersection of the tie line and the mixing line with pure E provides the overall composition of the reaction mixture and contains information on the relative size of each phase.

for three different temperatures 5 °C, 60 °C and 100 °C. While the temperature dependency of the miscibility gap is clearly visible, all reaction equilibria fall on the same point because of the independence of K^{eq} from T. Starting with the binary

system of A and C, the reaction progresses until the reaction equilibrium is reached. Subsequently, the extracting agent is dosed which can be visualized via a mixing line between the system composition and pure E. This dosing initiates the phase separation into a product rich (red) and a substrate rich (violet) phase which both lie on the binodal curve of 5 °C. The overall composition of the system can be found at the intersection of the mixing line with the tie line between the substrate and product rich phases.

4.4.2 Conclusion

When interpreting the control profiles of the mpEPF formulation, an optimal process for the generic example model can be found which does not only aim at the maximum product yield but also its separation from unconverted substrates. This is achieved by associating the controls in the first 19 min to a reactor unit with individually controllable heating zones and the approximately last minute to a vessel in which species E is mixed with the reaction mixture to achieve the extraction of product C.

This single minute which is associated with the extraction is, of course, only due to the finite dosing flux of the extracting agent. It cannot be interpreted as the time required for the extraction, i.e., the mass transfer kinetics, are unknown. Despite this restriction which is caused by missing information and not related to shortcomings of the theoretical foundation of the approach, these results validate the ability of the mpEPF formulation to compute control profiles which allow for the design of reactor-separator sequences with L/L separations in the downstream process.

4.5 Chapter Summary

In this chapter, the extension of the EPF methodology w.r.t. the consideration of multiphasic systems under transient conditions is discussed.

Methodology. This multiphase elementary process functions (mpEPF) formulation builds on top of the simultaneous consideration and tracking of multiple fluid elements from Xie and Freund [XF18c] by introducing thermodynamic information to perform phase equilibrium calculations during the calculation of optimal control profiles. Due to missing kinetic information on the phase equilibrium, instantaneous phase separation or phase union is assumed even though the theoretical foundation allows for the incorporation of this information as well. By leveraging the lifted formulation

for the phase equilibrium calculation from section 2.1, the "online" calculation of the phase equilibrium is possible so that no prior formulation of a surrogate model is necessary to infer the system state including the number of and concentration in the phases. However, even though it is not required, introducing a surrogate model to describe the phase equilibrium is still possible in the mpEPF formulation and leads to greatly reduced computational loads. While the mpEPF approach is only exemplified for systems with L/L equilibria, the approach generalizes to arbitrary phase equilibria and, therefore, separation methods. This enables the identification of reactor-separator sequences and even integrated reactor-separator process units from the control profiles of the mpEPF formulation.

Hydroaminomethylation. In the first example case in section 4.3, the mpEPF formulation is applied to the hydroaminomethylation of 1-decene using the reaction kinetics from chapter 3 with the activity coefficient ANN from appendix C. Four different scenarios are calculated which differ in terms of the availability of species dosing and the presence of solvents in the fluid elements. For the hydroaminomethylation, monophasic behavior is required to prevent significant catalyst leaching into an aqueous phase. However, due to the good solubility of the product amine and water, this is ensured for all cases without any impact on the optimal control profiles. Therefore, the presence of solvents only leads to a (minor) decrease in the product yield due to its diluting effect. In contrast, the presence of species dosing has a significant effect on the shape of the control profiles even though the difference in product yield between these cases is negligible. Without species dosing, all substrates are present in the fluid elements from the beginning of the time horizon which leads to the simultaneous formation of all intermediate and final products. In the case of species dosing, the optimizer decides for a complete separation of the two composing reactions, the hydroformylation of 1-decene and the reductive amination of 1-undecanal, into two reaction zones by delaying the dosing of the second substrate DEA. Independent of the scenario, a product selectivity over 98 % at full conversion is achieved which serves as the upper bound for all process variants investigated here.

Generic Model. To exemplify the capabilities of the mpEPF formulation, a generic example model is designed in section 4.4 which allows for the design of a reactor-separator sequence. Each of the three pseudo-species A, C, and E receives an activity coefficient model using modUNIFAC so that the substrate A is comparatively non-polar while product C is increasingly polar. Species E does not take part in the reaction network but acts as a polar extracting agent for C due to its even more polar

nature. This leads to the calculation of control profiles in which the temperature is reduced over time to initiate the dosing of E in the latest possible moment for pushing the reaction mixture in the center of the temperature-dependent miscibility gap. The resulting phase separation yields a substrate rich, non-polar and a product rich, polar phase. The control profiles can be separated in three reaction zones (constant temperature, dynamic temperature and dosing zone) from which two are associated with the reaction and the third reflects the downstream purification of the product. This verifies the capability of the mpEPF to design reactor-separator sequences for L/L multiphase systems.

4.6 Chapter Outlook

Even though the mpEPF formulation is able to proof the ability to detect and actively exploit the available information on the phase state, many additional scenario considerations and extensions are required for the mpEPF formulation to become a tool which can be reliably used for the design of reactor-separator networks. Before going into detail on possible directions for future research, the following section is dedicated to the discussion of a pitfall when applying the mpEPF formulation for the design of integrated reactor-separator process units and networks.

4.6.1 Thermodynamic Consistency Requirement

Generic Model Adjustment. As already discussed in the model design for the generic example reaction, the reaction parameters can be minimally adjusted to exemplify the case of a reactive extraction. This is achieved by setting the activation energy to zero which, in turn, removes the temperature dependency of the reaction kinetics. It needs to be emphasized at this point that this scenario is purely designed to highlight a specific requirement when using the mpEPF formulation for the design of integrated reactor-separator units. This scenario does not claim to be directly translatable to any real world scenario.

Expectations. With the reaction kinetics independent of the temperature, the optimizer is able to perform the reaction at the lower temperature bound without any negative consequences for the product yield. This means that it is beneficial to operate the system under biphasic conditions for the entire time horizon since the backwards reaction of product C to substrate A is impeded in the product

and extracting agent rich, polar phase according to the inhibition term in eq. (4.1). Additionally, special penalization of the objective function w.r.t. a desired phase state is not required any longer since the multiphasic operation is now favored. Consequently, for an infinite time horizon, the reaction needs to reach the reaction equilibrium together with the phase equilibrium for both phases to achieve the chemical equilibrium.

Results. However, when visualizing this scenario in fig. 4.8, this chemical equilibrium is not achieved. As expected, the reaction is performed under biphasic conditions

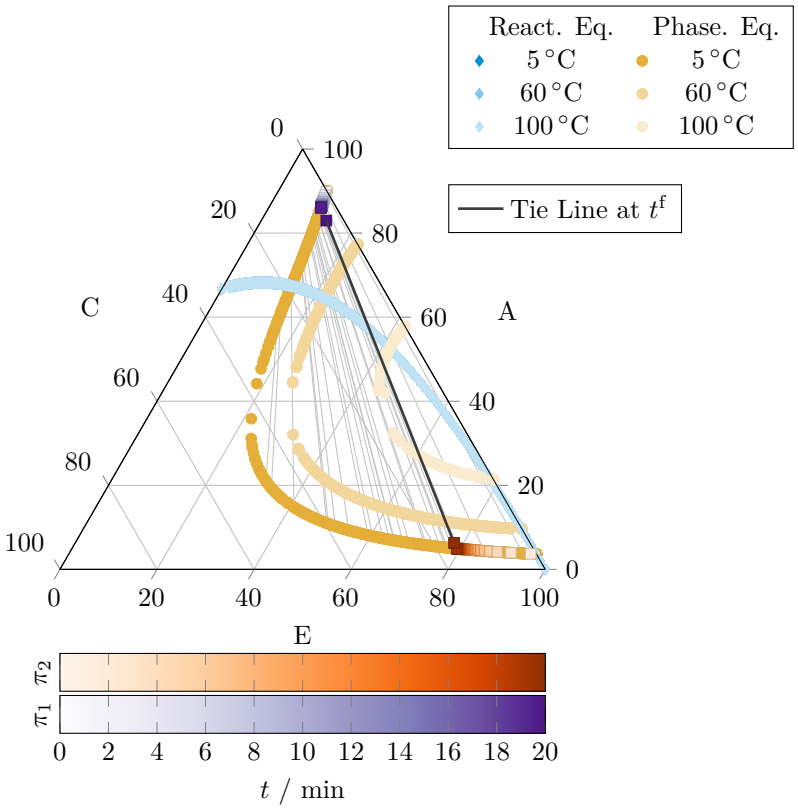

Fig. 4.8.: Ternary diagram containing the substrate A, product C and extracting agent E of the generic example model with $E_A = 0$. The binodal curves for 5 °C, 60 °C and 100 °C are available with tie lines at selected compositions for 5 °C. Additionally, the reaction equilibrium is visualized for the same temperatures. The tie line between both phases of the final reaction mixture at t^f is highlighted. Thermodynamic consistency is not achieved in this model since no intersection of the reaction equilibrium and binodal curve is available which are simultaneously connected via a tie line.

and progresses toward the reaction equilibrium in the non-polar phase with the simultaneous accumulation of product C in the polar, extracting agent rich phase. Since the polar phase moves away from the reaction equilibrium, or more precisely

the intersection of the reaction equilibrium curve and the binodal curve at 5 °C, there has to be a tipping point where the backwards reaction from C to A in the polar phase exceeds the forward reaction despite the inhibiting effect of E on the reaction kinetics. This would mean that an unsteady reaction system is formed which oscillates between states of high substrate and high product yield.

Solution. This oscillating behavior does not represent the true system behavior but stems from a thermodynamically inconsistent formulation of the reaction rate in eq. (4.1). If activities would have been used instead of concentrations, the reaction equilibrium curves would have intersection points with the binodal curves at which tie lines are available which connect the phases at both intersections.

Learnings. This hypothetical example clearly demonstrates the need for thermodynamically consistent formulations of reaction kinetics within the mpEPF formulation. Additionally, it serves as a word of caution to the practitioner when applying the technique to reaction kinetics from the literature as these are normally formulated in a thermodynamically inconsistent way using concentrations. Simultaneously, this example should also be interpreted as an appeal to all scientists working on the development of reaction kinetic models to consider a thermodynamically consistent formulation to greatly improve the transferability and applicability of their models.

4.6.2 Directions for Future Research

The mpEPF formulation described in this chapter is applied to liquid multiphase systems under transient conditions and the capabilities for designing simple reactor-separator sequences are shown. To broaden the applicability of this formulation and increase the predictive capabilities, future research should consider the following aspects:

- **Alternative Systems.** Due to its general formulation of considering the phase equilibrium in the EPF methodology, the mpEPF formulation can be applied to arbitrary multiphasic systems such as V/L and S/L. Further example cases in which these systems are considered would greatly help the development of the formulation as system-dependent requirements can be addressed and potentially generalized. Additionally, this would broaden the scope as separation techniques like distillation and crystallization would be incorporated naturally in the FPA.

- **Alternating Reactor-Separator Sequences and Complex Separations.** While a simple sequence of one or multiple reactors followed by a separation can be designed with the mpEPF formulation, the design of alternating sequences of reactors and separators requires additional methodological contributions. In particular, if a separation is performed, the resulting phases need to be connected to either the process outlet or internally in the process. Even though this interconnection is possible in the current state of the mpEPF formulation, it does not adhere to the idea of the EPF methodology where the uppermost potential of the process should be identified. Theoretically, it is possible to perform further downstream processing to the separated phases, e.g., in the case of distillation columns or via multi-step separations, so that additional optimization potential is available. This is currently not in the scope of the mpEPF formulation and needs to be appended.

5 Process Operation Strategies

5.1 Motivation

The realization of the optimal reactor and reactor-separator networks designed by the EPF and mpEPF methodologies enables better performing and/or more efficient processes with increased product yields and an efficient use of raw materials. However, translation of the optimal control trajectories into real-world reactor units using, e.g., the FPA, might be challenging depending on the type of reactor unit. On one hand, a CSTR can be realized with minimal constructional adjustments of the reactor vessel due to its time-independent control parameters. On the other hand, implementation of a DSR or even a PFR with pronounced temperature profiles require approximations of the optimal control trajectories in the form of discrete dosing positions or individual heating zones. Additionally, once constructed and implemented in the process, alteration of these reactor types according to changing optimal control profiles due to, e.g., (i) improved reaction kinetic models, (ii) fluctuations in the substrate quality and (iii) utilization for different reactions or in different operation windows, might be infeasible or at least cost-intensive. For instances where a minimal axial dispersion is beneficial for the reaction performance, an ideal reactor vessel can be imagined in which direct application of the optimal control trajectories is possible without prior constructional adjustments while simultaneously sharing the low axial dispersion of plug flow reactors. One reactor type which addresses all of these requirements is the repeatedly, i.e., periodically, operated semibatch reactor (RSBR). In the RSBR concept, a classical SBR is integrated into a continuously operated process. This is achieved by interfacing the SBR to the rest of the process via two buffer tank vessels, one prior to the SBR and one after the reactor vessel. In addition to fresh substrate, the feed buffer tank receives recycles streams from the continuous part of the process to feed the SBR as soon as a new process cycle commences. After the reaction, the reaction mixture is then transferred to the flash buffer tank from which the continuous (downstream) process is operated. This allows for the continuous operation of the entire process while the SBR is operated periodically in cycles. One major advantage of this concept is the capability of directly applying (optimal) control profiles, like temperature, pressure and dosing profiles, in time in contrast to the axial reactor dimension as it is the case for

classical, continuously-operated reactors with minimal axial dispersion like PFRs or DSRs. Without any prior introduction to the example process, the curious reader can find a schematic representation of a process with the RSBR concept in fig. 5.1.

Chapter Overview. This chapter explores the utilization of a RSBR for the hydroformylation of 1-dodecene and is based on the works from Rätze et al. [Rät+19], Jokiel et al. [Jok+19], and Jokiel [Jok20] in addition to Kaiser et al. [Kai+17] who derived a fully continuous and a periodically operated hydroformylation processes using the EPF methodology. In section 5.2, the design of the RSBR process is summarized and advantages of the reactor concept are provided which justify its further investigation. Before the experimental evaluation of the reactor concept is given greater attention to in section 5.4, section 5.3 discusses the formulation of a dynamic process model which is able to consider special traits and requirements of the RSBR. This dynamic process model is verified using a steady-state equivalent in section 5.4.1 alongside the identification of the time required to achieve cyclic steady-state (CSS). The subsequent proof-of-concept experimental investigation with and without dodecene isomer recycle is discussed in section 5.4.2 and compared to the model predictions before a second experimental study evaluates the potential of the RSBR process by optimally controlling the SBR and CSTR in section 5.4.3. Finally, this chapter concludes with a summary and outlook in section 5.5.

5.2 Process Design

Optimal Control Profiles. Kaiser et al. [Kai+17] applied the EPF methodology to the hydroformylation of 1-dodecene in a DMF/decane TMS to identify optimal reactor networks w.r.t. the selectivity toward the linear aldehyde while maintaining high conversion. It was found that two consecutive reaction zones are required for optimal operation in which the first reaction zone combines pronounced dynamic temperature and gas composition profiles with the requirement for low axial dispersion. In the second reaction zone, high temperature coupled with high axial dispersion and elevated hydrogen pressures boost the process performance by allowing backwards isomerization of the previously formed dodecene isomers. For ease of reference, the reaction network which resembles the one from Jörke et al. [Jör+17] can be found in fig. B.1 of appendix B.4 alongside the corresponding reaction kinetic model from Hentschel et al. [Hen+15].

Reactor Network Candidates. The control profiles of both reaction zones were approximated and associated with ideal reactor units, thus forming optimal process candidates. For the first reactor-network candidate, classical continuous reactors units are employed. While the second reaction zone can be approximated easily via a CSTR which fits all the requirements, the dynamic control trajectories of the first reaction zone can be approximated via a DSR with a temperature profile and continuous dosing of CO and H_2 over the reaction coordinate. Alternatively, the control profiles can be realized using the SBR of the RSBR concept which is interconnected with the continuously-operated CSTR and subsequent process units via a downstream buffer tank (Dbuffer). The upstream (feed) buffer tank (Ubuffer) prior to the SBR is used to terminate and store make-up streams and recycle loops from the downstream process until the next process cycle is initiated. These recycle loops include (i) the polar, catalyst-rich phase from the TMS separation in the decanter and (ii) the distillate stream of the distillation column which contains unconverted substrates and the non-polar solvent. A process cycle is started by transferring the liquid hold-up from the Ubuffer to the SBR and dosing fresh substrate. Thus, the two buffer tanks allow for the continuous operation of the overall process while the SBR is operated in a periodic manner, forming a RSBR. A simplified flowsheet of the RSBR process concept is depicted in fig. 5.1.

RSBR Characteristics. In spite of additional coordination effort for synchronizing the RSBR with the continuous process part as well as the additional time required to periodically fill and empty the SBR, this process concept can be realized using off-the-shelf process units while simultaneously achieving the absence of axial dispersion and a close-to-ideal realization of all control profiles including temperature, pressure, and dosing of various species. Besides its rapid dimensioning and construction, the RSBR process excels at enabling a flexible process operation as control profiles can be adjusted on a per-cycle basis to counteract fluctuations in the (renewables') feed quality or to drive the plant into a different operating point. All of these benefits justify a more detailed look into the operation of a RSBR process and its prediction via detailed simulations and optimizations. This includes the investigation of the start-up behavior of such a process to identify the time required to achieve the (cyclic) steady-state and a stable operation. Therefore, the next section is dedicated to the methodological approach to formulate a dynamic process model of the RSBR hydroformylation process.

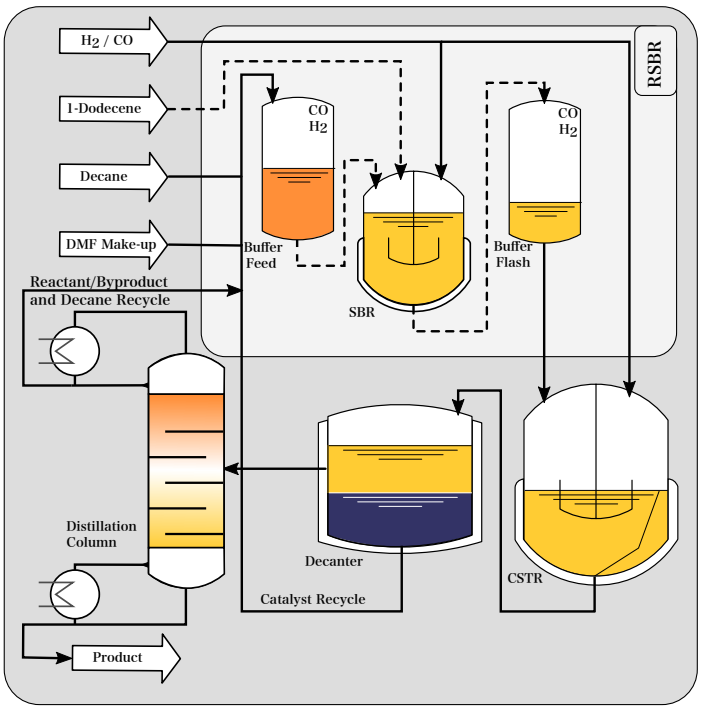

Fig. 5.1.: Simplified process flowsheet for the hydroformylation of 1-dodecene in a DMF/decane TMS as proposed by [Kai+17]. Two recycle loops ensure the retention of the homogeneous rhodium catalyst and its BiPhePhos ligands (decanter) in addition to the recovery of unconverted substrates (distillation column). The process concept contains a periodically operated SBR which is connected to the continuous overall process via two buffer tanks, forming a RSBR. The second reaction zone is formed by a CSTR. Solid and dashed lines represent continuous and periodic streams, respectively. Adapted from Rätze et al. [Rät+19].

5.3 Methodological Approach

The operation of a SBR in a continuous overall process requires repeated filling and emptying of the SBR to initiate a new process cycle. Simultaneously the new process cycle marks the feed of the second part of the process including additional reaction stages and the downstream process. This transfer of the reaction mixture from one process vessel to the next causes delays which need to be accounted for in the total residence time of the process to achieve comparability to alternative process configurations. In the remainder of this chapter, the total residence time refers to the total residence time of the reaction section since no kinetic information on the separation units are available. Figure 5.2 provides a visual representation of the concentration profiles of a generic substrate and product in the SBR for multiple, consecutive process cycles. Besides the expected conversion of substrate to the desired product, time periods with stagnating product concentrations are observable. In each of these periods, the liquid hold-up of the SBR is transferred to the Dbuffer

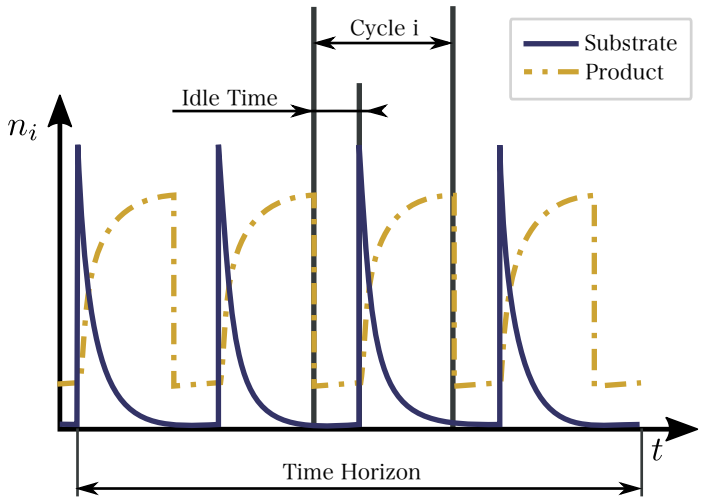

Fig. 5.2.: Visual representation of a cyclic SBR operation including a preparation time for filling and emptying of the reactor vessel. This preparation time is denoted as *Idle Time*. Adapted from Rätze et al. [Rät+19].

so that the hold-up in the Ubuffer can be transferred to the SBR in a subsequent step. During this process, no fresh substrate is added to the SBR which leads to either stagnating concentrations or less pronounced concentration profiles due to residual amounts of substrate present in the recycle streams. The elevated product concentrations during this idle time occur due to crossmixing of the product in the polar phase of the decanter.

Handling of Discontinuities. Creating a process model which describes multiple process cycles over a specified time horizon is challenging as non-smooth transitions in the state variables occur during the filling/emptying of the SBR and the feed of fresh substrate. If state-of-the-art numerical, gradient-based solvers are applied, the DOP needs to be reformulated to a NLP by discretizing the time horizon. However, these non-smooth transitions require attention as discontinuities negatively impact the convergence toward the optimal solution. Numerous strategies can be found in the literature which range from the introduction of integer variables alongside the application of specialized solvers over formulations like generalized disjunctive programming (GDP) to smoothing functions such as sigmoidal approximations or complementarity constraints [BRB08]. While the utilization of integer variables leads to MINLPs with considerably higher problem complexity [BB09], the application of complementarity constraints requires the careful design of the optimization problem and selection of an adequate solver or algorithm due to the violation of the linear independency constraint qualification (LICQ) at each feasible point of the resulting problem [BRB08]. Fortunately, it is possible to formulate the dynamic RSBR

model as a sequence of optimization problems whose scope is limited to one process cycle only. This decomposition enables further reformulation, which is discussed in the next paragraphs, so that all non-smooth transitions can be removed from the optimization problem. Eventually, this leads to the solution of a sequence of regular, smaller sized NLPs instead of one large-scale DOP. However, this comes at the expense of more complex process constraints which need to be fulfilled in subsequent process cycles but require adjustment of the control variables in previous cycles. Examples for this kind of constraints include the specification of a desired product yield, conversion or selectivity after a specific number of process cycles and the fulfillment of volume requirements or species composition ratios in the SBR and decanter, respectively, which can be influenced primarily via the make-up stream of the previous process cycle.

Problem Decomposition. One possible formulation of the optimization problem for one process cycle is exemplified schematically in fig. 5.3. In this and the subsequent paragraph, the decomposition of one process cycle into three stages is presented which serves as a high-level overview over the functionality of the dynamic RSBR process model. For a detailed mathematical formulation of the model, the reader is referred to appendix H.9.2.

Before commencing the model overview, a convention is necessary to simplify the notation when referencing a specific process cycle:

> A new process cycle i always starts at the SBR when the liquid hold-up of the Ubuffer is transferred to the SBR vessel. If no hold-up is present in the Ubuffer as it is the case during start-up, the addition of the fresh reaction mixture marks the beginning of the process cycle. Under regular operating conditions, the SBR and the continuous part of the process operate simultaneously. While the SBR operates on the reaction mixture of process cycle i, the reaction mixture of cycle $i-1$ is processed in the continuous part.

In addition to the cycle convention, three distinct stages can be identified in the schematic process flowsheet—the *Idle*, *Reaction* and *Continuous* stage. Even though only one physical SBR is present in the process model, it is beneficial to separate the preparation phase of the SBR from the actual reaction inside the SBR for two major reasons: First, by separating the *Idle* stage of the SBR into its own optimization problem, no smoothing formulations need to be introduced to model the discrete dosing of fresh substrate. Secondly, this reduces the size of the optimization problem further since no controls are available during the *Idle* stage. Consequently, solving

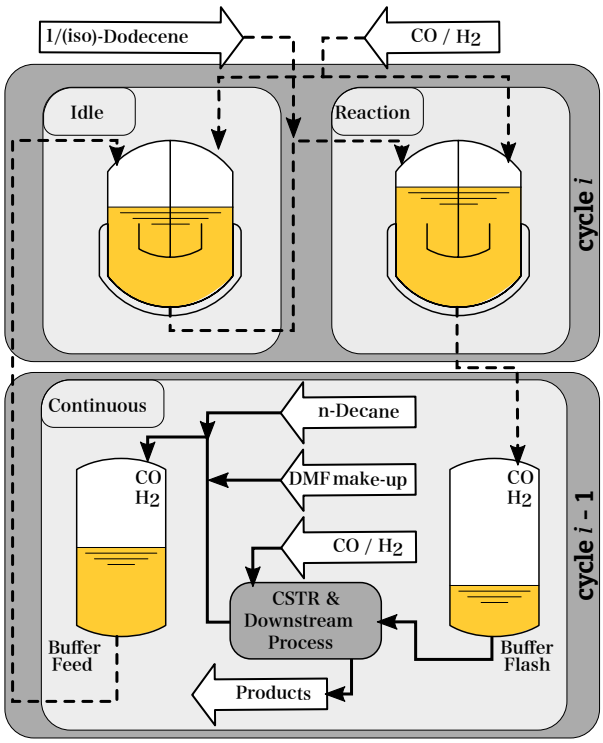

Fig. 5.3.: Schematic representation of the three-stage implementation of the dynamic, cycle-based RSBR process model. The SBR is modeled as two separate stages—*Idle* and *Reaction*. While the *Idle* stage minorly contributes to the reaction progress due to only residual substrate concentrations from the recycling streams and the comparatively short preparation time, the *Reaction* stage is initiated by the dosing of fresh substrate. When new substrate is processed in the *Idle* and *Reaction* stage in cycle i, the continuously operating process part operates on the reaction mixture from cycle $i-1$. Solid and dashed lines represent continuous and periodic streams, respectively. Adapted from Rätze et al. [Rät+19].

the *Idle* stage separately from the rest of process cycle which includes the *Reaction* stage of the SBR and the *Continuous* stage in its own optimization problem improves the numeric convergence properties and stability without any loss of generality.

Problem Formulation. Due to the absence of decision variables in the *Idle* stage optimization problem, it can be solved by computing an initial value problem via integration instead of employing optimization solvers. In its optimization problem formulation, the *Idle* stage model can be found in eq. (H.30) in appendix H.9.2. The *Reaction* and the *Continuous* stage are combined in one optimization problem which is summarized in eq. (H.31) in the same appendix. In its formulation, eq. (H.31) contains all process units which are depicted in fig. 5.1 while considering all available DoF of the SBR and CSTR for optimization. For the interested reader, detailed information on the process unit models can be found in the appendices H.1 to H.7.

This optimization problem for the *Reaction* and the *Continuous* stage serves as a template as it is adjusted in the next sections w.r.t. the available DoF and process structure to fit specific requirements for the validation of the process model and the experimental evaluation. However, independent of the concrete formulation of the *Reaction* and the *Continuous* stage optimization problem, solving multiple process cycles with the RSBR model requires a repeated computation of both optimization problems according to algorithm 3 in appendix H.9.2.

Section Summary. In summary, the dynamic RSBR model comprises two optimization problems, one for the *Idle* and one for the *Reaction* and *Continuous* stage. Combined, both optimization problems describe one process cycle in which the reaction mixture enters the SBR vessel and terminates either in the bottom stream of the distillation column or in the Ubuffer vessel as recycles. The repeated evaluation of these optimization problems with initial conditions adjusted to the respective previous process cycle enables the simulation and optimization of the dynamic behavior of a RSBR process including the start-up and shutdown behavior as well as the responses to fluctuations in multiple process inputs.

5.4 Results

In this section, the RSBR process is simulated for multiple operating conditions. After performing a model verification with the help of a steady-state model equivalent, the impact of the RSBR on the process performance is studied computationally and experimentally in two steps. In a first step, the constructional changes by the addition of the RSBR are evaluated in terms of substrate conversion and product selectivity in reference to an existing hydroformylation process from Dreimann et al. [Dre+16b]. For the sake of a fair comparison, the total residence time of the RSBR process is adjusted to match the residence time of the reference process. Consequently, the benefit of utilizing different zones of axial dispersion is evaluated even though the full potential of the RSBR in the form of optimized temperature, pressure, and gas composition profiles is not exhausted. In the second step, the potential of the RSBR hydroformylation process is investigated by adjusting the total residence time and enabling optimal control parameters and trajectories. At this point, it needs to be mentioned that all experimental investigations were primarily performed and published by Michael Jokiel and collaborators [Jok+19; Jok20].

5.4.1 Model Verification and Dynamic Insights

Before employing the dynamic RSBR model for determining suitable operating conditions and controls, a model verification is necessary to identify if the CSS of the dynamic model represents a valid operating point and converges to the same solution as a comparable steady-state RSBR process model. Such a validation is a valuable investment since the steady-state model is less complex and, consequently, easier to solve numerically. One example for this steady-state model can be found in eq. (H.29) in appendix H.9.1 with its dynamic counterpart described in eqs. (H.30) and (H.32) in appendix H.9.2. Please note that the operating point used for this model verification is not directly comparable to the reference process from Dreimann et al. [Dre+16b] since the total residence time exceeds 375 min in contrast to the 210 min due to a fixed batch time $t_{\mathrm{SBR}} = 60\,\mathrm{min}$ and idle time $t_{\mathrm{idle}} = 30\,\mathrm{min}$. This total residence time is calculated according to

$$\tau_{\mathrm{total}} = t_{\mathrm{idle}} + t_{\mathrm{SBR}} + \tau_{\mathrm{CSTR}} + \tau_{\mathrm{Dbuffer}}, \tag{5.1}$$

with the residence time in the CSTR and Dbuffer following

$$\tau_{\mathrm{CSTR}} = \frac{V_{\mathrm{Liq}}^{\mathrm{CSTR}}}{\dot{V}} = \frac{\phi_{\mathrm{Liq}}^{\mathrm{V,CSTR}} V^{\mathrm{CSTR}}}{\dot{V}}, \tag{5.2}$$

$$\tau_{\mathrm{Dbuffer}} = \frac{0.5 V_{\mathrm{Liq}}^{\mathrm{SBR}}(t = t_{\mathrm{SBR}}^{\mathrm{f}})}{\dot{V}} \overset{\rho=\mathrm{const.}}{\approx} \frac{0.5 \phi_{\mathrm{Liq}}^{\mathrm{V,SBR}} V^{\mathrm{SBR}}}{\dot{V}}, \tag{5.3}$$

with $\phi_{\mathrm{Liq}}^{\mathrm{V},j} = V_{\mathrm{Liq}}^{j}(V_{\mathrm{Liq}}^{j} + V_{\mathrm{Gas}}^{j})^{-1}$. The Dbuffer is included in the calculation as it represents an additional reaction zone due to elevated temperatures to prevent separation of the TMS components. However, no gas dosing and stirring is available in the buffer tanks which is considered in the buffer tank models via adjusted gas-liquid mass transfer coefficients. The factor 0.5 used in the Dbuffer residence time calculation represents a heuristic factor to account for the residence time distribution of the reaction mixture due to the continuous depletion of the liquid hold-up. For the correct operation of the RSBR without any accumulation of reaction mixture in one of the buffer tanks from cycle to cycle, the clock time of the *Continuous* stage needs to suffice

$$t_{\Sigma} = t_{\mathrm{SBR}} + t_{\mathrm{idle}}, \tag{5.4}$$

to empty the Dbuffer to a residual liquid hold-up $V_{\mathrm{Liq,min}}^{\mathrm{Dbuffer}}$. This constraint is also present in each steady-state and dynamic optimization problem in appendix H.9.

Conversion and Selectivity Comparison. The results of the steady-state and dynamic model comparison are summarized in fig. 5.4a. While fig. 5.4a depicts the conversion

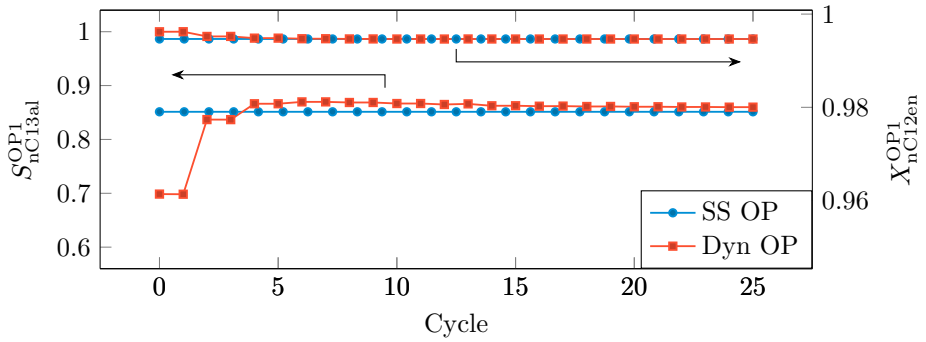

(a) Steady-state and dynamic process model conversion and selectivity. The steady-state conversion and selectivity are extended over all process cycles for easier reference.

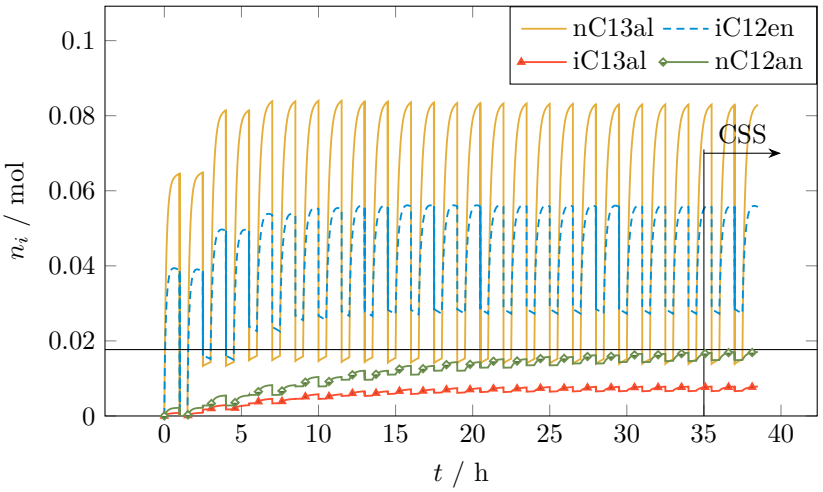

(b) Molar amount profiles of selected species in the SBR including the *Idle* and *Reaction* stages. The cyclic steady-state (CSS) is marked.

Fig. 5.4.: Optimization results of the RSBR model. The steady-state data represents the solution of eq. (H.29) while the dynamic data is achieved by solving eqs. (H.30) and (H.32) repeatedly for 25 cycles.

of 1-dodecene and the selectivity toward the linear aldehyde n-tridecanal (nC13al) of both models according to eq. (H.26) in appendix H.8, fig. 5.4b contains information regarding the molar amount profiles for the major species in the SBR over 25 simulated process cycles. Because of the simulation of the RSBR start-up using the dynamic model, no recycle streams in the first two process cycles are available which limits the product selectivity to approximately 70 % while nearly complete conversion of the substrate is achieved with 99.6 %. As soon as dodecene isomers are recycled over the distillate stream, the selectivity increases dramatically up to 87 % with a minor loss in conversion. The impact of the isomer recycle can also be

observed clearly in the concentration profiles where the tridecanal amount increases significantly alongside the dodecene isomer amount. It is clear that the increase in selectivity cannot be attributed directly to higher tridecanal concentrations due to the significant share of tridecanal in the recycle of the polar phase from the decanter. Instead, less dodecene isomers are formed from the substrate due to a reduced driving force toward the isomerization equilibrium, leading to a better utilization of the available residence time in the SBR and CSTR to produce the desired linear aldehyde. This leads to a selectivity and conversion after 25 process cycles of 86 % and 99.5 %, respectively, in contrast to a selectivity of 85.2 % at the same conversion for the steady-state model. The negligible difference in selectivity can be explained by the higher degree of detail of the dynamic model, especially w.r.t. the buffer tank models. Consequently, this accurate agreement of dynamic and steady-state model results validates the dynamic model.

Convergence to Cyclic Steady-State. When taking a closer look at the molar amount profiles in fig. 5.4b, multiple interesting details attract attention. Rigorous consideration of the *Idle* stage is advisable despite the absence of fresh substrate in the reaction mixture because of the continuing conversion of recycled dodecene isomers primarily toward the linear tridencanal. A second aspect involves the concentration profiles of branched aldehydes (iC11al) and the hydrogenation product dodecane (nC12an). Both byproducts accumulate slowly over the considered time horizon due to the decanter and distillation column recycles. While the branched aldehydes achieve static profiles after approximately 25 h, dodecane requires over 35 h to approach a stable level. Therefore, this is also the time which the RSBR process requires to achieve cyclic steady-state (CSS). It is important to note that solving the *Reaction* stage of the SBR together with the *Continuous* stage in one optimization problem is mandatory for the CSS to be achieved. In the *Continuous* stage, the gas composition in the CSTR as well as the make-up streams are calculated which determine the composition and the amount of the reaction mixture in the Ubuffer for the next cycle. Both information are important to prevent an overfilling of the SBR and to achieve a successful TMS separation in the decanter in the consecutive process cycle. The combined solution of the *Reaction* and *Continuous* stage introduces additional DoF for the optimizer in the form of temperature, pressure, and gas composition profiles in the SBR which simplifies the fulfillment of all volume and species ratio constraints.

When considering that the major cause of the prolonged start-up time is the distillate stream which recycles the majority of the hydrogenation product, equivalent, continuously operated reactor concepts would exhibit a comparable or even higher start-up

time to reach a steady-state due to limited DoFs. Therefore, the RSBR process only inherits the characteristics and limitations of the downstream process and does not represent the bottleneck for the start-up time in industrial applications.

5.4.2 Experimental Comparison

After its verification, the dynamic RSBR model can be employed to estimate species streams between different process units, estimate the necessary time to achieve the CSS and split the total residence time between different reaction zones to achieve comparability to other reactor concepts.

Experiment Concept. In a first proof-of-concept experiment, the RSBR process was build in miniplant-scale similar to the setup depicted in fig. 5.1 but without the addition of a distillation column for dodecene isomer recycling. Detailed information about the miniplant construction can be found in Rätze et al. [Rät+19], Jokiel et al. [Jok+19], and Jokiel [Jok20]. Instead of a physical dodecene isomer recycle, a dodecene isomer mixture is fed as make-up stream to simulate the recycle loop experimentally. This allows investigating the effect of the dodecene isomer recycle on the RSBR process in three operating points, OP1, OP2.1 and OP2.2, in which a feed without dodecene isomers and a fixed ratio of 1-dodecene to dodecene isomers is supplied to the process, respectively. Both, OP2.1 and OP2.2, only differ in terms of the 1-dodecene to isomer ratio. In all operating points, a total residence time of 210 min is set to ensure the comparability of the newly developed reactor concept to the miniplant setup from Dreimann et al. [Dre+16b] which serves as a reference process. This total residence time needs to be allocated to the reaction sections according to eq. (5.1) under consideration of eqs. (5.2) and (5.3). While the idle time t_{idle} is fixed by the operating staff, eqs. (5.2) and (5.3) depend on the volume flow $\dot{V}$ which can be calculated via

$$\dot{V} = \frac{V_{\mathrm{Liq}}^{\mathrm{SBR}}(t = t_{\mathrm{SBR}}^{\mathrm{f}})}{t_{\Sigma}} \overset{\rho=\mathrm{const.}}{\approx} \frac{\phi_{\mathrm{Liq}}^{\mathrm{V}} V^{\mathrm{SBR}}}{t_{\Sigma}}, \tag{5.5}$$

since the entire liquid hold-up of the SBR is transferred over the Dbuffer into the continuous process part for each process cycle. Reformulation of eq. (5.5) with eq. (5.4) results in

$$t_{\mathrm{SBR}}(\dot{V}) = \frac{\phi_{\mathrm{Liq}}^{\mathrm{V,SBR}} V^{\mathrm{SBR}}}{\dot{V}} - t_{\mathrm{idle}}, \tag{5.6}$$

$$\dot{V}(\tau_{\mathrm{total}}) = \frac{1.5\phi_{\mathrm{Liq}}^{\mathrm{V,SBR}} V^{\mathrm{SBR}} + \phi_{\mathrm{Liq}}^{\mathrm{V,CSTR}} V^{\mathrm{CSTR}}}{\tau_{\mathrm{total}}}. \tag{5.7}$$

Due to the assumption of a constant mixture density in eq. (5.5) which does not hold for strong fluctuations in the SBR (or during start-up as shown in fig. 5.4b), t_{SBR} and $\dot{V}$ are calculated using the dynamic RSBR model. The corresponding optimization problems can be found in eq. (H.33) in appendix H.9.2. For a simplified process operation, the residence times calculated in CSS are used for all process cycles (see table 5.1) with t_{SBR} rounded to 30 min.

Tab. 5.1.: Residence times of different reaction zones for the miniplant operation of the hydroformylation of 1-dodecene RSBR process without simulated distillation column recycle. The residence times in cyclic steady-state are displayed with identical time ratios for OP1 and OP2 [Jok+19].

Process Unit i	τ_i^{CSS}, t_i^{CSS} / min
Idle	30.00
SBR	28.71
DBuffer	31.35
CSTR	119.93
$\sum$	210.00

The conversion and yields of major products and byproducts are visualized over the plant operation time in fig. 5.5 with the corresponding steady-state values summarized in table 5.2. In both cases, the experimental measurements and model predictions are shown for comparison. Please note that the experimental investigations were performed by Michael Jokiel, Jan-Peter Hollenbeck, Kai U. Künnemann and Jens M. Dreimann [Jok+19]. Before going into detail on the process performance in each operating point, special attention needs to be paid to the definition of conversion, yield, and selectivity in both, figs. 5.5a and 5.5b. While it is possible to calculate the conversion and product yields with 1-dodecene as reference substrate, this is not possible for OP2 due to the additional feed of dodecene isomers for the distillate recycle stream simulation. Due to the elevated dodecene isomer concentrations in the feed and the consumption of 1-dodecene in the hydroformylation, backwards isomerization toward 1-dodecene occurs, leading

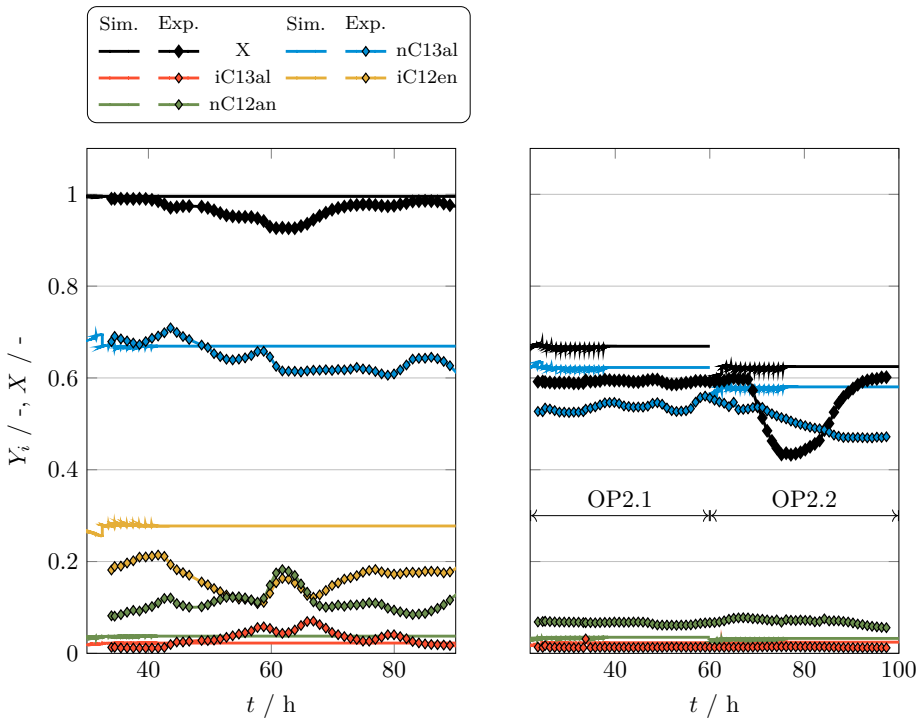

(a) OP1: w/ decanter recycle, w/o distillate recycle

(b) OP2: w/ decanter recycle, w/ simulated distillate recycle

Fig. 5.5.: Experimental and predicted conversion and yields of the substrate, main product and byproducts of a long-term miniplant campaign for the hydroformylation of 1-dodecene. The experimental setup is equivalent to fig. 5.1 without the distillation column and the associated non-polar solvent/dodecene isomer recycle. For the first operating point OP1 (left), the process is operated only with the catalyst recycle from the decanter and the conversion and yield metrics are calculated according to eq. (H.26) in appendix H.8. In operating point OP2 (right), the non-polar recycle from the distillation column is simulated by adding dodecene isomers to the decane make-up stream with the ratios $\phi^{\mathrm{m}}_{\mathrm{iC12en,nC12en}} = 0.5\,\mathrm{g\,g^{-1}}$ (OP2.1) and $0.75\,\mathrm{g\,g^{-1}}$ (OP2.2), respectively [Jok+19]. Here, the performance metrics follow the definition in eq. (H.28).

to an additional substrate source. Consequently, the regular definition of conversion and yield in eq. (H.26) has to be adapted to a combined reference of 1-dodecene and its isomers in eq. (H.28).

Discussion of OP1. In fig. 5.5a, the conversion and yields of the main product and byproducts are displayed for OP1. Strong fluctuations of the performance measures occur during the experiment so that a comparison of experimental and simulated data can only be conducted when considering average values while highlighting changes in the profile trends. When focusing first on unexpected events in the profiles, hour 60 stands out because of a sudden increase in the hydrogenation activity simultaneous

Tab. 5.2.: Experimental and predicted conversion, yield, and selectivity of the substrate 1-dodecene and main product tridecanal for multiple operating points of the 1-dodecene hydroformylation miniplant according to fig. 5.1 without distillation column. The values represent averages over the last 5 h of the respective experiment. The dodecene isomer recycle of the distillation column is simulated in the process model and experimentally by supplying dodecene isomers in the ratios $\phi^{\mathrm{m}}_{\mathrm{iC12en,nC12en}} = 0.5\,\mathrm{g\,g^{-1}}$ and $0.75\,\mathrm{g\,g^{-1}}$ for OP2.1 and OP2.2, respectively. Numbers in parentheses are calculated using eq. (H.28) while all other performance measure follow eq. (H.26) [Jok+19]. Reference process: [Dre+16a].

		Experimental			Model Prediction		
. / %	Ref.*	OP1	OP2.1	OP2.2	OP1	OP2.1	OP2.2
X	84.5	95.1 (80.3)	(59.2)	(59.3)	99.5 (70.7)	99.4 (66.7)	99.3 (62.3)
Y_{nC13al}	62.5	63.2 (64.4)	(53.4)	(47.0)	66.8 (66.0)	78.0 (62.2)	87.1 (57.9)
S_{nC13al}	74.0	66.5 (80.2)	(90.2)	(79.3)	67.1 (93.3)	78.5 (93.2)	87.8 (93.0)

to a drop in the substrate conversion. An increase in the byproduct formation is normally caused by an insufficient concentration of (catalyst) ligands in the reaction mixture. Prior to this abrupt dodecane accumulation, a gradual increase in the branched aldehyde and dodecane concentration in combination with a decrease in the dodecene isomer concentration already hint to this ligand depletion. As a counter measure, the DMF make-up stream was increased after hour 67 since the catalyst and ligand are dissolved in the DMF in a 1:3.3 ratio [Jok+19]. After this adjustment, the trends in the conversion and byproduct yield profiles reverse which validates the assumed lack of sufficient ligands.

Except for this unexpected event, the deviations between experiment and simulation are reasonably small w.r.t. the conversion, n-tridecanal and branched aldehyde yields. Exemplarily, the average experimental product yield of 63.2 % is only 3.6 percentage points lower than the simulated yield of 66.8 %. Strong deviations from the simulated yields are observable for the dodecene isomers and dodecane. The experimental results indicate a strong hydrogenation activity in the reactor which also explains the reduced dodecene isomer concentrations matching the dodecane excess. Possible reasons for these deviations are (i) an imperfect separation in the decanter, (ii) uncertainties in the decanter model, (iii) variations in the gas phase compositions, (iv) a local parameter set or an inaccurate description of the hydrogenation equilibrium for the considered operating point, or (v) a deactivation of the catalyst (central atom and/or its ligands).

Discussion of OP2. The conversion and yield profiles of OP2 are depicted in fig. 5.5b. In terms of the byproduct yields, the branched aldehyde yields are predicted ac-

curately while the dodecane yield is underestimated. Similar to OP1, multiple explanations for this plant model mismatch are available with the deactivation of the catalyst ligand representing the most probable hypothesis. No dodecene isomer yield profile can be found in the figure due to the change of the reference substrate in the conversion and yield definition according to eq. (H.28). The combination of 1-dodecene and its isomers in one pseudo-reference-substrate causes the absence of the dodecene isomer profiles and the overall lower conversion and yield in OP2. Strong deviations between the predicted and experimental conversion and n-tridecanal yield can be found throughout the experiment. When concentrating on the conversion of the pseudo-substrate, a lower experimental conversion is explainable by an either impeded conversion of fresh 1-dodecene or the added dodecene isomers. Assuming similar error sources as in OP1, a possible reason for the larger offset is again a less active catalyst which is not able to perform the backwards isomerization of the additional dodecene isomers in the available residence time to a sufficient degree. A hint supporting this theory can be found in the raw data of the experiment where a significant amount of 1-dodecene is still present at the CSTR outlet. While the simulation predicts a nearly complete conversion of 1-dodecene, the elevated 1-dodecene concentrations in the experiment may be caused by the added dodecene isomers. However, in the case of a low catalyst activity, this backwards isomerization requires more time leading to a limitation of the hydroformylation activity in the later stages of the reactor sequence.

Comparison of OP2.1 and OP2.2. A comparison of OP2.1 with OP2.2 yields interesting results as the conversion and tridecanal yield drops when increasing the amount of dodecene isomers in the feed. This is true for the experiment but also for the simulation and can be expected in cases where the additional dodecene isomers are not converted entirely. However, the significant drop in the combined 1-dodecene and dodecene isomer conversion in the experiment cannot be explained by this effect. Possible reasons for the behavior include (i) a dodecene isomer excess which causes excessive backwards isomerization while the hydroformylation is impeded in the available residence time, (ii) an unstable operating point due to significant adjustments of the feed during process operation, and (iii) an insufficient operation time under OP2.2 conditions to achieve CSS.

Comparison of the RSBR and Reference Process. Direct comparison to the reference process in terms of conversion, selectivity, and yield is only possible for OP1 of the RSBR process due to missing information on the conversion and yield definition as well as the composition and mass flow of the polar recycle stream from Dreimann

et al. [Dre+16b]. In terms of conversion, the RSBR process represents a significant improvement compared to the reference process with an increase of over 10 percentage points at OP1. Even in the case of a slight decrease when closing the dodecene isomer recycle loop, this increase can be mainly attributed to the new reactor setup as predicted by Kaiser et al. [Kai+17]. In terms of selectivity, OP1 is clearly inferior to the reference process with a decrease of about 7 percentage points. This drop in selectivity is caused by the absence of the isomer recycle as the model predictions mirror the experimental selectivity (see table 5.2).

For the second operating point, the experimental drop in performance in OP2.2 cannot be explained by the process model so that OP2.1 is used for comparison. Even though the conversion of 59.2 % appears significantly lower compared to the reference process, this is only due to different conversion definitions. When utilizing the model predictions of 66.7 % as a reference, it can be assumed that the experimental conversion according to eq. (H.26) should exceed 90 %. Similarly, the experimental selectivity can be expected to be around or slightly above the reference value, leading to an overall greater product yield.

These results represent the first experimental validation that the EPF methodology is capable of designing reactor networks with significantly improved performance measures over a comparable reference process.

Summary. In summary, the dynamic model is able to predict the experimental conversion and product yield reasonably in OP1 while the hydrogenation is significantly underestimated. In OP2, larger deviations between model predictions and experimental results occur, especially for the conversion and tridecanal yield. The comparison to the reference process hints at an improved conversion at a comparable or slightly increased selectivity under consideration of recycled dodecene isomers thanks to the RSBR concept.

5.4.3 Optimal SBR Control

With the promising experimental results from the proof-of-concept miniplant setup, the potential of the RSBR is investigated in a next step by identifying optimal controls and control profiles for the SBR and CSTR while simultaneously increasing the total residence time to 300 min as originally intended in the dimensioning [Kai+17]. Similar to the previous studies, no distillation column is available in the experimental setup. Also, no experimental simulation of the isomer recycle is performed due to

the more complex interpretation of the results and the possibility to evaluate the effect of dodecene isomer recycling and optimal control orthogonally.

Optimization Problem. Optimal control of the temperature, pressure, and gas phase composition in the SBR is added to the dynamic RSBR model in eq. (H.34) in appendix H.9.2. In addition to the SBR, the temperature and gas phase composition in the CSTR are considered as additional degrees of freedom. The experience of the operators from previous experiments with the RSBR setup allows for the reduction of the idle time to 20 min which, in addition to the increase in total residence time to 300 min, requires the recalculation of the residence time split between the reaction zones as shown in table 5.3. In comparison to table 5.1, the reduction of the idle time

Tab. 5.3.: Residence times of different reaction zones for the optimally controlled miniplant operation of the hydroformylation of 1-dodecene RSBR process without distillation column [Jok20].

Process Unit i	τ_i^{CSS}, t_i^{CSS} / min
Idle	20.00
SBR	39.20
DBuffer	34.20
CSTR	206.60
$\sum$	300.00

of the SBR directly leads to an equivalent increase in residence time in the *Reaction* stage of the SBR. In order to maintain the mass flow between the Dbuffer and the CSTR identical to the previous experiments at $120\,\mathrm{g\,h^{-1}}$ [Jok20], the constraint on the liquid hold-up in the CSTR needs to be removed. This is due to the increase of the total residence time which requires either lower volume streams or higher liquid hold-ups. While the liquid hold-up in the SBR and Dbuffer cannot be adjusted without replacing the vessels in the existing plant to maintain a sufficiently large gas phase, the CSTR liquid hold-up is increased to 560 mL or 56 % [Jok20] of the total vessel volume, thus increasing the residence time in the CSTR. The impact of the reduced gas phase of the CSTR is negligible because of a less pronounced reaction activity and gas consumption.

Results. The optimized control profiles and the corresponding experimental and simulated product yields are depicted in figs. 5.6 and 5.7, respectively. The control profiles of temperature and gas phase composition in the SBR outline two distinct sections. While the first section contains a characteristic temperature increase together with an elevated CO content in the gas phase, a constant, high

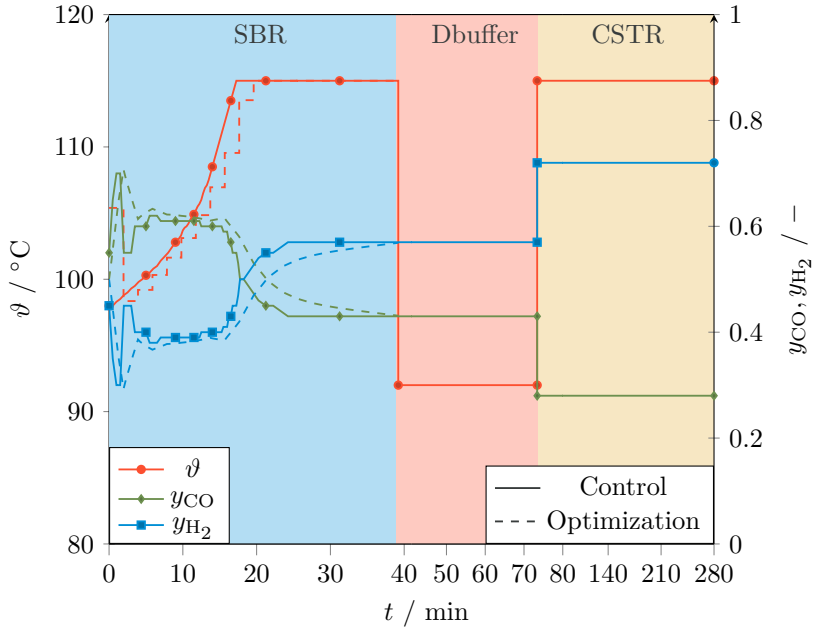

Fig. 5.6.: Optimal temperature and gas phase composition control profiles of the RSBR with subsequent CSTR for the hydroformylation of 1-dodecene. The x-axis refers to the total reaction time. The idle time of 20 min is not displayed. The optimized control profiles are smoothed and shifted 1.5 min to 2.5 min in time to account for the thermal inertia of the thermostat. Adapted from [Jok20]. Gas phase molar fraction bounds: $y^{\mathrm{SBR}}_{\mathrm{CO,H_2}} \in [0,1]$, $y^{\mathrm{Dbuffer}}_{\mathrm{CO,H_2}} = y^{\mathrm{SBR}}_{\mathrm{CO,H_2}}(t_{\mathrm{SBR}})$, $y^{\mathrm{CSTR}}_{\mathrm{CO,H_2}} \in [0,1]$. Temperature bounds: $\vartheta^{\mathrm{SBR}} \in [95,115]\,°\mathrm{C}$, $\vartheta^{\mathrm{Dbuffer}} = 91\,°\mathrm{C}$, $\vartheta^{\mathrm{CSTR}} \in [95,115]\,°\mathrm{C}$.

temperature and hydrogen excess represent typical marks for the second reaction zone (see [Kai+17]). Surprisingly, this second reaction zone is already reached inside of the SBR while Kaiser et al. [Kai+17] originally intended the CSTR to serve as the corresponding reactor vessel. Please note the slight offset in the time domain and the smoothing of the control trajectories in the SBR which were applied in the experiment to account for the time required for the actuators and the thermostat to perform the required operations. After the Dbuffer, which is considered as a reaction zone of minor importance due to the drop in temperature and the absence of gas dosing and mixing, the CSTR mimics the second reaction zone of the SBR but with an even higher hydrogen content of 72 % in the gas phase.

Because of the absence of a dodecene isomer recycle, the yields in fig. 5.7 can be calculated using 1-dodecene as reference substrate. Thus, direct comparison to OP1 in fig. 5.5a of the proof-of-concept experiment is possible. In this experimental campaign, the conversion and all experimental yields are predicted with high accuracy. In terms of experimental yields, optimally controlling the SBR and CSTR and adjusting the total residence time increases the product yield from 63.2 % in OP1 to

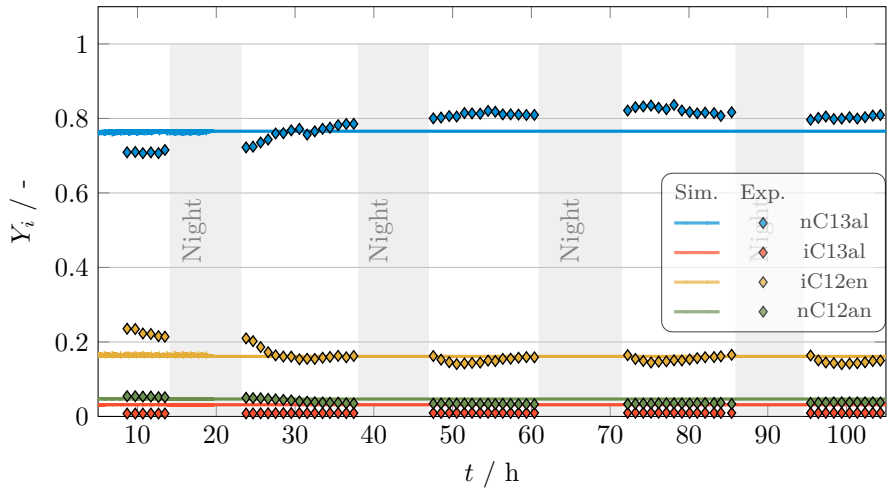

Fig. 5.7.: Experimental and predicted yields of the main product and byproducts of a long-term miniplant campaign for the hydroformylation of 1-dodecene with optimally controlled SBR and CSTR. The experimental setup is equivalent to fig. 5.1 without the distillation column and the associated byproduct recycle. The yields are calculated according to eq. (H.26) in appendix H.8. All pumps are stopped over night, leading to the gaps in the yield profiles.

80 % which represents a significant step in process performance. While the dodecane concentration in OP1 significantly exceeded the simulated results, dodecane as well as the dodecene isomer yields are accurately predicted in the optimized setup, leading to an overall quantitative representation of the experiment by the dynamic RSBR model. Consequently, the hypothesis of inaccurate reaction kinetics leading to an underestimation of the hydrogenation activity is less likely in contrast to the possibility of experimental uncertainties, such as oxidation of the ligand, influencing the proof-of-concept experimental campaign from section 5.4.2.

Conclusion. The dynamic RSBR model is able to identify control trajectories and optimal operating conditions for the SBR and CSTR which lead to a significant increase in product yield while simultaneously ensuring full conversion of the substrate. Additionally, applying these control trajectories experimentally in miniplant-scale validates the process model by yielding concentrations profiles which match the predictions quantitatively.

5.5 Chapter Summary and Outlook

Summary. This chapter exemplifies the translation of optimal control profiles from calculations using the EPF methodology to an optimal reactor setup for the hydro-

formylation of 1-dodecene. In particular, a repeatedly operated semibatch reactor (RSBR) which utilizes two buffer tanks to interface a discontinuously operated SBR to a continuous overall process. The additional effort required to operate this process type is accompanied by significant potential in terms of construction costs (off-the-shelf vessels), optimal control and flexibility in process operation.

Process design and operation requires accurate knowledge over expected mass flows and the time required to achieve the cyclic steady-state. Therefore, a detailed, dynamic RSBR model is developed and verified w.r.t. plausibility using a comparable steady-state model. Under consideration of all recycle loops, the cyclic steady-state is reached after 35 h under ideal conditions, providing valuable information for the experimental validation.

A first, proof-of-concept operation with heuristically chosen control parameters is performed with promising results w.r.t. the expected conversion and product selectivity. Byproduct yields exceed the expected margin of error between simulation and experimental results so that only qualitative predictions are possible. However, in the scope of all presented investigations, strong indications are present that these deviations are caused by experimental issues and do not stem from model weaknesses.

An experimental campaign with optimized control trajectories and parameters for the SBR and CSTR with adapted residence times is performed to identify the experimental potential of the RSBR process. With the dynamic RSBR model providing the necessary residence time for each process unit and the optimal trajectories, experimental results are achieved which not only match the predicted yields but also proof the superiority of the RSBR setup over the reference process by increasing conversion and yield over 15 and 17 percentage points, respectively, even without recycling of the dodecene isomers. These results represent the first experimental validation of the capabilities of the EPF methodology to design optimal reactor networks with superior performance measures.

For a concise overview of the results in this chapter, fig. 5.8 contains all predicted and experimentally verified conversions, product yields and selectivities from this chapter in addition to reference points such as the reference process from Dreimann et al. [Dre+16b] and the calculations using the EPF methodology from Kaiser et al. [Kai+17].

Outlook. The RSBR represents an interesting concept for non-conventional process operation due to its use of off-the-shelf reactor vessels, fast construction, the complete

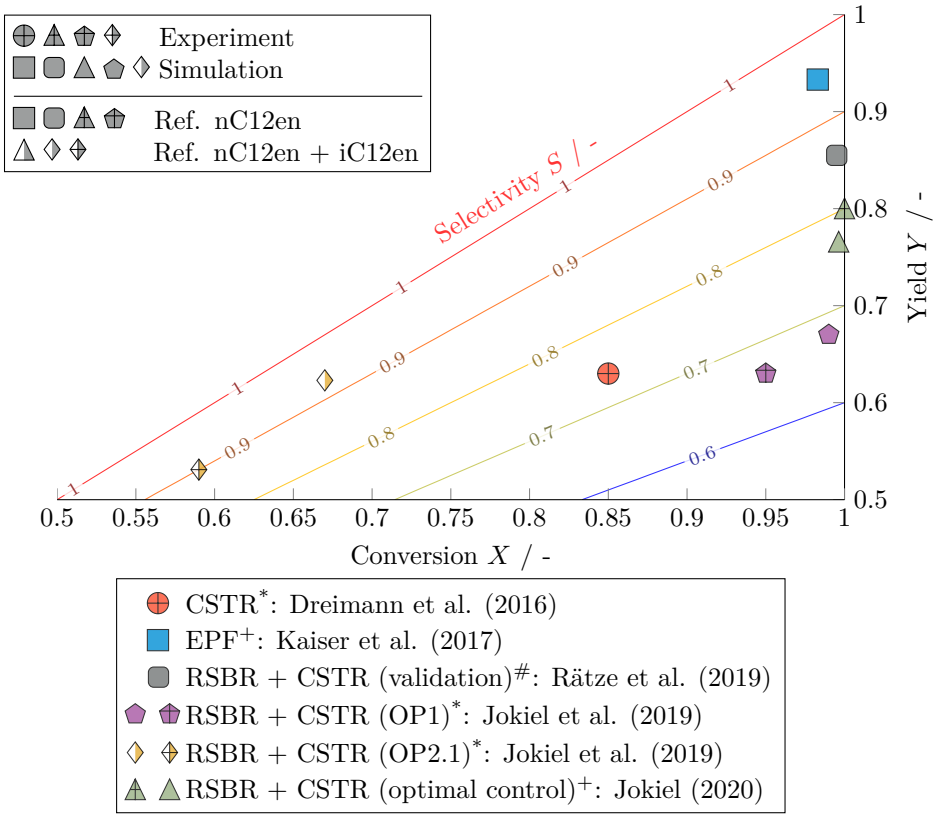

Fig. 5.8.: Conversion-Yield-Selectivity diagram containing multiple process configurations and operating conditions for the hydroformylation of 1-dodecene. All experimental results are marked with plus signs in the corresponding marks in contrast to their simulative counterparts. Depending on the measurement setup, the conversion and yield are either calculated based on the 1-dodecene concentration according to eq. (H.26) or the combined concentrations of 1-dodecene and dodecene isomers with eq. (H.28). The latter data points are marked with half-filled marks. Data points from process configurations with 210 min, 300 min and 375 min total residence times are indicated with $\square^{*}$, $\square^{+}$ and $\square^{\#}$, respectively. Adapted from [Jok20].

absence of axial dispersion, the possibility to apply not only temperature and pressure but also dosing profiles over time and its flexibility to account for fluctuations in the substrate quality, changes in the residence times or even the application in multi-purpose plants while maintaining the possibility for providing optimal control profiles for each operating point. Downsides of the RSBR setup include a more complex process operation to handle all transitions of the reaction mixture from one vessel to the other, reduced space-time-yields as well as limitations in terms of process upscaling. For the latter aspect, a numbering-up, where a greater number of SBRs are employed which operate in parallel to supply the continuous process part, is conceivable [Jok20]. However, before its application in production plants,

further investigations of the RSBR are recommendable. The following list contains some ideas for future research:

- **Online Control.** With the dynamic RSBR model presented in this work, it is possible to perform online calculations of the optimal control profiles if accurate measurements w.r.t. the concentrations in the recycle streams are available. Besides additional improvements of the conversion and product selectivity, the process model enables process monitoring and, ultimately, model predictive control. In addition to this application, further investigations w.r.t. observability, controllability and stability of such a process are necessary.

- **Alternative Reactions.** The presented process for the hydroformylation of 1-dodecene in a TMS represents only one example for the successful application of a RSBR. Investigations of this process concept for alternative reactions in different solvent systems are necessary to substantiate the findings from this work. In an ongoing and currently unpublished joint-work together with Volodymyr Kozachynskyi, Karsten L. Duch and Markus Illner and Jens-Uwe Repke from TU Berlin, the RSBR is implemented in a miniplant for the reductive amination of 1-undecanal, a subset of the HAM reaction network, in a micellar emulsion system (MES). With the optimal control profiles from an online variant of the dynamic RSBR model, initial results indicate a conversion, yield, and selectivity of 79.2 %, 57.2 % and 71.0 %, respectively, over a comparable conventional process with a CSTR and performance measures of 70.5 %, 34.0 % and 48.4 % at an identical total residence time. In addition to these encouraging results, changing the operation mode of the MES-based process from continuous to a cyclically-operated variant has two additional advantages. Besides the removal of unnecessary buffer vessels which increases the space-time-yield, the decanter operation is simplified, leading to a more robust process operation. These findings inspire further applications using the RSBR concept in the future.

- **Additional Optimization Potential.** While the RSBR is able to significantly improve the performance through advanced process control, additional optimization potential should be explored by considering the complete process flowsheet including the reactors as well as separators. By following this idea from process sytems engineering, the investigated hydroformylation process could be envisioned using an extraction instead of a TMS for catalyst recovery since the reaction can be performed in the polar solvent DMF alone. With the use of dodecane—a byproduct in the reaction network—as extraction agent and an alternative connection of the recycle streams, selectivities of

over 83 % at 97 % conversion (steady-state process simulation using the hydroformylation kinetics from Hentschel et al. [Hen+15] and the Kriging model from McBride et al. [MKS17]) are achievable with a CSTR as a single reactor vessel. However, these results assume the same reaction kinetics from eq. (B.2) so that additional research is necessary to validate the existing or identify suitable reaction kinetics for such promising process candidates and operating conditions.

6 Conclusions

6.1 Summary

In the present work, three major steps in the synthesis of chemical production processes are examined to provide methodological contributions which aid in the design of innovative, efficient, and flexible process variants for the transition toward a sustainable chemical industry. Achieving this improved sustainability in chemicals production requires the utilization of alternative, biomass-based raw materials instead of further relying on fossil resources. However, this transition of feedstock cannot be considered in an isolated fashion as the feedstock heavily influences the general conditions and requirements for the production process. Established processes are unable to cope with the new requirements like increased hydrocarbon chain lengths, functionalized substrates and fluctuating feedstock qualities. Therefore, new processes need to be developed which are able to meet these requirements. In order to facilitate the design of such processes, this work takes a holistic view on the process design task and applies the methodological contributions to the industrially relevant, homogeneously rhodium-catalyzed hydroaminomethylation in a liquid multiphase system under transient conditions for catalyst recovery as an example process. Following the idea of systematic and informed decision making, model-based approaches are used in each step of the design process which encompasses (i) the model-based identification of reaction kinetic models, (ii) the conceptual, model-based design of reactor- and reactor-separator network candidates and (iii) the translation of reactor network candidates into high-performance production processes alongside their subsequent operation.

Model-Based Kinetic Model Identification

Despite the availability of a preliminary reaction kinetic model for the hydroaminomethylation of 1-decene in a methanol/dodecane thermomorphic multiphase system (TMS), the influence of water on the reaction and the behavior of the reaction under edge operating conditions was not yet investigated. To improve the reaction kinetic model for the application in process design and operation, preliminary parameter sensitivity studies are performed to enable the application of model-based optimal

experimental design (mbOED) for parameter identification. In mbOED, a (dynamic) optimization problem is formulated and solved using a reaction kinetic model of the investigated reaction system. The goal of this task lies in the identification of operating conditions and control profiles which maximize the information content of a set of designed experiments. Major achievements regarding the design of experiments include

- the rigorous incorporation of phase equilibrium calculations and monophasic constraints to successfully prevent the formation of an aqueous phase which leads to mass transfer limitations and the separation of catalyst and reactant in different phases,
- the formulation of a PC-SAFT-based artificial neural network (ANN) to reliably and efficiently predict the activity coefficients during optimization for all species of the hydroaminomethylation reaction system,
- the consideration of experimental limitations in the experimental design, including feasible rates of temperature and pressure change as well as the minimal time interval between and the total number of measurement points, to facilitate the applicability in the laboratory,
- the formulation of a multi-step initialization algorithm to aid in the identification of suitable initial guesses to prevent local optima in complex, large-scale mbOED problems for the simultaneous design of multiple experiments,
- the identification of non-intuitive yet interpretable control profiles for five experiments and the association of their importance for the accurate prediction of one or more model parameters.

In addition to these conceptual achievements, the identified optimal experimental designs were applied in laboratory experiments. In combination, the experimental designs and experiments enabled

- the identification and correction of a mismatch between experimental setup and reactor vessel model via the implementation of a rigorous gas phase model,
- the structural extension of the catalyst pre-equilibrium w.r.t. the inhibiting effects of high CO and low H_2 concentrations,
- the model calibration with a set of identifiable parameters which enables the quantitative reproduction of the experimental concentration profiles for a broad operating window.

In all cases, the achievements are critically discussed and remarks w.r.t. limited model applicability and assumptions are provided.

Multiphase Elementary Process Functions Methodology

Model-based process design is able to systematically identify process configurations which are optimal w.r.t. one or more predefined objective functions. In contrast to other model-based process design approaches, the elementary process functions (EPF) methodology is able to design processes without adhering to the combination of known process units. This is achieved by formulating a dynamic optimization problem in which species, heat, and energy fluxes can be controlled to identify an optimal path of a Lagrangian fluid element through thermodynamic state space. This optimal path or rather the underlying optimal control profiles can be interpreted using the flux profile analysis (FPA) and yield promising process candidates for in-depth assessment.

Previous implementations of the EPF methodology primarily rely on reaction kinetic information for the process design. Depending on the reaction system, this may not be sufficient as neglected physical and/or chemical phenomena either lead to infeasible process candidates or sub-optimal operating modes. For liquid reaction systems, the incorporation of thermodynamic information represents a valuable addition as it facilitates the exploitation of different species polarities to (i) improve the process performance or (ii) ensure the compliance with process constraints. Methodologically, this addition enables the extension of the EPF methodology from an approach for the reactor-network design toward a tool for the design of reactor-separator sequences and, ultimately, (integrated) reactor-separator networks.

In this work, the methodological foundation for the incorporation of thermodynamic information in the form of activity coefficients and phase equilibrium calculations in the EPF methodology is provided, leading to the multiphase elementary process functions (mpEPF) formulation. Major contributions include

- the design of an EPF formulation with steady-state phase equilibrium calculations at specific points on the fluid element's path through state space,
- the application of the mpEPF idea using the improved hydroaminomethylation reaction kinetics to design optimal reactor-network candidates for multiple operating scenarios,
- the exemplification of the reactor-(L/L)-separator sequence design by the mpEPF formulation using a generic example reaction.

In addition to these contributions, mpEPF formulation is discussed critically and a motivation for the necessity of thermodynamically consistent reaction kinetics for the design of integrated process units is provided.

Dynamic Process Operation Strategies

The translation of the optimal control profiles from the EPF or mpEPF approaches into real-world reactor- and (integrated) reactor-separator networks represents a challenging task as compromises and approximations lead to the possibility of designing multiple candidate processes of different degrees of complexity, operability, and performance. However, instead of relying on the interconnection of standard, ideal reactors such as continuously stirred tank reactors, plug-flow reactors and differential side-stream reactors, the realization of the control profiles in new and innovative reactor concepts with interesting operating scenarios may be advantageous. One such process unit concept is the repeatedly operated semibatch reactor (RSBR) in which direct realization of the control profiles is possible due to their application in time rather than space (in particular the axial reactor dimension). This reactor concept can be interfaced to a continuous process via the utilization of two buffer tanks and is able to provide comparable performance to an ideal DSR with significantly less constructional but increased operational effort. In this work, the performance of a RSBR is investigated for the homogeneously rhodium-catalyzed hydroformylation of 1-dodecene. Major achievements of this investigation include

- the formulation and verification of a rigorous, dynamic RSBR process model for the simulation of the process start-up and the time required to achieve cyclic steady-state,
- the comparison of dynamic simulation results with experimental long-term investigations of the process candidate on miniplant scale under open and closed recycling conditions of a substrate-rich distillate stream,
- the identification of optimal control profiles under miniplant constraints and the quantitative agreement of experiment and simulation results with a 15 and 17 percentage point increase of conversion and yield, respectively, over the reference process.

All of these achievements are summarized in a conversion-yield-selectivity diagram to visually assess the performance of the simulated and miniplant scale RSBR process under multiple operating points.

6.2 Outlook

The research vision and goals from chapter 1 emphasize the need for the development of new and improved model-based process design techniques to aid in the rapid transformation toward a sustainable, biomass-based chemical industry. By encompassing the steps of model identification, conceptual design and process operation in the scope of this work, new approaches for the incorporation and handling of liquid multiphase systems under transient conditions are provided which show their potential in the application to challenging, commercially relevant example processes. With the promising results of this work, the continuation of the methodological development and their practical application presents interesting new questions for future research. In the following paragraphs, a subset of these questions are outlined.

Rigorous (Integrated) Reactor-Separator-Network Design

The rigorous consideration of the appearance and disappearance of phases in the EPF methodology allows for the incorporation of a completely new set of process and process unit designs. It is shown that reactor-separator sequences can be predicted using the mpEPF approach. However, the design of more complex reactor-separator networks and integrated process units requires additional development to achieve fast, robust, and intuitively interpretable predictions.

Integrated Process Unit Design. Considering the capabilities of the current mpEPF implementation, the design of integrated process units is already possible for liquid multiphase systems if thermodynamically consistent reaction kinetics are available. In a next step, this capability should be presented in the form of an optimal reactive-extraction or reactive-distillation process unit design exemplified for a concrete real-world process.

A second interesting aspect for future research would include the incorporation of mass transfer kinetics to demonstrate the benefit of the simultaneous consideration of reaction and mass transfer kinetics. For selected example systems, this additional information may lead to high-performance yet non-intuitive process designs and operating conditions where the relative difference in time scale of these kinetics can be exploited.

Reactor-Separator-Network Design. In terms of the design of efficient reactor-separator networks, new methodological extensions are required to identify ideas for the handling of multiple phases in the case of intermediate separations. While it is theoretically possible to perform consecutive phase equilibrium calculations on already separated phases, this approach introduces branching points to the optimization problem since multiple, consecutive separation steps are imaginable. To ensure a sufficiently large design space in which the optimal reactor-separator-network design can be identified, additional solvent molecules would need to be included in the mpEPF formulation so that the solver can choose the best solvent system and, consequently, the best separation strategy from the available set of species. Due to the multi-level calculation of phase equilibria, this approach would lead to an explosion of numeric complexity which is difficult to handle with state-of-the-art, gradient-based NLP solvers.

Alternatively, the incorporation of an additional layer of ideal separators, i.e., process units which ideally separate all species in a mixture into separate phases, after the rigorous phase equilibrium calculations would present a feasible approach to minimize computational load while providing a simple interface to previous reactor-separator-network design studies by Kaiser [Kai19]. Instead of relying on the a priori selection of the number of ideal separators, the phase equilibrium calculations identify thermodynamically feasible points for phase separation using the available degrees of freedom. In the next step, the ideal separation of all species in the separated phase(s) allow for recycling following the storage tank approach from Kaiser et al. [KFS17]. Hence, a combination of the mpEPF formulation with the previous work from Kaiser would allow for the rigorous identification of thermodynamically feasible separation scenarios while maintaining the idea of minimal limitations in the early levels of the MLRD approach. One downside of this strategy lies in the number of different separation approaches, i.e., extraction, distillation, crystallization, which have to be incorporated simultaneously in the mpEPF formulation to remove implicit restrictions from the reaction system and allow for the identification of optimal reactor-separator network candidates.

Computer-Aided Phase System Selection and Process Design

The inclusion of thermodynamic information in the form of phase equilibria in the reaction kinetic model identification as well as the conceptual design shows that the design of efficient chemical processes using new substrates requires a broader view on the available restrictions and degrees of freedom. One key aspect is the simultaneous consideration of all these information which motivates developments such as

computer-aided molecular and process design (CAMPD) frameworks [Lin+22]. In an even larger scope than the simultaneous molecular and process design, the selection of the general class of solvent systems should be performed simultaneous to the process design, giving rise to the computer-aided phase system selection (caPSS). In conjunction with the methodological development of the mpEPF formulation from the previous paragraph, a systematic, model-based investigation of the influences of solvent systems and distinct solvents for these candidate systems would need to be performed. These influences on the process performance under consideration of different aspects, such as feasibility, complexity, profitability, and environmental impact, would greatly simplify the identification of optimal processes by providing guidelines and structures for informed decision making. An initial draft on a possible formulation for caPSS is proposed by Rätze et al. [Rät+22].

Flexible and Reusable Reactor Units for Multipurpose Plants

In the last suggestion for future research perspectives, the focus lies on the extended investigation and application of the RSBR. Its unique features allow for the direct realization of updated control profiles in the face of new information, fluctuations in the substrate quality or adapted regulations and requirements which makes it an interesting reactor candidate for new processes in the transforming chemical industry. In addition to its constructional and operational benefits like the standardized format, the absence of axial dispersion and the interface to a continuously operated downstream process with its superior throughput and robustness, the RSBR presents the possibility of a conceptual shift of the reactor design for homogeneously catalyzed reactions. Instead of viewing the reactor design as the product of a one-time engineering effort under a given set of information and constraints, it evolves to a continuous service in which the design of a continuous process—represented by control profiles—can be continuously updated based on new information and restrictions similar to a software product. To improve the visibility of these benefits to stakeholders in the chemical industry, additional demonstrations of the RSBR for other reaction and solvent systems are necessary. Ultimately, extended research in this direction has the ability to aid in the transformation toward a digital and green chemical industry.

Phase Equilibria

A

This appendix provides a brief introduction to the calculation of the chemical potential using different reference states. For an extended discussion on the fundamental thermodynamic equations and the calculation of phase equilibria, the interested reader is referred to Pfennig [Pfe04] who provides a structured and comprehensive introduction to this topic. Major parts of the following paragraphs are taken from chapter 4 and 5 thereof.

Fugacity Formulation. As the chemical potential $\mu_i^{(\pi)}\left(T, p, \{x_j\}\right)$ of species $i \in \mathcal{SPC}$ and phase $\pi \in \Pi$ represents a state variable, different paths and, therefore, different reference states can be used for its calculation. By employing the fundamental equation of the Helmholtz energy $A\left(T, v, \{x_j\}\right)$, the chemical potential is calculated as

$$
\begin{aligned}
&\mu_i\left(T, v, \{x_j\}\right) = && \text{Contribution from …}\\
&\quad \sum_{k=1}^{n_{\text{atoms},i}} \nu_{i,k}\left(H_k^*(T^{\text{ref}}) - TS_k^*(T^{\text{ref}}, p^{\text{ref}})\right) && \text{a) elements at reference}\\
&\quad + \Delta_{\text{f}} H_i^{\text{IG}}(T^{\text{ref}}) - T\Delta_{\text{f}} S_j^{\text{IG}}(T^{\text{ref}}, p^{\text{ref}}) && \text{b) molecule formation at reference}\\
&\quad + \int_{T^{\text{ref}}}^{T} c_{\text{p},i}^{\text{IG}}(T')\,\mathrm{d}T' - T\int_{T^{\text{ref}}}^{T} \frac{c_{\text{p},i}^{\text{IG}}(T')}{T'}\,\mathrm{d}T' && \text{c) raising the temperature}\\
&\quad + RT\ln\frac{p}{p^{\text{ref}}} && \text{d) raising the pressure}\\
&\quad + RT\ln x_i && \text{e) ideal gas mixture}\\
&\quad + \left(\frac{\partial n\left(A - A^{\text{IG}}\right)}{\partial n_i}\right)_{T,v,n_{j\neq i}} - RT\ln Z, && \text{f) non-ideal fluid mixture}
\end{aligned}
\tag{A.1}
$$

assuming that no reactions take place. Please note that the notation $\{x_j\}$ represents an abbreviation of the set $\{x_j\}$ with $j \in \mathcal{SPC}$ and $\mathcal{SPC}$ representing the set of all species in the mixture. Without going into detail on the origin of each contribution in eq. (A.1), the main purpose of each term is briefly summarized on the right hand side. In the case of a phase equilibrium calculation where eq. (2.1a) is fulfilled

and all temperature-dependent contributions are summarized in the term $\mu_i^{\mathrm{ref}}(T)$, eq. (A.1) becomes

$$\mu_i - \mu_i^{\mathrm{ref}} = RT \ln \frac{p}{p^{\mathrm{ref}}} + RT \ln x_i + \left(\frac{\partial n \left(A - A^{\mathrm{IG}} \right)}{\partial n_i} \right)_{T,v,n_{j \neq i}} - RT \ln Z. \tag{A.2}$$

To achieve similarity of eq. (A.2) to the ideal gas (IG)-case

$$\left(\mu_i - \mu_i^{\mathrm{ref}} \right)^{\mathrm{IG}} = RT \ln \frac{p}{p^{\mathrm{ref}}} + RT \ln x_i = RT \ln \frac{p_i}{p^{\mathrm{ref}}}, \tag{A.3}$$

the fugacity f_i is defined as a non-ideal pressure equivalent, leaving

$$\mu_i - \mu_i^{\mathrm{ref}} = RT \ln \frac{f_i}{f_i^{\mathrm{ref}}}. \tag{A.4}$$

When formulating the reference state as a pure component, ideal gas at T and v, the reference fugacity is equal to the reference pressure $f_i^{\mathrm{ref}} = p^{\mathrm{ref}}$, so that the same structure as in eq. (A.2) is achieved with an additional term

$$RT \ln \phi_i = \left(\frac{\partial n \left(A - A^{\mathrm{IG}} \right)}{\partial n_i} \right)_{T,v,n_{j \neq i}} - RT \ln Z, \tag{A.5}$$

containing the fugacity coefficient ϕ_i which represents the non-ideality. The chemical potential can therefore be expressed as

$$\mu_i - \mu_i^{\mathrm{ref}} = RT \ln \frac{p}{p^{\mathrm{ref}}} + RT \ln x_i + RT \ln \phi_i. \tag{A.6}$$

Activity Formulation. For the calculation of liquid-phase chemical potentials, the selection of a different reference state is preferable. By choosing a different route in

state space, the chemical potential may be formulated over the Gibbs free enthalpy fundamental equation $G\left(T, p, \{x_j\}\right)$ as

$$
\begin{aligned}
&\mu_i\left(T, p, \{x_j\}\right) = && \text{Contribution from …} \\
&\quad \sum_{k=1}^{n_{\text{atoms},i}} \nu_{i,k}\left(H_k^*(T^{\text{ref}}) - TS_k^*(T^{\text{ref}}, p^{\text{ref}})\right) && \text{a) elements at reference} \\
&\quad + \Delta_{\text{f}} H_i^{\text{IG}}(T^{\text{ref}}) - T\Delta_{\text{f}} S_j^{\text{IG}}(T^{\text{ref}}, p^{\text{ref}}) && \text{b) molecule formation at reference} \\
&\quad + \int_{T^{\text{ref}}}^{T} c_{\text{p},i}^{\text{IG}}(T')\,\mathrm{d}T' - T\int_{T^{\text{ref}}}^{T} \frac{c_{\text{p},i}^{\text{IG}}(T')}{T'}\,\mathrm{d}T' && \text{c) raising the temperature} \\
&\quad + RT\ln\phi_i^{\text{ref}}\left(T, p_i^{\text{sat}}(T)\right) + RT\ln\frac{p_i^{\text{sat}}(T)}{p^{\text{ref}}} && \text{d) non-ideal gas} \\
&\quad + \int_{p_i^{\text{sat}}(T)}^{p} v_i\left(T, p'\right)\mathrm{d}p' && \text{e) compressing the liquid} \\
&\quad + RT\ln x_i && \text{f) ideal mixture} \\
&\quad + \mu_i^{\text{E}}\left(T, p, \{x_j\}\right). && \text{g) non-ideal mixture}
\end{aligned}
\tag{A.7}
$$

Both formulations of the chemical potential are identical from term a) to c). However, one decisive difference to eq. (A.1) is the separation of the non-ideal behavior of the liquid mixture into the non-ideality of the pure components d) and non-ideal mixing behaviors g). This enables the definition of the reference state as a pure, liquid component at T and p which leads to

$$\mu_i - \mu_i^{\text{ref}} = \mu_i^{\text{E}}\left(T, p, \{x_j\}\right) + RT\ln x_i. \tag{A.8}$$

Please note that μ_i^{ref} is not equivalent to μ_i^{ref} in eq. (A.2) because of the different reference point. By introducing the activity coefficient

$$RT\ln\gamma_i = \mu_i^{\text{E}}\left(T, p, \{x_j\}\right), \tag{A.9}$$

as a representation for the partial molar Gibbs excess enthalpy $\mu_i^{\text{E}}\left(T, p, \{x_j\}\right)$, eq. (A.8) can be written as

$$\mu_i - \mu_i^{\text{ref}} = RT\ln\gamma_i + RT\ln x_i = RT\ln a_i, \tag{A.10}$$

where a_i represents a corrected molar fraction, the activity, of species i which accounts for the non-ideality due to mixing. The term $\mu_i^{\text{M}} = RT\ln a_i$ is often

denoted as the partial molar Gibbs enthalpy of mixing with the corresponding Gibbs enthalpy of mixing

$$G^{\mathrm{M}} = RT \sum_{i \in \mathcal{SPC}} x_i \ln a_i. \tag{A.11}$$

For an ideal mixture (IM), the activity coefficient is $\gamma_i^{\mathrm{IM}} = 1$ and $\mu_i^{\mathrm{E}}\left(T, p, \{x_j\}\right) = 0$.

B Model Equations and Parameters

This appendix contains relevant model parameters for the hydroformylation of 1-decene and 1-dodecene, the reductive amination of 1-undecanal and the hydroaminomethylation of 1-decene.

B.1 Model Parameters for the Hydroformylation of 1-Decene

The temperature-centered formulation of Henry's law which is employed by Jörke et al. [Jör+15] reads for each species $i \in \mathcal{SPC}^{\mathrm{Gas}} = \{\mathrm{H_2}, \mathrm{CO}\}$

$$H_i(T) = k_{0,i} \exp\left(\frac{\Delta_\mathrm{s} H_i}{R T_\mathrm{ref}}\left(\frac{T_\mathrm{ref}}{T} - 1\right)\right). \tag{B.1}$$

The kinetic parameters, equilibrium constants and inhibition constants as well as the Henry coefficients and mass transfer parameters for the hydroformylation of 1-decene are presented in tables B.1 to B.3, respectively. The polynomial parameters for the equilibrium constant of the isomerization are summarized in table B.4.

Tab. B.1.: Kinetic parameters for the Hyfo of 1-decene [Jör+17].

i	A_i / −	B_i / −
Iso, 1	11.04	18.53
Iso, 2	6.94	15.63
Iso, 3	6.96	15.63
Iso, 4	5.96	15.63
Hyfon	20.41	9.65
Hyfoni	19.10	18.04
Hyfoi	14.90	18.04
HydDec	12.73	20.44

Tab. B.2.: Equilibrium and inhibition constants for the Hyfo of 1-decene [Jör+17].

K_{cat} / $\mathrm{L\,mol^{-1}}$	5496.70
$K_{\mathrm{Iso,I}}$ / −	33.77
$K_{\mathrm{Iso,II}}$ / −	0.96
$K_{\mathrm{Iso,III}}$ / −	1.00
$K_{\mathrm{Iso,IV}}$ / −	0.50
$K_{\mathrm{Hyfo,I}}$ / $\mathrm{L\,mol^{-1}}$	92.10
$K_{\mathrm{Hyfo,II}}$ / $\mathrm{L^2\,mol^{-2}}$	1063.60
$K_{\mathrm{Hyfo,III}}$ / $\mathrm{L\,mol^{-1}}$	5775.00
$K_{\mathrm{Hyfo,IV}}$ / $\mathrm{L^2\,mol^{-2}}$	0.00
K_{HydDec} / $\mathrm{L\,mol^{-1}}$	10.20

Tab. B.3.: Mass transfer and Henry coefficient parameters for the Hyfo of 1-decene [JSH15].

i	$k_{0,i}$ / $\mathrm{bar\,L\,mol^{-1}}$	$\Delta_{\mathrm{s}}H_i$ / $\mathrm{kJ\,mol^{-1}}$	$\beta_{\mathrm{eff},i}$ / $\mathrm{min^{-1}}$
H_2	201.36	4.1959	2.412 15
CO	123.52	1.9283	2.412 15

Tab. B.4.: Parameters for the lumped equilibrium constant K_{Iso} of the isomerization reaction in the Hyfo reaction network of 1-decene [Jör+15].

a / $\mathrm{°C^{-4}}$	b / $\mathrm{°C^{-3}}$	c / $\mathrm{°C^{-2}}$	d / $\mathrm{°C^{-1}}$	e / -
2.330×10^{-7}	-1.610×10^{-4}	4.404×10^{-2}	-6.114	4.395×10^{2}

B.2 Model Parameters for the Reductive Amination of 1-Undecanal

Kinetic parameters, Gibbs reaction enthalpies, Henry coefficients and mass transfer parameters for the reductive amination of 1-undecanal can be found in tables B.5 to B.7, respectively.

Tab. B.5.: Kinetic parameters for the RA of 1-undecanal including the enamine condensation Cond, enamine hydrogenation HydEn, aldehyde hydrogenation HydUndec and aldol addition Add [Kir+20a].

j	$k_{0,j}$		$E_{\mathrm{A},j}$ / kJ mol^{-1}
Cond	8.776×10^{1}	L mol^{-1} min^{-1}	13.9
HydEn	2.570×10^{7}	L^2 mol^{-2} min^{-2}	19.4
HydUndec	2.240×10^{8}	L^2 mol^{-2} min^{-2}	44.0
Add	1.400×10^{5}	L mol^{-1} min^{-1}	42.3

Tab. B.6.: Free Gibbs reaction enthalpies $\Delta G_{\mathrm{r,Cond}}$ in kJ mol^{-1} of the equilibrium reaction in the RA of 1-undecanal. The Gibbs reaction enthalpies were calculated using the density functional BP86D3(BJ) with def2-TZVP as a basis set and COSMO-RS as model for solvent effects [Kir+20a].

T / °C	$\phi^{\mathrm{n}}_{\mathrm{MeOH,nC12an}} = 1$	$\phi^{\mathrm{n}}_{\mathrm{MeOH,nC12an}} = 99$
85	0.3	−1.4
100	0.6	−1.1
115	4.0	−0.8

Tab. B.7.: Mass transfer and corrected Henry coefficients for the RA of 1-undecanal [Kir+20a].

	$\phi^{\mathrm{n}}_{\mathrm{MeOH,nC12an}}$ / mol mol^{-1}	99	1	1
	$\phi^{\mathrm{V},0}_{\mathrm{H_2O}}$ / L L^{-1}	0.00	0.00	0.01
β_{eff} / s^{-1}		0.0384	0.0345	0.0392
	T / °C			
	85	349	334	
H / bar L mol^{-1}	100	342	315	344
	115	327	313	

Tab. B.8.: Isomerization experiments for 1-decene (nC10en). Different isomers are lumped together in the pseudo-species decene isomers (iC10en). The initial reaction mixture comprises 16.038 g MeOH, 3.6573 g nC10en (Alfa Aesar, 95.75 % purity), 2.2734 g DEA (Sigma-Aldrich, 99.5 % purity) and 16.0425 g nC12an (99.27 % purity), leading to a liquid volume of 50 mL. 6.73 g of catalyst precursor (acetylacetonato)(1,5-cyclooctadiene)rhodium(I) (Rh(acac)(COD)) and 59.62 g 4,5-bis(diphenylphosphino)-9,9-dimethyl-2,7-disulfoxanthene disodium salt (SulfoXantphos) are prepared for the reaction mixture which represents a molar phosphor to rhodium ratio of 7:1. Catalyst preforming is carried out with syngas of the ratio $CO:H_2$ 1:2 at 10 bar for 30 min while heating to the respective experiment temperature. Under reaction conditions, the vessel is pressurized to 25 bar with N_2.

ϑ / °C	t_{sp} / min	c_{nC10en} / mol L^{-1}	c_{iC10en} / mol L^{-1}	K_{Iso}^{eq} / -
140	30	0.013	0.362	28.6
140	30	0.008	0.331	41.0
140	60	0.013	0.365	29.0
140	90	0.011	0.362	33.4
120	30	0.009	0.361	40.0
120	30	0.007	0.332	47.1
100	30	0.010	0.361	36.9
100	60	0.009	0.361	38.5
100	60	0.008	0.341	44.9
100	90	0.007	0.338	50.4
			mean	39.0

Experiments performed by Wieland Kortuz, OvGU.

B.3 Model Parameters for the Hydroaminomethylation of 1-Decene

The data of preliminary isomerization experiments under hydroaminomethylation conditions is summarized in table B.8. Inhibition constants, Gibbs reaction enthalpies, Henry, and mass transfer coefficients as well as initial guesses for the kinetic parameters of the hydroaminomethylation can be found in tables B.9 to B.11, respectively. Additional parameters such as the stoichiometric matrix, molar masses of each species and the density correlation parameters are summarized in tables B.12 to B.15. Parameters for the phase equilibrium calculation and the mbOED are presented in table B.16.

Tab. B.9.: Preliminary equilibrium constants and Gibbs reaction enthalpies for the HAM of 1-decene [JSH15; Jör+17; Kir+20a; Kor20]. The Gibbs reaction enthalpy for the condensation reaction is selected for $\phi^{\mathrm{m}}_{\mathrm{MeOH,nC12an}} = 1$ from Kirschtowski et al. [Kir+20a] from the suggested BP86D3(BJ)/def2-TZVP with COSMO-RS model at $\vartheta = 115\,^{\circ}\mathrm{C}$ due to the elevated temperature in the HAM (cf. table B.6).

K_{cat} / $\mathrm{L\,mol^{-1}}$	5496.70	[Jör+17]
$K_{\mathrm{Hyfo,\,I}}$ / $\mathrm{L\,mol^{-1}}$	92.10	[Jör+17]
$K_{\mathrm{Hyfo,\,II}}$ / $\mathrm{L^2\,mol^{-2}}$	1063.60	[Jör+17]
$\Delta G_{\mathrm{r,\,Cond}}$ / $\mathrm{J\,mol^{-1}}$	4000.00	[Kir+20a]
$K^{\mathrm{eq}}_{\mathrm{Iso}}$ / -	39.00	this work
K_{HydDec} / $\mathrm{L\,mol^{-1}}$	10.20	[Jör+17]
K_{HydEn} / $\mathrm{L\,mol^{-1}}$	6.49	[Kor20]

Tab. B.10.: Henry coefficients and effective mass transfer coefficients for the HAM of 1-decene [Kor+22].

i	H_i / $\mathrm{bar\,L\,mol^{-1}}$	$\beta_{\mathrm{eff},i}$ / $\mathrm{min^{-1}}$
H_2	352	2.367
CO	260.7	3.964

Tab. B.11.: Initial kinetic parameter estimates for the HAM of 1-decene [Kor20].

i	A_i / −	B_i / −
Iso	4.7288	39.5375
Hyfo	16.4542	30.2846
Cond	−1.6520	22.1437
HydEn	15.2544	5.9063
HydDec	8.3631	33.5518

Tab. B.12.: Stoichiometric matrix for the HAM of 1-decene.

	Cond	HydDec	HydEn	Hyfo	Iso
Amine	0	0	1	0	0
CO	0	0	0	−1	0
DEA	−1	0	0	0	0
Enamine	1	0	−1	0	0
H_2	0	−1	−1	−1	0
H_2O	1	0	0	0	0
MeOH	0	0	0	0	0
iC10en	0	0	0	0	1
nC10an	0	1	0	0	0
nC10en	0	−1	0	−1	−1
nC11al	−1	0	0	1	0
nC12an	0	0	0	0	0

Tab. B.13.: Molar masses for the species in the HAM of 1-decene.

i	$\tilde{M}_i$ / g mol^{-1}
nC10en	140.27
iC10en	140.27
nC11al	170.29
DEA	73.14
Enamine	225.43
Amine	227.43
nC10an	142.29
H_2O	18.02
MeOH	32.04
nC12an	170.34
H_2	2.00
CO	28.01

Tab. B.14.: Parameters for chemical properties handbook (CPH) density correlations [Yaw99].

i	a_i / g mL^{-1}	b_i / −	c_i / −	d_i / K
DEA	2.4111×10^{-1}	2.5362×10^{-1}	2.7280×10^{-1}	4.9660×10^{2}
H_2O	3.4710×10^{-1}	2.7400×10^{-1}	2.8571×10^{-1}	6.4713×10^{2}
MeOH	2.7197×10^{-1}	2.7192×10^{-1}	2.3310×10^{-1}	5.1258×10^{2}
iC10en	2.3981×10^{-1}	2.5776×10^{-1}	2.8562×10^{-1}	6.1705×10^{2}
nC10an	2.3276×10^{-1}	2.5240×10^{-1}	2.8570×10^{-1}	6.1845×10^{2}
nC10en	2.3981×10^{-1}	2.5776×10^{-1}	2.8562×10^{-1}	6.1705×10^{2}
nC11al	2.6946×10^{-1}	2.6210×10^{-1}	3.0963×10^{-1}	6.7200×10^{2}
nC12an	2.3403×10^{-1}	2.5183×10^{-1}	2.8960×10^{-1}	6.5820×10^{2}

Tab. B.15.: Density parameters for the design institute for physical properties (DIPPR) 105 equation [Des19].

i	a_i / mol mL^{-1}	b_i / −	c_i / K	d_i / −
Amine	2.5878×10^{-1}	2.1792×10^{-1}	6.9289×10^{2}	2.8804×10^{-1}
DEA	1.9404×10^{-10}	3.0000×10^{-6}	-7.5735×10^{5}	-1.0883×10^{2}
Enamine	2.5878×10^{-1}	2.1792×10^{-1}	6.9289×10^{2}	2.8804×10^{-1}
H_2O	2.8480×10^{-2}	2.2030×10^{-2}	4.4725×10^{2}	1.4091×10^{-2}
nC11al	1.5050	5.0133×10^{-1}	5.9841×10^{2}	5.2735×10^{-1}
nC12an	1.9385	5.8748×10^{-1}	5.0601×10^{2}	7.1269×10^{-1}

Tab. B.16.: Parameter values for the phase equilibrium and mbOED calculation of the HAM process.

$\beta^{(\pi)}$ / $\mathrm{mol\,min^{-1}\,m^{-2}}$	1×10^3
κ / −	0.3
h_{FE} / −	$[0.01, 1]$
n_{sp} / −	10
n_{exp} / −	5
$n_{\mathrm{phases,max}}$ / −	2

B.4 Model Equations and Parameters for the Hydroformylation of 1-Dodecene

This appendix section contains the model structure and necessary parameters for the hydroformylation of 1-dodecene reaction kinetics. Derived and parameterized by Hentschel et al. [Hen+15], the dodecene hydroformylation kinetics comprise the reaction set $\mathcal{RCT}^{\text{Hyfo}} = \{\text{Iso}, \text{Hyfon}, \text{Hyfoi}, \text{Hyfoni}, \text{Hydn}, \text{Hydi}\}$ with the reaction network displayed in fig. B.1. In contrast to the C10 hydroformylation kinetics in

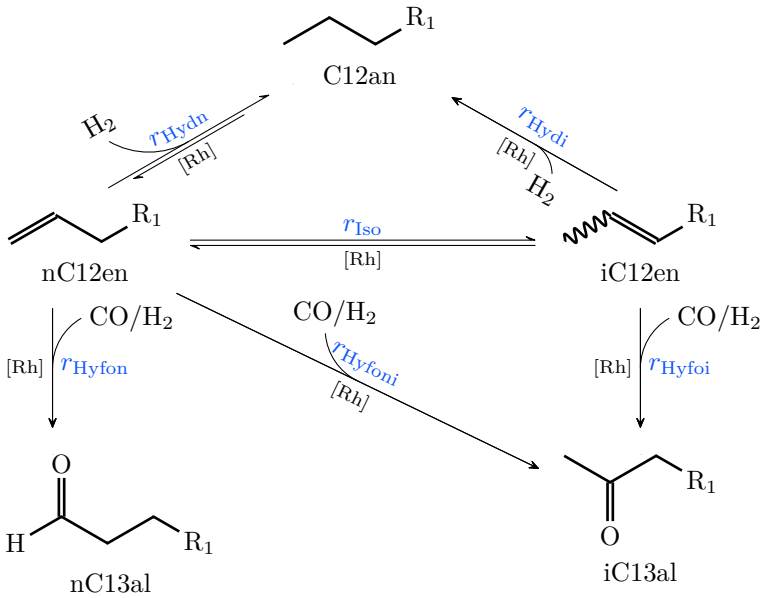

Fig. B.1.: Reaction network of the Hyfo of 1-dodecene in a DMF/C10an TMS (adopted from [Hen+15]). R_1: C_9H_{19}.

fig. 2.12, this kinetic model uses a lumped representation of the dodecene isomers to reduce the number of necessary model parameters and kinetic equations. To achieve

molar mass-based reaction rate equations, the catalyst mass-based reaction rate equations

$$r^{\mathrm{m}}_{\mathrm{Hyfon}} = \frac{k_{\mathrm{Hyfon}} c_{\mathrm{nC12en}} c_{\mathrm{H_2}} c_{\mathrm{CO}}}{1 + K_{\mathrm{Hyfon,1}} c_{\mathrm{nC12en}} + K_{\mathrm{Hyfon,2}} c_{\mathrm{nC13al}} + K_{\mathrm{Hyfon,3}} c_{\mathrm{H_2}}}, \tag{B.2a}$$

$$r^{\mathrm{m}}_{\mathrm{Iso}} = \frac{k_{\mathrm{Iso}} \left(c_{\mathrm{nC12en}} - \frac{c_{\mathrm{iC12en}}}{K^{\mathrm{eq}}_{\mathrm{Iso}}} \right)}{1 + K_{\mathrm{Iso,1}} c_{\mathrm{nC12en}} + K_{\mathrm{Iso,2}} c_{\mathrm{iC12en}}}, \tag{B.2b}$$

$$r^{\mathrm{m}}_{\mathrm{Hydn}} = \frac{k_{\mathrm{Hydn}} \left(c_{\mathrm{nC12en}} c_{\mathrm{H_2}} - \frac{c_{\mathrm{nC12an}}}{K^{\mathrm{eq}}_{\mathrm{Hydn}}} \right)}{1 + K_{\mathrm{Hydn,1}} c_{\mathrm{nC12en}} + K_{\mathrm{Hydn,2}} c_{\mathrm{nC12an}} + K_{\mathrm{Hydn,3}} c_{\mathrm{H_2}}}, \tag{B.2c}$$

$$r^{\mathrm{m}}_{\mathrm{Hydi}} = k_{\mathrm{Hydi}} c_{\mathrm{iC12en}} c_{\mathrm{H_2}}, \tag{B.2d}$$

$$r^{\mathrm{m}}_{\mathrm{Hyfoi}} = k_{\mathrm{Hyfoi}} c_{\mathrm{iC12en}} c_{\mathrm{H_2}} c_{\mathrm{CO}}, \tag{B.2e}$$

$$r^{\mathrm{m}}_{\mathrm{Hyfoni}} = k_{\mathrm{Hyfoni}} c_{\mathrm{nC12en}} c_{\mathrm{H_2}} c_{\mathrm{CO}}, \tag{B.2f}$$

need to be converted using

$$r_j = c_{\mathrm{cat}} \tilde{M}_{\mathrm{cat}} r^{\mathrm{m}}_j, \tag{B.3}$$

and $j \in \mathcal{RCT}^{\mathrm{Hyfo}}$ with the catalyst molar mass specified in table B.17. In addition to the molar masses of each species $i \in \mathcal{SPC}$, density correlation parameters are provided in table B.17 which are used to calculate the temperature-dependent liquid phase volume

$$V_{\mathrm{Liq}} = \frac{\sum_{k \in \mathcal{SPC}} \tilde{M}_k n_k}{\rho}, \tag{B.4}$$

$$\rho = \left(\sum_{k \in \mathcal{SPC}} w_k {\rho_k}^{-1} \right)^{-1}, \tag{B.5}$$

$$w_i = \frac{\tilde{M}_i n_i}{\sum_{k \in \mathcal{SPC}} \tilde{M}_k n_k}, \tag{B.6}$$

$$\rho_i = a_{0,i} + b_{1,i} T, \tag{B.7}$$

and the liquid phase species concentrations

$$c_i = \frac{n_i}{V_{\mathrm{Liq}}}. \tag{B.8}$$

The kinetic factors are modeled using the centered Arrhenius approach

$$k_j = k_{0,j} \exp\left(\frac{-E_{\mathrm{A},j}}{R} \left(\frac{1}{T} - \frac{1}{T_{\mathrm{ref}}} \right) \right), \tag{B.9}$$

Tab. B.17.: Density parameters and molar masses for the hydroformylation of 1-dodecene [McB+16; Kie+14].

i	a_i / $\mathrm{kg\,m^{-3}}$	b_i / $\mathrm{kg\,m^{-3}\,K^{-1}}$	$\tilde{M}_i$ / $\mathrm{g\,mol^{-1}}$
C10an	981.5951	−0.8354	142.2817
DMF	1256.5163	−1.0306	73.0938
nC12en	993.8919	−0.7888	168.3190
iC12en	993.8919	−0.7888	168.3190
nC13al	1068.1228	−0.8018	198.3449
iC13al	1068.1228	−0.8018	198.3449
nC12an	977.0381	−0.7674	170.3348
H_2	–	–	2.0159
CO	–	–	28.0101
cat	–	–	258.0300

with the reference temperature $T_{\mathrm{ref}} = 378.15\,\mathrm{K}$ and kinetic parameters as well as inhibition constants in table B.18. The catalyst pre-equilibrium which determines

Tab. B.18.: Kinetic parameters and inhibition constants for the hydroformylation of 1-dodecene [Hen+15].

j	$k_{0,j}$		$E_{\mathrm{A},j}$ / $\mathrm{kJ\,mol^{-1}}$
Hyfon	4.904×10^{16}	$\mathrm{mL^3\,g^{-1}\,min^{-1}\,mol^{-2}}$	113.08
Iso	4.878×10^{6}	$\mathrm{mL\,g^{-1}\,min^{-1}}$	136.89
Hydn	2.724×10^{8}	$\mathrm{mL^2\,g^{-1}\,min^{-1}\,mol^{-1}}$	76.11
Hydi	2.958×10^{4}	$\mathrm{mL^2\,g^{-1}\,min^{-1}\,mol^{-1}}$	102.26
Hyfoi	3.702×10^{10}	$\mathrm{mL^3\,g^{-1}\,min^{-1}\,mol^{-2}}$	120.84
Hyfoni	3.951×10^{11}	$\mathrm{mL^3\,g^{-1}\,min^{-1}\,mol^{-2}}$	113.08

j	$K_{j,1}$ / $\mathrm{mL\,mol^{-1}}$	$K_{j,2}$ / $\mathrm{mL\,mol^{-1}}$	$K_{j,3}$ / $\mathrm{mL\,mol^{-1}}$
Hyfon	574 876.0	3 020 413.0	11 732 838.0
Iso	38 632.0	223 214.0	0.0
Hydn	2661.2	7100.0	1280.0
	$K_{j,1}$ / −	$K_{j,2}$ / −	$K_{j,3}$ / −
cat	30 410	–	0.644

the concentration of the active catalyst species follows

$$c_{\mathrm{cat}} = \frac{c_{\Sigma\mathrm{cat}}}{1 + K_{\mathrm{cat},1} c_{\mathrm{CO}}^{K_{\mathrm{cat},3}} + K_{\mathrm{cat},2} \frac{c_{\mathrm{CO}}^{K_{\mathrm{cat},3}}}{c_{\mathrm{H_2}}}}, \tag{B.10}$$

where $c_{\Sigma\mathrm{cat}}$ denotes the total catalyst concentration. Modeling of the chemical equilibria uses the equilibrium constant

$$K_j^{\mathrm{eq}} = \exp\left(\frac{-\Delta G_{\mathrm{r},j}}{RT}\right), \tag{B.11}$$

$$\Delta G_{\mathrm{r},j} = a_j + b_j T + c_j T^2, \tag{B.12}$$

with $j \in \{\mathrm{Iso}, \mathrm{Hydn}\}$ and the thermodynamic parameters in table B.19.

Tab. B.19.: Free Gibbs reaction enthalpy parameters for the hydroformylation of 1-dodecene [Hen+15].

	$\Delta G_{\mathrm{r,Iso}}$	$\Delta G_{\mathrm{r,Hydn}}$
a / $\mathrm{J\,mol^{-1}}$	$-1.100\,34 \times 10^4$	$-1.262\,750 \times 10^5$
b / $\mathrm{J\,mol^{-1}\,K^{-1}}$	0.0	1.266×10^2
c / $\mathrm{J\,mol^{-1}\,K^{-2}}$	0.0	6.803×10^{-3}

C

Artificial Neural Network for Liquid-Phase Activity Coefficients

This appendix contains additional information about the artificial neural network (ANN) design to approximate the activity coefficients provided by the perturbed-chain statistical associating fluid theory (PC-SAFT) for the hydroaminomethylation of 1-decene.

Literature Review. Direct utilization of PC-SAFT in gradient-based optimization is challenging due to its iterative nature. Therefore, surrogate models are required which are trained based on simulation data from the PC-SAFT model [NE19; NKE21]. In their work, Nentwich and Engell [NE19] and Nentwich et al. [NVE19] studied the influence of different surrogate models, sampling strategies for data generation and modeling approaches for the application on LLEs in the hydroformylation of 1-dodecene. The authors used combinations of ANNs and Kriging models for predicting the biphasic region and phase compositions with training data either in the form of fugacity coefficients (indirect) or calculation results of the phase equilibrium (direct). When using the indirect approach, the phase equilibrium calculations need to be performed when the surrogate model is used during simulation or optimization. For the hydroformylation, direct surrogate modeling with ANN showed a superior performance in comparison to all other combinations of surrogate models and modeling strategies [Nen21].

Modeling Decisions. The HAM reaction mixture contains twelve species which are present in the liquid phase. If hydrogen and carbon monoxide are neglected because of their minor influence on the phase system, ten species remain from which only two pairs (nC10en, iC10en and C10an; enamine and amine) exhibit similar polarities, and thus allow for the reduction of the input vector. Together with the significant influence of the temperature on the phase equilibrium, this high dimensional input vector is not suited for the utilization together with a Kriging model. Consequently, an ANN is chosen. In terms of the modeling approach, indirect surrogate modeling by approximating the fugacity or activity coefficients is selected to reduce the computation time or, depending on the data generation strategy, surrogate-model

error. In the former case, solving the phase equilibrium with direct evaluation of the SAFT equations for a sufficiently fine grid in eight dimensions leads to significant computational challenges, despite the efficient calculation of the phase equilibrium with the integration approach from section 2.1. In contrast, training a first ANN on the PC-SAFT fugacity/activity coefficients which is used to calculate the phase equilibria required for the training of a second ANN introduces additional approximation errors.

ANN Construction. The ANN is designed using molar fractions x_i with $i \in \mathcal{SPC}^{\mathrm{ANN}} = \{\mathrm{nC10en}, \mathrm{DEA}, \mathrm{nC11al}, \mathrm{Am}, \mathrm{MeOH}, \mathrm{nC12an}, \mathrm{H_2O}\}$ and the temperature T as inputs $u^\top = \left[x^\top, T\right]$ which are centered and scaled using the training data mean $\overline{u}$ and standard deviation σ_u via

$$\tilde{u} = \frac{u - \overline{u}}{\sigma_u}. \tag{C.1}$$

The scaled model inputs $\tilde{u}$ propagate to the ANN output $y_i = \ln \gamma_i$ with $i \in \mathcal{SPC}^{\mathrm{ANN}}$ according to the composition

$$g_0 = \phi\left(\tilde{u}^\top W_0 + w'_0\right), \tag{C.2a}$$

$$g_j = \phi\left(g_{j-1}^\top W_j + w'_j\right), \quad j \in \{1, 2, \ldots, n_{\mathrm{hidden}}\}, \tag{C.2b}$$

$$y = g_{n_{\mathrm{hidden}}}^\top W_{n_{\mathrm{hidden}}+1} + w'_{n_{\mathrm{hidden}}+1}, \tag{C.2c}$$

with ϕ, W_k, w'_k denoting the activation function, the weight matrix and bias vector of each layer $k \in \{0, 1, \ldots, n_{\mathrm{hidden}}, n_{\mathrm{hidden}} + 1\}$, respectively. Please note that layer 0 represents the input while $n_{\mathrm{hidden}} + 1$ denotes the output layer. While the shape of the bias vector in layer j only depends on the number of nodes in the subsequent layer, i.e., $w'_{j-1} \in \mathbb{R}^{n_{\mathrm{nodes},j}}$ with $j \in \{1, 2, \ldots, n_{\mathrm{hidden}} + 1\}$, the weight matrices which connect two layers have the dimension $W_{j-1} \in \mathbb{R}^{n_{\mathrm{nodes},j-1} \times n_{\mathrm{nodes},j}}$.

Data Generation. The training data for the ANN is generated by designing multiple barycentric grids for the molar fractions with different node spacings. To improve the prediction accuracy in the operating window where the switching between mono- and biphasic operation occurs, the maximum water content is limited to $\phi^{\mathrm{V}}_{\mathrm{H_2O}} \leq 0.05$ which is equivalent to a molar fraction of approximately $0.18\,\mathrm{mol\,mol^{-1}}$ and a mass fraction of $0.07\,\mathrm{g\,g^{-1}}$. This restriction is also in accordance with the operating window of the HAM where the water content is kept below $0.05\,\mathrm{g\,g^{-1}}$. Each of

these barycentric grids is evaluated for a temperature window from 100 °C to 140 °C, leading to a total number of 69 900 training data sets.

Training and Validation. With the activation function set to $\phi = \tanh$ to reduce the computational effort of generating the Jacobian and Hessian matrix by automatic differentiation (AD) software, the optimal number of nodes for each hidden layer is identified in a three-fold grid search cross-validation with the maximum error selected as scoring function. From the set $\{50, 60, \ldots, 100\}$ of nodes per layer, $n_{\text{nodes}} = 70$ nodes for each of the two hidden layers is identified as the optimal configuration. Finally, the parameterized ANN is tested using a dedicated set of test data which is created analogous to the training data but with a different node spacing. This ensures, in contrast to the common training/test split, sufficient coverage of the input space and the inclusion of composition edge cases in the 4113 data entries encompassing set. The performance scores and the maximum prediction error of the ANN for each species can be found in table C.1 for the training and test data set. A visual representation of the surrogate model's prediction performance is provided in the form of a parity plot in fig. C.1. Finally, fig. C.2 shows a set of ternary diagrams

Tab. C.1.: Training and test dataset performance scores for the PC-SAFT-based HAM activity coefficient ANN.

Dataset		Training	Test
Score		0.9996	0.9995
Average absolute Error		0.0033	0.0038
Maximum absolute Error	nC10en	0.1410	0.0570
	DEA	0.0860	0.0390
	nC11al	0.1124	0.0570
	Am	0.1272	0.0390
	MeOH	0.0760	0.0680
	nC12an	0.1071	0.0820
	H_2O	0.0490	0.0340

containing the polar (methanol) and non-polar (dodecane) solvents in addition to a third component of the reaction mixture for the hydroaminomethylation. The phase equilibrium is calculated using the activity coefficients from modUNIFAC and PC-SAFT via the ANN for comparison. While modUNIFAC predicts two liquid phases for all ternary mixtures and especially at the operating points where monophasic behavior of the TMS is experimentally verified at elevated temperatures [Sch+21], the PC-SAFT-based ANN only predicts biphasic behavior in the presence of water.

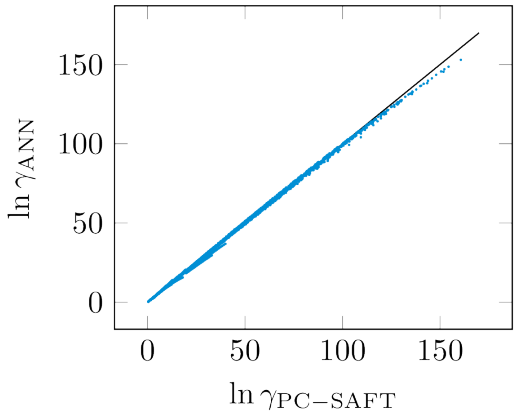

Fig. C.1.: Activity coefficient parity plot between the PC-SAFT model and the ANN. From 518 091 data points, 95 261 data points with an absolute error ≥ 0.02 are visualized. The maximum relative error is 4.78 %.

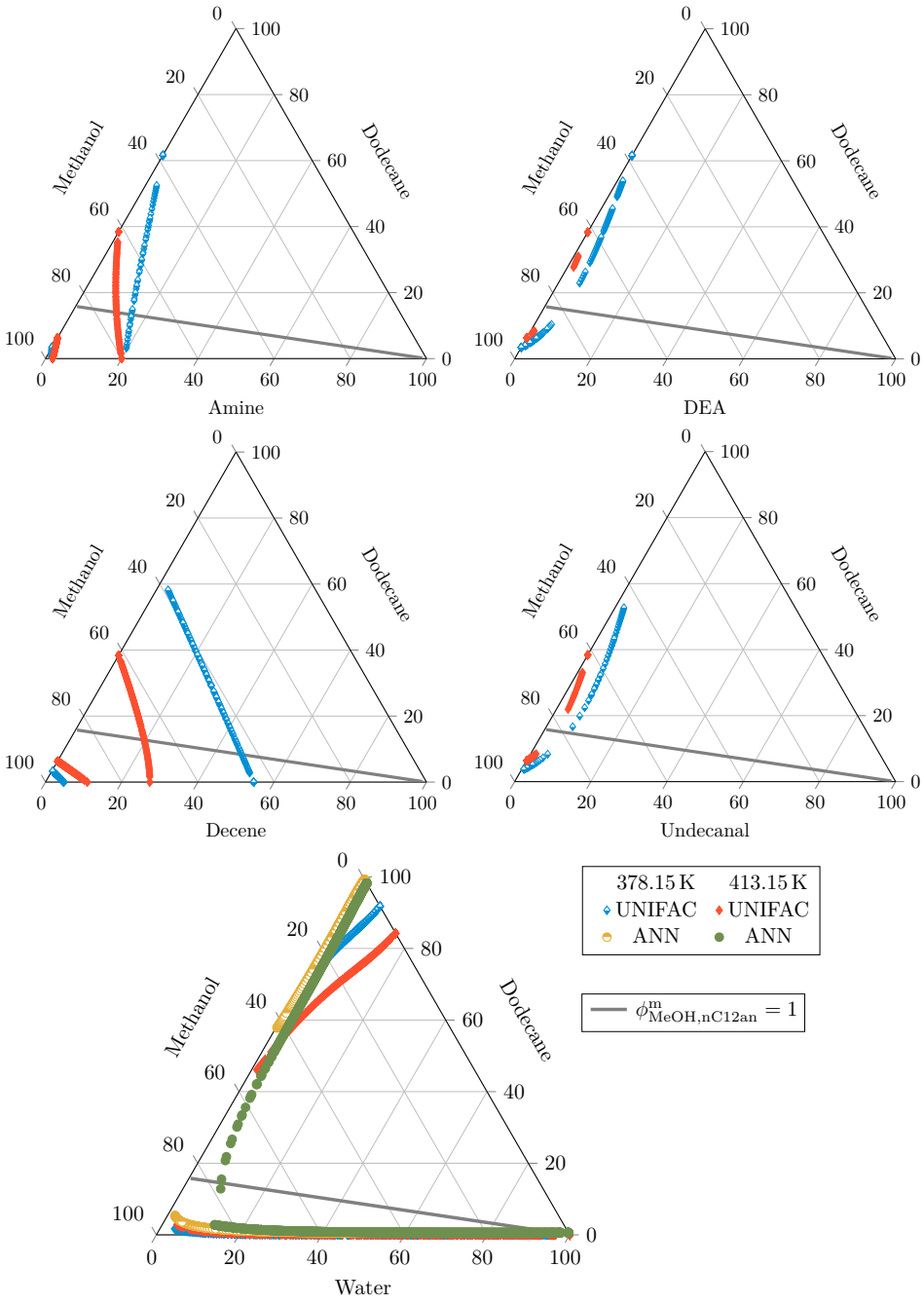

Fig. C.2.: Molar fraction-based ternary diagrams for the TMS components MeOH and nC12an together with a third component. Universal functional activity coefficient (UNIFAC) [GLS93] (parameters from 2017)-based and PC-SAFT surrogate-based calculations for 105 °C and 140 °C. — TMS composition $\phi^{m}_{MeOH,nC12an} = 1$.

Initialization of the Model-Based Optimal Experimental Design

D

This appendix provides a detailed overview over the algorithm used for the initialization of the SM-mbOED problem.

Algorithm 1 mbOED Initialization

Require: Define the times $t \in \mathcal{T} = \left[0, t^{\mathrm{f}}\right]$ and $t_{\mathrm{PhaseEq}} \in \mathcal{T}_{\mathrm{PhaseEq}} = \left[0, t^{\mathrm{f}}_{\mathrm{PhaseEq}}\right]$.

Require: The category variables $\varkappa : \mathcal{T} \to \mathbb{R}^{n_\varkappa}$, $u : \mathcal{T} \to \mathbb{R}^{n_u}$, $y : \mathcal{T} \to \mathbb{R}^{n_y}$, $p \in \left[p_{\mathrm{L},i}, p_{\mathrm{U},i}\right]^{n_p}$, $\varkappa^0 \in \left[\varkappa^0_{\mathrm{L}}, \varkappa^0_{\mathrm{U}}\right]^{n_\varkappa}$ and $c \in \mathbb{R}^{n_c}$ according to eq. (3.5).

Require: The number of grid points $n_{\mathrm{sp},\varkappa^0} \in {\mathbb{N}_0}^{n_\varkappa}$ and $n_{\mathrm{sp},p} \in {\mathbb{N}_0}^{n_p}$.

Require: The number of experiments $n_{\mathrm{exp}} \in \mathbb{N}_+$ and measurement times $t_{\mathrm{sp}} \in \mathbb{R}^{n_{\mathrm{sp}}}_{>0}$.

Require: The measurement covariance matrix $\Sigma_y \in \mathbb{R}^{n_y \times n_y}$ with $\Sigma_y = \Sigma_y^\top$.

$\mathcal{C} \leftarrow$ Grid Generation$((\varkappa^0, p), (n_{\mathrm{sp},\varkappa^0}, n_{\mathrm{sp},p}))$.
$\mathcal{D} \leftarrow$ Data Generation$(\varkappa^0,\ p,\ c,\ \mathcal{C},\ 0.95,\ 1 \times 10^{-4}\ )$.
$s, d \leftarrow$ Combination Search$(\mathcal{D}, n_{\mathrm{exp}}, 1 \times 10^6, \Sigma_y, t_{\mathrm{sp}})$.
$\varkappa^{0*}, p^*, u^*(t), \varkappa^*(t), \left(\frac{\mathrm{d}y}{\mathrm{d}\theta}\right)^*(t) \leftarrow$ Sequential Optimization(d, Σ_y, c).
return $\varkappa^{0*}, p^*, u^*(t), \varkappa^*(t), \left(\frac{\mathrm{d}y}{\mathrm{d}\theta}\right)^*(t)$.

procedure Sequential Optimization$(d,\ \Sigma_y,\ c\ )$
  for all $j \in \{1, 2, \ldots, n_{\mathrm{exp}}\}$ **do**
    Let d_j denote the jth element of tuple d.
    Calculate the FIM for $n_{\mathrm{exp}} - 1$ designs $F \leftarrow$ FIM Calculation$(d,\ t_{\mathrm{sp}},\ \Sigma_y,\ \{1, 2, \ldots, n_{\mathrm{exp}}\} \setminus \{j\}\ )$.
    Let $\varkappa^0$, p and $u(t)$ denote the first, second, and third element of tuple d_j, respectively.
    Solve the mbOED optimization problem $\varkappa^*(t), u^*(t), \left(\frac{\mathrm{d}y}{\mathrm{d}\theta}\right)^*(t), p^*, \varkappa^{0*} \leftarrow$ eq. (3.6) $(\varkappa^0, p, u(t), c)$ with $n_{\mathrm{exp}} = 1$ and $F_{\mathrm{prior}} = F$.
    Set $d_j = \left(\varkappa^{0*}, p^*, u^*(t), \varkappa^*(t), \left(\frac{\mathrm{d}y}{\mathrm{d}\theta}\right)^*(t)\right)$.
  return d

procedure COMBINATION SEARCH($\mathcal{D}$, $n_{\text{exp}} \in \mathbb{N}_+$, $\varepsilon \gg 0$, Σ_y, $t_{\text{sp}} \in {\mathbb{N}_+}^{n_{\text{sp}}}$)

Initialize the score $s \leftarrow \varepsilon$.

Create all experiment combinations via the Cartesian product $\mathcal{D}' \leftarrow \{(d_1, \ldots, d_{n_{\text{exp}}}) \mid d_j \in \mathcal{D} \quad \forall j \in \{1, 2, \ldots, n_{\text{exp}}\}\}$.

for all $d' \in \mathcal{D}'$ **do**

  $F \leftarrow$ FIM CALCULATION(d', t_{sp}, Σ_y, $\{1, 2, \ldots, n_{\text{exp}}\}$).

  Calculate the new score $s' \leftarrow$ EQ. (3.6a)(F).

  if $s' < s$ **then**

    Update the score $S \leftarrow S'$.

    Save optimal combination $d'^* \leftarrow d'$.

return s, d'^*

procedure FIM CALCULATION(d, t_{sp}, Σ_y, $\mathcal{EXP} \subset \mathbb{N}_+$)

Initialize the FIM $F \leftarrow 0_{n_\theta, n_\theta}$ where n_θ denotes the number of uncertain parameters.

for all $j \in \mathcal{EXP}$ **do**

  Let d_j denote the jth entry of tuple d.

  Let $\frac{\mathrm{d}y}{\mathrm{d}\theta}(t)$ denote the fourth entry of tuple d_j.

  Update the FIM $F \leftarrow F +$ EQ. (2.13)($\frac{\mathrm{d}y}{\mathrm{d}\theta}(t_{\text{sp}}), \Sigma_y$).

return F

procedure GRID GENERATION($x \in [x_{\text{L}}, x_{\text{U}}]^{n_x}$, $n_{\text{sp},x} \in {\mathbb{N}_0}^{n_x}$)

Create equidistant grids $\mathcal{G}_i = \left\{ y \in \mathbb{R} \mid y = (x_{\text{U},i} - x_{\text{L},i}) {n_{\text{sp},x,i}}^{-1} j + x_{\text{L},i}, \right.$ $\left. j \in \{0, 1, \ldots, n_{\text{sp},x,i}\} \right\}$ for each tuple element $i \in \{1, 2, \ldots, n_x\}$ of x.

Generate all combinations of the grid elements via the Cartesian product $\mathcal{C} = \{(g_1, \ldots, g_{n_x}) \mid g_i \in \mathcal{G}_i \, \forall i \in \{1, 2, \ldots, n_x\}\}$.

Ensure feasibility of each combination in $\mathcal{C}$.

return $\mathcal{C}$

procedure DATA GENERATION($\mathcal{X}^0$, p, c, $\mathcal{C} \in \mathbb{R}^{n_{\mathcal{X}^0} n_p}$, $\delta_{\mathrm{H_2O}} \in [0,1]$, $0 \leq \varepsilon \ll 1$)

- Initialize the results set $\mathcal{D} \leftarrow \emptyset$.
- **for all** $c \in \mathcal{C}$ **do**
  - Update $\mathcal{X}^0$ and p based on the respective elements in tuple c.
  - Set $u_i(t) \leftarrow 0$ for each $i \in \{1, 2, \dots n_u\}$.
  - Initialize the absolute molar fraction difference $|\Delta x_i^{(\pi,\alpha)}| \leftarrow 1$ for all species $i \in \mathcal{SPC}$ and phases $\pi, \alpha \in \Pi$.
  - **while** $\exists \Delta x_i^{(\pi,\alpha)}$ for all $i \in \mathcal{SPC}$ and $\pi, \alpha \in \Pi$ such that $|\Delta x_i^{(\pi,\alpha)}| > \varepsilon$ **do**
    - **if** $|\Delta x_i^{(\pi,\alpha)}| > \varepsilon$ **then**
      - Decrease the water volume fractions $\phi_{\mathrm{H_2O}}^{\mathrm{V},0} \leftarrow \phi_{\mathrm{H_2O}}^{\mathrm{V},0} \delta_{\mathrm{H_2O}}$.
      - Update the corresponding tuple element in c with $\phi_{\mathrm{H_2O}}^{\mathrm{V},0}$.
    - Solve $\mathcal{X}(t), \frac{\mathrm{d}y}{\mathrm{d}\theta}(t) \leftarrow$ EQ. (3.5) WITH EQ. (2.15)$(\mathcal{X}^0, p, u(t), c)$ with the sensitivity matrix $\frac{\mathrm{d}y}{\mathrm{d}\theta}(t) \in \mathbb{R}^{n_y \times n_\theta}$.
    - Get the molar amount vector $n(t^{\mathrm{f}}) \in \mathbb{R}_{\geq 0}^{|\mathcal{SPC}|}$, where $|\mathcal{SPC}|$ represents the number of species in $\mathcal{SPC}$, and the temperature $T(t^{\mathrm{f}}) \in \mathbb{R}_{\geq 0}$ from tuple $\mathcal{X}(t^{\mathrm{f}})$.
    - Distribute each species across multiple phases by evaluating $n^0 \leftarrow$ EQ. (2.6)$(n(t^{\mathrm{f}}))$ with $n^0 \in \mathbb{R}_{\geq 0}^{|\mathcal{SPC}| \times |\Pi|}$ and $|\Pi|$ denoting the number of phases in Π.
    - Solve the phase equilibrium $n(t_{\mathrm{PhaseEq}}) \leftarrow$ (EQ. (3.6d) WITH EQ. (3.6e))$(T(t^{\mathrm{f}}), n^0)$ with $n(t_{\mathrm{PhaseEq}}) \in \mathbb{R}_{\geq 0}^{|\mathcal{SPC}| \times |\Pi|}$.
    - Calculate the molar fraction difference $\Delta x^{(\pi,\alpha)} \in \mathbb{R}_{\geq 0}^{|\mathcal{SPC}|}$ for all phases $\pi, \alpha \in \Pi$ using $n(t_{\mathrm{PhaseEq}}^{\mathrm{f}})$.
  - Collect the results $d = \left(\mathcal{X}^0, p, u(t), \mathcal{X}(t), \frac{\mathrm{d}y}{\mathrm{d}\theta}(t)\right)$.
  - **if** $d \notin \mathcal{D}$ **then**
    - $\mathcal{D} \leftarrow \{d\} \cup \mathcal{D}$.
- **return** $\mathcal{D}$

E Sensitivity Analyses for the Hydroaminomethylation of 1-Decene

This appendix contains multiple investigations w.r.t. the sensitivity of uncertain parameters and the impact of control parameters on the mbOED for the hydroaminomethylation of 1-decene. In the first section, a sensitivity study is presented and discussed to identify the uncertain parameter vector θ. The second section contains a derivation of the variational equations w.r.t. the dimensionless kinetic parameters A and B so that the interested reader can reconstruct the argumentation in appendix E.1. In the third section, the influence of initial water dosing on the information content of specific experimental designs is investigated.

E.1 Parameter Sensitivity Study

Simultaneous calculation of multiple dynamic experimental designs in eq. (3.6) while calculating the phase equilibrium to ensure monophasic conditions is computationally challenging. Reducing the number of parameters considered in the mbOED problem for the HAM, therefore, significantly simplifies the optimization and speeds up the convergence. To identify the most relevant parameters in terms of their impact on the measured species concentrations $y_i = c_i(t)$ with $i \in \mathcal{SPC}^y$, a parameter sensitivity study is performed. For this investigation, the measurement sensitivities w.r.t. the uncertain parameters $\frac{\mathrm{d}y}{\mathrm{d}\theta}(\chi(t), u(t), p, c)$ are computed. If calculated for a non-linear system, these measurement sensitivities are a function of the uncertain parameters themselves and depend on the operating scenario, leading to the possibility of local or global parameter sensitivity investigations.

Local and Global Parameter Sensitivities. While both methods need to be applied for different operating scenarios, local sensitivity investigations rely on the evaluation of the parameter sensitivities at specific parameter values, e.g., using the expectation values $\hat{\theta}$. In contrast, global methods take the uncertainty of the unknown

parameter θ into account by evaluating the measurement sensitivities for multiple parameter values. A formalization of these global parameter sensitivity studies represents the analysis of variance (ANOVA) framework [ASS97] which is introduced comprehensively in [Sob93; Sob01; Sal+05; Sal+10]. Here, the total variance Σ_y is decomposed into 2^n sub-variances

$$\Sigma_y = \sum_{i=1}^{n_\theta} \sum_{\theta_1 < \cdots < \theta_i}^{n_\theta} \Sigma_y^{\theta_1,\ldots,\theta_i}, \tag{E.1}$$

where Σ_y denotes the uncertainty of the model output y and $\Sigma_y^{\theta_1,\ldots,\theta_i}$ the contribution of each parameter θ_i in the set $\mathcal{X} = \{\theta_i\}_{i=1}^{n_\theta}$ to the model output uncertainty. The global sensitivity indices of the parameter interactions, often called Sobol indices, represent the ratio

$$\mathcal{S}_{\theta_1,\ldots,\theta_i} = \frac{\Sigma_y^{\theta_1,\ldots,\theta_i}}{\Sigma_y}. \tag{E.2}$$

For analyzing the influence of each uncertain parameter θ_i separately, the set $\mathcal{X}$ is partitioned into $\mathcal{X}_i$ and $\mathcal{X}_{\neg i}$ (read as *not* i) with cardinality one and $n_\theta - 1$, respectively. Drawing n_{sp} samples for each parameter $\theta_j \in \Theta$ in $\mathcal{X}_{\neg i}$ yields the matrix $X_{\neg i} \in \mathbb{R}^{n_{\text{sp}} \times n_\theta}$. By taking the expectation value $\mathrm{E}_{X_{\neg i}}(y \,|\, \theta_i)$ for all parameter values in $X_{\neg i}$ while fixing θ_i, the influence of θ_i on the model output is identified. The global parameter sensitivity is achieved by determining the variance of the expectation value for all possible values of $\theta_i \in \Theta$. If n_{sp} samples are drawn and summarized in $X_i \in \mathbb{R}^{n_{\text{sp}}}$, the first order global sensitivity index of θ_i can be computed via

$$\mathcal{S}_{\theta_i} = \frac{\mathrm{Var}_{X_i} \mathrm{E}_{X_{\neg i}}(y \,|\, \theta_i)}{\Sigma_y}. \tag{E.3}$$

Since eq. (E.3) does not contain mixed parameter interactions, the total order index [HS96]

$$\mathcal{S}_{\mathrm{T},\theta_i} = 1 - \frac{\mathrm{Var}_{X_{\neg i}} \mathrm{E}_{X_i}(y \,|\, \theta_{\neg i})}{\Sigma_y}, \tag{E.4}$$

contains all first and higher order interactions.

Sensitivity Scenarios. To achieve detailed information on the parameter influence in the HAM model, multiple scenarios need to be considered for which the first order

and total order Sobol indices are calculated. These scenarios are constructed by varying the most influential parameters T^0, p^0, $y^0_{\mathrm{H_2}}$, $\phi^{\mathrm{n},0}_{\mathrm{DEA,sub}}$ and $\phi^{\mathrm{V},0}_{\mathrm{H_2O}}$ on a full, linearly spaced grid with five sampling points per dimension between their respective lower and upper bound in table 3.1. Please note that $y_{\mathrm{N_2}}(t) = s_T(t) = s_p(t) = s_{y_{\mathrm{H_2}}}(t) = s_{y_{\mathrm{CO}}}(t) = 0$ is assumed for the sensitivity study. Additionally, the Sobol indices are calculated for three, linearly spaced time points $t \in \{45, 90, 135\}$ min. With the sample generation and calculation of the Sobol indices performed using the sensitivity analysis library (SALib) [HU17], the average total order indices representing the sensitivities of the species concentrations w.r.t. each uncertain model parameter are depicted in fig. E.1 for each control parameter dimension and each measured species concentration.

Scenario Influence. The comparison of the absolute total order Sobol indices ensures the comparability of the effect of each model parameter on the species concentrations. Except for the last category where the sensitivity of the species concentration w.r.t. each model parameter is visualized, the concentration sensitivities are averaged over all species and remaining categories to highlight the influence of the investigated control parameter. Regarding the control parameter categories, variation of the temperature and gas composition exhibit the most notable influence on the measurement sensitivities, especially for the enamine and substrate hydrogenation. In contrast, the initial DEA and water amount as well as the pressure appear to have negligible influences so that the measurement sensitivities are equally independent of the selected operating scenario.

Parameter Influence. When focusing on the impact of the uncertain parameter variation on the sensitivities, the collision factors in the form of the dimensionless parameter A stand out in comparison to all other factors in the considered, averaged scenarios. Please note that although a negligible influence of the inhibition and equilibrium constants including the Gibbs reaction enthalpy is observed, these parameters may still be highly relevant in edge cases, i.e., in the absence of hydrogen or CO in the gas phase, which only contribute to a minor extend in fig. E.1. Especially the inhibition factors $K_{\mathrm{I,Hyfo}}$, $K_{\mathrm{II,Hyfo}}$, K_{HydDec}, K_{HydEn} and $K_{\mathrm{cat,CO}}$ have a comparatively small effect on the reaction rates in eq. (3.1) when multiplied with the liquid phase gas concentrations (cf. table B.9) under nominal, non mass transfer limited conditions. Therefore, accurate identification of these parameters requires dedicated gas perturbation experiments with accurate control trajectory realization and measurements. As the focus of the parameterization of the HAM kinetics lies on the adequate representation of the species concentrations with a

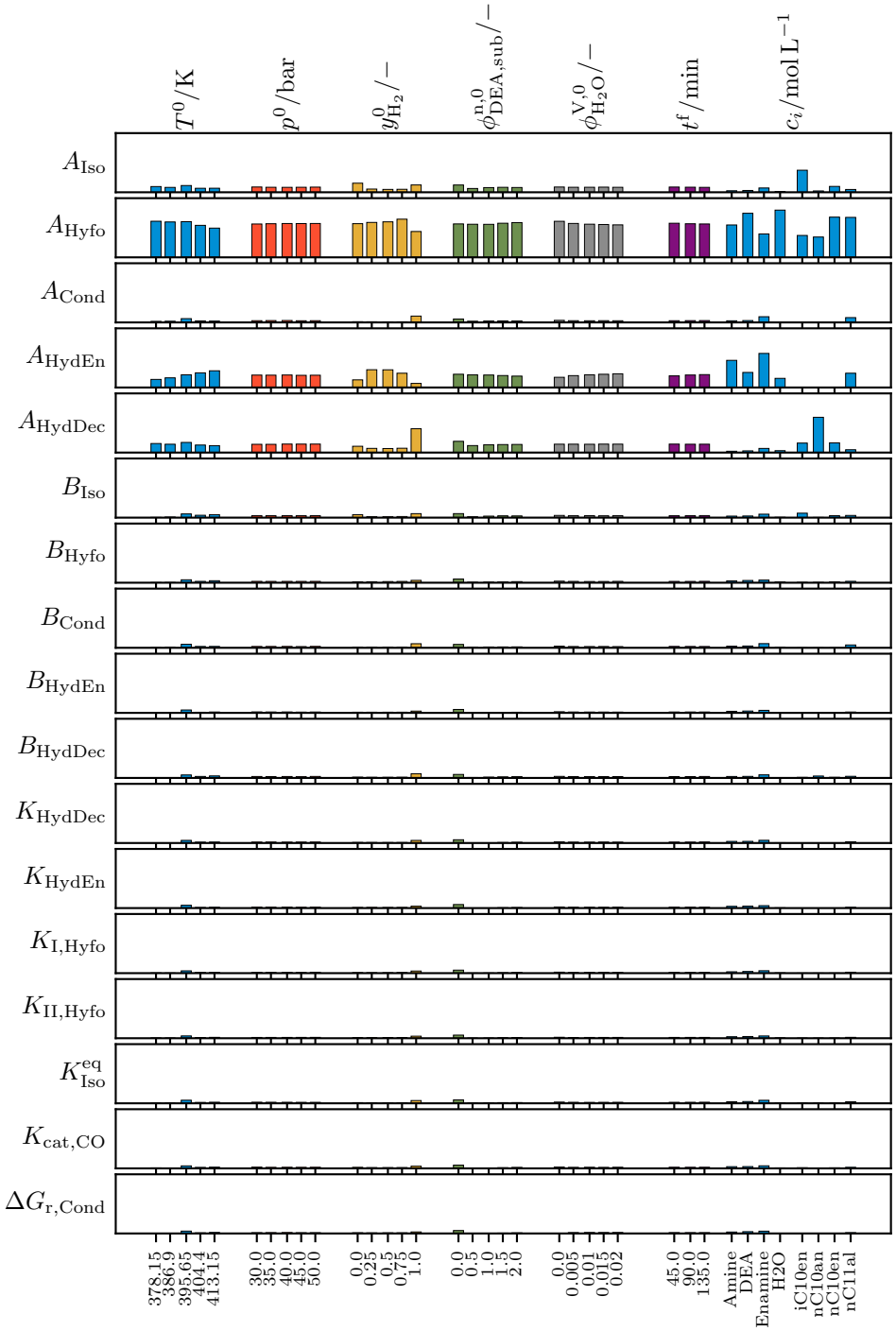

Fig. E.1.: Total order Sobol indices for the species concentrations w.r.t. all parameters in the HAM reaction kinetics in eq. (3.1). Averaged Sobol indices are presented for different control parameter choices, measurement time points and species concentrations. For the visual representation of each category, all other categories are averaged. Indications of the y-axis domain $[0, 1]$ are omitted for improved readability. The control parameter values are chosen on a linearly spaced, five element grid between the respective lower and upper bound values in table 3.1. Additionally, the sensitivities are calculated for each scenario at $t \in \{45, 90, 135\}$ min. For each scenario and time point, $2^8\,(n_\theta + 2)$ samples are drawn from a uniform distribution between $\pm 5\,\%$ of the nominal value value of the uncertain parameters in tables B.8, B.9 and B.11 [Sal+10].

limited number of experiments, experimental design for these parameters is of minor importance. Consequently, the inhibition parameters remain constant during mbOED. Likewise, $K_{\mathrm{Iso}}^{\mathrm{eq}}$ and $\Delta G_{\mathrm{r,Cond}}$ are fixed. While $K_{\mathrm{Iso}}^{\mathrm{eq}}$ is identified in separate, preliminary experiments (see fig. 3.2 in section 3.2), the Gibbs reaction enthalpy of the enamine condensation was identified by Kirschtowski et al. [Kir+20a] under comparable operating conditions.

Dimensionless Parameter Influence. Neglecting all inhibition and equilibrium parameters in the mbOED leads to a remaining set of uncertain parameters comprising the dimensionless kinetic parameters A_j and B_j with $j \in \mathcal{RCT}^{\mathrm{HAM}}$. In fig. E.1, the influence of A_j in contrast to B_j on the species concentrations is significantly more pronounced despite both entering in the exponential term of the temperature-centered Arrhenius approach in eq. (2.22). This is caused by the multiplication of the partial derivative $\frac{\partial f}{\partial \theta}$ in eq. (2.15) by $T_{\mathrm{red}}(t) = 1 - T_{\mathrm{ref}} T(t)^{-1}$ with T_{ref} on the same order of magnitude as T. Since this multiplicative factor does not lead to qualitative differences in the experimental designs, focusing the FIM on either A_j or B_j yields a significant reduction of the problem complexity and, thus, improves computational performance. However, regardless of the qualitatively similar sensitivity expressions for both dimensionless parameters, both still hold different information because of the reduced temperature $T_{\mathrm{red}}(t)$, especially in the case of dynamic temperature trajectories. Due to the need for complexity reduction of the eq. (3.6), the uncertain parameter vector θ is selected to contain the dimensionless activation energies B_j. A more detailed discussion of this topic can be found in appendix E.2.

Additional Complexity Reduction. In the last step, a physically motivated reduction of the set of uncertain parameters for the mbOED is applied. While estimating the hydroformylation of nC10en, subsequent condensation and hydrogenation of the enamine is critical in the reaction network in fig. 3.1 as it represents the main reaction pathway, the incorporation of the isomerization and hydrogenation of nC10en is debatable. Targeted experiments without the addition of co-substrate (DEA) may be better suited for the identification of the respective reaction parameters, since no constraints to ensure monophasic behavior need to be enforced under these operating conditions. Nevertheless, the dimensionless activation energy of the isomerization reaction B_{Iso} is considered in the uncertain parameter vector θ to support future investigations for the refinement of the reaction kinetic network w.r.t. isomer hydroformylation similar to Jörke et al. [Jör+17] and Hentschel et al. [Hen+15] as

well as aldehyde isomer reductive amination. Thus, the uncertain parameter vector for the following mbOED case study is represented by

$$\theta = \left[B_{\mathrm{Iso}}, B_{\mathrm{Hyfo}}, B_{\mathrm{Cond}}, B_{\mathrm{HydEn}}\right]. \tag{E.5}$$

E.2 Fisher Information Matrix Design for the Hydroaminomethylation of 1-Decene

Extension of the HAM process model in eq. (3.5) with the variational equations in eq. (2.15) for multiple experiments leads to a large-scale, complex DOP. To improve the optimization performance and reduce the degree of non-linearity, minimizing the number of variational equations by limiting the number of uncertain parameters is desirable. One approach to achieve this reduction relies on the analysis and simplification of the sensitivity matrices which are used to build the FIM.

For the HAM process model, the concentrations of selected species are considered as measured variables $y_i = c_i = n_i {V_{\mathrm{Liq}}}^{-1}$ with $i \in \mathcal{SPC}^y = \{$nC10en, iC10en, nC11al, DEA, En, Am, C10an, $H_2O\}$. As the influence of the kinetic parameters on and the dynamic behavior of the liquid volume V_{Liq} is negligible, the variational equations for experiment $k \in \{1, 2, \ldots, n_{\mathrm{exp}}\}$ can be simplified to

$$\begin{aligned}
\frac{\mathrm{d}}{\mathrm{d}t}\left(\frac{\mathrm{d}c_{i,k}}{\mathrm{d}\theta}\right) &= \frac{\mathrm{d}}{\mathrm{d}t}\left({V_{\mathrm{Liq}}}^{-1}\frac{\mathrm{d}n_{i,k}}{\mathrm{d}\theta} + n_{i,k}\frac{\mathrm{d}{V_{\mathrm{Liq}}}^{-1}}{\mathrm{d}\theta}\right) \\
&\approx \frac{\mathrm{d}}{\mathrm{d}t}\left({V_{\mathrm{Liq}}}^{-1}\frac{\mathrm{d}n_{i,k}}{\mathrm{d}\theta}\right) \\
&\approx {V_{\mathrm{Liq}}}^{-1}\frac{\mathrm{d}}{\mathrm{d}t}\left(\frac{\mathrm{d}n_{i,k}}{\mathrm{d}\theta}\right) \\
&= {V_{\mathrm{Liq}}}^{-1}\left(\frac{\partial f}{\partial n_{i,k}}\frac{\mathrm{d}n_{i,k}}{\mathrm{d}\theta} + \frac{\partial f}{\partial \theta}\right), \quad \frac{\mathrm{d}n_{i,k}}{\mathrm{d}\theta}\left(t^0\right) = 0.
\end{aligned} \tag{E.6}$$

The partial derivative $\frac{\partial f}{\partial n_{i,k}}$ and the initial condition of the ODE system are identical for all possible sets of uncertain parameters so that $\frac{\partial f}{\partial \theta}$ needs to be investigated for reduction potential. The parameter vector θ is split into $\theta^{\mathrm{A}} = \left[A_{\mathrm{Iso}}, A_{\mathrm{Hyfo}}, A_{\mathrm{HydDec}}, A_{\mathrm{Cond}}, A_{\mathrm{HydEn}}\right]$ and $\theta^{\mathrm{B}} = \left[B_{\mathrm{Iso}}, B_{\mathrm{Hyfo}}, B_{\mathrm{HydDec}}, B_{\mathrm{Cond}}, B_{\mathrm{HydEn}}\right]$ for better visualization of the resulting FIM. With the uncertain parameters enter-

ing multiplicatively in the reaction rate equations, the reaction rate for reaction $j \in \mathcal{RCT}^{\mathrm{HAM}}$ can be written as $r_j = k_j(A_j, B_j, T(t), .)\zeta\left(c(t), .\right)$, leading to

$$\frac{\partial r_j}{\partial \theta_m^{\mathrm{A}}} = \begin{cases} k_j\left(A_j, B_j, T(t), .\right)\zeta\left(c(t), .\right) & \text{if } j = m, \\ 0 & \text{else,} \end{cases} \tag{E.7}$$

$$\frac{\partial r_j}{\partial \theta_m^{\mathrm{B}}} = \begin{cases} T_{\mathrm{red}}(t) k_j\left(A_j, B_j, T(t), .\right)\zeta\left(c(t), .\right) & \text{if } j = m, \\ 0 & \text{else,} \end{cases} \tag{E.8}$$

with $m \in \mathcal{RCT}^{\mathrm{HAM}}$ and $T_{\mathrm{red}}(t) = 1 - T_{\mathrm{ref}} T(t)^{-1}$. Please note that the experiment index is omitted for improved readability. At this point it becomes already clear that the sensitivity matrices and FIM w.r.t. θ^{B} only differ from the matrices concerning θ^{A} by the multiplicative factor $T_{\mathrm{red}}(t)$ and $T_{\mathrm{red}}^2(t)$, respectively. This also explains the significantly smaller Sobol indices in fig. E.1 for all dimensionless activation energies B_j because $0 \leq T_{\mathrm{red}}^2(t) \ll 1$. Although factorization of T_{red} from the resulting FIM $F(\theta^{\mathrm{B}})$ is not possible in the case of dynamic temperature trajectories or multiple experiments with different temperatures, this multiplicative factor does not change the entries in the matrix relative to each other but scales the entire matrix. Consequently, performing mbOED with either $F(\theta^{\mathrm{A}})$ or $F(\theta^{\mathrm{B}})$ leads to experimental designs with equal importance placed on each of the reaction rates.

E.3 The Impact of Water on Experimental Designs

The mbOED for the hydroaminomethylation of 1-decene yields two experimental designs in which water is provided to the reaction system in addition to the water formation during the enamine condensation. Apart from the increase of the phase separation risk during the experiment, it is not clear whether this application of the optimized control parameter results in a beneficial reduction of the parameter uncertainties. Therefore, both designs are simulated again using the same control profiles and control parameters from table 3.3 but with $\phi_{\mathrm{H_2O}}^{\mathrm{V},0} = 0$. A comparison of the simulated concentration profiles to the original designs is depicted in fig. E.2.

Interpretation. The reduction of the water content leads to an increase in the product concentration alongside an expected decrease in DEA concentration. More pronounced concentration differences can be found for 1-undecanal (nC11al) and the enamine. By adding additional water to the reaction mixture, the equilibrium of the

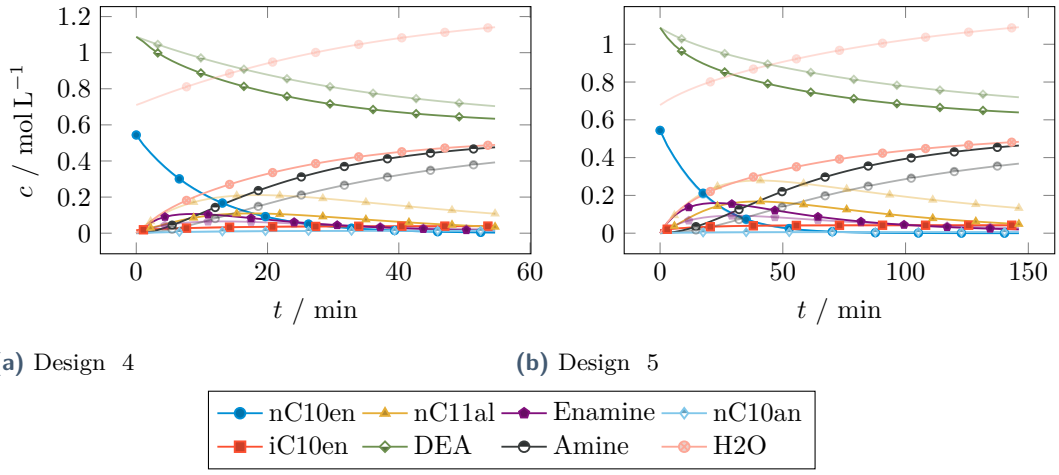

(a) Design 4 **(b)** Design 5

Fig. E.2.: Concentration profile comparison for designs 4 and 5 with (opaque plot lines) and without initial dosing of water.

condensation reaction (see eq. (3.1d)) is significantly shifted toward the aldehyde. When checking the difference in the size of the uncertainty ellipsoid volume, the standard deviations and parameter correlations in table E.1, both designs without additional water feed score worse. In the case of the uncertainty ellipsoid volume,

Tab. E.1.: Uncertainty ellipsoid volume $\Delta \det F^{-1} = \det F(\det F^{-1}_{\neg \mathrm{H_2O},k} - \det F^{-1})^{-1}$, standard deviation $\Delta\sigma_i = \left(\sigma_{i,\neg \mathrm{H_2O},k} - \sigma_i\right)\sigma_i^{-1}$ and correlation matrix $\Delta|\rho_{i,j}| = |\rho_{i,j,\neg \mathrm{H_2O},k}| - |\rho_{i,j}|$ difference with $i,j \in \{\text{Iso, Hyfo,Cond, HydEn}\}$ where the index $\square_{\neg \mathrm{H_2O},k}$ indicates the absence of initial water dosing in experimental design $k \in \{4,5\}$. Positive values negatively impact the respective performance measure in the case of no initial water dosing. The standard deviations and correlation coefficients are associated with the dimensionless activation energy B.

	$\Delta \det F^{-1}$ / %	$\Delta\sigma$ / %		Absolute Correlation Difference $\Delta\lvert\rho\rvert$			
				Iso	Hyfo	Cond	HydEn
Design 4	16	Iso	−0.04	Iso	-	0.00	0.00	0.00
		Hyfo	−2.28	Hyfo	-	-	0.01	−0.01
		Cond	−0.28	Cond	-	-	-	0.01
		HydEn	10.59	HydEn	-	-	-	-
Design 5	39	Iso	−0.13	Iso	-	0.00	0.00	0.00
		Hyfo	0.31	Hyfo	-	-	0.01	0.01
		Cond	0.30	Cond	-	-	-	0.02
		HydEn	17.92	HydEn	-	-	-	-

an increase of up to 39 % is visible accompanied by an approximately 18 % larger standard deviation for the enamine hydrogenation. Especially the latter aspect is interesting since reduced enamine concentrations are observable when adding water

to the system. Consequently, slowing down the fast enamine hydrogenation improves the identifiability of the corresponding kinetic parameters drastically.

F

Experimental Investigation and Parameter Identification for the Hydroaminomethylation of 1-Decene

This appendix contains additional information w.r.t. the experimental investigation of and subsequent parameter identification for the hydroaminomethylation of 1-decene.

F.1 Experiments

All experiments were performed by Wieland Kortuz from the Otto von Guericke University in Magdeburg. In the following paragraphs, the reactor setup is described briefly, an overview over all experiments is presented and the motivation for the different experiment categories is discussed. The information concerning the reactor setup were either provided directly by Wieland Kortuz or taken from Kortuz et al. [Kor+22] and the Bachelor Thesis [Bau21]. For detailed information regarding the experiment procedure, please consult these references and resources.

Experimental Setup. For the investigation of the reaction system, a multi-reactor system (MRS 5000) with six heated reactor vessels and six gas burettes from Parr were used. A schematic picture of the setup is displayed in fig. F.1. Each reactor vessel consists of a reactor lid and a reactor pot (75 mL) with a total volume of 135.47 mL. The reactors are operated with a magnetic stirrer, heated via a heating/cooling jacket, pressurized through the gas burettes up to 100 bar and depressurized using a vacuum pump which is also able to remove flue gases. The reactor lid contains additional fittings which allow for sampling and insertion of the temperature as well as pressure sensors. While samples are drawn by opening valve V2 and analyzed with an offline gas chromatograph with flame ionization detector, the substrate enters the system through valve V3 in the case of negative pressure in the receiver vessel G (47.5 mL). From this tank, valve V1 controls the

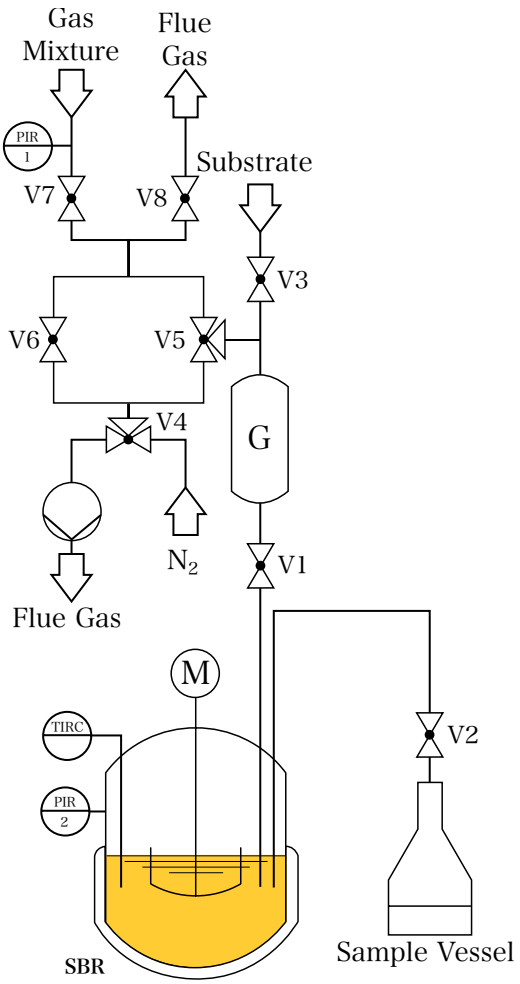

Fig. F.1.: Experimental setup for the kinetic investigation of the hydroaminomethylation of 1-decene. M: Stirrer, V: Valve, G: Receiver tank, PIR: Pressure sensor, TIRC: Temperature sensor and control.

connection to the reactor vessel. Pressurization via the gas mixture is controlled by valves V5 and V7 while depressurization and nitrogen purging is performed using valves V5 and V4. To improve the mixing of the gas phase in the reactor vessel, periodic purging of the gas phase is enabled by an additional pipe connected to the flue gas outlet (see table F.1 for the indication *Mod. Setup*). This supplementary purge pipe is not shown in fig. F.1.

Experiment Overview. An overview over all experiments is presented in table F.1. This table contains not only experiments which were performed according to the experimental designs from section 3.4 (first half) but also previous published [Kor20; Kor+22] and unpublished experiments by Kortuz et al. (second half). The incorporation of these additional experimental results is necessary to prevent a local

Tab. F.1.: Experiment plan for the HAM of 1-decene in a MeOH/nC12an TMS with the SulfoXantphos ligand and $n^0_{sub} = 27.20\,mmol$, $\phi^m_{MeOH,nC12an} = 1$, $\phi^{n,0}_{cat,sub} = 0.08 \times 10^{-2}$, $\phi^n_{Lig,\Sigma cat} = 3.5$. From the total vessel volume of 135.47 mL, the liquid phase requires 50 mL at 25 °C. The purities of methanol, decene, dodecane, and diethylamine are above 99 %, 98 %, 99 %, and 99.5 %, respectively, with decene containing over 95 % of 1-decene and approximately 3 % of decene isomers and decane. While the regular experimental setup operates in terms of gas supply in semibatch mode which maintains the desired pressure by replenishing the consumed gas from a burette, a periodic purge of the gas phase is performed in the modified setup to reduce the accumulation of individual gas species. All experiments were performed by Wieland Kortuz from the Otto von Guericke University. The second half of the table contains published [Kor20; Kor+22] and unpublished experimental data from Kortuz et al. which add additional information on the temperature dependency and ensure validity of the extended reaction kinetic model.

Exp	t^f	$\phi^{n,0}_{DEA,sub}$	$\phi^{V,0}_{H_2O}$	y_{H_2}	y_{CO}	y_{N_2}	ϑ	p	Mod.	Fit
	min	–	vol%		mol %		°C	bar	Setup	
49a_D1	53	0.50	0.00	80	20	0	140	dyn	no	yes
49b_D1#	53	0.48	0.00	80	20	0	140	dyn	no	yes
48a_D2	50	0.71	0.00	80	20	0	133	50	no	yes
53a_D3	144	2.07	0.00	10	20	70	140	50	no	yes
53b_D3	180	2.02	0.00	10	20	70	140	50	yes	yes
53c_D3	180	2.02	0.00	10	20	70	140	50	yes$^+$	yes
54a_D3	180	1.15	0.00	10	20	70	140	50	yes	yes
55a_D3	150	2.02	0.00	33	67	0	140	30	no	no
55b_D3#	150	2.01	0.00	33	67	0	140	30	no	no
56a_D3	150	2.04	0.00	33	67	0	140	50	no	yes
50a_D4	55	2.03	1.26*	33	67	0	140	50	no	yes
50b_D4	55	2.01	1.26*	33	67	0	140	50	yes	yes
16a	180	1.17	0.00	67	33	0	125	40	no	yes
16b#	180	1.17	0.00	67	33	0	125	40	no	no
19a	180	1.18	0.00	67	33	0	140	40	no	yes
19b#	180	1.19	0.00	67	33	0	140	40	no	no
20a$^-$	180	1.18	0.00	67	33	0	100	40	no	yes
20b#	180	1.18	0.00	67	33	0	100	40	no	no
22a	180	1.17	0.00	67	33	0	125	30	no	yes
22b#	180	1.16	0.00	67	33	0	125	30	no	no
27a	180	1.19	0.00	67	33	0	115	30	no	yes
27b#	180	1.17	0.00	67	33	0	115	30	no	no

Identical repetition. * Reduced water content as a safety margin. $^+$ Changed gas sequence for the burette preparation. $^-$ Monophasic conditions checked via simulation.

parameter optimum during parameter identification (see section 3.4.3). In addition to the five designs from the mbOED, experiment repetitions (e.g., 49a_D1 and 49b_D1, 55a_D3 and 55b_D3), experiments with a modified experimental setup (e.g., 53b_D3 and 53c_D3, 50a_D4 and 50b_D4) and experiments with alterations to the original design (all D3 experiments) can be found.

Modified Experimental Setup. Besides repetition experiments which were performed to verify the reproducibility of an experiment in the case of surprising concentration profiles, the modified experimental setup was used to test the hypothesis of the accumulation of selected gases in the gas phase due to an elevated consumption of the opposing gaseous species in the reaction. Prior to the introduction of a rigorous gas phase model (see section 3.5.1), an additional exhaust pipe was installed to allow for the periodic manual purge of a portion of the gas phase in the reactor vessel so that the gas mixing is promoted and the original gas ratio from the burette is restored. The influence of this periodic purge is observable in fig. F.2 for four selected experiments. Experiment 53a_D3 and 53b_D3 as well as 50a_D4 and 50b_D4 represent pairwise repetitions of the same experimental design where one is performed without (a) and one with (b) periodic purging of the gas phase. The pressure of both experiments with gas purging indicates that only a small percentage of the gas phase is exchanged to prevent evaporation of DEA because of its low vapor pressure. Consequently, the effect on the gas phase composition is negligible as indicated in the control profiles. Only in experiment 53b_D3, where hydrogen is exhausted after approximately 20 min, periodic purging and replenishing the gas phase has a measurable impact on the amine, water, and isomer concentrations.

Design Variations. Variations of experimental designs were performed to test the hypotheses of (i) a negative effect of increased DEA concentrations on the catalyst (compare 53a_D3 with 54a_D3), (ii) the impact of the filling sequence of the gases in the burette (compare 53b_D3 with 53c_D3) and (iii) a negative influence of nitrogen on the reaction (compare 53a_D3 with 55a_D3 and 55b_D3). Owing to the increased number of experiments and its similarity to experiment 56a_D3, design 5 from fig. 3.3 was not experimentally tested.

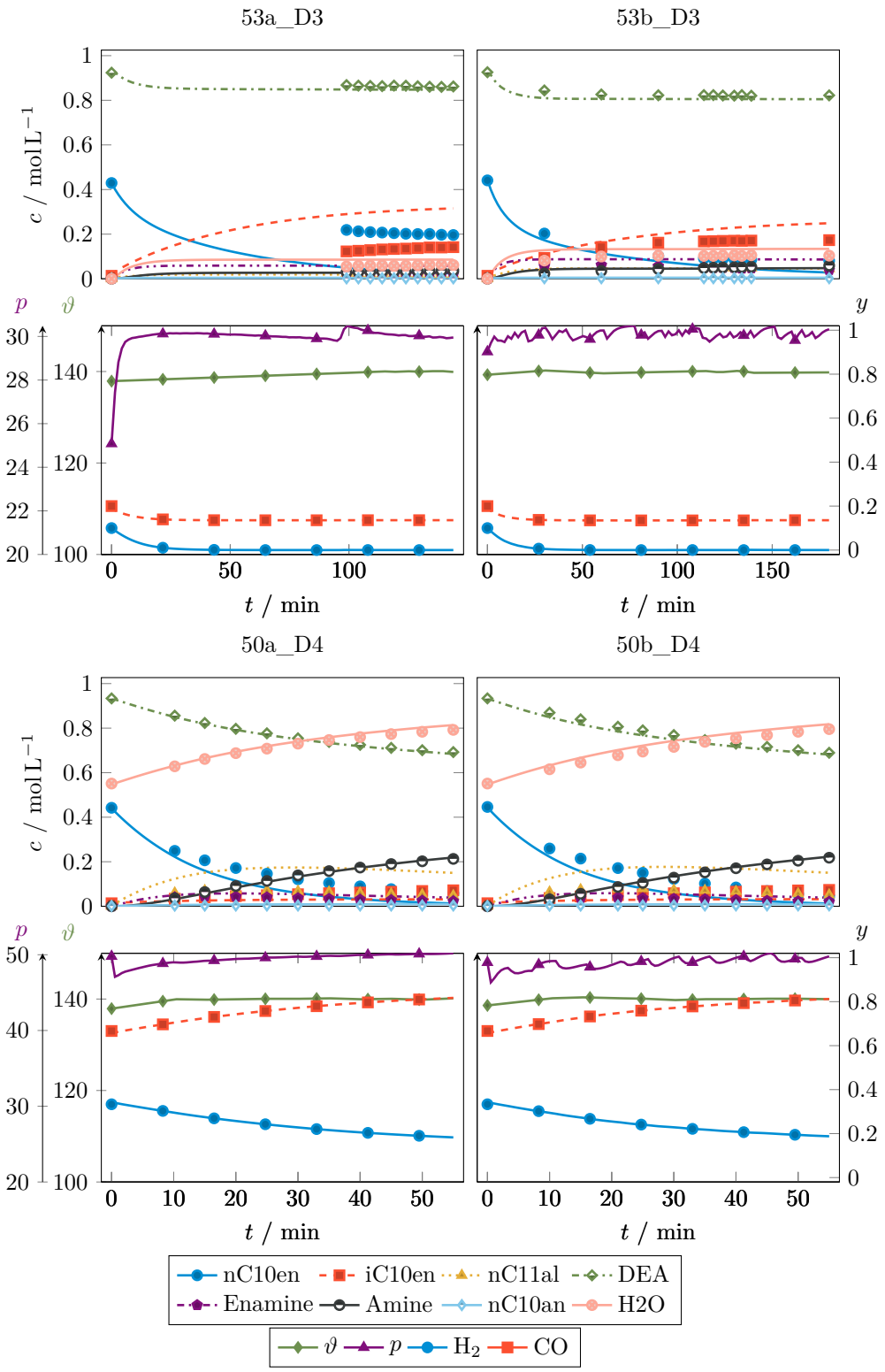

Fig. F.2.: Comparison of predicted concentration profiles for two experimental designs using the parameters from tables B.9 and B.11. Left: Nominal experimental setup. Right: Periodic purge of the gas phase.

F.2 Parameter Identification

The parameter identification for the kinetic model of the hydroaminomethylation of 1-decene is performed according to algorithm 2.

Algorithm 2 Multistart Parameter Estimation

Require: Reactor vessel model eq. (3.5) with the rigorous gas phase model from eq. (3.10).

Require: Experiment data in the form of output trajectories $\eta_i(t_{\mathrm{sp},j,k})$ at all measurement points $k \in \{1, 2, \ldots, n_{\mathrm{sp},j}\}$ with $i \in \mathcal{SPC}^y$, temperature $T(t_j)$ and pressure $p(t_j)$ profiles in addition to the control parameters p_j for all $j \in \mathcal{EXP} = \{1, 2, \ldots, n_{\mathrm{exp}}\}$ experiments.

Require: Initial parameter guesses θ^0, e.g., from tables B.9 and B.11 and parameter bounds $\theta_i \in \Theta_i = \left[\theta_i^{\mathrm{L}}, \theta_i^{\mathrm{U}}\right]$ with $i \in \{1, 2, \ldots, n_\theta\}$.

Require: The measurement covariance matrix $\Sigma_y \in \mathbb{R}^{n_y \times n_y}$ with $\Sigma_y = \Sigma_y^\top$.

Require: The invertibility and collinearity thresholds $\kappa_{\max} = \left(n_\theta \sqrt{\varepsilon}\right)^{-1}$ [Jör+17] and $\gamma_{\max} = 15$ [Bar+13], respectively, with ε denoting the machine precision.

Initialize the results set $\mathcal{D} \leftarrow \emptyset$.
Solve the generalized LSQ problem $\hat{\theta}, \Sigma_\theta, \frac{\mathrm{d}y}{\mathrm{d}\theta}, \phi \leftarrow$ eq. (2.17)$(\eta, \theta^0, \Theta,$ eqs. (3.5) and (3.10)$)$.
Evaluate $n_{\theta,+}, \hat{\theta}_+ \leftarrow$ Parameter Subset Selection$(\hat{\theta}, \frac{\mathrm{d}y}{\mathrm{d}\theta})$.
while $n_{\theta,+} < n_\theta$ **do** ▷ *Find an identifiable parameter set*
  Set $n_\theta, \theta^0 \leftarrow n_{\theta,+}, \hat{\theta}_+$.
  Adjust Θ to the new number of parameters n_θ.
  Resolve the LSQ problem $\hat{\theta}, \Sigma_\theta, \frac{\mathrm{d}y}{\mathrm{d}\theta}, \phi \leftarrow$ eq. (2.17)$(\eta, \theta^0, \Theta,$ eqs. (3.5) and (3.10)$)$.
  Evaluate $n_{\theta,+}, \hat{\theta}_+ \leftarrow$ Parameter Subset Selection$(\hat{\theta}, \frac{\mathrm{d}y}{\mathrm{d}\theta})$.
Store the first result $\mathcal{D} \leftarrow \left\{(\hat{\theta}_+, \Sigma_\theta, \phi)\right\} \cup \mathcal{D}$.
Set $n_\theta, \theta^0 \leftarrow n_{\theta,+}, \hat{\theta}_+$.
Adjust Θ to the new number of parameters n_θ.
Create a Sobol sampling grid $\mathcal{G} = \left\{\theta_1^0, \theta_2^0, \ldots, \theta_m^0\right\}$ [Sob67] with $\theta_i^0 \in \Theta$, $i \in \{1, 2, \ldots, m\}$ and $m = 2^2(2n_{\theta,+} + 2)$ grid points from $\Theta \subset \mathbb{R}^{n_\theta}$.
▷ *Continued on the next page* ◁

For a concise overview over the model prediction quality, parity plots for all liquid species can be found in fig. F.3. A detailed insight in the prediction quality is possible via the concentration profiles for all experiments from table F.1 in fig. F.4.

▷ *Continued* ◁

for all $\theta^0 \in \mathcal{G}$ **do** ▷ *Multistart*

Solve the LSQ problem $\hat{\theta}, \Sigma_\theta, \frac{\mathrm{d}y}{\mathrm{d}\theta}, \phi \leftarrow$ EQ. (2.17)$(\eta, \theta^0, \Theta,$ eqs. (3.5) and (3.10)$)$.

Compute $n_{\theta,+,\kappa} \leftarrow$ INVERTIBILITY CHECK$(\frac{\mathrm{d}y}{\mathrm{d}\theta})$.

Compute $n_{\theta,+,\gamma} \leftarrow$ COLLINEARITY CHECK$(\frac{\mathrm{d}y}{\mathrm{d}\theta})$.

if $n_{\theta,+,\kappa} = n_{\theta,+,\gamma} = n_\theta$ **then**

Store the results $\mathcal{D} \leftarrow \left\{(\hat{\theta}, \Sigma_\theta, \phi)\right\} \cup \mathcal{D}$.

Find the minimum cost $\phi_{\min} = \operatorname{argmin} \{\phi_k\}_{k=1}^{|\mathcal{G}|}$ from the entries in $\mathcal{D}$ and the associated parameter estimates $\hat{\theta}_{\min}$ and uncertainties $\Sigma_{\theta_{\min}}$.

return $\hat{\theta}_{\min}$, $\Sigma_{\theta_{\min}}$

---

procedure PARAMETER SUBSET SELECTION($\hat{\theta} \in \mathbb{R}^{n_\theta}$, $\frac{\mathrm{d}y}{\mathrm{d}\theta} \in \mathbb{R}^{n_{\mathrm{exp}} n_{\mathrm{sp}} n_y \times n_\theta}$)

▷ *Procedure from Barz et al. [Bar+13]* ◁

$n_{\theta,+,\kappa} \leftarrow$ INVERTIBILITY CHECK$(\frac{\mathrm{d}y}{\mathrm{d}\theta})$.

$n_{\theta,+,\gamma} \leftarrow$ COLLINEARITY CHECK$(\frac{\mathrm{d}y}{\mathrm{d}\theta})$.

if $n_{\theta,+,\kappa} = n_{\theta,+,\gamma} = n_\theta$ **then**

return n_θ, $\hat{\theta}$.

else

Determine $n_{\theta,+} = \min(n_{\theta,+,\kappa}, n_{\theta,+,\gamma})$.

$P \leftarrow$ QR DECOMPOSITION$(\frac{\mathrm{d}y}{\mathrm{d}\theta})$ with $P \in \mathbb{R}^{n_\theta \times n_\theta}$ denoting the permutation matrix.

Sort the parameter vector $\tilde{\theta} = P^\top \hat{\theta}$.

Partition the sorted parameter vector $\tilde{\theta} = \left(\tilde{\theta}_+, \tilde{\theta}_-\right)$ so that $\tilde{\theta}_+ \in \mathbb{R}^{n_{\theta,+}}$ contains the first $n_{\theta,+}$ parameters.

return $n_{\theta,+}$, $\tilde{\theta}_+$

procedure INVERTIBILITY CHECK($\frac{\mathrm{d}y}{\mathrm{d}\theta} \in \mathbb{R}^{n_{\mathrm{exp}} n_{\mathrm{sp}} n_y \times n_\theta}$)

Calculate the singular values $s = \mathrm{SVD}\left(\frac{\mathrm{d}y}{\mathrm{d}\theta}\right) \in \mathbb{R}^{n_\theta}$.

Compute $\kappa = \max(s) s^{-1}$.

Determine $n_{\theta,+}$ as the number of entries in κ which fulfill $\kappa < \kappa_{\max}$.

return $n_{\theta,+}$

procedure COLLINEARITY CHECK($\frac{\mathrm{d}y}{\mathrm{d}\theta} \in \mathbb{R}^{n_{\mathrm{exp}} n_{\mathrm{sp}} n_y \times n_\theta}$)

Calculate the singular values $s = \mathrm{SVD}\left(\frac{\mathrm{d}y}{\mathrm{d}\theta}\right) \in \mathbb{R}^{n_\theta}$.

Compute $\gamma = s^{-1}$.

Determine $n_{\theta,+}$ as the number of entries in γ which fulfill $\gamma < \gamma_{\max}$.

return $n_{\theta,+}$

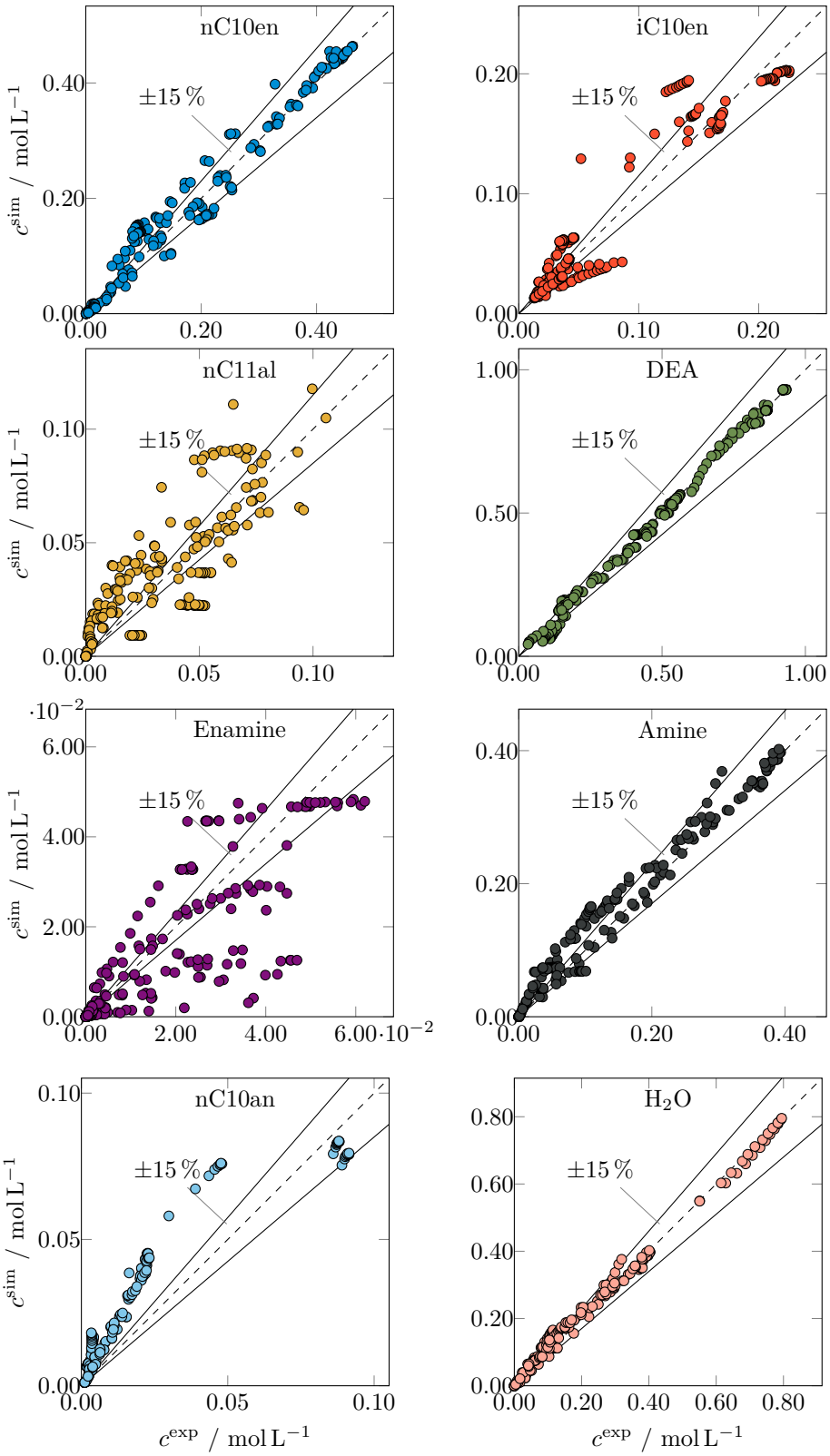

Fig. F.3.: Parity plots comparing the predicted $\square^{\mathrm{sim}}$ and experimental $\square^{\mathrm{exp}}$ concentrations for the hydroaminomethylation experiments from table F.1 without experiment 55a_D3 and 55b_D3. For the predictions, the estimated parameters from table 3.5 are used.

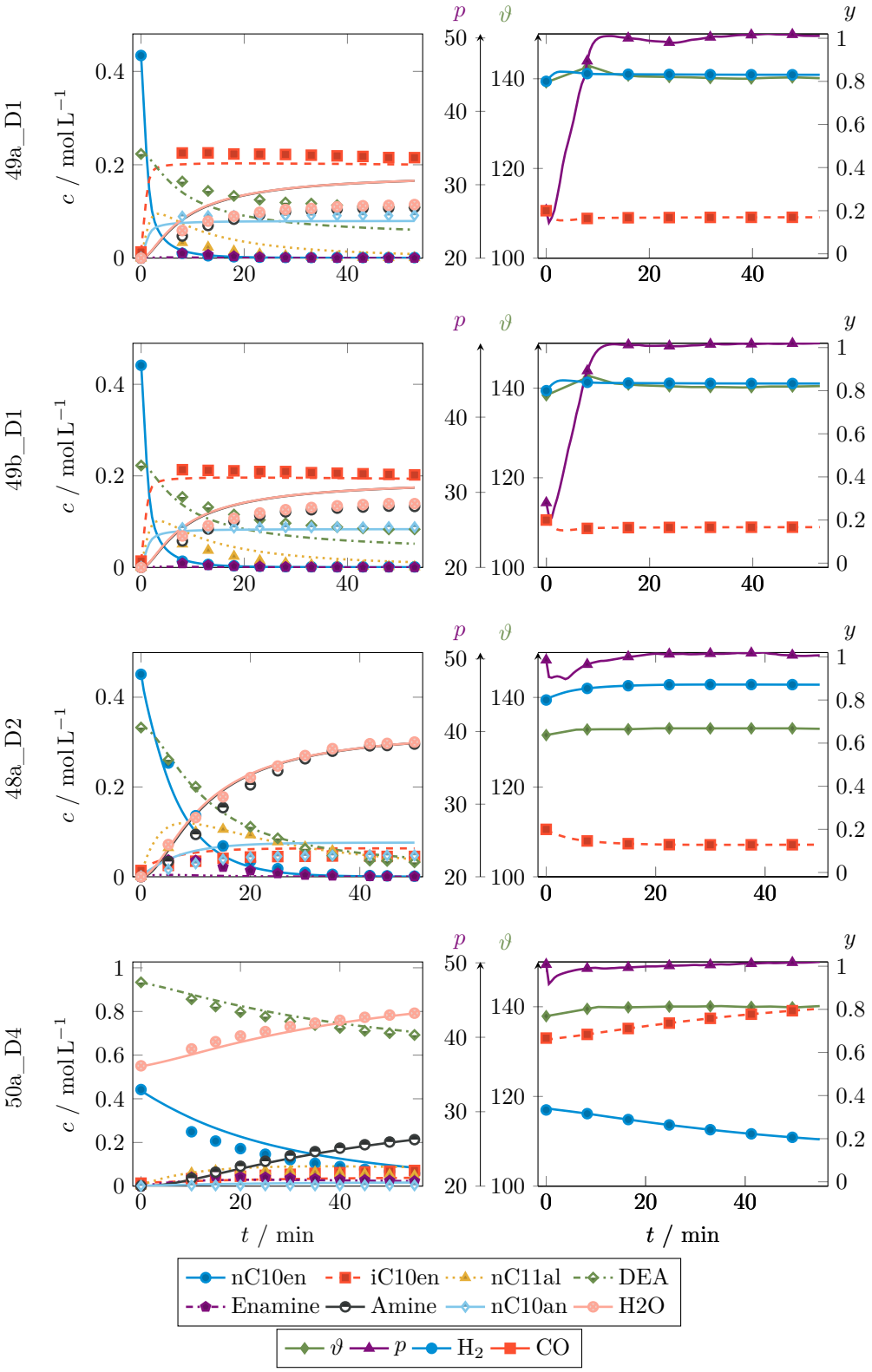
49a_D1
49b_D1
48a_D2
50a_D4
c / mol L⁻¹
p
ϑ
y
t / min
nC10en
iC10en
nC11al
DEA
Enamine
Amine
nC10an
H2O
ϑ
p
H2
CO

(F.4-1) Part 1/6.

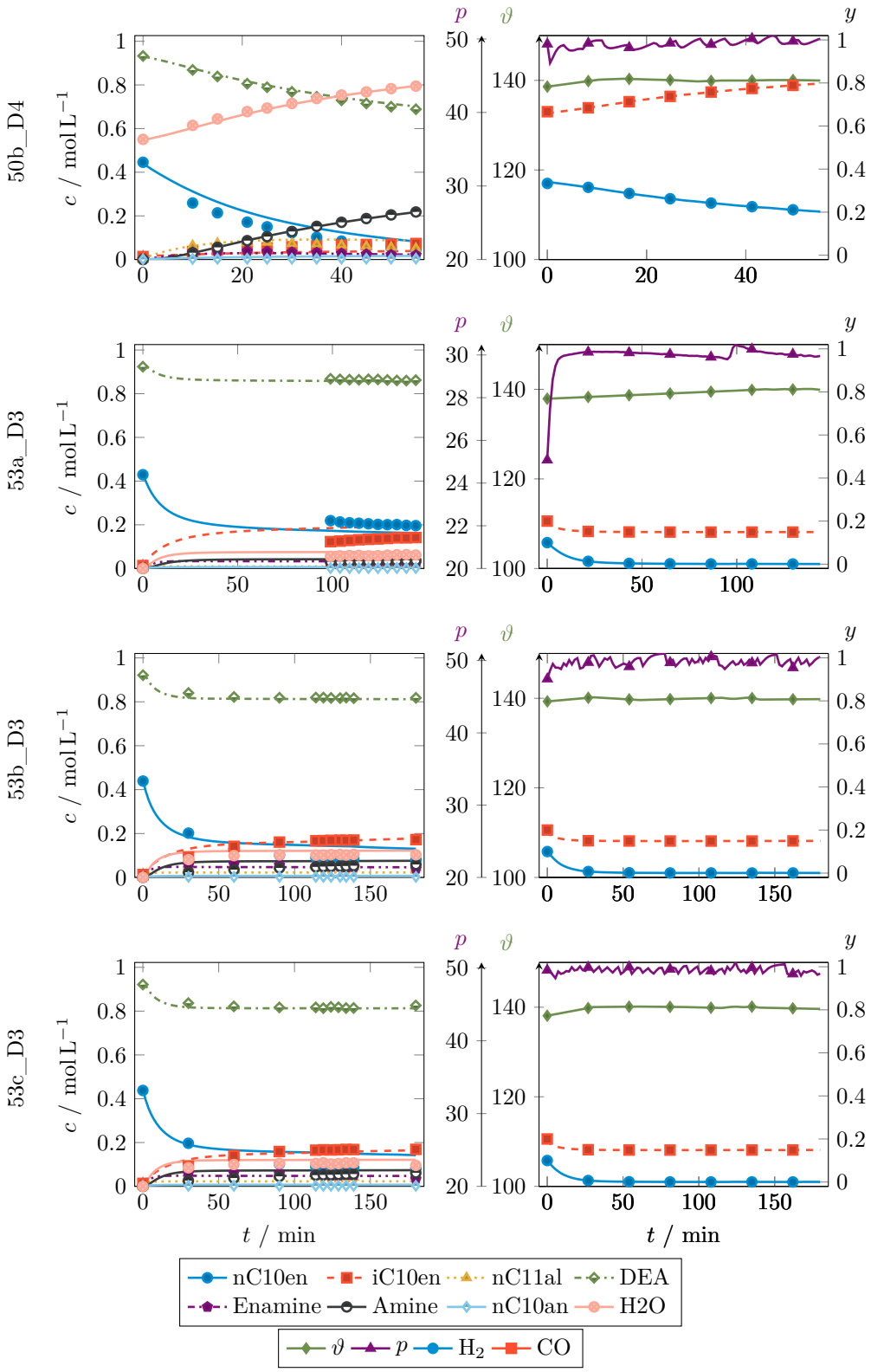
50b_D4
53a_D3
53b_D3
53c_D3
c / mol L⁻¹
p
ϑ
y
t / min
nC10en
iC10en
nC11al
DEA
Enamine
Amine
nC10an
H2O
ϑ
p
H2
CO

(F.4-2) Part 2/6.

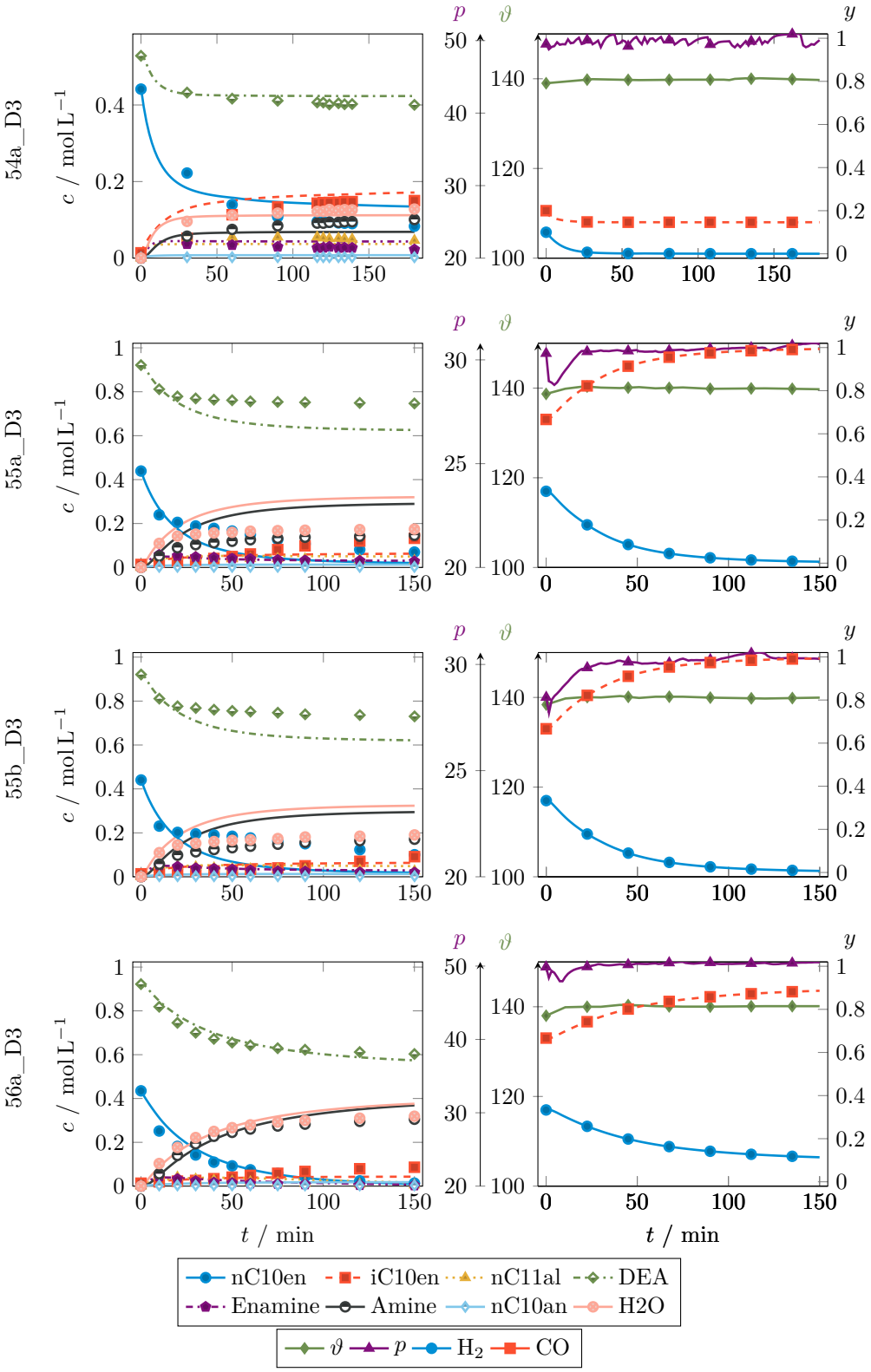
54a_D3
55a_D3
55b_D3
56a_D3
c / mol L−1
p
ϑ
y
t / min
nC10en
iC10en
nC11al
DEA
Enamine
Amine
nC10an
H2O
ϑ
p
H2
CO

(F.4-3) Part 3/6.

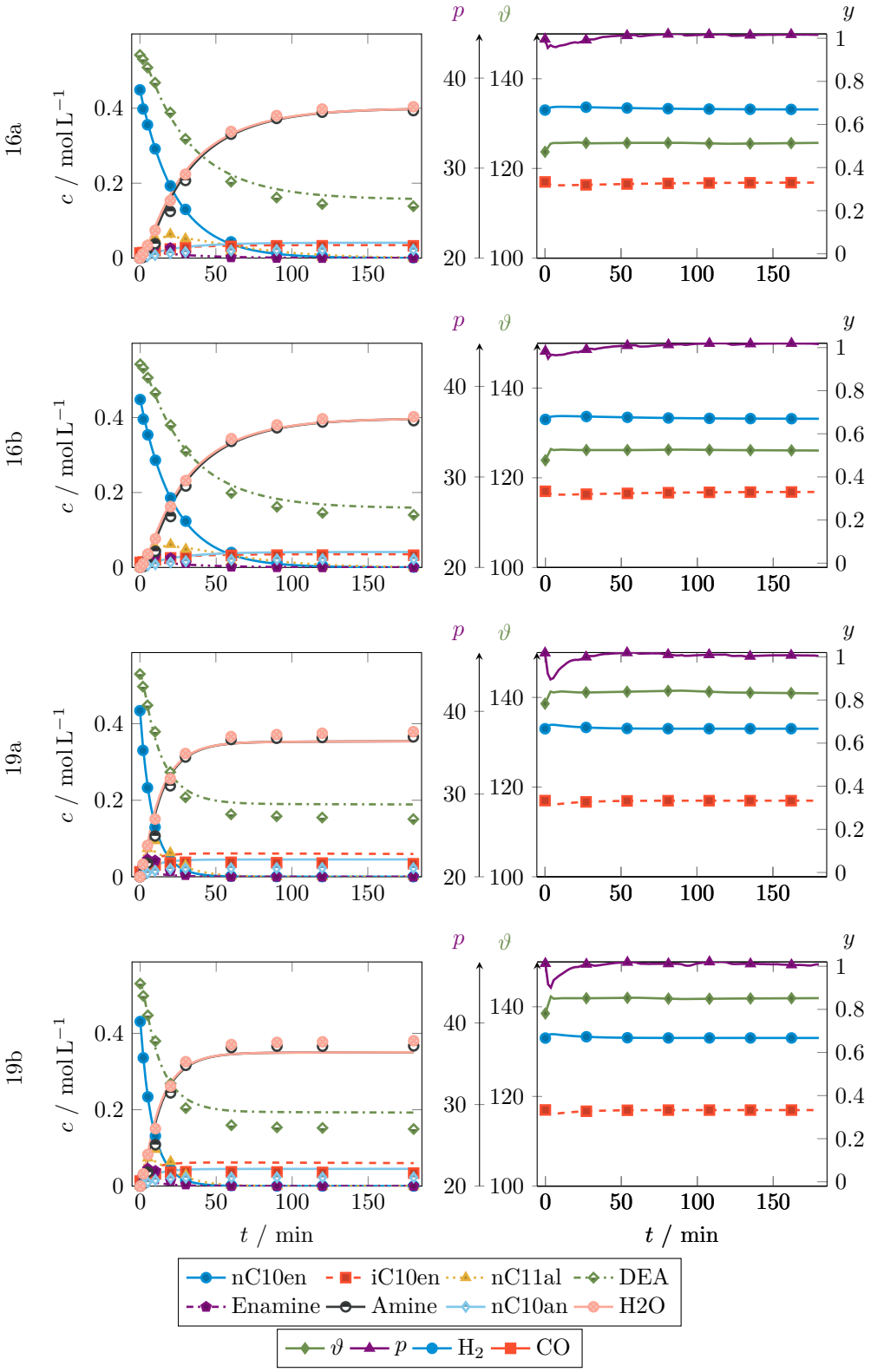
16a
16b
19a
19b
c / mol L⁻¹
p
ϑ
y
t / min
nC10en
iC10en
nC11al
DEA
Enamine
Amine
nC10an
H2O
ϑ
p
H2
CO

(F.4-4) Part 4/6.

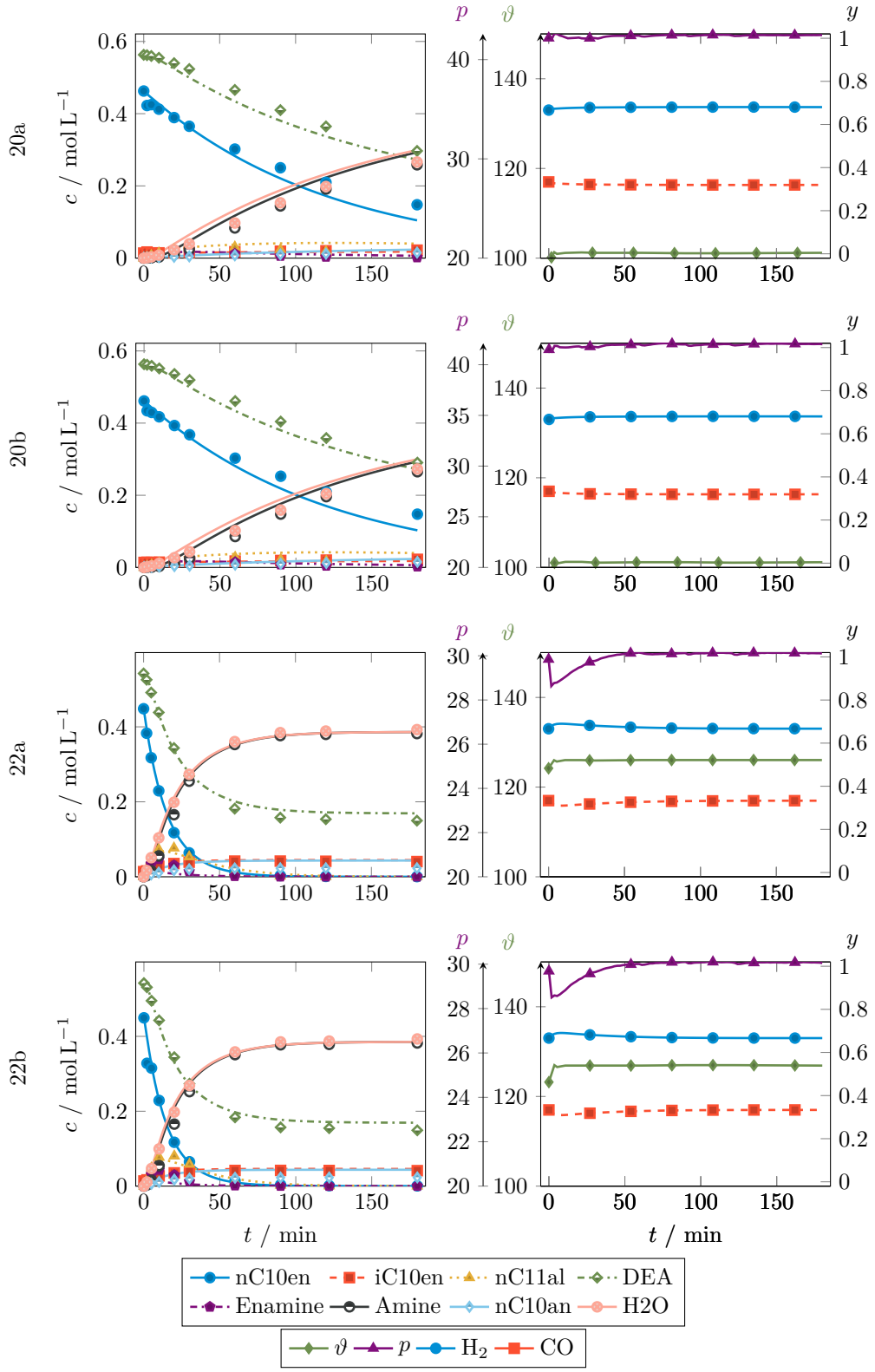
20a
20b
22a
22b
c / mol L⁻¹
p
ϑ
y
t / min
nC10en
iC10en
nC11al
DEA
Enamine
Amine
nC10an
H2O
ϑ
p
H2
CO

(F.4-5) Part 5/6.

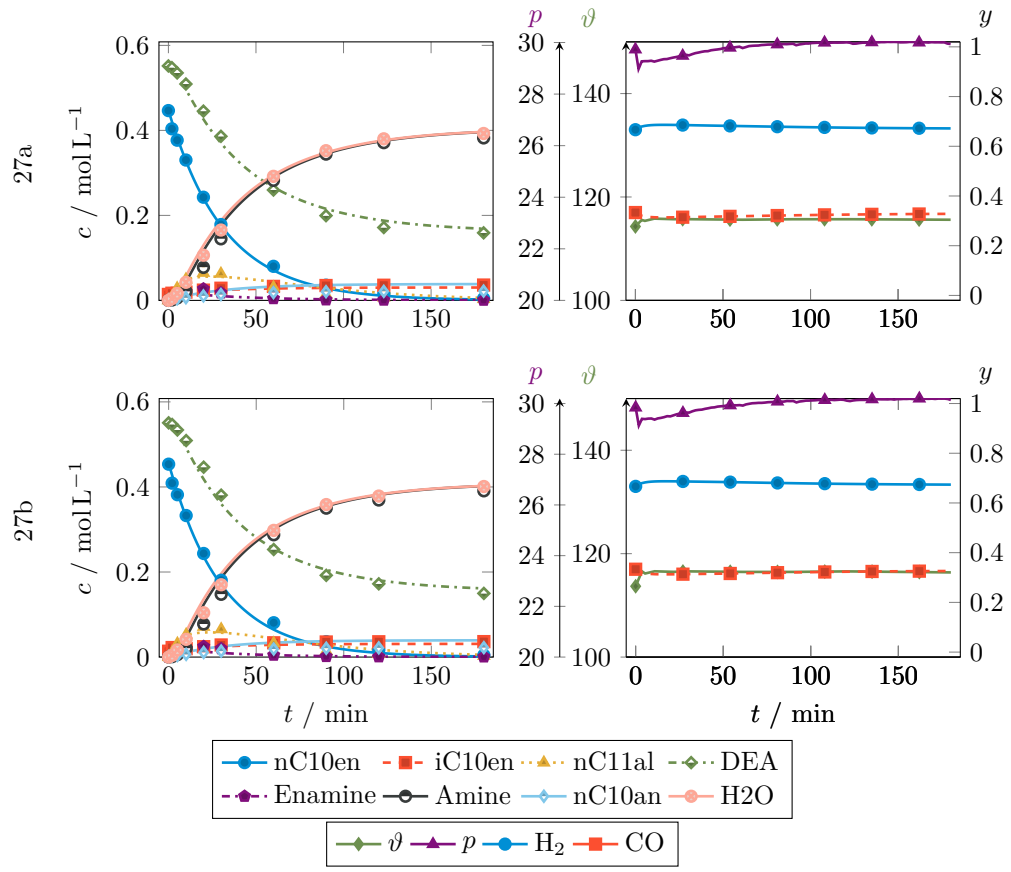

(F.4-6) Part 6/6.

Fig. F.4.: Comparison of predicted and experimental concentration profiles for all experimental designs from table F.1. For the prediction, the rigorous gas phase model from eq. (3.10) together with the estimated parameters from table 3.5 is used. Left: Predicted and experimental concentration profiles. Lines visualize the simulated trajectories while marks represent the experimental data. Right: Total pressure, gas phase composition and the temperature control profiles. Please note that the nitrogen content can be calculated over the closing condition.

G Process Models for the mpEPF Formulation

This appendix contains implementation details for the mpEPF formulation and its application to the hydroaminomethylation as well as to the generic example reaction.

G.1 Hydroaminomethylation

The hydroaminomethylation reaction kinetics need to be embedded in a model formulation which fits the requirements of the EPF methodology.

EPF Model Requirements. This model formulation contains mass balances using molar amounts to track species $i \in \mathcal{SPC}$ in the fluid element(s)/phase $\pi \in \Pi$. Due to the consideration of external dosing fluxes to improve process performance by simulating distributed dosing of substrates or axial dispersion, storage tanks need to be included via additional states $n_{\mathrm{ST},i}(t)$. These storage tanks hold a predefined amount for each species i at $t = 0$ which the optimizer may use for dosing into phase π. In addition to constraints which ensure closed mass balances for intermediate and final products (see Kaiser et al. [KFS17] for a detailed explanation of the storage tank formulation for the EPF methodology), control variables need to be selected which (i) can be technically implemented in the process and (ii) allow for sufficiently smooth control profiles to improve numeric stability. A model formulation for the hydroaminomethylation which considers all of the prior requirements reads

$$\text{Mass Balance of Fluid Element:} \begin{cases} \frac{\mathrm{d}n_i^{(\pi)}}{\mathrm{d}t} = j_i^{(\pi)} + V_{\mathrm{Liq}}^{(\pi)} \sum\limits_{j \in \mathcal{RCT}^{\mathrm{HAM}}} \nu_{i,j} r_j^{(\pi)}, \\ n_i^{(\pi)}\left(t^0\right) = n_i^{(\pi),0}, \end{cases} \tag{G.1a}$$

$$\text{Stoichiometry: Table B.12,} \tag{G.1b}$$

$$\text{Mass Balance of Storage: } \frac{\mathrm{d}n_{\mathrm{ST},i}}{\mathrm{d}t} = -\sum_{\pi \in \Pi} j_i^{(\pi)}, \quad n_{\mathrm{ST},i}\left(t^0\right) = n_{\mathrm{ST},i}^0, \tag{G.1c}$$

$$\text{Reaction Kinetics: Equations (2.22) and (3.1), table 3.5,}$$

$$\text{Assumptions:}\quad c_k^{(\pi)} = c_k^{\text{sat}}, \tag{G.1d}$$

Saturate Gas Concentration: Equation (2.24), table B.10,

$$\text{Summation:}\quad y_{\text{CO}}(t) = 1 - y_{\text{H}_2}(t), \tag{G.1e}$$

Catalyst Pre-Equilibrium: Equation (3.12),

Enamination Equilibrium: Equation (2.28),

$$\text{Control States:}\quad \begin{cases} \frac{\mathrm{d}T}{\mathrm{d}t} = s_T\left(t\right), T\left(t_0\right) = T^0, \\ \frac{\mathrm{d}y_{\text{H}_2}}{\mathrm{d}t} = s_{y_{\text{H}_2}}\left(t\right), y_{\text{H}_2}\left(t_0\right) = y_{\text{H}_2}^0, \\ \frac{\mathrm{d}p}{\mathrm{d}t} = s_p\left(t\right), p\left(t_0\right) = p^0, \end{cases} \tag{G.1f}$$

Composition Ratios: Equation (2.29c),

Thermodynamic Activities: Equation (3.6e),

$$\text{Concentration:}\quad c_i^{(\pi)}(t) = n_i^{(\pi)}(t) V_{\text{Liq}}^{(\pi)}(t)^{-1}, \tag{G.1g}$$

$$\text{Liquid Volume:}\quad \begin{cases} V_{\text{Liq}}^{(\pi)}(t) = \sum_{i \in \mathcal{SPC}} V_{\text{Liq},i}^{(\pi)}(t), \\ V_{\text{Liq},i}^{(\pi)}(t) = m_i^{(\pi)}(t) \rho_i(T)^{-1}, \\ m_i^{(\pi)}(t) = \tilde{M}_i n_i^{(\pi)}(t), \\ \text{Equation (3.4)}, \\ \text{Tables B.13 to B.15}, \end{cases} \tag{G.1h}$$

Reference Temperature: Equation (3.5j), (G.1i)

Bounds: Table G.1, (G.1j)

$$\text{Sets and Indices:}\quad \begin{cases} i \in \mathcal{SPC} = \{\text{nC10en, iC10en, C10an, DEA,} \\ \qquad\qquad \text{nC11al, En, Am, } \text{H}_2\text{O}, \\ \qquad\qquad \text{MeOH, nC12an}\}, \\ k \in \mathcal{SPC}^{\text{Gas}} = \{\text{H}_2, \text{CO}\}, \pi \in \Pi = \{\pi_1, \pi_2\}, \\ \mathcal{RCT}^{\text{HAM}} = \{\text{Iso, Hyfo, HydDec,} \\ \qquad\qquad \text{Cond, HydEn}\}, \\ \mathcal{SPC}^{\text{ANN}} = \{\text{nC10en, DEA, nC11al, Am,} \\ \qquad\qquad \text{H}_2\text{O, MeOH, nC12an}\}. \end{cases}$$

Associated model parameters are summarized in table G.1.

Tab. G.1.: States, control, and discretization parameters for the mpEPF calculation using the HAM model. All indices i and π relate to their corresponding set according to $i \in \mathcal{SPC}$ and $\pi \in \Pi$ from eq. (G.1). For the definition of the phase equilibrium calculation-related variables, please see section 2.1.

		Values		
Parameter	Unit	Init	LB	UB
$n_{\mathrm{max},i}$	mol	1	–	–
$n_i^{(\pi)}$	mol	$n_{\mathrm{max},i}/\lvert\Pi\rvert$	0	$\max(\nu)\sum_i n_{\mathrm{max},i}$
$n_{\mathrm{ST},i}$	mol	0	0	$n_{\mathrm{max},i}$
ϑ	°C	140	100	140
s_T	$\mathrm{K\,min^{-1}}$	0	−50	50
p	bar	50	30	50
s_p	$\mathrm{bar\,min^{-1}}$	0	−50	50
$y_{\mathrm{H_2}}$	$\mathrm{mol\,mol^{-1}}$	0.66	0	1
$s_{y_{\mathrm{H_2}}}$	$\mathrm{min^{-1}}$	0	−10	10
j_i	$\mathrm{mol\,min^{-1}}$	1	0	1
$\mathcal{A}$	$\mathrm{m^2}$	1×10^3	1	1×10^6
t^{f}	min	180	–	–
$\beta^{(\pi)}$	$\mathrm{mol\,min^{-1}\,m^{-2}}$	1	–	–
κ	$\mathrm{mol\,mol^{-1}}$	0.3	–	–
n_{FE}	–	20	–	–
h_{FE}	–	0.05	0.05	0.05
$n_{\mathrm{FE}}^{\mathrm{eq}}$	–	15	–	–
$h_{\mathrm{FE}}^{\mathrm{eq}}$	–	0.0667	0.05	0.10
n_{CP}, $n_{\mathrm{CP}}^{\mathrm{eq}}$	–	3	–	–

mpEPF DOP Formulation. Using this model, a DOP can be designed which connects the regular EPF methodology with phase equilibrium calculations, leading to the mpEPF formulation

$$\min_{u(t),p,\mathcal{X}^0} \quad \phi \tag{G.2a}$$

s. t.

Process Model: Equation (G.1) or eq. (G.5),

$$\text{Operating Constraints:} \begin{cases} j_i^{(\pi)}(t) = j_i^{(\alpha)}(t), \\ \sum_{\pi\in\Pi} n_i^{(\pi),0} + n_{\mathrm{ST},i}^0 = n_{\mathrm{max},i}, \\ n_i^{(\pi),0} = n_i^{(\alpha),0}, \\ n_{\mathrm{ST,sub}}(t^{\mathrm{f}}) = 0, \\ n_{\mathrm{ST},k}(t^{\mathrm{f}}) = n_{\mathrm{ST},k}(t^0) + \sum_{\pi\in\Pi} n_k^{(\pi)}(t^0), \end{cases} \tag{G.2b}$$

$$
\text{Phase Equilibrium:}\begin{cases}
\text{ODE System:}\begin{cases}
\text{Equations (2.4) and (2.5)},\\
t \coloneqq t_{\text{PhaseEq}},\\
n^{(\pi)}_{\text{PhaseEq},i}(t_{\text{PhaseEq}}) \coloneqq n^{(\pi)}_i(t),\\
T_{\text{PhaseEq}}(t_{\text{PhaseEq}}) \coloneqq T(t),
\end{cases}\\
\text{Convergence:}\begin{cases}
\text{RHS of eq. (2.4) at } n^{(\pi)}_{\text{PhaseEq},i}(t^{\text{f}}_{\text{PhaseEq}}) \leq \varepsilon,\\
\forall t_{\text{sp}} \in \mathcal{T}^{\text{PhaseEq}},
\end{cases}\\
\text{Forward Connection:}\begin{cases}
\text{Equation (2.6) applied to } \sum\limits_{\pi\in\Pi} n^{(\pi)}_i(t_{\text{sp}}),\\
T_{\text{PhaseEq}}(t_{\text{PhaseEq}}) = T(t = t_{\text{sp}}),
\end{cases}\\
\text{Backwards Connection:}\begin{cases}
n^{(\pi)}_i(t_{\text{sp}} + \delta t) = n^{(\pi)}_{\text{PhaseEq},i}(t^{\text{f}}_{\text{PhaseEq}}),\\
T(t_{\text{sp}} + \delta t) = T_{\text{PhaseEq}}(t^{\text{f}}_{\text{PhaseEq}}),
\end{cases}
\end{cases}
\qquad \text{(G.2c)}
$$

$$
\text{Variables and Controls:}\begin{cases}
\mathcal{x}(t) = \{n^{(\pi)}_i(t) \mid i \in \mathcal{SPC}, \pi \in \Pi\} \cup \{T(t), p(t), y_{\text{H}_2}(t)\},\\
u(t) = \{j^{(\pi)}_i(t) \mid i \in \mathcal{SPC}, \pi \in \Pi\} \cup \left\{s_T(t), s_p(t), s_{y_{\text{H}_2}}(t)\right\},\\
p = \{\mathcal{A}(t_{\text{sp}}) \mid t_{\text{sp}} \in \mathcal{T}^{\text{PhaseEq}}\},\\
\mathcal{x}^0 = \{n^{(\pi),0}_i \mid i \in \mathcal{SPC}, \pi \in \Pi\} \cup \left\{T^0, p^0, y^0_{\text{H}_2}\right\},\\
t \in \left[0, t^{\text{f}}\right],\\
t_{\text{PhaseEq}} \in [0, 1],
\end{cases}
$$

$$
\text{Sets and Indices:}\begin{cases}
i \in \mathcal{SPC},\\
k \in \mathcal{SPC}^{\text{prod}},\\
\pi, \alpha \in \Pi,\\
t_{\text{sp}} \in \mathcal{T}^{\text{PhaseEq}} = \left\{t_1, t_2, \ldots, t_{n_{\text{PhaseEq}}}\right\}.
\end{cases}
$$

A closed mass balance for initially added or dosed intermediate or final products is ensured via the last constraint in eq. (G.2b). Please note that, depending on the reaction system, $\mathcal{SPC}^{\text{prod}}$ may contain additional species besides the desired product. For instance, the enamine and amine need to be considered for the hydroaminomethylation since the enamine can be converted easily to the product amine via hydrogenation. To ensure convergence of the phase equilibrium calculations using the dynamic method from section 2.1, additional constraints in eq. (G.2c) are appended to the DOP. For the utilization of state-of-the-art, gradient-based solvers like IPOPT, the DOP is reformulated using collocation on finite elements on the time t and for each virtual time $t_{\text{PhaseEq,FE}}$. Information on the discretization parameters can be found in table G.1.

System-Specific Restrictions. As already discussed in section 4.3, prevention of phase separation during the hydroaminomethylation is mandatory. The gradual accumulation of water during the reaction may lead to the formation of a second, water-rich, polar phase which could cause severe leaching of the polar catalyst ligand SulfoXantphos. Therefore, penalizing the yield-based objective function w.r.t. phase splitting using

$$\phi = -Y_{\text{prod}}(t^{\text{f}}) + \sum_{i \in \mathcal{SPC}} \sum_{\pi \in \Pi} \sum_{\alpha \in \Pi} \sum_{\text{FE} \in \left\{1,2,\ldots,n_{\text{PhaseEq}}\right\}} \left(\Delta x^{(\pi,\alpha)}_{\text{PhaseEq},i}(t^{\text{f}}_{\text{sp,FE}}) \right)^2, \tag{G.3}$$

with

$$Y_{\text{prod}} = \frac{\sum_{\pi \in \Pi} n^{(\pi)}_{\text{prod}}(t) - n^{(\pi)}_{\text{prod}}(t^0) - \int_{t^0}^{t^{\text{f}}} j^{(\pi)}_{\text{prod}} \, \mathrm{d}t}{\sum_{\pi \in \Pi} n^{(\pi)}_{\text{sub}}(t^0) + \int_{t^0}^{t^{\text{f}}} j^{(\pi)}_{\text{sub}} \, \mathrm{d}t}, \tag{G.4}$$

is advisable to achieve the desired behavior. Theoretically, this penalization is not necessary in the mpEPF methodology as it is able to identify the negative impact of catalyst ligand leaching automatically. However, due to the missing data for SulfoXantphos in the activity coefficient ANN from appendix C, significant computational effort can be prevented using this foregoing consideration.

G.2 Generic Example Reaction

The model for the generic example reaction can be written analogous to the hydroaminomethylation model as

$$\text{Mass Balance of Fluid Element:} \quad \begin{cases} \frac{\mathrm{d}n^{(\pi)}_i}{\mathrm{d}t} = j^{(\pi)}_i + V^{(\pi)}_{\text{Liq}} \nu_i r^{(\pi)}, \\ n^{(\pi)}_i \left(t^0\right) = n^{(\pi),0}_i, \end{cases} \tag{G.5a}$$

$$\text{Mass Balance of Storage:} \quad \frac{\mathrm{d}n_{\text{ST},i}}{\mathrm{d}t} = -\sum_{\pi \in \Pi} j^{(\pi)}_i, \quad n_{\text{ST},i}\left(t^0\right) = n^0_{\text{ST},i}, \tag{G.5b}$$

$$\text{Reaction Kinetics:} \quad \text{Equations (4.1) and (4.2)}, \tag{G.5c}$$

$$\text{Control States:} \quad \frac{\mathrm{d}T}{\mathrm{d}t} = s_T(t), \quad T\left(t^0\right) = T^0, \tag{G.5d}$$

$$\text{Concentration:} \quad c^{(\pi)}_i(t) = n^{(\pi)}_i(t) V^{(\pi)}_{\text{Liq}}(t)^{-1}, \tag{G.5e}$$

$$\text{Liquid Volume:} \quad \begin{cases} V^{(\pi)}_{\text{Liq}}(t) = \sum_{i \in \mathcal{SPC}} V^{(\pi)}_{\text{Liq},i}(t), \\ V^{(\pi)}_{\text{Liq},i}(t) = m_i(t) {\rho_i}^{-1}, \\ m^{(\pi)}_i(t) = \tilde{M}_i n^{(\pi)}_i(t), \end{cases} \tag{G.5f}$$

$$\text{Data: Table G.2,}$$

$$\text{Bounds: Table G.3,}$$

$$\text{Thermodynamic Activities:} \quad \begin{cases} \gamma_{\mathrm{A}}^{(\pi)} = \gamma_{\mathrm{modUNIFAC,nC10en}}^{(\pi)}, \\ \gamma_{\mathrm{C}}^{(\pi)} = \gamma_{\mathrm{modUNIFAC,1-Butanol}}^{(\pi)}, \\ \gamma_{\mathrm{E}}^{(\pi)} = \gamma_{\mathrm{modUNIFAC,DMF}}^{(\pi)}, \end{cases} \tag{G.5g}$$

$$\text{Sets and Indices:} \quad \begin{cases} i \in \mathcal{SPC} = \{\mathrm{A},\ \mathrm{C},\ \mathrm{E}\}, \\ \pi \in \Pi = \{\pi_1, \pi_2\}. \end{cases} \tag{G.5h}$$

Due to its simpler structure, only the temperature gradient and the species dosing are considered as dynamic control variables. With the corresponding model parameters in table G.2 and the control variable bounds and discretization parameters in table G.3, the generic reaction model can be used in the mpEPF DOP eq. (G.2) for the identification of the optimal control profiles. Please note that the discretization

Tab. G.2.: Species data, kinetic, and equilibrium parameters for the mpEPF generic example model.

i	$\tilde{M}_i$ / $\mathrm{g\,mol^{-1}}$	ρ_i / $\mathrm{g\,L^{-1}}$
A	1	1
C	2	1
E	10	1

R / $\mathrm{J\,mol^{-1}\,K^{-1}}$	8.3145
k_0 / $\mathrm{L\,mol^{-1}\,min^{-1}}$	0.1
E_{A} / $\mathrm{J\,mol^{-1}}$	120
K^{eq} / –	1
K_{E} / $\mathrm{L\,mol^{-1}}$	1

of the DOP is analogous to the procedure for the hydroaminomethylation example in appendix G.1. The objective function is defined as

$$\phi = -Y_{\mathrm{prod}}(t^{\mathrm{f}}) - \sum_{\pi\in\Pi}\sum_{\alpha\in\Pi}\left(\Delta x_{\mathrm{PhaseEq,prod}}^{(\pi,\alpha)}(t_{\mathrm{sp},n_{\mathrm{PhaseEq}}}^{\mathrm{f}})\right)^2, \tag{G.6}$$

to promote phase separation at the final time for the isolation of product C.

Tab. G.3.: States, control, and discretization parameters for the mpEPF calculation using the generic example model. All indices i and π relate to their corresponding set according to $i \in \mathcal{SPC}$ and $\pi \in \Pi$ from eq. (G.5). For the definition of the phase equilibrium calculation-related variables, please see section 2.1.

		Values		
Parameter	Unit	Init	LB	UB
$n_{\mathrm{max},i}$	mol	1	–	–
$n_i^{(\pi)}$	mol	$n_{\mathrm{max},i}/\lvert\Pi\rvert$	0	$\max(\nu)\sum_i n_{\mathrm{max},i}$
$n_{\mathrm{ST},i}$	mol	0	0	$n_{\mathrm{max},i}$
ϑ	°C	120	5	120
s_T	$\mathrm{K\,min^{-1}}$	0	−10	10
j_i	$\mathrm{mol\,min^{-1}}$	1	0	1
$\mathcal{A}$	$\mathrm{m^2}$	1×10^2	1	1×10^7
t^{f}	min	20	–	–
$\beta^{(\pi)}$	$\mathrm{mol\,min^{-1}\,m^{-2}}$	1	–	–
κ	$\mathrm{mol\,mol^{-1}}$	0.1	–	–
n_{FE}	–	25	–	–
h_{FE}	–	0.04	0.0286	0.0667
$n_{\mathrm{FE}}^{\mathrm{eq}}$	–	15	–	–
$h_{\mathrm{FE}}^{\mathrm{eq}}$	–	0.0667	0.05	0.1
n_{CP}, $n_{\mathrm{CP}}^{\mathrm{eq}}$	–	3	–	–

H RSBR Process Model and Parameters

This appendix is based on the works of Rätze et al. [Rät+19] and Jokiel et al. [Jok+19] and contains process unit models which are connected to formulate steady-state and dynamic flowsheet optimization problems for the RSBR hydroformylation process of 1-dodecene. Additionally, an algorithm for the simulation and optimization of a dynamic RSBR process model is provided.

H.1 Universal Equations

Most of the process unit models include mass transfer of hydrogen and CO from the gas to the liquid phase. As a driving force, the concentration difference between the liquid phase concentration c_i and the saturate concentration c_i^{sat} with $i \in \mathcal{SPC}^{\mathrm{Gas}}$ is used. The saturate concentration is calculated with the Henry law according to

$$c_i^{\mathrm{sat}} = \frac{p_i}{H_i}, \tag{H.1}$$

$$H_i = H_i^0 \exp\left(\frac{-\Delta_{\mathrm{s}} H_i}{RT}\right) \quad \forall i \in \mathcal{SPC}^{\mathrm{Gas}}, \tag{H.2}$$

with the parameters summarized in table H.1.

Tab. H.1.: Henry coefficient parameters for the hydroformylation of 1-dodecene [Hen+15].

i	H_i^0 / $10^4\,\mathrm{bar\,mL\,mol^{-1}}$	$\Delta_{\mathrm{s}} H_i$ / $10^3\,\mathrm{J\,mol^{-1}}$
H_2	6.64	−3.06
CO	7.39	−0.84

H.2 Semibatch Reactor

The SBR model comprises a model for the liquid and gas phase according to

$$\frac{\mathrm{d}n_{\mathrm{Liq},i}^{\mathrm{SBR}}}{\mathrm{d}t} = \begin{cases} V_{\mathrm{Liq}}\beta_{\mathrm{eff},i}\left(c_i^{\mathrm{sat}} - c_i\right) + V_{\mathrm{Liq}}\sum_{j\in\mathcal{RCT}^{\mathrm{Hyfo}}}\nu_{i,j}r_j & \text{if } i \in \mathcal{SPC}^{\mathrm{Gas}}, \\ V_{\mathrm{Liq}}\sum_{j\in\mathcal{RCT}^{\mathrm{Hyfo}}}\nu_{i,j}r_j & \text{else,} \end{cases} \tag{H.3a}$$

$$\frac{\mathrm{d}n_{\mathrm{Gas},i}^{\mathrm{SBR}}}{\mathrm{d}t} = j_i - V_{\mathrm{Liq}}\beta_{\mathrm{eff},i}\left(c_i^{\mathrm{sat}} - c_i\right), \quad i \in \mathcal{SPC}^{\mathrm{Gas}} \tag{H.3b}$$

with

$$n_{\mathrm{Liq},i}^{\mathrm{SBR}}\left(t^0\right) = n_{\mathrm{Liq},i}^{\mathrm{SBR},0}, \tag{H.3c}$$

$$n_{\mathrm{Gas},i}^{\mathrm{SBR}}\left(t^0\right) = n_{\mathrm{Gas},i}^{\mathrm{SBR},0}, \tag{H.3d}$$

and $i \in \mathcal{SPC}$ if not specified otherwise. The pressure in the gas phase is calculated for the molar amount using the assumption of an ideal gas. In the case of a steady-state flowsheet simulation, the ratios of polar to non-polar solvent, substrate to solvent and the catalyst amount follow

$$m_{\mathrm{C10an}}^{\mathrm{SBR}} = \phi_{\mathrm{C10an,DMF}}^{\mathrm{m}} m_{\mathrm{DMF}}^{\mathrm{SBR}}, \tag{H.4a}$$

$$m_{\mathrm{C10an}}^{\mathrm{SBR}} = \phi_{\mathrm{C10an,nC12en}}^{\mathrm{m}} m_{\mathrm{nC12en}}^{\mathrm{SBR}}, \tag{H.4b}$$

$$n_{\mathrm{cat}}^{\mathrm{SBR},0} = \phi_{\mathrm{cat,nC12en}}^{0,\mathrm{n}} n_{\mathrm{nC12en}}^{0,\mathrm{SBR}}, \tag{H.4c}$$

and the liquid SBR hold-up is constrained via

$$0 = V^{\mathrm{SBR}}\phi_{\mathrm{Liq}}^{\mathrm{V,SBR}} - V_{\mathrm{Liq}}^{\mathrm{SBR}}(t_{\mathrm{SBR}} = 0). \tag{H.5}$$

For the dynamic flowsheet simulation, these constraints need to be formulated differently to accommodate for the two-stage optimization problem. Therefore, the species ratios and the liquid hold-up are written as

$$m_{\mathrm{C10an}}^{\mathrm{Ubuffer}}(t_\Sigma) = \phi_{\mathrm{C10an,DMF}}^{\mathrm{m}} m_{\mathrm{DMF}}^{\mathrm{Ubuffer}}(t_\Sigma), \tag{H.6a}$$

$$m_{\mathrm{C10an}}^{\mathrm{Ubuffer}}(t_\Sigma) = \phi_{\mathrm{C10an,nC12en}}^{\mathrm{m}}\left(m_{\mathrm{nC12en}}^{\mathrm{Ubuffer}}(t_\Sigma^{\mathrm{f}}) + m_{\mathrm{nC12en,fresh}}^{\mathrm{SBR}}\right), \tag{H.6b}$$

$$n_{\mathrm{cat}}^{\mathrm{Ubuffer}}(t_\Sigma) = \phi_{\mathrm{cat,nC12en}}^{\mathrm{n}}\left(n_{\mathrm{nC12en}}^{\mathrm{Ubuffer}}(t_\Sigma^{\mathrm{f}}) + n_{\mathrm{nC12en,fresh}}^{\mathrm{SBR}}\right), \tag{H.6c}$$

and

$$0 = V_{\mathrm{Liq}}^{\mathrm{Ubuffer}}(t_\Sigma) + V_{\mathrm{Liq,nC12en,fresh}} - V^{\mathrm{SBR}}\phi_{\mathrm{Liq}}^{\mathrm{V,SBR}}, \tag{H.7}$$

where t_Σ^{f} denotes the final time of the continuous part of the RSBR process.

H.3 Flash Buffer Tank

The flash buffer tank is connected to the SBR via

$$0 = n_i^{\mathrm{SBR}}(t = t_{\mathrm{SBR}}^{\mathrm{f}}) - n_i^{0,\mathrm{Dbuffer}}, \tag{H.8}$$

with $i \in \mathcal{SPC}$. As the flash buffer tank represents an additional reaction zone due to elevated temperatures but without stirring of the liquid phase, the process unit model is similar to that of the SBR. In the case of a steady-state flowsheet simulation, changes in the species concentrations can be modeled according to

$$\frac{\mathrm{d}c_i^{\mathrm{Dbuffer}}}{\mathrm{d}t} = \begin{cases} \beta_{\mathrm{eff},i}\left(c_i^{\mathrm{sat}} - c_i\right) + \sum_{j\in\mathcal{RCT}^{\mathrm{Hyfo}}} \nu_{i,j} r_j & \text{if } i \in \mathcal{SPC}^{\mathrm{Gas}}, \\ 0 & \text{if } i \in \{\mathrm{cat}\}, \\ \sum_{j\in\mathcal{RCT}^{\mathrm{Hyfo}}} \nu_{i,j} r_j & \text{else,} \end{cases} \tag{H.9a}$$

$$c_i\left(t^0\right) = c_i^0. \tag{H.9b}$$

A connection between the flash buffer tank and the subsequent process unit requires averaging of the species concentrations over time via

$$\overline{\dot{N}}_i^{\mathrm{Dbuffer}} = \frac{1}{t_\Sigma}\int_0^{t_\Sigma} \dot{V} c_i^{\mathrm{Dbuffer}}(t'_\Sigma)\,\mathrm{d}t'_\Sigma, \tag{H.10}$$

where the volume flow is determined by

$$\dot{V} = \frac{V_{\mathrm{Liq}}^{\mathrm{Dbuffer}}(t_\Sigma = 0) - V_{\mathrm{Liq,min}}^{\mathrm{Dbuffer}}}{t_\Sigma}. \tag{H.11}$$

Here, $V_{\mathrm{Liq,min}}^{\mathrm{Dbuffer}}$ denotes a minimum liquid hold-up which remains in the buffer vessel after one process cycle terminates.

For a dynamic flowsheet simulation, the flash buffer tank can be modeled more accurately via a mass balance which considers the continuous outflow into the subsequent process unit

$$\frac{\mathrm{d}n_i^{\mathrm{Dbuffer}}}{\mathrm{d}t} = \begin{cases} -\dot{V}c_i + V_{\mathrm{Liq}}\beta_{\mathrm{eff},i}\left(c_i^{\mathrm{sat}} - c_i\right) + V_{\mathrm{Liq}}\sum_{j\in\mathcal{RCT}^{\mathrm{Hyfo}}} \nu_{i,j} r_j & \text{if } i \in \mathcal{SPC}^{\mathrm{Gas}}, \\ -\dot{V}c_i & \text{if } i \in \{\mathrm{cat}\}, \\ -\dot{V}c_i + V_{\mathrm{Liq}}\sum_{j\in\mathcal{RCT}^{\mathrm{Hyfo}}} \nu_{i,j} r_j & \text{else,} \end{cases} \tag{H.12a}$$

$$n_i\left(t^0\right) = n_i^0. \tag{H.12b}$$

In contrast to the steady-state model, the volume flow is treated as an optimization variable which is determined by the optimizer through a penalty term w.r.t. the flash buffer volume at the end of one process cycle $(V_{\text{Liq}}^{\text{Dbuffer}}(t_{\Sigma}^{\text{f}}) - V_{\text{Liq,min}}^{\text{Dbuffer}})^2$ in the objective function. This formulation improves the numeric stability. To further increase the accuracy of the process unit model, pressure changes due to varying hold-up levels can be accounted for via

$$p^{\text{Dbuffer}}(t_{\Sigma}) = p^{\text{Dbuffer}}(t_{\Sigma}=0)\frac{1-\frac{V_{\text{Liq}}^{\text{Dbuffer}}(t_{\Sigma}=0)}{V^{\text{Dbuffer}}}}{1-\frac{V_{\text{Liq}}^{\text{Dbuffer}}(t_{\Sigma})}{V^{\text{Dbuffer}}}}, \tag{H.13}$$

assuming isothermal operation. The initial pressure and liquid hold-up can be taken from the experimental setup.

H.4 Feed Buffer Tank

For the steady-state flowsheet simulation, the feed buffer tank does not need to be considered rigorously. It is sufficient to accumulate all recycled streams for a species $i \in \mathcal{SPC}$ including the polar catalyst recycle, the non-polar distillate stream and the make-up stream via

$$n_i^{\text{SBR},0} = \int_0^{t_{\Sigma}} \left[\left(1-\phi_{\text{purge}}^{\text{n,Dec}}\right) \dot{N}_i^{\text{P,Dec}} + \left(1-\phi_{\text{purge}}^{\text{n,Dist}}\right) \dot{N}_i^{\text{top,Dist}} + \dot{N}_{\text{make-up},i} \right] \mathrm{d}t. \tag{H.14}$$

In contrast, the dynamic simulation utilizes a rigorous vessel model which considers gas-liquid mass transfer according to

$$\frac{\mathrm{d}n_i^{\text{Ubuffer}}}{\mathrm{d}t} = \begin{cases} V_{\text{Liq}}\beta_{\text{eff},i}\left(c_i^{\text{sat}} - c_i\right) & \text{if } i \in \mathcal{SPC}^{\text{Gas}}, \\ \sum_{k\in\mathcal{STR}^{\text{Ubuffer}}} \dot{N}_{i,k} & \text{else}, \end{cases} \tag{H.15a}$$

$$n_i^{\text{Ubuffer}}\left(t^0\right) = n_i^{\text{Ubuffer},0}, \tag{H.15b}$$

with $\mathcal{STR} = \left\{\dot{N}_i^{\text{P,Dec}}, \dot{N}_i^{\text{top,Dist}}, \dot{N}_{\text{make-up},i}\right\}$. Please note that no reactions are considered in the feed buffer tank due to the residual amount of substrate, comparatively low temperatures and low pressures (compare table H.4).

H.5 CSTR

The CSTR model is identical for the steady-state and dynamic simulation. It considers gas-liquid mass transfer in addition to the reactions according to

$$\dot{N}_i^{\mathrm{CSTR}} = \begin{cases} \dot{N}_{i,\mathrm{in}} + V_{\mathrm{Liq}}\beta_{\mathrm{eff},i}\left(c_i^{\mathrm{sat}} - c_i\right) + V_{\mathrm{Liq}}\sum_{j\in\mathcal{RCT}^{\mathrm{Hyfo}}}\nu_{i,j}r_j & \text{if } i \in \mathcal{SPC}^{\mathrm{Gas}}, \\ \dot{N}_{i,\mathrm{in}} + V_{\mathrm{Liq}}\sum_{j\in\mathcal{RCT}^{\mathrm{Hyfo}}}\nu_{i,j}r_j & \text{else.} \end{cases} \tag{H.16}$$

H.6 Decanter

The decanter ($\square^{\mathrm{Dec}}$) for the separation of a DMF/C10an TMS for the hydroformylation of 1-dodecene was investigated in detail by McBride et al. [MKS17]. They used modified UNIFAC Dortmund [WG87] with refitted parameters [MS15] to predict the LLE. Additionally, the catalyst split factors were determined via COSMOtherm [EK06] and combined with the LLE data in a data-driven Kriging surrogate model. To reduce the input dimensions, similar species are grouped together, leading to the molar fraction input vector x_k with $k \in \{\mathrm{DMF}, \mathrm{C10an} + \mathrm{nC12an}, \mathrm{nC13al} + \mathrm{iC13al}, \mathrm{nC12en}{+}\mathrm{iC12en}\}$. Together with the temperature T, the Kriging model (KR) returns the molar split factors of each species $i \in \{\mathrm{DMF}, \mathrm{C10an}, \mathrm{nC13al}, \mathrm{nC12en}, \mathrm{BPP}\}$

$$\phi_i^{\mathrm{n,P}} = \mathrm{KR}\left(x, T\right) = \frac{n_i^{\mathrm{P}}}{n_i^{\mathrm{P}} + n_i^{\mathrm{NP}}} = \frac{\dot{N}_i^{\mathrm{P}}}{\dot{N}_i^{\mathrm{P}} + \dot{N}_i^{\mathrm{NP}}}. \tag{H.17}$$

Here, the superscripts $\square^{\mathrm{P}}$ and $\square^{\mathrm{NP}}$ denote the polar and non-polar phase, respectively. If we define $\tilde{\phi}^{\mathrm{n,P}}$, such that $\tilde{\phi}_j^{\mathrm{n,P}} = \phi_i^{\mathrm{n,P}}$ with j, i being the first and second element of each tuple in $\{(\mathrm{DMF}, \mathrm{DMF}), (\mathrm{C10an}, \mathrm{C10an}), (\mathrm{nC12an}, \mathrm{C10an}), (\mathrm{nC13al}, \mathrm{nC13al}), (\mathrm{iC13al}, \mathrm{nC13al}), (\mathrm{nC12en}, \mathrm{nC12en}), (\mathrm{iC12en}, \mathrm{nC12en}), (\mathrm{cat}, \mathrm{BPP})\}$, we yield the split factors for all species. With this definition, the decanter outlet streams can be computed following

$$\dot{N}_j^{\mathrm{P}} = \begin{cases} 0 & \text{if } j \in \mathcal{SPC}^{\mathrm{Gas}}, \\ \tilde{\phi}_j^{\mathrm{n,P}}\dot{N}_{j,\mathrm{in}}^{\mathrm{Dec}} & \text{else.} \end{cases} \tag{H.18a}$$

$$\dot{N}_j^{\mathrm{NP}} = \begin{cases} 0 & \text{if } j \in \mathcal{SPC}^{\mathrm{Gas}}, \\ \dot{N}_{j,\mathrm{in}}^{\mathrm{Dec}} - \dot{N}_j^{\mathrm{Dec}} & \text{else.} \end{cases} \tag{H.18b}$$

H.7 Distillation Column

The distillation column is modeled using the Fenske-Underwood correlations from Kaiser et al. [Kai+17]. By first specifying the desired recovery $\phi_i^{\mathrm{n,top}}$ of the light and heavy keys $i \in \{\mathrm{LK}, \mathrm{HK}\} \subset \mathcal{SPC}$, the outlet streams for these two components can be computed with

$$\dot{N}_i^{\mathrm{top}} = \phi_i^{\mathrm{n,top}} \dot{N}_{\mathrm{in}}, \tag{H.19a}$$

$$\dot{N}_i^{\mathrm{bot}} = \left(1 - \phi_i^{\mathrm{n,top}}\right) \dot{N}_{\mathrm{in}}. \tag{H.19b}$$

In the next step, the minimum number of trays n_{min} is calculated using

$$n_{\mathrm{min}} = \frac{\ln \frac{\left(x_{\mathrm{LK}}/x_{\mathrm{HK}}\right)_{\mathrm{top}}}{\left(x_{\mathrm{LK}}/x_{\mathrm{HK}}\right)_{\mathrm{bot}}}}{\ln \alpha_{\mathrm{LK,HK}}} = \frac{\ln \frac{\dot{N}_{\mathrm{LK}}^{\mathrm{top}} \dot{N}_{\mathrm{HK}}^{\mathrm{bot}}}{\dot{N}_{\mathrm{LK}}^{\mathrm{bot}} \dot{N}_{\mathrm{HK}}^{\mathrm{top}}}}{\ln \alpha_{\mathrm{LK,HK}}}, \tag{H.20}$$

which requires the relative volatility for species $i, j \in \mathcal{SPC}$

$$\alpha_{i,j} = \frac{\gamma_i p_i^{\mathrm{sat}}}{\gamma_j p_j^{\mathrm{sat}}} \overset{\gamma=1}{\approx} \frac{p_i^{\mathrm{sat}}}{p_j^{\mathrm{sat}}}, \tag{H.21}$$

and saturate pressure correlations

$$p_i^{\mathrm{sat}} = \begin{cases} 133.322 \times 10^{-6} \cdot 10^{\left(a_i + \frac{b_i}{T} + c_i \log_{10} T + d_i T + e_i T^2\right)} & \text{if } i \in \mathcal{SPC} \setminus \mathcal{SPC}^{\mathrm{Gas}} \setminus \\ & \quad \{\mathrm{iC12en}, \mathrm{iC13al}\}, \\ 0.1 \cdot \exp\left(a_i + \frac{b_i}{T} + c_i \ln T + d_i T^{e_i}\right) & \text{if } i \in \{\mathrm{iC12en}, \mathrm{iC13al}\}, \end{cases} \tag{H.22}$$

with the corresponding parameters in table H.2. The outlet streams for all remaining

Tab. H.2.: Vapor pressure parameters for the hydroformylation of 1-dodecene [McB+16].

i	a_i / −	b_i / K	c_i / −	d_i / K^{-1}	e_i / K^{-2}
C10an	26.5125	−3358.4	−6.1174	-3.3225×10^{-10}	4.8554×10^{-7}
DMF	−47.9857	−2385.0	28.8000	-5.8596×10^{-2}	3.1386×10^{-5}
nC12en	−8.5899	−3524.1	10.8060	-2.8161×10^{-2}	1.4267×10^{-5}
iC12en	75.7900	−9964.0	−8.9650	4.9400×10^{-18}	6.0000
nC13al	161.5042	−9766.0	−55.5910	2.1036×10^{-2}	5.5498×10^{-13}
iC13al	10.4200	−6149.0	0.1970	-2.0000×10^{-4}	1.0000
nC12an	−5.5630	−3470.0	9.0270	-2.3190×10^{-2}	1.1240×10^{-5}

species are calculated using the geometric average of the respective species $i \in \mathcal{SPC}$ and the heavy key with

$$\overline{\alpha}_{\mathrm{LK,HK}} = \sqrt[n]{\prod_{n} \alpha_{\mathrm{LK,HK}}{}^{(n)}}, \tag{H.23}$$

in

$$\dot{N}_i^{\mathrm{bot}} = \frac{\dot{N}_{i,\mathrm{in}}}{1 + \frac{\dot{N}_{\mathrm{HK}}^{\mathrm{top}}}{\dot{N}_{\mathrm{HK}}^{\mathrm{bot}}} \overline{\alpha}_{i,\mathrm{HK}}^{n_{\mathrm{min}}}}, \tag{H.24a}$$

$$\dot{N}_i^{\mathrm{top}} = \dot{N}_{i,\mathrm{in}} - \dot{N}_i^{\mathrm{bot}}. \tag{H.24b}$$

In the experimental validation of the RSBR process model, no distillation column is operated. Instead, a decane/dodecene isomer mixture is prepared which is fed as a make-up stream to simulate the distillate recycle. This simulated version of the distillate recycle requires the dodecene isomer to 1-dodecene ratio $\phi^{\mathrm{m}}_{\mathrm{iC12en,nC12en}}$ and can be calculated via

$$m_{\mathrm{iC12en,fresh}} = \phi^{\mathrm{m}}_{\mathrm{iC12en,nC12en}} m^{\mathrm{SBR}}_{\mathrm{nC12en,fresh}}, \tag{H.25a}$$

$$\dot{N}_{\mathrm{make-up,iC12en}} = \frac{m_{\mathrm{iC12en,fresh}}}{\tilde{M}_{\mathrm{iC12en}} t_{\Sigma}}. \tag{H.25b}$$

H.8 Performance Measures

Process performance measures for the hydroformylation of 1-dodecene generally use 1-dodecene as reference substrate, so that the conversion, yield, and selectivity for major products and byproducts $i \in \{\mathrm{nC13al, iC12en, iC13al, nC12an}\}$ can be calculated via

$$X_{\mathrm{nC12en}} = 1 - \frac{c^{\mathrm{Dec}}_{\mathrm{nC12en,in}}}{c^{\mathrm{SBR}}_{\mathrm{nC12en}}(t_{\mathrm{SBR}} = 0)}, \tag{H.26a}$$

$$Y_{i,\mathrm{nC12en}} = \frac{c^{\mathrm{Dec}}_{i,\mathrm{in}} - c^{\mathrm{SBR}}_{i}(t_{\mathrm{SBR}} = 0)}{c^{\mathrm{SBR}}_{\mathrm{nC12en}}(t_{\mathrm{SBR}} = 0)}, \tag{H.26b}$$

$$S_{i,\mathrm{nC12en}} = \frac{Y_{i,\mathrm{nC12en}}}{X_{\mathrm{nC12en}}}, \tag{H.26c}$$

Additionally, the linear to branched aldehyde ratio is defined as

$$\phi^{\mathrm{n}}_{\mathrm{n/iso}} = \frac{c^{\mathrm{Dec}}_{\mathrm{nC13al,in}}}{\left(c_{\mathrm{nC13al,in}} + c_{\mathrm{iC13al,in}}\right)^{\mathrm{Dec}}}. \tag{H.27}$$

Due to experimental setups in which dodecene isomers are fed into the process to simulate a distillate recycle, alternative definitions of the performance measures are necessary to account for the additional substrate. These performance measures use 1-dodecene and its isomers as reference and follow

$$X_{\mathrm{C12en}} = 1 - \frac{c^{\mathrm{Dec}}_{\mathrm{nC12en+iC12en,in}}}{c^{\mathrm{SBR}}_{\mathrm{nC12en+iC12en}}(t_{\mathrm{SBR}} = 0)}, \tag{H.28a}$$

$$Y_{i,\mathrm{C12en}} = \frac{c^{\mathrm{Dec}}_{i,\mathrm{in}} - c^{\mathrm{SBR}}_{i}(t_{\mathrm{SBR}} = 0)}{c^{\mathrm{SBR}}_{\mathrm{nC12en+iC12en}}(t_{\mathrm{SBR}} = 0)}, \tag{H.28b}$$

$$S_{i,\mathrm{C12en}} = \frac{Y_{i,\mathrm{C12en}}}{X_{\mathrm{C12en}}}, \tag{H.28c}$$

with $i \in \{\mathrm{nC13al, iC13al, nC12an}\}$. This alternative definition is necessary since no differentiation of the substrate source (either 1-dodecene or its recycled isomers) for the final product concentration in the reaction mixture is possible. Hence, the application of eq. (H.26) in these cases would lead to conversions greater 100 % and deviations in the product selectivity and yield.

H.9 Optimization Problems

Depending on the experimental setup, the RSBR flowsheet simulations and optimizations need to consider the shortcut distillation column model or contain an additional make-up stream in the form of pre-synthesized dodecene isomers. In this section, steady-state and dynamic optimization problems with varying degrees of freedom and with or without a dedicated distillation column are summarized.

H.9.1 Steady-State

The steady-state optimization problem does not utilize all available degrees of freedom of the SBR and CSTR tandem as it primarily serves as a validation of the dynamic RSBR flowsheet model. In particular, this steady-state model is used to

identify if the same (cyclic) steady-state is achieved for both process models under connection of all available recycle loops and can be summarized as

$$\min_{\substack{j_i^{\mathrm{SBR}}(t_{\mathrm{SBR}}),\\ \dot{N}_{\mathrm{make-up},i},\, i\in\mathcal{SPC}}} \quad -S_{\mathrm{nC13al}} \tag{H.29}$$

s. t.

Kinetic Model: Equations (B.2), (B.3) and (B.9) to (B.12),

Gas-liquid (G/L) Mass Transfer: Equations (H.1) and (H.2),

Constitutive Equations: Equations (B.4) to (B.7) and (B.8),

Times: Equation (5.4),

Data: Tables B.17 to B.19, H.1, H.3 and H.4,

Process Units:

- SBR:
  - ODE System: Equation (H.3),
  - Fill Volume: Equation (H.5),
  - Species Ratios: Equation (H.4),
- Flash Buffer:
  - ODE System: Equation (H.9),
  - Volumetric Flowrate: Equation (H.11),
  - Outlet Flow: Equation (H.10),
- CSTR: Equation (H.16),
- Decanter: Equations (H.17) and (H.18),
- Distillation Column:
  - Outlet Streams: Equations (H.19) and (H.24),
  - Tray Number: Equation (H.20),
  - Saturate Pressure: Equation (H.22),
  - Volatility: Equations (H.21) and (H.23),
- Feed Buffer:
  - Accumulator: Equation (H.14),
  - Makeup: $\dot{N}_{\mathrm{make-up},i} = 0, i \in \mathcal{SPC} \setminus \{\mathrm{C10an}, \mathrm{DMF}, \mathrm{cat}\}$,
- Closing Condition: $\sum_{i\in\mathcal{SPC}^{\mathrm{Gas}}} y_i^{\mathrm{SBR}}(t) = \sum_{i\in\mathcal{SPC}^{\mathrm{Gas}}} y_i^{\mathrm{CSTR}} = 1$,

Interconnection:

- SBR – Dbuffer:
  - Flow: Equation (H.8),
  - Controls: $y_i^{\mathrm{Dbuffer}}(t_\Sigma) = y_i^{\mathrm{SBR}}(t_{\mathrm{SBR}}^{\mathrm{f}}),\ i \in \mathcal{SPC}^{\mathrm{Gas}}$,
- Dbuffer – CSTR: $\dot{N}_{i,\mathrm{in}}^{\mathrm{CSTR}} = \overline{\dot{N}_i}^{\mathrm{Dbuffer}},\ i \in \mathcal{SPC}$,
- CSTR – Dec: $\dot{N}_{i,\mathrm{in}}^{\mathrm{Dec}} = \dot{N}_i^{\mathrm{CSTR}},\ i \in \mathcal{SPC}$,
- Dec – Dist: $\dot{N}_{i,\mathrm{in}}^{\mathrm{Dist}} = \dot{N}_i^{\mathrm{NP,Dec}},\ i \in \mathcal{SPC}$,

$$\text{Performance Measures:} \begin{cases} X,\ S,\ \text{n/iso: Equations (H.26a), (H.26c) and (H.27),} \\ \text{n/iso Bound: } \phi^{\text{n}}_{\text{n/iso}} \geq 0.95, \end{cases}$$

$$\text{Inequality Constraints:} \left\{ \dot{N}_i \geq 0,\ n_i(t) \geq 0,\ c_i(t) \geq 0,\ i \in \mathcal{SPC}, \right.$$

$$\text{Sets:} \begin{cases} \mathcal{SPC} = \{\text{C10an, DMF, nC12an, iC10en, nC13al, iC13al,} \\ \qquad\qquad \text{nC12an, } H_2\text{, CO, cat}\}, \\ \mathcal{SPC}^{\text{Gas}} = \{H_2\text{, CO}\}, \\ \mathcal{RCT}^{\text{Hyfo}} = \{\text{Iso, Hyfon, Hyfoi, Hyfoni, Hydn, Hydi}\}. \end{cases}$$

In contrast to the EPF calculations from Kaiser et al. [Kai+17], the reactor vessel dimensions and the liquid hold-ups are adapted to the conditions from Dreimann et al. [Dre+16b]. The *Idle* time and reaction time in the SBR are fixed to 30 min and 60 min, respectively, which leads to a total residence time of 375 min based on eqs. (5.1) to (5.3).

Tab. H.3.: Operating conditions of the decanter and distillation column in addition to process-wide operating parameters [Rät+19].

	Parameter	Unit	Value
Dec	ϑ	°C	5
Dist	ϑ_{top}	°C	58
	ϑ_{bot}	°C	138
	$\phi^{\text{n,top}}_{\text{LK}}$	mol mol^{-1}	0.95
	$\phi^{\text{n,top}}_{\text{HK}}$	mol mol^{-1}	0.05
Dec	T	°C	5
Process	$\phi^{\text{m}}_{\text{C10an,DMF}}$	g g^{-1}	1
	$\phi^{\text{m}}_{\text{C10an,nC12en}}$	g g^{-1}	42/16
	$\phi^{\text{n}}_{\text{cat,nC12en}}$	mol mol^{-1}	1/4000
	$\phi^{\text{n}}_{\text{cat,BPP}}$	mol mol^{-1}	1/5

Tab. H.4.: Steady-state and dynamic model operating conditions for model validation [Rät+19].

			SS Validation			Dyn Validation		
	Parameter	Unit	Init	LB	UB	Init	LB	UB
SBR	ϑ	°C	105	–	–	105	–	–
	$\beta_{\mathrm{eff,H_2}}$	$\mathrm{min^{-1}}$	9.57	–	–	9.57	–	–
	$\beta_{\mathrm{eff,CO}}$	$\mathrm{min^{-1}}$	7.08	–	–	7.08	–	–
	$^*V$	mL	240	–	–	240	–	–
	$^*\phi^{\mathrm{V}}_{\mathrm{Liq}}$	$\mathrm{mL\,mL^{-1}}$	0.66	–	–	0.66	–	–
	t_{SBR}	min	60	–	–	60	–	–
	$^*t_{\mathrm{idle}}$	min	30	–	–	30	–	–
	$^*p^0$	bar	19	–	–	19	–	–
	$y_{\mathrm{H_2}}$	$\mathrm{mol\,mol^{-1}}$	0.5	0	1	0.5	0	1
	y_{CO}	$\mathrm{mol\,mol^{-1}}$	0.5	0	1	0.5	0	1
	$j_{\mathrm{H_2}}$	$\mathrm{mol\,s^{-1}}$	$n^{\mathrm{SBR},0}_{\mathrm{Gas,H_2}}/t_{\mathrm{SBR}}$	0	∞	$n^{\mathrm{SBR},0}_{\mathrm{Gas,H_2}}/t_{\mathrm{SBR}}$	0	∞
	j_{CO}	$\mathrm{mol\,s^{-1}}$	$n^{\mathrm{SBR},0}_{\mathrm{Gas,CO}}/t_{\mathrm{SBR}}$	0	∞	$n^{\mathrm{SBR},0}_{\mathrm{Gas,CO}}/t_{\mathrm{SBR}}$	0	∞
Dbuffer	$^*\vartheta$	°C	91	–	–	91	–	–
	$^*p^0$	bar	16.21	–	–	16.21	–	–
	$^*p$	bar	16.21	–	–	16.21	0	∞
	$y_{\mathrm{H_2}}$	$\mathrm{mol\,mol^{-1}}$	$y^{\mathrm{SBR}}_{\mathrm{H_2}}(t_{\mathrm{SBR}})$			$y^{\mathrm{SBR}}_{\mathrm{H_2}}(t_{\mathrm{SBR}})$		
	y_{CO}	$\mathrm{mol\,mol^{-1}}$	$y^{\mathrm{SBR}}_{\mathrm{CO}}(t_{\mathrm{SBR}})$			$y^{\mathrm{SBR}}_{\mathrm{CO}}(t_{\mathrm{SBR}})$		
	$\beta_{\mathrm{eff,H_2}}$	$\mathrm{min^{-1}}$	9.57/10	–	–	9.57/10	–	–
	$\beta_{\mathrm{eff,CO}}$	$\mathrm{min^{-1}}$	7.08/10	–	–	7.08/10	–	–
	$^*V$	mL	/			430	–	–
	$^*V_{\mathrm{Liq,min}}$	mL	25	–	–	25	–	–
	$\dot{V}$	$\mathrm{mL\,h^{-1}}$	(H.11)			$V^{\mathrm{SBR}}_{\mathrm{Liq}}(t_{\mathrm{SBR}})/t_{\Sigma}$	0	∞
CSTR	$^*\vartheta$	°C	115	–	–	115	–	–
	$^*p$	bar	21	–	–	21	–	–
	$^*y_{\mathrm{H_2}}$	$\mathrm{mol\,mol^{-1}}$	0.5	–	–	0.5	–	–
	$^*y_{\mathrm{CO}}$	$\mathrm{mol\,mol^{-1}}$	0.5	–	–	0.5	–	–
	$\beta_{\mathrm{eff,H_2}}$	$\mathrm{min^{-1}}$	9.57	–	–	9.57	–	–
	$\beta_{\mathrm{eff,CO}}$	$\mathrm{min^{-1}}$	7.08	–	–	7.08	–	–
	$^*V$	mL	1000	–	–	1000	–	–
	$^*\phi^{\mathrm{V}}_{\mathrm{Liq}}$	$\mathrm{mL\,mL^{-1}}$	0.3	–	–	0.3	–	–
Ubuffer	ϑ	°C				96	–	–
	$^*p^0$	bar				2.875	–	–
	$^*p$	bar				2.875	0	∞
	$y_{\mathrm{H_2}}$	$\mathrm{mol\,mol^{-1}}$	/			0.5	–	–
	y_{CO}	$\mathrm{mol\,mol^{-1}}$				0.5	–	–
	$\beta_{\mathrm{eff,H_2}}$	$\mathrm{min^{-1}}$				9.57/10	–	–
	$\beta_{\mathrm{eff,CO}}$	$\mathrm{min^{-1}}$				7.08/10	–	–
	$^*V$	mL				260	–	–
Process	$\phi^{\mathrm{n,Dec}}_{\mathrm{purge}}$	$\mathrm{mol\,mol^{-1}}$	0	–	–	0	–	–
	$\phi^{\mathrm{n,Dist}}_{\mathrm{purge}}$	$\mathrm{mol\,mol^{-1}}$	0	–	–	0	–	–
	$\phi^{\mathrm{n}}_{\mathrm{n/iso}}$	$\mathrm{mol\,mol^{-1}}$	0.95	0	1	0.95	0	1

* Data taken from the experimental setup form Dreimann et al. [Dre+16b] and Rätze et al. [Rät+19].

H.9.2 Dynamic

The dynamic RSBR flowsheet model is a combination of two separate optimization problems which describe the behavior of the process during its *Idle* and *Reaction* plus *Continuous* stage, respectively. The optimization problem for the *Idle* stage only considers the SBR without the addition of fresh substrate and can be described as

$$\min \quad 0 \tag{H.30}$$

s. t.

Kinetic Model: Equations (B.2), (B.3) and (B.9) to (B.12),

G/L Mass Transfer: Equations (H.1) and (H.2),

Constitutive Equations: Equations (B.4) to (B.7) and (B.8),

Data: Tables B.17 to B.19 and H.1, either tables H.4 to H.6 ,

Process Units:
$$\begin{cases} \text{SBR: Equation (H.3)}, \\ \text{Closing Condition:} \quad \sum_{i \in \mathcal{SPC}^{\text{Gas}}} y_i^{\text{SBR}}(t) = 1, \end{cases}$$

Inequality Constraints: $n_i(t) \geq 0$, $c_i(t) \geq 0$, $i \in \mathcal{SPC}$,

Sets:
$$\begin{cases} \mathcal{SPC} = \{\text{C10an, DMF, nC12an, iC10en, nC13al, iC13al,} \\ \qquad\qquad \text{nC12an, } H_2\text{, CO, cat}\}, \\ \mathcal{SPC}^{\text{Gas}} = \{H_2\text{, CO}\}, \\ \mathcal{RCT}^{\text{Hyfo}} = \{\text{Iso, Hyfon, Hyfoi, Hyfoni, Hydn, Hydi}\}. \end{cases}$$

The *Reaction* and *Continuous* stage describes the reaction in the SBR and the subsequent continuous process from the flash to the feed buffer tank. With the

maximum DoF in the SBR and CSTR, the optimization problem can be summarized as

$$\min_{\substack{T^{\mathrm{SBR}}(t_{\mathrm{SBR}}),\, p^{0,\mathrm{SBR}},\, j_i^{\mathrm{SBR}}(t_{\mathrm{SBR}}),\\ T^{\mathrm{CSTR}},\, p^{\mathrm{CSTR}},\, y_{i\in\mathcal{SPC}^{\mathrm{Gas}}}^{\mathrm{CSTR}},\\ \phi_{\mathrm{Liq}}^{\mathrm{V,SBR}},\, \phi_{\mathrm{Liq}}^{\mathrm{V,CSTR}},\\ \dot{N}_{\mathrm{make-up},i,\, i\in\mathcal{SPC}},\, \dot{V}}} \quad -S_{\mathrm{nC13al}} + \left(V_{\mathrm{Liq}}^{\mathrm{Dbuffer}}(t_\Sigma^{\mathrm{f}}) - V_{\mathrm{Liq,min}}^{\mathrm{Dbuffer}}\right)^2 \tag{H.31}$$

s. t.

Kinetic Model: Equations (B.2), (B.3) and (B.9) to (B.12),

G/L Mass Transfer: Equations (H.1) and (H.2),

Constitutive Equations: Equations (B.4) to (B.7) and (B.8),

Times: Equations (5.1) to (5.4) and (5.6),

Data: Tables B.17 to B.19, H.1, H.3 and H.5,

Process Units:

- SBR:
  - ODE System: Equation (H.3),
  - Fill Volume: Equation (H.7),
  - Species Ratios: Equation (H.4),
- Flash Buffer:
  - ODE System: Equation (H.12),
  - Outlet Flow: $\dot{N}_i^{\mathrm{Dbuffer}}(t_\Sigma) = \dot{V} c_i^{\mathrm{Dbuffer}}(t_\Sigma),\ i \in \mathcal{SPC}$,
  - Pressure: Equation (H.13),
- CSTR: Equation (H.16),
- Decanter: Equations (H.17) and (H.18),
- Distillation Column:
  - Outlet Streams: Equations (H.19) and (H.24),
  - Tray Number: Equation (H.20),
  - Saturate Pressure: Equation (H.22),
  - Volatility: Equations (H.21) and (H.23),
- Feed Buffer:
  - ODE System: Equation (H.15), $n_i^{\mathrm{Ubuffer},0} = 0,\ i \in \mathcal{SPC}$,
  - Makeup: $\dot{N}_{\mathrm{make-up},i} = 0, i \in \mathcal{SPC} \setminus \{\mathrm{C10an}, \mathrm{DMF}, \mathrm{cat}\}$,
- Closing Condition: $\sum_{i\in\mathcal{SPC}^{\mathrm{Gas}}} y_i^{\mathrm{SBR}}(t_{\mathrm{SBR}}) = \sum_{i\in\mathcal{SPC}^{\mathrm{Gas}}} y_i^{\mathrm{CSTR}} = 1$,

$$
\text{Interconnection:}\begin{cases}
\text{SBR – Dbuffer:} & \begin{cases}\text{Flow: Equation (H.8)},\\ \text{Controls: } y_i^{\text{Dbuffer}}(t_\Sigma) = y_i^{\text{SBR}}(t_{\text{SBR}}^{\text{f}}),\ i \in \mathcal{SPC}^{\text{Gas}},\end{cases}\\
\text{Dbuffer – CSTR:} & \dot{N}_{i,\text{in}}^{\text{CSTR}} = \dot{N}_i^{\text{Dbuffer}},\ i \in \mathcal{SPC},\\
\text{CSTR – Dec:} & \dot{N}_{i,\text{in}}^{\text{Dec}} = \dot{N}_i^{\text{CSTR}},\ i \in \mathcal{SPC},\\
\text{Dec – Dist:} & \dot{N}_{i,\text{in}}^{\text{Dist}} = \dot{N}_i^{\text{NP,Dec}},\ i \in \mathcal{SPC},
\end{cases}
$$

$$
\text{Performance Measures:} \begin{cases} X,\ S\text{: Equations (H.26a) and (H.26c)}, \end{cases}
$$

$$
\text{Inequality Constraints: } \dot{N}_i(t) \geq 0,\ n_i(t) \geq 0,\ c_i(t) \geq 0,\ i \in \mathcal{SPC},
$$

$$
\text{Sets:}\begin{cases}
\mathcal{SPC} = \{\text{C10an, DMF, nC12an, iC10en, nC13al, iC13al,}\\
\qquad\qquad \text{nC12an, } H_2\text{, CO, cat}\},\\
\mathcal{SPC}^{\text{Gas}} = \{H_2\text{, CO}\},\\
\mathcal{RCT}^{\text{Hyfo}} = \{\text{Iso, Hyfon, Hyfoi, Hyfoni, Hydn, Hydi}\},\\
\mathcal{STR}^{\text{Ubuffer}} = \{\text{Dist}^{\text{top}}\text{, Dec}^{\text{P}}\text{, make} - \text{up}\}.
\end{cases}
$$

For the simulation of multiple process cycles including the reactor start-up, eqs. (H.30) and (H.31) need to be solved repeatedly in a specific sequence. This sequence is described in detail in algorithm 3.

For the model validation, the temperature and total pressure in the SBR in addition to temperature, pressure, and gas phase composition in the CSTR as well as the liquid hold-ups are fixed, leading to the optimization problem

$$
\min_{\substack{j_i^{\text{SBR}}(t_{\text{SBR}}),\\ \dot{N}_{\text{make}-\text{up},i},\, i \in \mathcal{SPC},\, \dot{V}}} \quad -S_{\text{nC13al}} + \left(V_{\text{Liq}}^{\text{Dbuffer}}(t_\Sigma^{\text{f}}) - V_{\text{Liq,min}}^{\text{Dbuffer}}\right)^2 \tag{H.32}
$$

s. t.

Kinetic Model:	Equations (B.2), (B.3) and (B.9) to (B.12),
G/L Mass Transfer:	Equations (H.1) and (H.2),
Constitutive Equations:	Equations (B.4) to (B.7) and (B.8),
Times:	Equation (5.4),
Data:	Tables B.17 to B.19, H.1, H.3 and H.4,

$$
\begin{aligned}
&\text{Process Units:}\begin{cases}
\text{SBR:}\begin{cases}\text{ODE System: Equation (H.3)},\\ \text{Fill Volume: Equation (H.7)},\\ \text{Species Ratios: Equation (H.4)},\end{cases}\\
\text{Flash Buffer:}\begin{cases}\text{ODE System: Equation (H.12)},\\ \text{Outlet Flow: } \dot{N}_i^{\text{Dbuffer}}(t_\Sigma)=\dot{V}c_i^{\text{Dbuffer}}(t_\Sigma),\ i\in\mathcal{SPC},\\ \text{Pressure: Equation (H.13)},\end{cases}\\
\text{CSTR: Equation (H.16)},\\
\text{Decanter: Equations (H.17) and (H.18)},\\
\text{Distillation Column:}\begin{cases}\text{Outlet Streams: Equations (H.19) and (H.24)},\\ \text{Tray Number: Equation (H.20)},\\ \text{Saturate Pressure: Equation (H.22)},\\ \text{Volatility: Equations (H.21) and (H.23)},\end{cases}\\
\text{Feed Buffer:}\begin{cases}\text{ODE System: Equation (H.15)}, n_i^{\text{Ubuffer},0}=0,\ i\in\mathcal{SPC},\\ \text{Makeup: } \dot{N}_{\text{make-up},i}=0, i\in\mathcal{SPC}\setminus\{\text{C10an},\text{DMF},\text{cat}\},\end{cases}\\
\text{Closing Condition: } \sum_{i\in\mathcal{SPC}^{\text{Gas}}} y_i^{\text{SBR}}(t_{\text{SBR}})=\sum_{i\in\mathcal{SPC}^{\text{Gas}}} y_i^{\text{CSTR}}=1,
\end{cases}\\
&\text{Interconnection:}\begin{cases}
\text{SBR – Dbuffer:}\begin{cases}\text{Flow: Equation (H.8)},\\ \text{Controls: } y_i^{\text{Dbuffer}}(t_\Sigma)=y_i^{\text{SBR}}(t_{\text{SBR}}^{\text{f}}),\ i\in\mathcal{SPC}^{\text{Gas}},\end{cases}\\
\text{Dbuffer – CSTR: } \dot{N}_{i,\text{in}}^{\text{CSTR}}=\dot{N}_i^{\text{Dbuffer}},\ i\in\mathcal{SPC},\\
\text{CSTR – Dec: } \dot{N}_{i,\text{in}}^{\text{Dec}}=\dot{N}_i^{\text{CSTR}},\ i\in\mathcal{SPC},\\
\text{Dec – Dist: } \dot{N}_{i,\text{in}}^{\text{Dist}}=\dot{N}_i^{\text{NP,Dec}},\ i\in\mathcal{SPC},
\end{cases}\\
&\text{Performance Measures: }\{X,\ S\text{: Equations (H.26a) and (H.26c)},\\
&\text{Inequality Constraints: } \dot{N}_i(t)\geq 0,\ n_i(t)\geq 0,\ c_i(t)\geq 0,\ i\in\mathcal{SPC},\\
&\text{Sets:}\begin{cases}
\mathcal{SPC}=\{\text{C10an, DMF, nC12an, iC10en, nC13al, iC13al,}\\
\qquad\text{nC12an, H}_2\text{, CO, cat}\},\\
\mathcal{SPC}^{\text{Gas}}=\{\text{H}_2\text{, CO}\},\\
\mathcal{RCT}^{\text{Hyfo}}=\{\text{Iso, Hyfon, Hyfoi, Hyfoni, Hydn, Hydi}\},\\
\mathcal{STR}^{\text{Ubuffer}}=\{\text{Dist}^{\text{top}}\text{, Dec}^{\text{P}}\text{, make}-\text{up}\}.
\end{cases}
\end{aligned}
$$

Without the installation of a distillation column in the proof-of-concept experimental evaluation of the RSBR process, eq. (H.31) needs to be adapted, leading to

$$\min_{\substack{j_i^{\mathrm{SBR}}(t_{\mathrm{SBR}}),\\ \dot{N}_{\mathrm{make-up},i},\, i\in\mathcal{SPC},\, \dot{V}}} \quad -S_{\mathrm{nC13al}} + \left(V_{\mathrm{Liq}}^{\mathrm{Dbuffer}}(t_\Sigma^{\mathrm{f}}) - V_{\mathrm{Liq,min}}^{\mathrm{Dbuffer}}\right)^2 \tag{H.33}$$

s. t.

Kinetic Model: Equations (B.2), (B.3) and (B.9) to (B.12),

G/L Mass Transfer: Equations (H.1) and (H.2),

Constitutive Equations: Equations (B.4) to (B.7) and (B.8),

Times: Equations (5.1) to (5.4) and (5.6),

Data: Tables B.17 to B.19, H.1, H.3 and H.5,

Process Units:

- SBR:
  - ODE System: Equation (H.3),
  - Fill Volume: Equation (H.7),
  - Species Ratios: Equation (H.4),
- Flash Buffer:
  - ODE System: Equation (H.12),
  - Outlet Flow: $\dot{N}_i^{\mathrm{Dbuffer}}(t_\Sigma) = \dot{V} c_i^{\mathrm{Dbuffer}}(t_\Sigma)$, $i \in \mathcal{SPC}$,
  - Pressure: Equation (H.13),
- CSTR: Equation (H.16),
- Decanter: Equations (H.17) and (H.18),
- Distillation Column Equation (H.25),
- Feed Buffer:
  - ODE System: Equation (H.15), $n_i^{\mathrm{Ubuffer},0} = 0$, $i \in \mathcal{SPC}$,
  - Makeup: $\dot{N}_{\mathrm{make-up},i} = 0$, $i \in \mathcal{SPC} \setminus \{\mathrm{iC12en}, \mathrm{C10an}, \mathrm{DMF}, \mathrm{cat}\}$,
- Setpoints:
  - $y_i^{\mathrm{SBR}}(t_{\mathrm{SBR}}) = y_{i,\mathrm{set}}^{\mathrm{SBR}}$,
  - $y_i^{\mathrm{CSTR}} = y_{i,\mathrm{set}}^{\mathrm{CSTR}}$, $i \in \mathcal{SPC}^{\mathrm{Gas}}$

Interconnection:

- SBR – Dbuffer:
  - Flow: Equation (H.8),
  - Controls: $y_i^{\mathrm{Dbuffer}}(t_\Sigma) = y_i^{\mathrm{SBR}}(t_{\mathrm{SBR}}^{\mathrm{f}})$, $i \in \mathcal{SPC}^{\mathrm{Gas}}$,
- Dbuffer – CSTR: $\dot{N}_{i,\mathrm{in}}^{\mathrm{CSTR}} = \dot{N}_i^{\mathrm{Dbuffer}}$, $i \in \mathcal{SPC}$,
- CSTR – Dec: $\dot{N}_{i,\mathrm{in}}^{\mathrm{Dec}} = \dot{N}_i^{\mathrm{CSTR}}$, $i \in \mathcal{SPC}$,

Performance Measures: X, S: Equations (H.26a) and (H.26c),

Inequality Constraints: $\dot{N}_i(t) \geq 0$, $n_i(t) \geq 0$, $c_i(t) \geq 0$, $i \in \mathcal{SPC}$,

$$\text{Sets:} \begin{cases} \mathcal{SPC} = \{\text{C10an, DMF, nC12an, iC10en, nC13al, iC13al,} \\ \qquad \text{nC12an, } H_2\text{, CO, cat}\}, \\ \mathcal{SPC}^{\text{Gas}} = \{H_2\text{, CO}\}, \\ \mathcal{RCT}^{\text{Hyfo}} = \{\text{Iso, Hyfon, Hyfoi, Hyfoni, Hydn, Hydi}\}, \\ \mathcal{STR}^{\text{Ubuffer}} = \{\text{Dec}^{\text{P}}\text{, make} - \text{up}\}. \end{cases}$$

Please note that eq. (H.33) does not contain the temperature, pressure, and gas phase composition in the SBR and CSTR as optimization variables because the investigation aims at identifying the improvement over the hydroformylation process from Dreimann et al. [Dre+16b] in terms of the optimized axial dispersion profile over the total reaction time. For comparability, this also requires the total residence time to be set to 210 min.

In the second experimental study, the potential of the RSBR process is investigated by optimally controlling the temperature and gas phase composition in the SBR and CSTR. Without the distillation column and a simulated isomer recycle, the total residence time is increased to 300 min as originally intended by Kaiser et al. [Kai+17]. The corresponding optimization problem reads

$$\min_{\substack{T^{\text{SBR}}(t_{\text{SBR}}),\, p^{0,\text{SBR}},\, j_i^{\text{SBR}}(t_{\text{SBR}}),\\ T^{\text{CSTR}},\, p^{\text{CSTR}},\, y_i^{\text{CSTR}},\, i\in\mathcal{SPC}^{\text{Gas}},\\ \phi_{\text{Liq}}^{\text{V,CSTR}},\\ \dot{N}_{\text{make-up},i},\, i\in\mathcal{SPC},\, \dot{V}}} \quad -S_{\text{nC13al}} + \left(V_{\text{Liq}}^{\text{Dbuffer}}(t_\Sigma^{\text{f}}) - V_{\text{Liq,min}}^{\text{Dbuffer}}\right)^2 \tag{H.34}$$

s. t.

Kinetic Model:	Equations (B.2), (B.3) and (B.9) to (B.12),
G/L Mass Transfer:	Equations (H.1) and (H.2),
Constitutive Equations:	Equations (B.4) to (B.7) and (B.8),
Times:	Equations (5.1) to (5.4) and (5.6),
Data:	Tables B.17 to B.19, H.1, H.3 and H.6,

$$
\begin{aligned}
&\text{Process Units:}\begin{cases}
\text{SBR:}\begin{cases}\text{ODE System: Equation (H.3)},\\ \text{Fill Volume: Equation (H.7)},\\ \text{Species Ratios: Equation (H.4)},\end{cases}\\
\text{Flash Buffer:}\begin{cases}\text{ODE System: Equation (H.12)},\\ \text{Outlet Flow: } \dot{N}_i^{\text{Dbuffer}}(t_\Sigma) = \dot{V} c_i^{\text{Dbuffer}}(t_\Sigma),\ i \in \mathcal{SPC},\\ \text{Pressure: Equation (H.13)},\end{cases}\\
\text{CSTR: Equation (H.16)},\\
\text{Decanter: Equations (H.17) and (H.18)},\\
\text{Feed Buffer:}\begin{cases}\text{ODE System: Equation (H.15)}, n_i^{\text{Ubuffer},0} = 0,\ i \in \mathcal{SPC},\\ \text{Makeup: } \dot{N}_{\text{make-up},i} = 0, i \in \mathcal{SPC} \setminus \{\text{C10an}, \text{DMF}, \text{cat}\},\end{cases}\\
\text{Closing Condition: } \sum_{i \in \mathcal{SPC}^{\text{Gas}}} y_i^{\text{SBR}}(t_{\text{SBR}}) = \sum_{i \in \mathcal{SPC}^{\text{Gas}}} y_i^{\text{CSTR}} = 1,
\end{cases}\\
&\text{Interconnection:}\begin{cases}
\text{SBR – Dbuffer:}\begin{cases}\text{Flow: Equation (H.8)},\\ \text{Controls: } y_i^{\text{Dbuffer}}(t_\Sigma) = y_i^{\text{SBR}}(t_{\text{SBR}}^{\text{f}}),\ i \in \mathcal{SPC}^{\text{Gas}},\end{cases}\\
\text{Dbuffer – CSTR: } \dot{N}_{i,\text{in}}^{\text{CSTR}} = \dot{N}_i^{\text{Dbuffer}},\ i \in \mathcal{SPC},\\
\text{CSTR – Dec: } \dot{N}_{i,\text{in}}^{\text{Dec}} = \dot{N}_i^{\text{CSTR}},\ i \in \mathcal{SPC},
\end{cases}\\
&\text{Performance Measures: } \{X,\ S\text{: Equations (H.26a) and (H.26c)},\\
&\text{Inequality Constraints: } \dot{N}_i(t) \geq 0,\ n_i(t) \geq 0,\ c_i(t) \geq 0,\ i \in \mathcal{SPC},\\
&\text{Sets:}\begin{cases}
\mathcal{SPC} = \{\text{C10an, DMF, nC12an, iC10en, nC13al, iC13al,}\\
\qquad\qquad \text{nC12an, } H_2\text{, CO, cat}\},\\
\mathcal{SPC}^{\text{Gas}} = \{H_2\text{, CO}\},\\
\mathcal{RCT}^{\text{Hyfo}} = \{\text{Iso, Hyfon, Hyfoi, Hyfoni, Hydn, Hydi}\},\\
\mathcal{STR}^{\text{Ubuffer}} = \{\text{Dec}^{\text{P}}, \text{make} - \text{up}\}.
\end{cases}
\end{aligned}
$$

Due to a reduced idle time t_{idle}, a desired mass flow of $120\,\text{g}\,\text{h}^{-1}$ and the increase in total residence time, the residence time assignment to the different reaction zones is similar to the one performed solving eq. (H.33). To account for the desired mass flow, the liquid hold-up in the CSTR is considered as a decision variable.

Algorithm 3 Dynamic RSBR Simulation

Require: Define the idle time $t_{\text{idle}} \in \left[0, t^{\text{f}}_{\text{idle}}\right]$, batch time $t_{\text{SBR}} \in \left[0, t^{\text{f}}_{\text{SBR}}\right]$ and the continuous process time $t_{\text{SBR}} + t_{\text{idle}}$.

Require: Define the current cycle $k \in \left\{0, 1, \ldots, n_{\text{cycle}}\right\}$ with the maximum number of cycles $n_{\text{cycle}} \in [2, \infty) \subset \mathbb{N}_+$ and initialize $k \leftarrow 0$.

Require: Initial conditions $n^{\text{SBR},0,k}_{\text{Liq},i}$ with $i \in \mathcal{SPC}$ and $n^{\text{SBR},0,k}_{\text{Gas},i}$ with $i \in \mathcal{SPC}^{\text{Gas}}$, so that eq. (H.4) and eq. (H.5) are fulfilled under consideration of either tables H.4 to H.6.

Substitute all t in eq. (H.3) with t_{SBR} and in eqs. (H.12) and (H.15) with t_Σ.
$n^{\text{Ubuffer},k}(t^{\text{f}}_\Sigma)$, $n^k_{\text{nC12en,fresh}} \leftarrow$ EQ. (H.32) / EQ. (H.33) / EQ. (H.34) .
$n^{\text{idle},0,k+2} \leftarrow n^{\text{Ubuffer},k}(t^{\text{f}}_\Sigma)$.
$k \leftarrow k + 1$. ▷ *Recycle not yet available.*
$n^{\text{Ubuffer},k}(t^{\text{f}}_\Sigma)$, $n^k_{\text{nC12en,fresh}} \leftarrow$ EQ. (H.32) / EQ. (H.33) / EQ. (H.34) .
$n^{\text{idle},0,k+2} \leftarrow n^{\text{Ubuffer},k}(t^{\text{f}}_\Sigma)$.
for all $k \in \left\{2, 3, \ldots, n_{\text{cycle}}\right\}$ **do** ▷ *Recycle from $k-2$ available.*
    $n^{\text{idle},k}(t^{\text{f}}_{\text{idle}}) \leftarrow$ EQ. (H.30).
    $n^{\text{SBR},0,k}_{\text{Liq},i} \leftarrow n^{\text{idle},k}_i(t^{\text{f}}_{\text{idle}}), i \in \mathcal{SPC} \setminus \{\text{nC12en}\}$.
    $n^{\text{SBR},0,k}_{\text{Liq,nC12en}} \leftarrow n^{\text{idle},k}_{\text{nC12en}}(t^{\text{f}}_{\text{idle}}) + n^{k-2}_{\text{nC12en,fresh}}$.
    $n^{\text{Ubuffer},k}(t^{\text{f}}_\Sigma)$, $n^k_{\text{nC12en,fresh}} \leftarrow$ EQ. (H.32) / EQ. (H.33) / EQ. (H.34) .
    $n^{\text{idle},0,k+2} \leftarrow n^{\text{Ubuffer},k}(t^{\text{f}}_\Sigma)$.

Tab. H.5.: Maximum DoF and simulated distillation recycle operating conditions for the RSBR hydroformylation process [Jok+19].

			Maximum DoF			OP1 / OP2.1 / OP2.2		
	Parameter	Unit	Init	LB	UB	Init	LB	UB
SBR	ϑ	°C	105	95	115	105	–	–
	$\beta_{\mathrm{eff,H_2}}$	min^{-1}	9.57	–	–	9.57	–	–
	$\beta_{\mathrm{eff,CO}}$	min^{-1}	7.08	–	–	7.08	–	–
	$^{*}V$	mL	240	–	–	240	–	–
	$^{*}\phi^{\mathrm{V}}_{\mathrm{Liq}}$	$\mathrm{mL\,mL}^{-1}$	0.66	0.3	0.66	0.66	–	–
	t_{SBR}	min	30	10	∞	30	10	∞
	$^{*}t_{\mathrm{idle}}$	min	30	–	–	30	–	–
	p^0	bar	20	10	20	20	–	–
	$y_{\mathrm{H_2}}$	$\mathrm{mol\,mol}^{-1}$	0.5	0	1	0.5	–	–
	y_{CO}	$\mathrm{mol\,mol}^{-1}$	0.5	0	1	0.5	–	–
	$j_{\mathrm{H_2}}$	$\mathrm{mol\,s}^{-1}$	$n^{\mathrm{SBR},0}_{\mathrm{Gas,H_2}}/t_{\mathrm{SBR}}$	0	∞	$n^{\mathrm{SBR},0}_{\mathrm{Gas,H_2}}/t_{\mathrm{SBR}}$	0	∞
	j_{CO}	$\mathrm{mol\,s}^{-1}$	$n^{\mathrm{SBR},0}_{\mathrm{Gas,CO}}/t_{\mathrm{SBR}}$	0	∞	$n^{\mathrm{SBR},0}_{\mathrm{Gas,CO}}/t_{\mathrm{SBR}}$	0	∞
Dbuffer	$^{*}\vartheta$	°C	91	–	–	91	–	–
	$^{*}p^0$	bar	16.21	–	–	16.21	–	–
	$^{*}p$	bar	16.21	0	∞	16.21	0	∞
	$y_{\mathrm{H_2}}$	$\mathrm{mol\,mol}^{-1}$	$y^{\mathrm{SBR}}_{\mathrm{H_2}}(t_{\mathrm{SBR}})$			$y^{\mathrm{SBR}}_{\mathrm{H_2}}(t_{\mathrm{SBR}})$		
	y_{CO}	$\mathrm{mol\,mol}^{-1}$	$y^{\mathrm{SBR}}_{\mathrm{CO}}(t_{\mathrm{SBR}})$			$y^{\mathrm{SBR}}_{\mathrm{CO}}(t_{\mathrm{SBR}})$		
	$\beta_{\mathrm{eff,H_2}}$	min^{-1}	9.57/10	–	–	9.57/10	–	–
	$\beta_{\mathrm{eff,CO}}$	min^{-1}	7.08/10	–	–	7.08/10	–	–
	$^{*}V$	mL	430	–	–	430	–	–
	$^{*}V_{\mathrm{Liq,min}}$	mL	10	–	–	10	–	–
	$\dot{V}$	$\mathrm{mL\,h}^{-1}$	$V^{\mathrm{SBR}}_{\mathrm{Liq}}(t_{\mathrm{SBR}})/t_{\Sigma}$	0	∞	$V^{\mathrm{SBR}}_{\mathrm{Liq}}(t_{\mathrm{SBR}})/t_{\Sigma}$	0	∞
CSTR	$^{*}\vartheta$	°C	115	95	115	115	–	–
	$^{*}p$	bar	21	10	21	21	–	–
	$y_{\mathrm{H_2}}$	$\mathrm{mol\,mol}^{-1}$	0.5	0	1	0.5	–	–
	y_{CO}	$\mathrm{mol\,mol}^{-1}$	0.5	0	1	0.5	–	–
	$\beta_{\mathrm{eff,H_2}}$	min^{-1}	9.57	–	–	9.57	–	–
	$\beta_{\mathrm{eff,CO}}$	min^{-1}	7.08	–	–	7.08	–	–
	$^{*}V$	mL	1000	–	–	1000	–	–
	$^{*}\phi^{\mathrm{V}}_{\mathrm{Liq}}$	$\mathrm{mL\,mL}^{-1}$	0.3	0.3	0.66	0.3	–	–
Ubuffer	ϑ	°C	96	–	–	96	–	–
	$^{*}p^0$	bar	2.875	–	–	2.875	–	–
	$^{*}p$	bar	2.875	0	∞	2.875	0	∞
	$y_{\mathrm{H_2}}$	$\mathrm{mol\,mol}^{-1}$	0.5	–	–	0.5	–	–
	y_{CO}	$\mathrm{mol\,mol}^{-1}$	0.5	–	–	0.5	–	–
	$\beta_{\mathrm{eff,H_2}}$	min^{-1}	9.57/10	–	–	9.57/10	–	–
	$\beta_{\mathrm{eff,CO}}$	min^{-1}	7.08/10	–	–	7.08/10	–	–
	$^{*}V$	mL	260	–	–	260	–	–
Process	τ_{total}	min	300	–	–	210	–	–
	$\phi^{\mathrm{m}}_{\mathrm{iC12en,nC12en}}$	$\mathrm{g\,g}^{-1}$	–	–	–	0 / 0.5 / 0.75	–	–
	$\phi^{\mathrm{n}}_{\mathrm{n/iso}}$	$\mathrm{mol\,mol}^{-1}$	0.95	0	1	0.95	0	1

* Data taken from the experimental setup from Dreimann et al. [Dre+16b], Rätze et al. [Rät+19], and Jokiel et al. [Jok+19].

Tab. H.6.: RSBR hydroformylation process with optimal temperature and gas phase composition control [Jok20].

			Values		
	Parameter	Unit	Init	LB	UB
SBR	ϑ	°C	105	95	115
	$\beta_{\mathrm{eff,H_2}}$	min^{-1}	9.57	–	–
	$\beta_{\mathrm{eff,CO}}$	min^{-1}	7.08	–	–
	${}^{*}V$	mL	240	–	–
	${}^{*}\phi^{\mathrm{V}}_{\mathrm{Liq}}$	$\mathrm{mL\,mL}^{-1}$	0.66	–	–
	t_{SBR}	min	30	10	∞
	${}^{*}t_{\mathrm{idle}}$	min	20	–	–
	p^0	bar	19	10	19
	$y_{\mathrm{H_2}}$	$\mathrm{mol\,mol}^{-1}$	0.5	0	1
	y_{CO}	$\mathrm{mol\,mol}^{-1}$	0.5	0	1
	$j_{\mathrm{H_2}}$	$\mathrm{mol\,s}^{-1}$	$n^{\mathrm{SBR},0}_{\mathrm{Gas,H_2}}/t_{\mathrm{SBR}}$	0	∞
	j_{CO}	$\mathrm{mol\,s}^{-1}$	$n^{\mathrm{SBR},0}_{\mathrm{Gas,CO}}/t_{\mathrm{SBR}}$	0	∞
Dbuffer	${}^{*}\vartheta$	°C	91	–	–
	${}^{*}p^0$	bar	16.21	–	–
	${}^{*}p$	bar	16.21	0	∞
	$y_{\mathrm{H_2}}$	$\mathrm{mol\,mol}^{-1}$	$y^{\mathrm{SBR}}_{\mathrm{H_2}}(t_{\mathrm{SBR}})$		
	y_{CO}	$\mathrm{mol\,mol}^{-1}$	$y^{\mathrm{SBR}}_{\mathrm{CO}}(t_{\mathrm{SBR}})$		
	$\beta_{\mathrm{eff,H_2}}$	min^{-1}	9.57/10	–	–
	$\beta_{\mathrm{eff,CO}}$	min^{-1}	7.08/10	–	–
	${}^{*}V$	mL	430	–	–
	${}^{*}V_{\mathrm{Liq,min}}$	mL	10	–	–
	$\dot{V}$	$\mathrm{mL\,h}^{-1}$	$V^{\mathrm{SBR}}_{\mathrm{Liq}}(t_{\mathrm{SBR}})/t_{\Sigma}$	0	∞
CSTR	${}^{*}\vartheta$	°C	115	95	115
	${}^{*}p$	bar	21	–	–
	$y_{\mathrm{H_2}}$	$\mathrm{mol\,mol}^{-1}$	0.5	0	1
	y_{CO}	$\mathrm{mol\,mol}^{-1}$	0.5	0	1
	$\beta_{\mathrm{eff,H_2}}$	min^{-1}	9.57	–	–
	$\beta_{\mathrm{eff,CO}}$	min^{-1}	7.08	–	–
	${}^{*}V$	mL	1000	–	–
	${}^{*}\phi^{\mathrm{V}}_{\mathrm{Liq}}$	$\mathrm{mL\,mL}^{-1}$	0.3	0.3	0.66
Ubuffer	ϑ	°C	96	–	–
	${}^{*}p^0$	bar	2.875	–	–
	${}^{*}p$	bar	2.875	0	∞
	$y_{\mathrm{H_2}}$	$\mathrm{mol\,mol}^{-1}$	0.5	–	–
	y_{CO}	$\mathrm{mol\,mol}^{-1}$	0.5	–	–
	$\beta_{\mathrm{eff,H_2}}$	min^{-1}	9.57/10	–	–
	$\beta_{\mathrm{eff,CO}}$	min^{-1}	7.08/10	–	–
	${}^{*}V$	mL	260	–	–
Process	τ_{total}	min	300	–	–
	$\phi^{\mathrm{n}}_{\mathrm{n/iso}}$	$\mathrm{mol\,mol}^{-1}$	0.95	0	1

* Data taken from the experimental setup from Jokiel [Jok20].

Bibliography

[AF04] T. K. Abraham and M. Feinberg. “Kinetic Bounds on Attainability in the Reactor Synthesis Problem”. In: *Industrial & Engineering Chemistry Research* 43.2 (2004), pp. 449–457 (cit. on p. 22).

[AP75] D. S. Abrams and J. M. Prausnitz. “Statistical Thermodynamics of Liquid Mixtures: A New Expression for the Excess Gibbs Energy of Partly or Completely Miscible Systems”. In: *AIChE Journal* 21.1 (1975), pp. 116–128 (cit. on p. 8).

[AAF00] C. Adjiman, I. Androulakis, and C. Floudas. “Global Optimization of Mixed-Integer Nonlinear Problems”. In: *AIChE Journal* 46.9 (2000), pp. 1769–1797 (cit. on p. 23).

[Aga+08] V. Agarwal, S. Thotla, R. Kaur, and S. M. Mahajani. “Attainable Regions of Reactive Distillation. Part II: Single Reactant Azeotropic Systems”. In: *Chemical Engineering Science* 63.11 (2008), pp. 2928–2945 (cit. on pp. 22, 25).

[ATM08] V. Agarwal, S. Thotla, and S. M. Mahajani. “Attainable Regions of Reactive Distillation—Part I. Single Reactant Non-Azeotropic Systems”. In: *Chemical Engineering Science* 63.11 (2008), pp. 2946–2965 (cit. on pp. 22, 25).

[AW00] P. T. Anastas and J. C. Warner. *Green Chemistry: Theory and Practice*. First publ. new as paperback. Oxford: Oxford University Press, 2000. 135 pp. (cit. on pp. 2, 37).

[And+19] J. A. E. Andersson, J. Gillis, G. Horn, J. B. Rawlings, and M. Diehl. “CasADi: A Software Framework for Nonlinear Optimization and Optimal Control”. In: *Mathematical Programming Computation* 11.1 (2019), pp. 1–36 (cit. on p. 61).

[ASS97] G. E. B. Archer, A. Saltelli, and I. M. Sobol. “Sensitivity Measures, ANOVA-like Techniques and the Use of Bootstrap”. In: *Journal of Statistical Computation and Simulation* 58.2 (1997), pp. 99–120 (cit. on p. 164).

[Ari60] R. Aris. “Studies in Optimization—II: Optimum Temperature Gradients in Tubular Reactors”. In: *Chemical Engineering Science* 13.1 (1960), pp. 18–29 (cit. on p. 25).

[AHG14] N. Asiedu, D. Hildebrandt, and D. Glasser. “Experimental Simulation of a Two-Dimensional Attainable Region and Its Application in the Optimization of Production Rate and Process Time of an Adiabatic Batch Reactor”. In: *Industrial & Engineering Chemistry Research* 53.34 (2014), pp. 13308–13319 (cit. on p. 22).

[AM02] S. Asprey and S. Macchietto. “Designing Robust Optimal Dynamic Experiments”. In: *Journal of Process Control* 12.4 (2002), pp. 545–556 (cit. on pp. 13, 17).

[Bab+15] D. K. Babi, J. Holtbruegge, P. Lutze, et al. “Sustainable Process Synthesis–Intensification”. In: *Computers & Chemical Engineering*. Special Issue: Selected Papers from the 8th International Symposium on the Foundations of Computer-Aided Process Design (FOCAPD 2014), July 13-17, 2014, Cle Elum, Washington, USA 81 (2015), pp. 218–244 (cit. on p. 24).

[Bab+14] D. K. Babi, P. Lutze, J. M. Woodley, and R. Gani. “A Process Synthesis-Intensification Framework for the Development of Sustainable Membrane-Based Operations”. In: *Chemical Engineering and Processing: Process Intensification* 86 (2014), pp. 173–195 (cit. on p. 24).

[BB93] S. Balakrishna and L. T. Biegler. “A Unified Approach for the Simultaneous Synthesis of Reaction, Energy, and Separation Systems”. In: *Industrial & Engineering Chemistry Research* 32.7 (1993), pp. 1372–1382 (cit. on p. 25).

[BB92] S. Balakrishna and L. T. Biegler. “Targeting Strategies for the Synthesis and Energy Integration of Nonisothermal Reactor Networks”. In: *Industrial & Engineering Chemistry Research* 31.9 (1992), pp. 2152–2164 (cit. on p. 25).

[BAB08] E. Balsa-Canto, A. A. Alonso, and J. R. Banga. “Computational Procedures for Optimal Experimental Design in Biological Systems”. In: *IET Systems Biology* 2.4 (2008), pp. 163–172 (cit. on p. 13).

[BB10] E. Balsa-Canto and J. R. Banga. “AMIGO: A Model Identification Toolbox Based on Global Optimization and Its Applications in Biosystems”. In: *IFAC Proceedings Volumes* 43.6 (2010), pp. 132–137 (cit. on p. 13).

[BVV02] J. R. Banga, K. J. Versyck, and J. F. Van Impe. “Computation of Optimal Identification Experiments for Nonlinear Dynamic Process Models: A Stochastic Global Optimization Approach”. In: *Industrial & Engineering Chemistry Research* 41.10 (2002), pp. 2425–2430 (cit. on p. 13).

[BS04] S. D. Barnicki and J. J. Siirola. “Process Synthesis Prospective”. In: *Computers & Chemical Engineering* 28.4 (2004), pp. 441–446 (cit. on p. 19).

[BAW10] T. Barz, H. Arellano-Garcia, and G. Wozny. “Handling Uncertainty in Model-Based Optimal Experimental Design”. In: *Industrial & Engineering Chemistry Research* 49.12 (2010), pp. 5702–5713 (cit. on pp. 16, 62).

[Bar+13] T. Barz, D. C. López Cárdenas, H. Arellano-Garcia, and G. Wozny. “Experimental Evaluation of an Approach to Online Redesign of Experiments for Parameter Determination”. In: *AIChE Journal* 59.6 (2013), pp. 1981–1995 (cit. on pp. 62, 74, 178, 179, 260).

[Bau+00] I. Bauer, H. G. Bock, S. Körkel, and J. P. Schlöder. “Numerical Methods for Optimum Experimental Design in DAE Systems”. In: *Journal of Computational and Applied Mathematics* 120.1-2 (2000), pp. 1–25 (cit. on pp. 13, 18).

[Bau21] P. A. Baum. “Experimentelle Untersuchung der Kondensationsreaktion in der Tandemreaktion Hydroaminomethylierung”. BA thesis. Magdeburg: Otto von Guericke University, 2021. 86 pp. (cit. on p. 173).

[BB09] B. T. Baumrucker and L. T. Biegler. “MPEC Strategies for Optimization of a Class of Hybrid Dynamic Systems”. In: *Journal of Process Control* 19.8 (2009), pp. 1248–1256 (cit. on p. 109).

[BRB08] B. T. Baumrucker, J. Renfro, and L. T. Biegler. “MPEC Problem Formulations and Solution Strategies with Chemical Engineering Applications”. In: *Computers & Chemical Engineering* 32.12 (2008), pp. 2903–2913 (cit. on p. 109).

[BKB13] A. Behr, A. Kleyensteiber, and M. Becker. “A Novel Approach to Selecting Thermomorphic Multicomponent Solvent Systems (TMS) for Hydroaminomethylation Reactions”. In: *Chemical Engineering and Processing: Process Intensification* 69 (2013), pp. 15–23 (cit. on p. 41).

[BR05] A. Behr and R. Roll. “Temperaturgesteuerte Mehrkomponenten-Lösungsmittelsysteme für homogene übergangsmetallkatalysierte Reaktionen”. In: *Chemie Ingenieur Technik* 77.6 (2005), pp. 748–752 (cit. on p. 39).

[Beh08] A. Behr. *Angewandte Homogene Katalyse*. Weinheim: Wiley-VCH, 2008 (cit. on pp. 38, 39).

[Beh+05] A. Behr, G. Henze, D. Obst, and B. Turkowski. “Selection Process of New Solvents in Temperature-Dependent Multi-Component Solvent Systems and Its Application in Isomerising Hydroformylation”. In: *Green Chemistry* 7.9 (2005), p. 645 (cit. on p. 39).

[BV14] A. Behr and A. J. Vorholt. “Neue Trends in der Homogenen Übergangsmetallkatalyse”. In: *Chemie Ingenieur Technik* 86.12 (2014), pp. 2089–2104 (cit. on p. 37).

[BW11] A. Behr and A. Wintzer. “Baukastensystem zur Auswahl von Lösungsmitteln in homogenkatalytischen Reaktionen”. In: *Chemie Ingenieur Technik* 83.9 (2011), pp. 1356–1370 (cit. on p. 39).

[Bel+04] M. Beller, J. Seayad, A. Tillack, and H. Jiao. “Catalytic Markovnikov and Anti-Markovnikov Functionalization of Alkenes and Alkynes: Recent Developments and Trends”. In: *Angewandte Chemie International Edition* 43.26 (2004), pp. 3368–3398 (cit. on pp. 33, 35, 36).

[BAM05] L. Benabbas, S. P. Asprey, and S. Macchietto. “Curvature-Based Methods for Designing Optimally Informative Experiments in Multiresponse Nonlinear Dynamic Situations”. In: *Industrial & Engineering Chemistry Research* 44.18 (2005), pp. 7120–7131 (cit. on p. 17).

[BLO98] D. E. Bergbreiter, Y.-S. Liu, and P. L. Osburn. “Thermomorphic Rhodium(I) and Palladium(0) Catalysts”. In: *Journal of the American Chemical Society* 120.17 (1998), pp. 4250–4251 (cit. on pp. 37, 38).

[Bia+20a] J. Bianga, N. Kopplin, J. Hülsmann, D. Vogt, and T. Seidensticker. “Rhodium-Catalysed Reductive Amination for the Synthesis of Tertiary Amines”. In: *Advanced Synthesis & Catalysis* 362.20 (2020), pp. 4415–4424 (cit. on p. 41).

[Bia+20b] J. Bianga, K. U. Künnemann, L. Goclik, et al. “Tandem Catalytic Amine Synthesis from Alkenes in Continuous Flow Enabled by Integrated Catalyst Recycling”. In: *ACS Catalysis* 10.11 (2020), pp. 6463–6472 (cit. on pp. 34, 36, 37, 39–41, 60).

[Bia+19] J. Bianga, K. U. Künnemann, T. Gaide, et al. “Thermomorphic Multiphase Systems - Switchable Solvent Mixtures for the Recovery of Homogeneous Catalysts in Batch and Flow Processes”. In: *Chemistry - A European Journal* 25.50 (2019), pp. 11586–11608 (cit. on pp. 37, 41).

[Bou+15] J. Bouvin, S. Cajot, P.-J. D’Huys, et al. “Multi-Objective Experimental Design for 13 C-based Metabolic Flux Analysis”. In: *Mathematical Biosciences* 268 (2015), pp. 22–30 (cit. on pp. 13, 17).

[BM06] M.-J. Bruwer and J. F. MacGregor. “Robust Multi-Variable Identification: Optimal Experimental Design with Constraints”. In: *Journal of Process Control* 16.6 (2006), pp. 581–600 (cit. on p. 17).

[Bun21] Bundesrepublik Deutschland. “Erstes Gesetz Zur Änderung Des Bundes-Klimaschutzgesetzes”. In: *Bundesgesetzblatt Teil I* 59 (2021), p. 3905 (cit. on p. 1).

[Bun19] Bundesrepublik Deutschland. “Gesetz Zur Einführung Eines Bundes-Klimaschutzgesetzes Und Zur Änderung Weiterer Vorschriften”. In: *Bundesgesetzblatt Teil I* 48 (2019), p. 2513 (cit. on p. 1).

[BWM02] J. F. Burri, S. D. Wilson, and V. I. Manousiouthakis. “Infinite DimEnsionAl State-space Approach to Reactor Network Synthesis: Application to Attainable Region Construction”. In: *Computers & Chemical Engineering* 26.6 (2002), pp. 849–862 (cit. on p. 22).

[BM09] G. Buzzi-Ferraris and F. Manenti. “Kinetic Models Analysis”. In: *Chemical Engineering Science* 64.5 (2009), pp. 1061–1074 (cit. on p. 77).

[CG17] Q. Chen and I. Grossmann. “Recent Developments and Challenges in Optimization-Based Process Synthesis”. In: *Annual Review of Chemical and Biomolecular Engineering* 8.1 (2017), pp. 249–283 (cit. on pp. 19–21).

[Cor+97] J. C. Cordero, A. Davin, P. Floquet, L. Pibouleau, and S. Domenech. “Synthesis of Optimal Reactor Networks Using Mathematical Programming and Simulated Annealing”. In: *Computers & Chemical Engineering*. Supplement to Computers and Chemical Engineering 21 (1997), S47–S52 (cit. on p. 23).

[Cre15] S. Cremaschi. “A Perspective on Process Synthesis: Challenges and Prospects”. In: *Computers & Chemical Engineering*. Special Issue: Selected Papers from the 8th International Symposium on the Foundations of Computer-Aided Process Design (FOCAPD 2014), July 13-17, 2014, Cle Elum, Washington, USA 81 (2015), pp. 130–137 (cit. on p. 20).

[Cus09] E. L. Cussler. *Diffusion: Mass Transfer in Fluid Systems*. 3rd ed. New York: Cambridge University Press, 2009. 631 pp. (cit. on p. 10).

[DM08] B. Davis and V. Manousiouthakis. “Identification of the Attainable Region for Batch Reactor Networks”. In: AIChE Annual Meeting, Conference Proceedings. Code 83913. 2008 (cit. on p. 22).

[DLH19] S. E. Demirel, J. Li, and M. M. F. Hasan. “A General Framework for Process Synthesis, Integration, and Intensification”. In: *Industrial & Engineering Chemistry Research* 58.15 (2019), pp. 5950–5967 (cit. on pp. 24, 25).

[DLH17] S. E. Demirel, J. Li, and M. M. F. Hasan. “Systematic Process Intensification Using Building Blocks”. In: *Computers & Chemical Engineering*. Process Intensification 105 (2017), pp. 2–38 (cit. on pp. 24, 25).

[Des19] Design Institute for Physical Properties. *DIPPR Project 801*. Version 2019. Design Institute for Physical Properties, 2019 (cit. on p. 146).

[Dou85] J. M. Douglas. “A Hierarchical Decision Procedure for Process Synthesis”. In: *AIChE Journal* 31.3 (1985), pp. 353–362 (cit. on p. 21).

[DB15] A. W. Dowling and L. T. Biegler. “A Framework for Efficient Large Scale Equation-Oriented Flowsheet Optimization”. In: *Computers & Chemical Engineering* 72 (2015), pp. 3–20 (cit. on p. 23).

[Dre+16a] J. M. Dreimann, H. Warmeling, J. N. Weimann, et al. “Increasing Selectivity of the Hydroformylation in a Miniplant: Catalyst, Solvent, and Olefin Recycle in Two Loops”. In: *AIChE Journal* 62.12 (2016), pp. 4377–4383 (cit. on p. 119).

[Dre+16b] J. Dreimann, P. Lutze, M. Zagajewski, et al. “Highly Integrated Reactor–Separator Systems for the Recycling of Homogeneous Catalysts”. In: *Chemical Engineering and Processing: Process Intensification* 99 (2016), pp. 124–131 (cit. on pp. 95, 112, 113, 116, 120, 125, 204, 205, 211, 214).

[EK06] F. Eckert and A. Klamt. *COSMOtherm*. Version C2.1 Release 01.08. Leverkusen: COSMOlogic GmbH & Co. KG, 2006 (cit. on p. 199).

[Eil+99] P. Eilbracht, L. Bärfacker, C. Buss, et al. “Tandem Reaction Sequences under Hydroformylation Conditions: New Synthetic Applications of Transition Metal Catalysis”. In: *Chemical Reviews* 99.11 (1999), pp. 3329–3366 (cit. on p. 36).

[ERS17] A. El Sibai, L. K. Rihko Struckmann, and K. Sundmacher. “Model-Based Optimal Sabatier Reactor Design for Power-to-Gas Applications”. In: *Energy Technology* 5.6 (2017), pp. 911–921 (cit. on p. 29).

[ESK17] V. N. Emenike, R. Schenkendorf, and U. Krewer. “A Systematic Reactor Design Approach for the Synthesis of Active Pharmaceutical Ingredients”. In: *European Journal of Pharmaceutics and Biopharmaceutics* 126 (2017), pp. 75–88 (cit. on p. 29).

[ESK18] V. N. Emenike, R. Schenkendorf, and U. Krewer. “Model-Based Optimization of Biopharmaceutical Manufacturing in Pichia Pastoris Based on Dynamic Flux Balance Analysis”. In: *Computers & Chemical Engineering* 118 (2018), pp. 1–13 (cit. on p. 29).

[Eme+18] V. N. Emenike, X. Xie, R. Schenkendorf, A. C. Spiess, and U. Krewer. “Robust Dynamic Optimization of Enzyme-Catalyzed Carboligation: A Point Estimate-Based Back-off Approach”. In: *Computers & Chemical Engineering* 121 (2018), pp. 232–247 (cit. on p. 29).

[EF02] W. R. Esposito and C. A. Floudas. “Deterministic Global Optimization in Isothermal Reactor Network Synthesis”. In: *Journal of Global Optimization* 22.1 (2002), pp. 59–95 (cit. on p. 23).

[Eur06] European Union: European Parliament and Council. “Regulation (EC) No 1907/2006 of the European Parliament and of the Council of 18 December 2006 Concerning the Registration, Evaluation, Authorisation and Restriction of Chemicals (REACH), Establishing a European Chemicals Agency, Amending Directive 1999/45/EC and Repealing Council Regulation (EEC) No 793/93 and Commission Regulation (EC) No 1488/94 as Well as Council Directive 76/769/EEC and Commission Directives 91/155/EEC, 93/67/EEC, 93/105/EC and 2000/21/EC”. In: *OJ* L 396 (2006), pp. 1–849 (cit. on pp. 1, 37).

[Eur21] European Union: European Parliament and Council. “Regulation (EU) 2021/1119 of the European Parliament and of the Council of 30 June 2021 Establishing the Framework for Achieving Climate Neutrality and Amending Regulations (EC) No 401/2009 and (EU) 2018/1999 (‘European Climate Law’)”. In: *OJ* L 243 (2021), pp. 1–17 (cit. on p. 1).

[Exl+08] O. Exler, L. T. Antelo, J. A. Egea, A. A. Alonso, and J. R. Banga. “A Tabu Search-Based Algorithm for Mixed-Integer Nonlinear Problems and Its Application to Integrated Process and Control System Design”. In: *Computers & Chemical Engineering* 32.8 (2008), pp. 1877–1891 (cit. on p. 23).

[Faß+17] T. A. Faßbach, T. Gaide, M. Terhorst, A. Behr, and A. J. Vorholt. “Renewable Surfactants through the Hydroaminomethylation of Terpenes”. In: *ChemCatChem* 9.8 (2017), pp. 1359–1362 (cit. on pp. 36, 37).

[FSV18] T. A. Faßbach, F. O. Sommer, and A. J. Vorholt. “Hydroaminomethylation in Aqueous Solvent Systems - An Efficient Pathway to Highly Functionalized Amines”. In: *Advanced Synthesis & Catalysis* 360.7 (2018), pp. 1473–1482 (cit. on pp. 33, 37).

[Fei02] M. Feinberg. “Toward a Theory of Process Synthesis”. In: *Industrial & Engineering Chemistry Research* 41.16 (2002), pp. 3751–3761 (cit. on p. 22).

[FE01] M. Feinberg and P. Ellison. “General Kinetic Bounds on Productivity and Selectivity in Reactor—Separator Systems of Arbitrary Design: Principles”. In: *Industrial & Engineering Chemistry Research* 40.14 (2001), pp. 3181–3194 (cit. on p. 22).

[FH97] M. Feinberg and D. Hildebrandt. “Optimal Reactor Design from a Geometric Viewpoint—I. Universal Properties of the Attainable Region”. In: *Chemical Engineering Science* 52.10 (1997), pp. 1637–1665 (cit. on p. 22).

[FAC89] C. A. Floudas, A. Aggarwal, and A. R. Ciric. “Global Optimum Search for Nonconvex NLP and MINLP Problems”. In: *Computers & Chemical Engineering* 13.10 (1989), pp. 1117–1132 (cit. on p. 23).

[FM08] G. Franceschini and S. Macchietto. “Anti-Correlation Approach to Model-Based Experiment Design: Application to a Biodiesel Production Process”. In: *Industrial & Engineering Chemistry Research* 47.7 (2008), pp. 2331–2348 (cit. on pp. 13, 15, 17, 18, 81).

[FGR77] A. Fredenslund, J. Gmehling, and P. Rasmussen. *Vapor-Liquid Equilibria Using UNIFAC: A Group Contribution Method*. Amsterdam: Elsevier Scientific Pub. Co. ; distributors for the U.S. and Canada, Elsevier North-Holland, 1977. 380 pp. (cit. on p. 8).

[Fre+19] H. Freund, J. Maußner, M. Kaiser, and M. Xie. “Process Intensification by Model-Based Design of Tailor-Made Reactors”. In: *Current Opinion in Chemical Engineering* 26 (2019), pp. 46–57 (cit. on pp. 29, 30).

[FS08] H. Freund and K. Sundmacher. “Towards a Methodology for the Systematic Analysis and Design of Efficient Chemical Processes”. In: *Chemical Engineering and Processing: Process Intensification* 47.12 (2008), pp. 2051–2060 (cit. on pp. 3, 26, 27, 29).

[GMB07] F. Galvanin, S. Macchietto, and F. Bezzo. “Model-Based Design of Parallel Experiments”. In: *Industrial & Engineering Chemistry Research* 46.3 (2007), pp. 871–882 (cit. on pp. 15, 17, 62).

[GC81] D. A. Gardner and R. T. Clark. “United States Patent: 4255357 - Catalytic Process for Preparing Ethyl Amines”. Pat. 4255357. Pennwalt Corporation. 1981 (cit. on p. 34).

[Gar+19] N. Garg, J. M. Woodley, R. Gani, and G. M. Kontogeorgis. “Sustainable Solutions by Integrating Process Synthesis-Intensification”. In: *Computers & Chemical Engineering* 126 (2019), pp. 499–519 (cit. on pp. 24, 25).

[GCH87] D. Glasser, C. Crowe, and D. Hildebrandt. “A Geometric Approach to Steady Flow Reactors: The Attainable Region and Optimization in Concentration Space”. In: *Industrial & Engineering Chemistry Research* 26.9 (1987), pp. 1803–1810 (cit. on p. 22).

[GLS93] J. Gmehling, J. Li, and M. Schiller. “A Modified UNIFAC Model. 2. Present Parameter Matrix and Results for Different Thermodynamic Properties”. In: *Industrial & Engineering Chemistry Research* 32.1 (1993), pp. 178–193 (cit. on pp. 8, 60, 157).

[Gme+98] J. Gmehling, J. Lohmann, A. Jakob, J. Li, and R. Joh. “A Modified UNIFAC (Dortmund) Model. 3. Revision and Extension”. In: *Industrial & Engineering Chemistry Research* 37.12 (1998), pp. 4876–4882 (cit. on p. 8).

[GGB21] Q. Göttl, D. Grimm, and J. Burger. “Automated Process Synthesis Using Reinforcement Learning”. In: *Computer Aided Chemical Engineering* 50 (2021), pp. 209–214 (cit. on p. 23).

[GP17] A. R. Gottu Mukkula and R. Paulen. “Model-Based Optimal Experiment Design for Nonlinear Parameter Estimation Using Exact Confidence Regions”. In: *IFAC-PapersOnLine* 50.1 (2017), pp. 13760–13765 (cit. on p. 13).

[GR98] B. Gross and P. Roosen. “Total Process Optimization in Chemical Engineering with Evolutionary Algorithms”. In: *Computers & Chemical Engineering*. European Symposium on Computer Aided Process Engineering-8 22 (1998), S229–S236 (cit. on p. 23).

[GS02] J. Gross and G. Sadowski. “Application of the Perturbed-Chain SAFT Equation of State to Associating Systems”. In: *Industrial & Engineering Chemistry Research* 41.22 (2002), pp. 5510–5515 (cit. on p. 8).

[GS01] J. Gross and G. Sadowski. “Perturbed-Chain SAFT: An Equation of State Based on a Perturbation Theory for Chain Molecules”. In: *Industrial & Engineering Chemistry Research* 40.4 (2001), pp. 1244–1260 (cit. on pp. 8, 60).

[Hab+19] R. Haberfellner, O. de Weck, E. Fricke, and S. Vössner. *Systems Engineering: Fundamentals and Applications*. Cham: Springer International Publishing, 2019 (cit. on p. 2).

[Ham+08] B. Hamers, P. S. Bäuerlein, C. Müller, and D. Vogt. “Hydroaminomethylation of N-Alkenes in a Biphasic Ionic Liquid System”. In: *Advanced Synthesis & Catalysis* 350.2 (2008), pp. 332–342 (cit. on p. 37).

[Han07] C. M. Hansen. *Hansen Solubility Parameters: A User’s Handbook, Second Edition*. 2nd ed. CRC Press, 2007 (cit. on p. 39).

[Hay01] K. Hayes. “Industrial Processes for Manufacturing Amines”. In: *Applied Catalysis A: General* 221.1-2 (2001), pp. 187–195 (cit. on pp. 33–35).

[HSB11] P. Heidebrecht, K. Sundmacher, and L. T. Biegler. “Optimal Design of Nonlinear Temperature Programmed Reduction Experiments”. In: *AIChE Journal* 57.10 (2011), pp. 2888–2901 (cit. on p. 13).

[Hen+15] B. Hentschel, G. Kiedorf, M. Gerlach, et al. “Model-Based Identification and Experimental Validation of the Optimal Reaction Route for the Hydroformylation of 1-Dodecene”. In: *Industrial & Engineering Chemistry Research* 54.6 (2015), pp. 1755–1765 (cit. on pp. 29, 41, 51, 73, 106, 128, 148, 150, 151, 167, 195).

[Hen+14a] B. Hentschel, A. Peschel, H. Freund, and K. Sundmacher. “Simultaneous Design of the Optimal Reaction and Process Concept for Multiphase Systems”. In: *Chemical Engineering Science* 115 (2014), pp. 69–87 (cit. on p. 29).

[Hen+14b] B. Hentschel, A. Peschel, M. Xie, et al. “Model-Based Prediction of Optimal Conditions for 1-Octene Hydroformylation”. In: *Chemical Engineering Science* 115 (2014), pp. 58–68 (cit. on p. 29).

[HU17] J. Herman and W. Usher. “SALib: An Open-Source Python Library for Sensitivity Analysis”. In: *The Journal of Open Source Software* 2.9 (2017), p. 97 (cit. on p. 165).

[Hil04] M. Hillestad. “A Systematic Generation of Reactor Designs: I. Isothermal Conditions”. In: *Computers & Chemical Engineering* 28.12 (2004), pp. 2717–2726 (cit. on p. 25).

[Hil05] M. Hillestad. “A Systematic Generation of Reactor Designs: II. Non-isothermal Conditions”. In: *Computers & Chemical Engineering* 29.5 (2005), pp. 1101–1112 (cit. on p. 25).

[Hoa+13] M. D. Hoang, T. Barz, V. A. Merchan, L. T. Biegler, and H. Arellano-Garcia. “Simultaneous Solution Approach to Model-Based Experimental Design”. In: *AIChE Journal* 59.11 (2013), pp. 4169–4183 (cit. on pp. 13, 18, 19).

[HS96] T. Homma and A. Saltelli. “Importance Measures in Global Sensitivity Analysis of Nonlinear Models”. In: *Reliability Engineering & System Safety* 52.1 (1996), pp. 1–17 (cit. on p. 164).

[Hor64] F. Horn. *Attainable and Non-Attainable Regions in Chemical Reaction Technique*. London, UK: Pergamon Press, 1964 (cit. on p. 22).

[Hou+15] B. Houska, D. Telen, F. Logist, M. Diehl, and J. F. Van Impe. “An Economic Objective for the Optimal Experiment Design of Nonlinear Dynamic Processes”. In: *Automatica* 51 (2015), pp. 98–103 (cit. on p. 17).

[Hux+21] F. Huxoll, S. Schlüter, R. Budde, et al. “Phase Equilibria for the Hydroaminomethylation of 1-Decene”. In: *Journal of Chemical & Engineering Data* 66.12 (2021), pp. 4484–4495 (cit. on p. 60).

[InP21] InPROMPT. *SFB Transregio 63 - InPrompt*. Collaborative Research Center/-Transregio 63 Integrated Chemical Processes in Liquid Multiphase Systems. 2021. URL: `https://www.inprompt.tu-berlin.de/` (visited on Sept. 26, 2021) (cit. on p. 2).

[Jag+18] S. A. Jagtap, S. P. Gowalkar, E. Monflier, A. Ponchel, and B. M. Bhanage. “Rhodium Catalyzed Selective Hydroaminomethylation of Biorenewable Eugenol under Aqueous Biphasic Condition”. In: *Molecular Catalysis* 452 (2018), pp. 108–116 (cit. on p. 37).

[JK04] E. Johannessen and S. Kjelstrup. “Minimum Entropy Production Rate in Plug Flow Reactors: An Optimal Control Problem Solved for SO_2 Oxidation”. In: *Energy*. Efficiency, Costs, Optimization, Simulation and Environmental Impact of Energy Systems 29.12 (2004), pp. 2403–2423 (cit. on p. 25).

[Jok20] M. Jokiel. “Optimale Reaktionsführung Durch Reaktor-Tandems Am Beispiel Der Hydroformylierung von 1-Dodecen”. Universitäts- und Landesbibliothek Sachsen-Anhalt, 2020 (cit. on pp. xi, 106, 112, 116, 122, 123, 126, 215).

[Jok+19] M. Jokiel, K. H. G. Rätze, N. M. Kaiser, et al. “Miniplant-Scale Evaluation of a Semibatch-Continuous Tandem Reactor System for the Hydroformylation of Long-Chain Olefins”. In: *Industrial & Engineering Chemistry Research* 58.7 (2019), pp. 2471–2480 (cit. on pp. xi, 106, 112, 116–119, 195, 214).

[Jör+17] A. Jörke, T. Gaide, A. Behr, et al. “Hydroformylation and Tandem Isomerization–Hydroformylation of n-Decenes Using a Rhodium-BiPhePhos Catalyst: Kinetic Modeling, Reaction Network Analysis and Optimal Reaction Control”. In: *Chemical Engineering Journal* 313 (2017), pp. 382–397 (cit. on pp. 41–44, 52, 54, 74, 106, 141, 142, 145, 167, 178, 260).

[JSH15] A. Jörke, A. Seidel-Morgenstern, and C. Hamel. “Isomerization of 1-Decene: Estimation of Thermodynamic Properties, Equilibrium Composition Calculation and Experimental Validation Using a Rh-BiPhePhos Catalyst”. In: *Chemical Engineering Journal* 260 (2015), pp. 513–523 (cit. on pp. 42, 53, 142, 145).

[JSH17] A. Jörke, A. Seidel-Morgenstern, and C. Hamel. “Rhodium-BiPhePhos Catalyzed Hydroformylation Studied by Operando FTIR Spectroscopy: Catalyst Activation and Rate Determining Step”. In: *Journal of Molecular Catalysis A: Chemical* 426 (2017), pp. 10–14 (cit. on p. 42).

[Jör+15] A. Jörke, S. Triemer, A. Seidel-Morgenstern, and C. Hamel. “Kinetic Investigation Exploiting Local Parameter Subset Selection: Isomerization of 1-Decene Using a Rh-BiPhePhos Catalyst”. In: *Chemie Ingenieur Technik* 87.6 (2015), pp. 713–725 (cit. on pp. 42, 44, 71, 75, 141, 142).

[Jos+16] F. Jost, K. Rinke, T. Fischer, E. Schalk, and S. Sager. “Optimum Experimental Design for Patient Specific Mathematical Leukopenia Models”. In: *IFAC-PapersOnLine* 49.26 (2016), pp. 344–349 (cit. on p. 18).

[KF19] M. Kaiser and H. Freund. “A Multimodular Pseudoheterogeneous Model Framework for Optimal Design of Catalytic Reactors Exemplified by Methanol Synthesis”. In: *Chemical Engineering Science* 206 (2019), pp. 401–423 (cit. on p. 29).

[Kai19] N. M. Kaiser. “Dynamic Optimization Based Reactor Synthesis and Design under Uncertainty for Liquid Multiphase Processes”. PhD thesis. Magdeburg: Otto von Guericke University, 2019 (cit. on pp. 21, 26, 29, 31, 38, 85, 134).

[KFS16] N. M. Kaiser, R. J. Flassig, and K. Sundmacher. “Probabilistic Reactor Design in the Framework of Elementary Process Functions”. In: *Computers & Chemical Engineering* 94 (2016), pp. 45–59 (cit. on pp. 29, 30).

[KFS17] N. M. Kaiser, R. J. Flassig, and K. Sundmacher. “Reactor-Network Synthesis via Flux Profile Analysis”. In: *Chemical Engineering Journal* 335 (2017), pp. 1018–1030 (cit. on pp. 29–31, 41, 87, 90, 134, 187).

[Kai+17] N. M. Kaiser, M. Jokiel, K. McBride, R. J. Flassig, and K. Sundmacher. “Optimal Reactor Design via Flux Profile Analysis for an Integrated Hydroformylation Process”. In: *Industrial & Engineering Chemistry Research* 56.40 (2017), pp. 11507–11518 (cit. on pp. 29, 31, 90, 106, 108, 121, 123, 125, 200, 204, 211).

[KU18] P. Kalck and M. Urrutigoïty. “Tandem Hydroaminomethylation Reaction to Synthesize Amines from Alkenes”. In: *Chemical Reviews* 118.7 (2018), pp. 3833–3861 (cit. on p. 37).

[Kar+15] F. Karst, M. Maestri, H. Freund, and K. Sundmacher. “Reduction of Microkinetic Reaction Models for Reactor Optimization Exemplified for Hydrogen Production from Methane”. In: *Chemical Engineering Journal* 281 (2015), pp. 981–994 (cit. on p. 29).

[Kau+02] S. Kauchali, W. C. Rooney, L. T. Biegler, D. Glasser, and D. Hildebrandt. “Linear Programming Formulations for Attainable Region Analysis”. In: *Chemical Engineering Science* 57.11 (2002), pp. 2015–2028 (cit. on p. 22).

[KN00] V. V. Kelkar and K. M. Ng. “Screening Multiphase Reactors for Nonisothermal Multiple Reactions”. In: *AIChE Journal* 46.2 (2000), pp. 389–406 (cit. on p. 25).

[Keß+19] T. Keßler, C. Kunde, S. Linke, et al. “Systematic Selection of Green Solvents and Process Optimization for the Hydroformylation of Long-Chain Olefines”. In: *Processes* 7.12 (2019), p. 882 (cit. on p. 39).

[Kie+14] G. Kiedorf, D. Hoang, A. Müller, et al. “Kinetics of 1-Dodecene Hydroformylation in a Thermomorphic Solvent System Using a Rhodium-Biphephos Catalyst”. In: *Chemical Engineering Science* 115 (2014), pp. 31–48 (cit. on pp. 41, 42, 73, 150).

[Kir+20a] S. Kirschtowski, F. Jameel, M. Stein, A. Seidel-Morgenstern, and C. Hamel. “Kinetics of the Reductive Amination of 1-Undecanal in Thermomorphic Multicomponent System”. In: *Chemical Engineering Science* 230 (2020), p. 116187 (cit. on pp. 39, 41, 45–47, 52, 143, 145, 167).

[Kir+20b] S. Kirschtowski, C. Kadar, A. Seidel-Morgenstern, and C. Hamel. “Kinetic Modeling of Rhodium-Catalyzed Reductive Amination of Undecanal in Different Solvent Systems”. In: *Chemie Ingenieur Technik*. Chemie Ingenieur Technik 92.5 (2020), pp. 582–588 (cit. on pp. 39, 41, 45).

[Kla11] A. Klamt. “The COSMO and COSMO-RS Solvation Models”. In: *WIREs Computational Molecular Science* 1.5 (2011), pp. 699–709 (cit. on p. 8).

[Kni+93] J. F. Knifton, J. Lin, D. A. Storm, and S. Wong. “New Synthesis Gas Chemistry”. In: *Catalysis Today* 18.4 (1993), pp. 355–384 (cit. on p. 36).

[Koh+13] C. Kohlpaintner, M. Schulte, J. Falbe, et al. “Aldehydes, Aliphatic”. In: *Ullmann’s Encyclopedia of Industrial Chemistry*. Weinheim, Germany: Wiley-VCH Verlag GmbH & Co. KGaA, 2013 (cit. on p. 41).

[KF91] A. C. Kokossis and C. A. Floudas. “Synthesis of Isothermal Reactor—Separator—Recycle Systems”. In: *Chemical Engineering Science* 46.5 (1991), pp. 1361–1383 (cit. on p. 23).

[Kör+99] S. Körkel, I. Bauer, H. G. Bock, and J. P. Schlöder. “A Sequential Approach for Nonlinear Optimum Experimental Design in DAE Systems”. In: *Scientific Computing in Chemical Engineering II*. Vol. 2. Berlin Heidelberg: Springer-Verlag, 1999, pp. 338–345 (cit. on p. 13).

[Kör+04] S. Körkel, E. Kostina, H. G. Bock, and J. P. Schlöder. “Numerical Methods for Optimal Control Problems in Design of Robust Optimal Experiments for Nonlinear Dynamic Processes”. In: *Optimization Methods and Software* 19.3-4 (2004), pp. 327–338 (cit. on p. 13).

[Kor20] W. Kortuz. “Kopplung von Hydroformylierung und Reduktiver Aminierung in der Tandemreaktion Hydroaminomethylierung -kinetische Modellbildung und Beschreibung-”. MA thesis. Magdeburg: Otto von Guericke University, 2020 (cit. on pp. 51, 52, 54, 145, 174, 175).

[Kor+22] W. Kortuz, S. Kirschtowski, A. Seidel-Morgenstern, and C. Hamel. “Kinetics of the Rhodium-Catalyzed Hydroaminomethylation of 1-Decene in a Thermomorphic Solvent System”. In: *Chemie Ingenieur Technik* 94.5 (2022), pp. 760–765 (cit. on pp. 51, 145, 173–175).

[KS94] R. Krishna and S. T. Sie. “Strategies for Multiphase Reactor Selection”. In: *Chemical Engineering Science* 49.24 (1994), pp. 4029–4065 (cit. on p. 25).

[Kuh+18] H. Kuhlmann, H. Veith, M. Möller, et al. “Optimization-Based Approach to Process Synthesis for Process Intensification: Synthesis of Reaction-Separation Processes”. In: *Industrial & Engineering Chemistry Research* 57.10 (2018), pp. 3639–3655 (cit. on pp. 24, 25).

[LN95] C. F. Leibovici and J. Neoschil. “A Solution of Rachford-Rice Equations for Multiphase Systems”. In: *Fluid Phase Equilibria* 112.2 (1995), pp. 217–221 (cit. on p. 9).

[Lei+03] D. B. Leineweber, I. Bauer, H. G. Bock, and J. P. Schlöder. “An Efficient Multiple Shooting Based Reduced SQP Strategy for Large-Scale Dynamic Process Optimization. Part 1: Theoretical Aspects”. In: *Computers & Chemical Engineering* 27.2 (2003), pp. 157–166 (cit. on p. 13).

[LK04] X. Li and A. Kraslawski. “Conceptual Process Synthesis: Past and Current Trends”. In: *Chemical Engineering and Processing: Process Intensification* 43.5 (2004), pp. 583–594 (cit. on pp. 19, 20).

[Lie+18] G. Liesche, D. Schack, K. H. G. Rätze, and K. Sundmacher. “Thermodynamic Network Flow Approach for Chemical Process Synthesis”. In: *Computer Aided Chemical Engineering*. Vol. 43. Elsevier, 2018, pp. 881–886 (cit. on pp. 26, 29, 32).

[LSS19] G. Liesche, D. Schack, and K. Sundmacher. “The FluxMax Approach for Simultaneous Process Synthesis and Heat Integration: Production of Hydrogen Cyanide”. In: *AIChE Journal* 65.7 (2019), e16554 (cit. on pp. 26, 29, 32).

[LK03a] P. Linke and A. Kokossis. “Attainable Reaction and Separation Processes from a Superstructure-Based Method”. In: *AIChE Journal* 49.6 (2003), pp. 1451–1470 (cit. on p. 24).

[LK03b] P. Linke and A. Kokossis. “On the Robust Application of Stochastic Optimisation Technology for the Synthesis of Reaction/Separation Systems”. In: *Computers & Chemical Engineering* 27.5 (2003), pp. 733–758 (cit. on p. 23).

[Lin+22] S. Linke, T. Kessler, C. Kunde, A. Kienle, and K. Sundmacher. “Integrated Solvent and Process Design”. In: *Integrated Chemical Processes in Liquid Multiphase Systems - From Chemical Reaction to Process Design*. Ed. by M. Kraume, S. Enders, A. Drews, et al. 1st ed. De Gruyter, 2022 (cit. on p. 135).

[LMS20] S. Linke, K. McBride, and K. Sundmacher. “Systematic Green Solvent Selection for the Hydroformylation of Long-Chain Alkenes”. In: *ACS Sustainable Chemistry & Engineering* 8.29 (2020), pp. 10795–10811 (cit. on p. 39).

[Lju99] L. Ljung. *System Identification: Theory for the User*. 2nd ed. Prentice Hall, 1999 (cit. on p. 14).

[Log+09] F. Logist, P. M. M. Van Erdeghem, I. Y. Smets, and J. F. Van Impe. “Optimal Design of Dispersive Tubular Reactors at Steady-State Using Optimal Control Theory”. In: *Journal of Process Control* 19.7 (2009), pp. 1191–1198 (cit. on p. 25).

[Log+11] F. Logist, B. Houska, M. Diehl, and J. F. Van Impe. “Robust Multi-Objective Optimal Control of Uncertain (Bio)Chemical Processes”. In: *Chemical Engineering Science* 66.20 (2011), pp. 4670–4682 (cit. on pp. 13, 17).

[LBS92] T. Lohmann, H. G. Bock, and J. P. Schloeder. “Numerical Methods for Parameter Estimation and Optimal Experiment Design in Chemical Reaction Systems”. In: *Industrial & Engineering Chemistry Research* 31.1 (1992), pp. 54–57 (cit. on pp. 13, 17).

[Lut+13] P. Lutze, D. K. Babi, J. M. Woodley, and R. Gani. “Phenomena Based Methodology for Process Synthesis Incorporating Process Intensification”. In: *Industrial & Engineering Chemistry Research* 52.22 (2013), pp. 7127–7144 (cit. on pp. 21, 24, 25).

[Luy11] W. L. Luyben. “Heuristic Design of Reaction/Separation Processes with Two Recycles”. In: *Industrial & Engineering Chemistry Research* 50.8 (2011), pp. 4788–4795 (cit. on p. 22).

[Ma+19] Y. Ma, A. El-Khoruy, Z. Yang, et al. “Simultaneous Synthesis and Design of Integrated Reaction-Separation Systems Using Rigorous Models”. In: *Computer Aided Chemical Engineering* 47 (2019), pp. 371–376 (cit. on p. 23).

[MSG17] E. Manesso, S. Sridharan, and R. Gunawan. “Multi-Objective Optimization of Experiments Using Curvature and Fisher Information Matrix”. In: *Processes* 5.4 (2017), p. 63 (cit. on pp. 13, 17).

[MRO17] A. Marcilla, J. Reyes-Labarta, and M. Olaya. “Should We Trust All the Published LLE Correlation Parameters in Phase Equilibria? Necessity of Their Assessment Prior to Publication”. In: *Fluid Phase Equilibria* 433 (2017), pp. 243–252 (cit. on pp. 9, 12).

[MLK01] E. Marcoulaki, P. Linke, and A. Kokossis. “Design of Separation Trains and Reaction-Separation Networks Using Stochastic Optimization Methods”. In: *Chemical Engineering Research and Design* 79.1 (2001), pp. 25–32 (cit. on p. 23).

[MK99] E. Marcoulaki and A. Kokossis. “Scoping and Screening Complex Reaction Networks Using Stochastic Optimization”. In: *AIChE Journal* 45.9 (1999), pp. 1977–1991 (cit. on p. 23).

[Mar+13] J. Markert, Y. Brunsch, T. Munkelt, et al. “Analysis of the Reaction Network for the Rh-catalyzed Hydroformylation of 1-Dodecene in a Thermomorphic Multicomponent Solvent System”. In: *Applied Catalysis A: General* 462–463 (2013), pp. 287–295 (cit. on p. 41).

[MF82] J. V. Martinez de Pinillos and R. L. Fowlkes. “United States Patent: 4314084 - Synthesis of Lower Alkyl Amines”. Pat. 4314084. Air Products and Chemicals, Inc. 1982 (cit. on p. 34).

[Mat21] S. Matthes. *Handelsblatt Disrupt. BASF-CEO Brudermüller: “Wir brauchen eine andere Zusammenarbeit zwischen Politik und Industrie”*. Podcast audio on 2021-06-18. 2021 (cit. on p. 1).

[MP78] G. Maurer and J. M. Prausnitz. “On the Derivation and Extension of the Uniquac Equation”. In: *Fluid Phase Equilibria* 2.2 (1978), pp. 91–99 (cit. on p. 8).

[Mau+19] J. Maußner, C. Dreiser, O. Wachsen, and H. Freund. “Systematic Model-based Design of Tolerant Chemical Reactors”. In: *Journal of Advanced Manufacturing and Processing* 1.3 (2019) (cit. on pp. 29, 30).

[McB17] K. McBride. “Model-Based Process Design and Solvent Selection for the Efficient Recovery of Homogeneous Catalyst in Chemicals Production”. PhD thesis. Magdeburg: Otto von Guericke University, 2017 (cit. on p. 38).

[McB+16] K. McBride, T. Gaide, A. Vorholt, A. Behr, and K. Sundmacher. “Thermomorphic Solvent Selection for Homogeneous Catalyst Recovery Based on COSMO-RS”. In: *Chemical Engineering and Processing: Process Intensification* 99 (2016), pp. 97–106 (cit. on pp. 39, 150, 200).

[MKS17] K. McBride, N. M. Kaiser, and K. Sundmacher. “Integrated Reaction–Extraction Process for the Hydroformylation of Long-Chain Alkenes with a Homogeneous Catalyst”. In: *Computers & Chemical Engineering* 105 (2017), pp. 212–223 (cit. on pp. 24, 37, 128, 199).

[McB+18] K. McBride, S. Linke, S. Xu, and K. Sundmacher. “Computer Aided Design of Green Thermomorphic Solvent Systems for Homogeneous Catalyst Recovery”. In: *Computer Aided Chemical Engineering*. Vol. 44. Elsevier, 2018, pp. 1783–1788 (cit. on p. 39).

[MS15] K. McBride and K. Sundmacher. “Data Driven Conceptual Process Design for the Hydroformylation of 1-Dodecene in a Thermomorphic Solvent System”. In: *Industrial & Engineering Chemistry Research* 54.26 (2015), pp. 6761–6771 (cit. on p. 199).

[MDM68] M. R. McCorkle, P. L. DuBrow, and B. E. Marsh. “Beta-Amines”. In: *Journal of the American Oil Chemists’ Society* 45.1 (1968), A10–A47 (cit. on p. 35).

[MF97] C. M. McDonald and C. A. Floudas. “GLOPEQ: A New Computational Tool for the Phase and Chemical Equilibrium Problem”. In: *Computers & Chemical Engineering* 21.1 (1997), pp. 1–23 (cit. on p. 9).

[MK97] V. L. Mehta and A. Kokossis. “Development of Novel Multiphase Reactors Using a Systematic Design Framework”. In: *Computers & Chemical Engineering*. Supplement to Computers and Chemical Engineering 21 (1997), S325–S330 (cit. on p. 25).

[MK00] V. L. Mehta and A. C. Kokossis. “Nonisothermal Synthesis of Homogeneous and Multiphase Reactor Networks”. In: *AIChE Journal* 46.11 (2000), pp. 2256–2273 (cit. on p. 25).

[MGH13] D. Ming, D. Glasser, and D. Hildebrandt. “Application of Attainable Region Theory to Batch Reactors”. In: *Chemical Engineering Science* 99 (2013), pp. 203–214 (cit. on p. 22).

[MMO13] M. Miremadi, C. Musso, and J. Oxgaard. “Chemical Innovation: An Investment for the Ages”. In: *McKinsey & Company* (2013), p. 9 (cit. on p. 2).

[Mit+18] A. Mitsos, N. Asprion, C. A. Floudas, et al. “Challenges in Process Optimization for New Feedstocks and Energy Sources”. In: *Computers & Chemical Engineering* 113 (2018), pp. 209–221 (cit. on p. 19).

[Mon+21] M. S. Monjur, S. E. Demirel, J. Li, and M. M. F. Hasan. “SPICE_MARS: A Process Synthesis Framework for Membrane-Assisted Reactive Separations”. In: *Industrial & Engineering Chemistry Research* 60.20 (2021), pp. 7635–7655 (cit. on pp. 24, 25).

[Mos+12] S. Mosbach, A. Braumann, P. L. Man, et al. “Iterative Improvement of Bayesian Parameter Estimates for an Engine Model by Means of Experimental Design”. In: *Combustion and Flame* 159.3 (2012), pp. 1303–1313 (cit. on p. 13).

[MP19] A. R. G. Mukkula and R. Paulen. “Optimal Experiment Design in Nonlinear Parameter Estimation with Exact Confidence Regions”. In: *Journal of Process Control* 83 (2019), pp. 187–195 (cit. on p. 13).

[MBS10] D. Y. Murzin, A. Bernas, and T. Salmi. “Kinetic Modelling of Regioselectivity in Alkenes Hydroformylation over Rhodium”. In: *Journal of Molecular Catalysis A: Chemical* 315.2 (2010), pp. 148–154 (cit. on p. 41).

[NE19] C. Nentwich and S. Engell. “Surrogate Modeling of Phase Equilibrium Calculations Using Adaptive Sampling”. In: *Computers and Chemical Engineering* 126 (2019), pp. 204–217 (cit. on p. 153).

[Nen21] C. Nentwich. “Surrogate Modeling of Fugacity Coefficients Using Adaptive Sampling”. PhD thesis. TU Dortmund, Faculty for Bio- and Chemical Engineering, 2021 (cit. on p. 153).

[NKE21] C. Nentwich, S. Kaiser, and S. Engell. “Surrogate Models for Thermodynamic Equilibria of Gas-Liquid and Liquid-Liquid Systems”. In: *Integrated Chemical Processes in Liquid Multiphase Systems - From Chemical Reaction to Process Design*. Ed. by M. Kraume, S. Enders, A. Drews, et al. 1st ed. De Gruyter, 2021 (cit. on p. 153).

[NVE19] C. Nentwich, C. Varela, and S. Engell. “Optimization of Chemical Processes Applying Surrogate Models for Phase Equilibrium Calculations”. In: *2019 International Joint Conference on Neural Networks (IJCNN)*. 2019 International Joint Conference on Neural Networks (IJCNN). 2019, pp. 1–8 (cit. on p. 153).

[NK71] M. Newberger and R. Kadlec. “Optimal Operation of a Tubular Chemical Reactor”. In: *AIChE Journal* 17.6 (1971), pp. 1381–1387 (cit. on p. 25).

[Nez+18] M. Nezhadfard, L. S. Emami, N. Kasiri, et al. “Development of a Reaction/Distillation Matrix for Systematic Generation of Sequences in a Single Two Component Reaction-Separation Case Study”. In: *Computers & Chemical Engineering* 117 (2018), pp. 268–282 (cit. on p. 23).

[PF18] F. Päßler and H. Freund. “Modellbasierter Entwurf energieeffizienter Reaktoren”. In: *Chemie Ingenieur Technik* 90.6 (2018), pp. 852–863 (cit. on p. 29).

[PH70] J. D. Paynter and D. E. Haskins. “Determination of Optimal Reactor Type”. In: *Chemical Engineering Science* 25.9 (1970), pp. 1415–1422 (cit. on p. 25).

[PR76] D.-Y. Peng and D. B. Robinson. “A New Two-Constant Equation of State”. In: *Industrial & Engineering Chemistry Fundamentals* 15.1 (1976), pp. 59–64 (cit. on p. 8).

[PFS10] A. Peschel, H. Freund, and K. Sundmacher. “Methodology for the Design of Optimal Chemical Reactors Based on the Concept of Elementary Process Functions”. In: *Industrial & Engineering Chemistry Research* 49.21 (2010), pp. 10535–10548 (cit. on pp. 29, 30).

[Pes+12a] A. Peschel, B. Hentschel, H. Freund, and K. Sundmacher. “Design of Optimal Multiphase Reactors Exemplified on the Hydroformylation of Long Chain Alkenes”. In: *Chemical Engineering Journal* 188 (2012), pp. 126–141 (cit. on p. 29).

[Pes+11a] A. Peschel, B. Hentschel, H. Freund, and K. Sundmacher. “Optimal Reactor Design for the Hydroformylation of Long Chain Alkenes in Biphasic Liquid Systems”. In: *21st European Symposium on Computer Aided Process Engineering*. Vol. 29. Computer Aided Chemical Engineering. Elsevier, 2011, pp. 1246–1250 (cit. on p. 29).

[Pes+12b] A. Peschel, A. Jörke, K. Sundmacher, and H. Freund. “Optimal Reaction Concept and Plant Wide Optimization of the Ethylene Oxide Process”. In: *Chemical Engineering Journal* 207–208 (2012), pp. 656–674 (cit. on p. 29).

[Pes+11b] A. Peschel, F. Karst, H. Freund, and K. Sundmacher. “Analysis and Optimal Design of an Ethylene Oxide Reactor”. In: *Chemical Engineering Science* 66.24 (2011), pp. 6453–6469 (cit. on p. 29).

[Pfe04] A. Pfennig. *Thermodynamik der Gemische*. Berlin, Heidelberg: Springer Berlin Heidelberg, 2004 (cit. on p. 137).

[PKF18] A. Pietschak, M. Kaiser, and H. Freund. “Tailored Catalyst Pellet Specification for Improved Fixed-Bed Transport Characteristics: A Shortcut Method for the Model-Based Reactor Design”. In: *Chemical Engineering Research and Design* 137 (2018), pp. 60–74 (cit. on p. 29).

[PLM90] J. Pinto, M. Lobão, and J. Monteiro. “Sequential Experimental Design for Parameter Estimation: A Different Approach”. In: *Chemical Engineering Science* 45.4 (1990), pp. 883–892 (cit. on pp. 15, 17).

[PLM91] J. Pinto, M. Lobão, and J. Monteiro. “Sequential Experimental Design for Parameter Estimation: Analysis of Relative Deviations”. In: *Chemical Engineering Science* 46.12 (1991), pp. 3129–3138 (cit. on pp. 15, 17).

[Por20] A. W. Porter. “On the Vapour-Pressures of Mixtures”. In: *Transactions of the Faraday Society* 16 (December 1920), p. 336 (cit. on p. 8).

[PM08] A. Posada and V. Manousiouthakis. “Multi-Feed Attainable Region Construction Using the Shrink–Wrap Algorithm”. In: *Chemical Engineering Science* 63.23 (2008), pp. 5571–5592 (cit. on p. 22).

[Rät+22] K. H. G. Rätze, S. Linke, A. Weber, et al. “Selection Criteria for Liquid Multiphase Systems”. In: *Integrated Chemical Processes in Liquid Multiphase Systems - From Chemical Reaction to Process Design*. Ed. by M. Kraume, S. Enders, A. Drews, et al. 1st ed. De Gruyter, 2022 (cit. on pp. xi, 135).

[Rät+19] K. H. G. Rätze, M. Jokiel, N. M. Kaiser, and K. Sundmacher. “Cyclic Operation of a Semi-Batch Reactor for the Hydroformylation of Long-Chain Olefins and Integration in a Continuous Production Process”. In: *Chemical Engineering Journal* 377 (2019), p. 120453 (cit. on pp. xi, 106, 108, 109, 111, 116, 195, 204, 205, 214, 254).

[RJS22] K. H. G. Rätze, M. Jokiel, and K. Sundmacher. “Optimal Design of Reactors for Complex Reaction Systems”. In: *Integrated Chemical Processes in Liquid Multiphase Systems - From Chemical Reaction to Process Design*. Ed. by M. Kraume, S. Enders, A. Drews, et al. 1st ed. De Gruyter, 2022 (cit. on pp. xi, 28–31).

[Rät+23] K. H. Rätze, W. Kortuz, S. Kirschtowski, et al. “Optimal Experimental Design for the Identification of a Reaction Kinetic Model for the Hydroaminomethylation of 1-Decene in a Thermomorphic Multiphase System”. In: *Chemical Engineering Journal* 469 (2023), p. 143713 (cit. on pp. xi, 50).

[Rec+15] S. Recker, M. Skiborowski, C. Redepenning, and W. Marquardt. “A Unifying Framework for Optimization-Based Design of Integrated Reaction–Separation Processes”. In: *Computers & Chemical Engineering* 81 (2015), pp. 260–271 (cit. on pp. 24, 25).

[Rec+14] S. Recker, M. Skiborowski, C. Redepenning, and W. Marquardt. “Systematic and Optimization-Based Design of Integrated Reaction-Separation Processes”. In: *Comput Aided Chem Eng* 34 (2014), pp. 417–422 (cit. on p. 24).

[RK48] O. Redlich and A. T. Kister. “Algebraic Representation of Thermodynamic Properties and the Classification of Solutions”. In: *Industrial & Engineering Chemistry* 40.2 (1948), pp. 345–348 (cit. on p. 8).

[Rei+96] W. Reif, DE, L. Franz, et al. “United States Patent: 5530127 - Preparation of Amines”. Pat. 5530127. BASF Aktiengesellschaft, DE. 1996 (cit. on p. 34).

[RP68] H. Renon and J. M. Prausnitz. “Local Compositions in Thermodynamic Excess Functions for Liquid Mixtures”. In: *AIChE Journal* 14.1 (1968), pp. 135–144 (cit. on p. 8).

[RE99] T. Rische and P. Eilbracht. “One-Pot Synthesis of Pharmacologically Active Secondary and Tertiary 1-(3,3-Diarylpropyl)Amines via Rhodium-Catalysed Hydroaminomethylation of 1,1-Diarylethenes”. In: *Tetrahedron* 55.7 (1999), pp. 1915–1920 (cit. on pp. 36, 39).

[RE97] T. Rische and P. Eilbracht. “One-Pot Synthesis of Secondary and Tertiary Amines by Carbonylative Hydroaminomethylation of Alkenes Catalyzed by Di(-Chloro)Bis(H4-1,5-Cyclooctadiene)Dirhodium”. In: *Synthesis* 1997.11 (1997), pp. 1331–1337 (cit. on p. 36).

[Roj+96] A. Rojnuckarin, C. Floudas, H. Rabitz, and R. Yetter. “Methane Conversion to Ethylene and Acetylene: Optimal Control with Chlorine, Oxygen, and Heat Flux”. In: *Industrial and Engineering Chemistry Research* 35.3 (1996), pp. 683–696 (cit. on p. 25).

[Roj+93] A. Rojnuckarin, C. A. Floudas, H. Rabitz, and R. A. Yetter. “Optimal Control of a Plug Flow Reactor with a Complex Reaction Mechanism”. In: *The Journal of Physical Chemistry* 97.45 (1993), pp. 11689–11695 (cit. on p. 25).

[Roo+00] W. C. Rooney, B. P. Hausberger, L. T. Biegler, and D. Glasser. “Convex Attainable Region Projections for Reactor Network Synthesis”. In: *Computers & Chemical Engineering* 24.2 (2000), pp. 225–229 (cit. on p. 22).

[Roo+15] P. Roose, K. Eller, E. Henkes, R. Rossbacher, and H. Höke. “Amines, Aliphatic”. In: *Ullmann’s Encyclopedia of Industrial Chemistry*. Weinheim, Germany: Wiley-VCH Verlag GmbH & Co. KGaA, 2015 (cit. on pp. 33–36).

[Sag13] S. Sager. “Sampling Decisions in Optimum Experimental Design in the Light of Pontryagin’s Maximum Principle”. In: *SIAM Journal on Control and Optimization* 51.4 (2013), pp. 3181–3207 (cit. on pp. 14, 18).

[Sal+10] A. Saltelli, P. Annoni, I. Azzini, et al. “Variance Based Sensitivity Analysis of Model Output. Design and Estimator for the Total Sensitivity Index”. In: *Computer Physics Communications* 181.2 (2010), pp. 259–270 (cit. on pp. 164, 166).

[Sal+05] A. Saltelli, M. Ratto, S. Tarantola, and F. Campolongo. “Sensitivity Analysis for Chemical Models”. In: *Chemical Reviews* 105.7 (2005), pp. 2811–2828 (cit. on p. 164).

[Sch+20] D. Schack, A. Jastram, G. Liesche, and K. Sundmacher. “Energy-Efficient Distillation Processes by Additional Heat Transfer Derived From the FluxMax Approach”. In: *Frontiers in Energy Research* 8.134 (2020) (cit. on pp. 29, 32).

[SLS19] D. Schack, G. Liesche, and K. Sundmacher. “Simultaneous Heat and Mass Flow Optimization of a Distillation Column Applying the FluxMax Approach”. In: *Chemical Engineering Transactions* 76 (2019), pp. 337–342 (cit. on pp. 29, 32).

[SLS20] D. Schack, G. Liesche, and K. Sundmacher. “The FluxMax Approach: Simultaneous Flux Optimization and Heat Integration by Discretization of Thermodynamic State Space Illustrated on Methanol Synthesis Process”. In: *Chemical Engineering Science* 215 (2020), p. 115382 (cit. on pp. 29, 32).

[Sch+95] G. Schembecker, T. Dröge, U. Westhaus, and K. Simmrock. “READPERT - Development, Selection and Design of Chemical Reactors”. In: *Chemical Engineering and Processing: Process Intensification* 34.3 (1995), pp. 317–322 (cit. on p. 25).

[Sch+21] S. Schlüter, K. U. Künnemann, M. Freis, et al. “Continuous Co-Product Separation by Organic Solvent Nanofiltration for the Hydroaminomethylation in a Thermomorphic Multiphase System”. In: *Chemical Engineering Journal* 409 (2021), p. 128219 (cit. on pp. 37, 59, 155).

[SG10] B. Schmid and J. Gmehling. “From van Der Waals to VTPR: The Systematic Improvement of the van Der Waals Equation of State”. In: *The Journal of Supercritical Fluids* 55.2 (2010), pp. 438–447 (cit. on p. 8).

[SG16] B. Schmid and J. Gmehling. “Present Status of the Group Contribution Equation of State VTPR and Typical Applications for Process Development”. In: *Fluid Phase Equilibria* 425 (2016), pp. 443–450 (cit. on p. 8).

[SG11] B. Schmid and J. Gmehling. “The Universal Group Contribution Equation of State VTPR Present Status and Potential for Process Development”. In: *Fluid Phase Equilibria* 302.1-2 (2011), pp. 213–219 (cit. on p. 8).

[Sch+13] M. J. Schneider, M. Lijewski, R. Woelfel, M. Haumann, and P. Wasserscheid. “Continuous Gas-Phase Hydroaminomethylation Using Supported Ionic Liquid Phase Catalysts”. In: *Angewandte Chemie* 125.27 (2013), pp. 7134–7137 (cit. on p. 37).

[Soa72] G. Soave. “Equilibrium Constants from a Modified Redlich-Kwong Equation of State”. In: *Chemical Engineering Science* 27.6 (1972), pp. 1197–1203 (cit. on p. 8).

[Sob67] I. M. Sobol. “On the Distribution of Points in a Cube and the Approximate Evaluation of Integrals”. In: *USSR Computational Mathematics and Mathematical Physics* 7.4 (1967), pp. 86–112 (cit. on p. 178).

[Sob01] I. M. Sobol. “Global Sensitivity Indices for Nonlinear Mathematical Models and Their Monte Carlo Estimates”. In: *Mathematics and Computers in Simulation* 55.1-3 (2001), pp. 271–280 (cit. on p. 164).

[Sob93] I. M. Sobol. “Sensitivity Estimates for Nonlinear Mathematical Models”. In: *Mathematical Modelling and Computational Experiments* 4 (1993), pp. 407–414 (cit. on p. 164).

[SS15] H. Soltani and S. Shafiei. “Adiabatic Reactor Network Synthesis Using Coupled Genetic Algorithm with Quasi Linear Programming Method”. In: *Chemical Engineering Science* 137 (2015), pp. 601–612 (cit. on p. 23).

[Ste+99] E. Stein, A. Kienle, A. R. J. Esparta, K. D. Mohl, and E. D. Gilles. “Optimization of a Reactor Network for Ethylene Glycol Synthesis — An Algorithmic Approach”. In: *Computers & Chemical Engineering*. European Symposium on Computer Aided Process Engineering 23 (1999), S903–S906 (cit. on p. 23).

[SF10] K. Sundmacher and H. Freund. “Chemical Process Design: Moving Matter Elements along Optimal Travel Routes in the Thermodynamic State Space”. In: PSE Asia 2010: The 5th International Symposium on Design, Operation and Control of Chemical Processes. Singapore, 2010, pp. 1–7 (cit. on pp. 26–28).

[Tag+85] V. Taglieber, W. Hölderich, R. Kummer, W. D. Mross, and G. Saladin. “Verfahren Zur Herstellung von Aminen”. Pat. P 33 26 579.8 (Germany). BASF AG. 1985 (cit. on p. 35).

[Tas20] Task Force on Digital Financing of the Sustainable Development Goals. *People’s Money: Harnessing Digitalization to Finance a Sustainable Future*. United Nations, 2020 (cit. on p. 1).

[Tel+13] D. Telen, B. Houska, F. Logist, et al. “Optimal Experiment Design under Process Noise Using Riccati Differential Equations”. In: *Journal of Process Control* 23.4 (2013), pp. 613–629 (cit. on p. 13).

[Tel+12] D. Telen, F. Logist, E. Van Derlinden, I. Tack, and J. Van Impe. “Optimal Experiment Design for Dynamic Bioprocesses: A Multi-Objective Approach”. In: *Chemical Engineering Science* 78 (2012), pp. 82–97 (cit. on pp. 13, 17).

[Tih+08] A. Tihic, G. M. Kontogeorgis, N. von Solms, M. L. Michelsen, and L. Constantinou. “A Predictive Group-Contribution Simplified PC-SAFT Equation of State: Application to Polymer Systems”. In: *Industrial & Engineering Chemistry Research* 47.15 (2008), pp. 5092–5101 (cit. on p. 8).

[Uni15a] United Nations. *General Assembly Resolution: Transforming Our World: The 2030 Agenda for Sustainable Development*. A/RES/70/1. United Nations, 2015 (cit. on p. 1).

[Uni15b] United Nations. “Paris Agreement”. In: *United Nations Treaty Series*. United Nations Framework Convention on Climate Change. No. 54113. Paris, 2015 (cit. on p. 1).

[UQH11] A. A. Upadhye, W. Qi, and G. W. Huber. “Conceptual Process Design: A Systematic Method to Evaluate and Develop Renewable Energy Technologies”. In: *AIChE Journal* 57.9 (2011), pp. 2292–2301 (cit. on p. 22).

[vThi+16] S. van Thienen, A. Clinton, M. Mahto, and Brenna Sniderman. “Industry 4.0 and the Chemicals Industry: Catalyzing Transformation through Operations Improvement and Business Growth”. In: *Deloitte University Press* (2016), p. 24 (cit. on p. 1).

[Váz+13] M. Vázquez-Ojeda, J. G. Segovia-Hernández, S. Hernández, A. Hernández-Aguirre, and A. A. Kiss. “Design and Optimization of an Ethanol Dehydration Process Using Stochastic Methods”. In: *Separation and Purification Technology* 105 (2013), pp. 90–97 (cit. on p. 23).

[Ved+99] G. A. Vedage, K. S. Hayes, M. Leeaphon, and J. N. Armor. “United States Patent: 5932769 - Multi-metallic Actalysts for Amination of Alcohols to Form Alkylamines”. Pat. 5932769. Air Products and Chemicals, Inc. 1999 (cit. on p. 34).

[Ver21] Verband der Chemischen Industrie e.V. *Chemiemärkte Weltweit - Rankings*. 2021. URL: `https://www.vci.de/ergaenzende-downloads/chemiemaerkte-weltweit-rankings.pdf` (visited on Sept. 25, 2021) (cit. on p. 1).

[VCV98] K. Versyck, J. Claes, and J. Van Impe. “Optimal Experimental Design for Practical Identification of Unstructured Growth Models”. In: *Mathematics and Computers in Simulation* 46.5-6 (1998), pp. 621–629 (cit. on p. 17).

[VV98] K. Versyck and J. Van Impe. “Trade-Offs in Design of Fed-Batch Experiments for Optimal Estimation of Biokinetic Parameters”. In: *Proceedings of the 1998 IEEE International Conference on Control Applications (Cat. No.98CH36104)*. 1998 International Conference on Control Applications. Vol. 1. Trieste, Italy: IEEE, 1998, pp. 51–55 (cit. on p. 17).

[VG00] P. F. Vogt and J. J. Gerulis. “Amines, Aromatic”. In: *Ullmann’s Encyclopedia of Industrial Chemistry*. Weinheim, Germany: Wiley-VCH Verlag GmbH & Co. KGaA, 2000 (cit. on p. 34).

[Vor+17] A. J. Vorholt, S. Immohr, K. A. Ostrowski, S. Fuchs, and A. Behr. “Catalyst Recycling in the Hydroaminomethylation of Methyl Oleate: A Route to Novel Polyamide Monomers: Catalyst Recycling in the Hydroaminomethylation with Amino Nitriles”. In: *European Journal of Lipid Science and Technology* 119.5 (2017), p. 1600211 (cit. on p. 37).

[WB06] A. Wächter and L. T. Biegler. “On the Implementation of an Interior-Point Filter Line-Search Algorithm for Large-Scale Nonlinear Programming”. In: *Mathematical Programming* 106.1 (2006), pp. 25–57 (cit. on pp. 18, 61).

[WR19] E. A. Walker and K. Ravisankar. “Bayesian Design of Experiments: Implementation, Validation and Application to Chemical Kinetics”. In: *ArXiv* 1909.03861 (2019) (cit. on p. 13).

[Was+96] S. K. Wasylkiewicz, L. N. Sridhar, M. F. Doherty, and M. F. Malone. “Global Stability Analysis and Calculation of Liquid−Liquid Equilibrium in Multicomponent Mixtures”. In: *Industrial & Engineering Chemistry Research* 35.4 (1996), pp. 1395–1408 (cit. on p. 9).

[WG87] U. Weidlich and J. Gmehling. “A Modified UNIFAC Model. 1. Prediction of VLE, h^{E}, and γ^{∞}”. In: *Industrial & Engineering Chemistry Research* 26.7 (1987), pp. 1372–1381 (cit. on pp. 8, 199).

[Wes04] A. W. Westerberg. “A Retrospective on Design and Process Synthesis”. In: *Computers & Chemical Engineering* 28.4 (2004), pp. 447–458 (cit. on pp. 20, 21).

[Wil64] G. M. Wilson. “Vapor-Liquid Equilibrium. XI. A New Expression for the Excess Free Energy of Mixing”. In: *Journal of the American Chemical Society* 86.2 (1964), pp. 127–130 (cit. on p. 8).

[XF18a] M. Xie and H. Freund. “Fast Synthesis of Optimal Chemical Reactor Networks Based on a Universal System Representation”. In: *Chemical Engineering and Processing - Process Intensification* 123 (2018), pp. 280–290 (cit. on pp. 21, 29).

[XF18b] M. Xie and H. Freund. “Optimal Reactor Design and Operation Taking Catalyst Deactivation into Account”. In: *Chemical Engineering Science* 175 (2018), pp. 405–415 (cit. on p. 29).

[XF18c] M. Xie and H. Freund. “Rigorous Design of Multiphase Reactors: Identification of Optimal Conditions for Mass Transfer Limited Reactions”. In: *Chemical Engineering and Processing - Process Intensification* 124 (2018), pp. 174–185 (cit. on pp. 29, 30, 84, 85, 99).

[Yaw99] C. Yaws. *Chemical Properties Handbook: Physical, Thermodynamics, Environmental Transport, Safety & Health Related Properties for Organic &*. Chemical Engineering Books. McGraw-Hill Education, 1999 (cit. on p. 146).

[Ye+21] H. Ye, X. Zou, W. Zhu, et al. “Synthesis Framework for Distillation Sequence with Sidestream Columns: Application in Reaction-Separation-Recycle System”. In: *Chemical Engineering Research and Design* 166 (2021), pp. 172–190 (cit. on p. 23).

[Yue20] A. Yuen. “Synthesis of Performance-Optimal Heat Exchanger Networks Using Attainable Regions”. In: *Computers and Chemical Engineering* 142 (2020) (cit. on p. 22).

[ZM08] W. Zhou and V. I. Manousiouthakis. “On Dimensionality of Attainable Region Construction for Isothermal Reactor Networks”. In: *Computers & Chemical Engineering* 32.3 (2008), pp. 439–450 (cit. on p. 22).

[ZRS16] A. Zinser, L. Rihko-Struckmann, and K. Sundmacher. “Dynamic Method for Computation of Chemical and Phase Equilibria”. In: *Computers & Chemical Engineering* 89 (2016), pp. 1–10 (cit. on p. 9).

[ŽN16] L. A. ŽivkoviL and N. M. NikaLeviL. “A Method for Reactor Synthesis Based on Process Intensification Principles and Optimization of Superstructure Consisting of Phenomenological Modules”. In: *Chemical Engineering Research and Design* 113 (2016), pp. 189–205 (cit. on pp. 24, 25).

List of Symbols

Symbols

Greek		
Θ	set of uncertain parameters	various
Σ	variance-covariance matrix	various
Π	set comprising all phases	–
$\mathcal{T}$	time domain	min
α	relative volatility	$\mathrm{mol\,mol^{-1}}$
β	mass transfer coefficient	$\mathrm{min^{-1}}$
γ	activity coefficient, colinearity measure	–
ϵ	deviation between measurement and prediction	various
ε	machine precision, small number	various
η	measurement data	various
θ	uncertain parameters	various
ϑ	temperature	°C
κ	bleeding of species to secondary phases, invertibility measure	–
μ	chemical potential	$\mathrm{J\,mol^{-1}}$
ν	stoichiometric matrix	–
ρ	density, correlation matrix	$\mathrm{g\,L^{-1}}$, –
σ	standard deviation	various
τ	residence time	min
τ_A	surface stress	Pa
ϕ	fugacity coefficient, objective function, ratio, activation function	various
φ	differential reaction flux	–
ω	sampling decisions	–
Latin		
$\emptyset$	empty set	–
A	molar Helmholtz free energy, dimensionless kinetic constant	$\mathrm{J\,mol^{-1}}$, –

$\mathcal{A}$	surface area	m^2
B	dimensionless kinetic constant	–
C	approximated confidence region, capacity matrix	–, various
E	elementary process matrix	various
E_A	activation energy	$\mathrm{J\,mol^{-1}}$
$\mathcal{EXP}$	set of experiments	–
F	Fisher information matrix	various
G	molar Gibbs enthalpy, state of a fluid element	$\mathrm{J\,mol^{-1}}$, –
ΔG_r	Gibbs enthalpy of reaction	$\mathrm{J\,mol^{-1}}$
H	molar enthalpy, Henry coefficient	$\mathrm{J\,mol^{-1}}$, $\mathrm{bar\,L\,mol^{-1}}$
$\Delta_\mathrm{f} H$	molar enthalpy of formation	$\mathrm{J\,mol^{-1}}$
$\Delta_\mathrm{s} H$	molar enthalpy of solution	$\mathrm{J\,mol^{-1}}$
K^eq, K	equilibrium constant, distribution coefficient, inhibition coefficient	–
K_N	Nernst coefficient	–
$\tilde{M}$	molar mass	$\mathrm{g\,mol^{-1}}$
$\dot{N}$	molar flow	$\mathrm{mol\,min^{-1}}$
$\mathbb{N}_0$	positive natural numbers including zero	–
$\mathbb{N}_+$	positive natural numbers excluding zero	–
$\mathcal{P}$	time-independent control set	various
R	universal gas constant	$\mathrm{J\,K^{-1}\,mol^{-1}}$
$\mathcal{RCT}$	set of reactions	–
$\mathcal{RCT}^\mathrm{HAM}$	set of reactions in the hydroaminomethylation	–
$\mathcal{RCT}^\mathrm{Hyfo}$	set of reactions in the hydroformylation	–
$\mathcal{RCT}^\mathrm{RA}$	set of reactions in the reductive amination	–
$\mathbb{R}$	real numbers	–
S	selectivity, molar entropy	–, $\mathrm{J\,mol^{-1}\,K^{-1}}$
$\mathcal{S}$	first order Sobol index	–
$\mathcal{S}_\mathrm{T}$	total order Sobol index	–
$\mathcal{STR}$	set comprising all streams	–
$\Delta_\mathrm{f} S$	molar entropy of formation	$\mathrm{J\,mol^{-1}\,K^{-1}}$
$\mathcal{SPC}$	set of chemical species	–
$\mathcal{SPC}^\mathrm{ANN}$	set of chemical species in ANN	–

$\mathcal{SPC}^{\mathrm{Gas}}$	set of gaseous chemical species	–
$\mathcal{SPC}^{y}$	set of measured chemical species	–
T	temperature	K
$\mathcal{U}$	time-dependent control set	various
V	volume	L
$\dot{V}$	volumetric flow rate	$\mathrm{L\,min^{-1}}$
W	weight factor matrix	various
X	conversion	–
$\mathcal{X}$	states set	various
Y	yield	–
Z	compressibility factor	–
a	activity	–
c	molar concentration	$\mathrm{mol\,L^{-1}}$
c	constants	various
c_{p}	isobaric heat capacity	$\mathrm{J\,mol^{-1}\,K^{-1}}$
d_{TPD}	tangent plane distance	$\mathrm{J\,mol^{-1}}$
f	fugacity, RHS of an ODE system	bar, various
f_{V}	volume force	$\mathrm{N\,m^{-3}}$
g	AE system, rate of geometrical change of a fluid element, path inequality constraints	various
g^{f}	terminal inequality constraints	various
h	path equality constraints	various
h^{f}	terminal equality constraints	various
h_{FE}	finite element width	–
j	dosing / diffusion flow	$\mathrm{mol\,min^{-1}}$
k	kinetic rate factor	various
k_0	collision factor	various
m	mass	g
$\dot{m}$	mass flux	$\mathrm{g\,m^{-2}}$
n, n	molar amount, number of	mol, –
p	pressure	bar
p	time-independent decision variables	various
$\dot{q}$	heat flux	W
r	reaction rate	$\mathrm{mol\,min^{-1}\,L^{-1}}$
s	slope	various
t	time	min

u	inputs	various
$\boldsymbol{u}$	time-dependent decision variables	various
v	volume fraction, velocity	$\mathrm{L\,L^{-1}}$, $\mathrm{m\,s^{-1}}$
w	mass fraction	$\mathrm{g\,g^{-1}}$
w_t	technical work	J
w'	bias vector	various
x	molar fraction in the liquid phase	$\mathrm{mol\,mol^{-1}}$
x_t	total molar fraction	$\mathrm{mol\,mol^{-1}}$
$\boldsymbol{\chi}$	state variables	various
y	molar fraction in the gaseous phase	$\mathrm{mol\,mol^{-1}}$
$\boldsymbol{y}$	measured variables / outputs	various

Sub- and Superscripts

0	initial value
$\mathrm{A}, \mathrm{D}, \mathrm{E}$	optimality criteria
$\mathcal{A}$	areal relation
BPP	BiPhePhos
CP	collocation point
CSS	cyclic steady-state
E	excess
FE	finite element
Gas	gaseous
HK	high key component
IG	ideal gas
IM	ideal mixture
L	lower bound value
LK	light key component
Lig	ligand
Liq	liquid
M	(real) mixture
NP	non-polar
OP	operating point
P	polar
ST	storage tank
U	upper bound value
V	volume-based

bot	bottom position
cat	active catalyst
Σcat	catalyst precursor
cycle	process cycle
eff	effective
eq	equilibrium
exp	experiment
f	final value
fresh	fresh components entering the process
idle	simulation stage without reaction
in	inlet
m	mass-based
make − up	make-up stream
n	molar-based
n/iso	linear to branched aldehyde ratio
PhaseEq	phase equilibrium
prior	prior / previous information
prod	product
purge	purge
red	reduced
ref	reference
sat	saturation
set	setpoint
sim	simulation
sp	sampling point
sub	substrate
top	distillate stream
total	total
−	removal
+	dosing / addition
Σ	continuous
$\overline{\square}$	average value
$\dot{\square}$	flow
$\hat{\square}$	estimated value, expectation value
$\square_{\neg\square}$	without
$(\square)$	phase
$\tilde{\square}$	normalized, scaled, transformed variable

$\square^*$ optimal solution, true value, reference to an element

Acronyms and Abbreviations

AD	automatic differentiation
Add	(aldol) addition reaction of the reductive amination
AE	algebraic equation
amine	n,n-diethylundecylamine (hydrogenated)
ANN	artificial neural network
ANOVA	analysis of variance
AR	attainable region
BiPhePhos	6,6′-[(3,3′-Di-tert-butyl-5,5′-dimehtoxy-1,1′-biphenyl-2,2′-diyl)bis(oxy)]bis(dibenzo[d,f][1,3,2]dioxaphosphepin)
C10an	n-decane
C12en	dodecene isomers including nC12en
CAMPD	computer-aided molecular and process design
caPSS	computer-aided phase system selection
cf.	compare
CO	carbon monoxide
Cond	(enamine) condensation reaction of the hydroaminomethylation
CPH	chemical properties handbook
CRLB	Cramér-Rao lower bound
CSS	cyclic steady-state
CSTR	continuously stirred tank reactor
DAE	differential algebraic equation
Dbuffer	downstream buffer tank
DEA	diethylamine
Dec	decanter
DIPPR	design institute for physical properties
Dist	distillation column
DMF	n,n-dimethylformamide
DoE	design of experiments

DoF	degree of freedom
DOP	dynamic optimization program
DSR	differential side-stream reactor
enamine	n,n-diethylundecylamine
EoS	equation of state
EPF	elementary process functions
FD	factorial design
FE	finite element
FIM	Fisher information matrix
FPA	flux profile analysis
FTIR	Fourier transform infrared spectroscopy
G/L	gas-liquid
GC	group contribution
GDP	generalized disjunctive programming
GEM	Gibbs enthalpy minimization
H_2	hydrogen
H_2O	water
HAM	hydroaminomethylation
HydDec	1-decene hydrogenation in the hydroaminomethylation
HydEn	enamine hydrogenation in the hydroaminomethylation and reductive amination
Hydi	hydrogenation of dodecene isomers
Hydn	hydrogenation of 1-dodecene
HydUndec	1-undecanal hydrogenation in the hydroaminomethylation and reductive amination
Hyfo	hydroformylation
Hyfoi	hydroformylation of dodecene isomers
Hyfon	hydroformylation of 1-dodecene to n-tridecanal
Hyfoni	hydroformylation of 1-dodecene to tridecanal isomers
iC10en	decene isomers
iC11al	undecanal isomers

iC12en	dodecene isomers
iC13al	aldehyde isomers with 13 carbon atoms
IG	ideal gas
IL	ionic liquid
IM	ideal mixture
InPROMPT	Integrated Chemical Processes in Liquid Multiphase Systems
IPOPT	interior point optimizer
Iso	olefin isomerization reaction in the hydroaminomethylation
L/L	liquid-liquid
LCA	live cycle assessment
LICQ	linear independency constraint qualification
LLE	liquid-liquid equilibrium
LSQ	least-squares
mbOED	model-based optimal experimental design
MeOH	methanol
MES	micellar emulsion system
MINLP	mixed-integer non-linear optimization program
MLRD	multi-level reactor design
modUNIFAC	modified UNIFAC(Dortmund)
MPC	model predictive control
mpEPF	multiphase elementary process functions
N_2	nitrogen
nC10en	1-decene
nC11al	1-undecanal
nC12an	n-dodecane
nC12en	1-dodecene
nC13al	n-tridecanal
NLP	non-linear optimization program
NRTL	non-random two liquid
OCP	optimal control problem
ODE	ordinary differential equation

OFAT	one factor at a time
PBu3	tributylphosphine
PC-SAFT	perturbed-chain statistical associating fluid theory
PFR	plug-flow reactor
PI	process intensification
PSE	process sytems engineering
RA	reductive amination
REACH	Registration, Evaluation, Authorisation and Restriction of Chemicals
Rh(acac)(COD)	(acetylacetonato)(1,5-cyclooctadiene)rhodium(I)
RHS	right hand side
RSBR	repeatedly operated semibatch reactor
S/L	solid-liquid
SALib	sensitivity analysis library
SBR	semibatch reactor
SILP	supported ionic liquid phase catalyst
SM	simultaneous design
SQ	sequential design
SulfoXantphos	4,5-bis(diphenylphosphino)-9,9-dimethyl-2,7-disulfoxanthene disodium salt
TMS	thermomorphic multiphase system
TPD	tangent plane distance
Ubuffer	upstream (feed) buffer tank
UCST	upper critical solution temperature
UNIFAC	universal functional activity coefficient
UNIQUAC	universal quasi-chemical
V/L	vapor-liquid
VTRP	volume-translated Peng-Robinson
w.r.t.	with respect to

List of Figures

List of Tables

,

Colophon

This thesis was typeset with LaTeX 2$_\varepsilon$. It uses the *Clean Thesis* style developed by Ricardo Langner. The design of the *Clean Thesis* style is inspired by user guide documents from Apple Inc.

Download the *Clean Thesis* style at `http://cleanthesis.der-ric.de/`.